



Hybrid III-V on silicon lasers for telecommunication applications

Marco Lamponi

► To cite this version:

Marco Lamponi. Hybrid III-V on silicon lasers for telecommunication applications. Other [cond-mat.other]. Université Paris Sud - Paris XI, 2012. English. NNT : 2012PA112039 . tel-00769402

HAL Id: tel-00769402

<https://theses.hal.science/tel-00769402>

Submitted on 1 Jan 2013

HAL is a multi-disciplinary open access archive for the deposit and dissemination of scientific research documents, whether they are published or not. The documents may come from teaching and research institutions in France or abroad, or from public or private research centers.

L'archive ouverte pluridisciplinaire **HAL**, est destinée au dépôt et à la diffusion de documents scientifiques de niveau recherche, publiés ou non, émanant des établissements d'enseignement et de recherche français ou étrangers, des laboratoires publics ou privés.



THESE DE DOCTORAT

Spécialité : Physique

Ecole Doctorale “*Sciences et Technologies de l'Information des
Télécommunications et des Systèmes*”

LASERS INP SUR CIRCUITS SILICIUM POUR APPLICATIONS EN TELECOMMUNICATIONS

MARCO LAMPONI

Soutenue le 15 Mars 2012 devant le jury composé de :

M _{me}	Beatrice Dagens	Présidente du Jury
M _r	Daniel Dolfi	Examinateur
M _r	Guang-Hua Duan	Encadrant
M _r	Lorenzo Pavesi	Rapporteur
M _r	Jean-Marc Fedeli	Examinateur
M _r	Pierre Viktorovitch	Rapporteur
M _r	Laurent Vivien	Directeur de thèse

CONTENTS

1 Introduction and state of the art of III-V silicon lasers

1.1	Silicon photonics: motivation	12
1.2	State of the art of silicon laser.....	13
1.2.1	Silicon and Germanium sources	13
1.2.2	III-V laser on silicon.....	15
1.2.3	Integration routes.....	15
1.2.4	Bonding techniques.....	15
1.2.5	Fabry-Perot lasers.....	16
1.2.6	Racetrack resonator lasers	19
1.2.7	Distributed Bragg reflector lasers.....	20
1.2.8	Distributed feedback lasers	21
1.2.9	Array Waveguide Grating laser	22
1.2.10	Microdisk lasers and hybrid microring lasers	23
1.3	Our approach to hybrid silicon laser	25
1.4	Thesis context.....	26
1.5	Bibliography.....	28

2 Principle of the light coupling from III-V to silicon

2.1	Light coupling in hybrid lasers	32
2.2	Directional and adiabatic coupling.....	32
2.3	Hybrid III-V on SOI laser based on adiabatic taper.....	36
2.3.1	III-V and SOI used wafers.....	37
2.4	New concept on a double taper structure with deep ridge waveguide	38
2.4.1	Coupling section design.....	38
2.4.2	Optimization using Fimmwave	40
2.4.3	Tolerance analysis	45
2.5	Structure with double taper with shallow/deep ridge transition	47
2.5.1	Optimization using Fimmwave	48
2.6	Optimized adiabatic taper	50
2.6.1	From the analytical model to the taper shape	50
2.6.2	Coupling coefficient κ	51
2.6.3	Simulation results	52
2.6.4	Optimization for 400 and 500 nm thick silicon	53

2.7	Conclusions.....	58
2.8	Bibliography.....	59

3 How to achieve a single mode laser

3.1	DBR laser	62
3.1.1	Sampled Grating DBR	63
3.2	Rings resonator mirrors lasers.....	64
3.2.1	Microring resonator principle	64
3.2.2	One ring resonator design.....	66
3.2.3	Double ring based tunable laser designs.....	67
3.2.4	Spectral linewidth analysis	71
3.3	DFB laser.....	73
3.3.1	Grating on the III-V	74
3.3.2	Grating on silicon.....	78
3.4	AWG laser.....	86
3.4.1	Principle	86
3.5	Conclusions.....	87
3.6	Bibliography.....	89

4 Fabrication process

4.1	Fabrication steps	90
4.2	Bonding.....	91
4.2.1	Molecular bonding	91
4.2.2	DVS-BCB bonding.....	93
4.3	Lithography.....	95
4.3.1	Contact lithography	95
4.3.2	Electron Beam lithography.....	98
4.3.3	Conclusions.....	101
4.4	Etching on Hybrid III-V/SOI samples.....	101
4.4.1	Chemical etching	101
4.4.2	Dry etching	105
4.4.3	Conclusions.....	112
4.5	Metallization and annealing	113
4.6	Conclusions – Final identified process steps	115
4.7	Bibliography.....	117

5 Experimental results

5.1	Measurements setups	118
5.2	Fabry-Perot hybrid lasers by DVS-BCB bonding	119
5.2.1	Deep ridge design	119
5.2.2	Shallow/deep ridge design	120
5.2.3	Current threshold and slope efficiency simulations.....	122
5.3	Fabry-Perot hybrid lasers by molecular bonding	124
5.3.1	Shallow ridge design.....	124
5.3.2	Far field measurement	127
5.3.3	Comparison with DVS-BCB bonded devices.....	128
5.4	Ring resonator laser	129
5.4.1	L-I-V characteristics	129
5.4.2	Spectral analysis	130
5.4.3	Thermal analysis.....	132
5.4.4	Conclusions.....	135

6 Conclusions and outlook

REMERCIEMENTS

La fin de mes travaux de thèse approche à grands pas. Si je pense au temps qui s'est écoulé depuis ce 15 septembre 2008 quand tout a commencé, je revois dans mes souvenirs un grand nombre de visages, de discussions, de moments. Parmi toutes ces personnes qui m'apparaissent, beaucoup méritent ma gratitude : certains parce qu'ils ont directement contribué au succès de ces travaux en y participant activement, d'autres parce qu'ils n'ont cessé de me soutenir, de partager, de me corriger, d'être à mes côtés bien qu'ils n'aient été nullement impliqués dans mon projet de recherche.

Je voudrais essayer ici de les rappeler tous ; que ceux que je pourrais oublier ne m'en veuillent pas pour ce malheureux oubli.

Je tiens à démarrer par mes soutiens des premiers jours et je vais leur dire dans notre langue pour être sûrs de se comprendre. Grazie Clarita, grazie Leonello, grazie perché in fondo e senza dubbio alcuno è tutto merito vostro. Grazie a mio fratello, ai miei zii; e grazie a mia zia Laura ed ai miei nonni, che sarebbero stati felici di leggere queste pagine, ne sono sicuro.

Je voudrais ensuite remercier tous mes maîtres, que ce soit ceux de l'école maternelle, du lycée ou encore de l'université, toutes les personnes qui m'ont dédié leur temps avec passion pour me transmettre le goût d'apprendre.

Parmi eux, dernier en ligne chronologique, je remercie Guang-Hua Duan qui a encadré ces travaux avec disponibilité, exigence et passion. Duan a su, le long de ces trois années, diriger ma formation, répondre avec patience et gentillesse à mes questions, écouter et débattre avec intérêt de mes idées, propositions et convictions. Nous avons travaillé côté à côté de bonnes et de mauvaises journées, voyagé, défendu nos idées et nos résultats ; j'en garde un très bon souvenir.

Je remercie Guilhem de Valicourt, sans lui qu'aurait été cette thèse? Je ne peux même pas l'imaginer. Dans la vie parfois le hasard fait bien les choses et je n'aurais pu espérer trouver mieux pour partager mon bureau.

Presque tous ce que je connais de la fabrication des semiconducteurs je le dois à Francis Poingt. Il a su m'introduire dans le monde périlleux des salles blanches, entre ces machines qui m'étaient si étranges et qui me sont aujourd'hui si familières. Si j'ai finalement obtenu des composants qui fonctionnent, c'est en grande partie grâce à lui. Son humour, sa sensibilité et sa queue-de-cheval ont rendu mon chemin plus facile pendant ces trois ans. Merci.

Je remercie Laurent Vivien, mon directeur de thèse, je regrette de ne pas avoir profité plus (par ma faute) de sa disponibilité, de sa sympathie et de ses compétences. Nos discussions m'ont toujours permis de trouver de nouvelles perspectives sur ce que je faisais. Laurent a été simplement irréprochable avec moi et cela a été un plaisir de travailler avec lui.

Un merci à Alban Lelievre et Hoi Leung qui ont participé à la conception et à la mesure de certains des composants présentés dans ce travail. Merci à Christophe Jany qui s'est plus récemment occupé de la fabrication, à François Lelarge pour les epitaxies, à Dalila Make qui s'est chargée du clivage et du montage de puces, à Olivier Drisse et Estelle Deroin pour les écritures e-beam.

Je remercie Romain Brenot. Romain m'a beaucoup appris, les discussions techniques que j'ai eues avec lui ont été parmi les plus fructueuses et utiles de ma thèse. Sans oublier son caractère doux et aimable.

Je remercie Frédéric Vandijk pour toutes les réponses ponctuelles à mes questions ; Alain Accard pour son expérience très précieuse; Michael Tran et Bouzid Simozrag pour avoir écouté mes galères de technologue et m'avoir proposé de bonnes solutions ; Frederic Pommereau parce que est-ce que on ferait sans PomPom ?

Merci à Charles Cayron, protagoniste d'un inoubliable court-métrage de vulgarisation scientifique ; à Nadine Lagay pour son sourire contagieux ; à Nathalie Martin pour son précieux support psychologique. Et à Valérie Enjolras pour avoir corrigé mon français (s'il y a des erreurs, c'est sa faute).

1 INTRODUCTION AND STATE OF THE ART OF III-V SILICON LASERS

Ubi major minor cessat

Let's imagine you can add a photonic integrated circuit to a microelectronic chip. Let's imagine you can fabricate and sell billions of electronic-photonics integrated devices at an extremely low price. Let's imagine the huge number of applications that you could potentially address. Let's imagine, and you will quickly understand the extreme technological potential offered by silicon photonics.

In the last ten years, silicon photonics has known a dramatic acceleration. Many companies have invested in this technology and several ambitious research projects, in collaboration with universities and public research centers, have been launched.

What is silicon photonics? Silicon photonics aims to be the meeting point between silicon fabrication standards and photonics. On the one hand we want to bring the low cost of silicon manufacturing to photonics, integrating different photonics building blocks on a silicon on insulator wafer. On the other hand we want to join microelectronics and photonics worlds, realizing a single chip that embeds a photonic circuit and a microelectronic circuit.

In this thesis I describe our original approach to the key problem of silicon photonics laser source. Starting from the state of the art of silicon photonics lasers, I will introduce our heterogeneous integrated III-V on SOI lasers, discussing the design issues, analyzing the fabrication challenges and presenting the achieved results.

This chapter is organized as follows: in section 1.1 I describe the motivation of this work, in section 1.2 the state of the art of silicon photonics lasers is presented, section 1.3 introduces our approach to the design of a hybrid III-V on silicon laser and finally section 1.4 describes the thesis context.

1.1 Silicon photonics: motivation

What are the main potential applications that lead the development of silicon photonics today? Microelectronic industries need to solve the limitation of in-chip and intra-chip interconnects [1]. Telecommunication companies need to reduce the production costs of photonics devices to address high volume exponentially growing markets, as FTTH for example [2] [3]. The silicon photonics advantage, from a photonics point of view, is to take profit from the low cost mass production of a microelectronic fabrication line. From a microelectronics perspective, the advantage is the possibility to enable an on chip and intra-chip optical communications, to boost the speed of microprocessor and computer over the limit of copper line speed. INTEL and IBM proposed new architectures, integrating a photonic layer on microelectronic circuits, to profit from the large bandwidth and from the insensitivity to electromagnetic noise of optic communications. Alcatel-Lucent and NTT among the biggest communication industries, Kotura and Calliope among the small and new companies, provide a few examples of telecommunication actors that believe in a silicon solution to FTTH. They will probably launch some products based on this technology in the next five years.

As in microelectronics, the key for the success of integration in photonics is to realize a broad range of optical functionalities with a small set of elementary components, and to develop a generic wafer-scale technology for integration. Functional demonstration of major building blocks has been demonstrated. Passive devices like waveguides, array waveguide gratings, MMI, vertical couplers, polarization rotators, filters, etc. on silicon on insulator wafers show decent performances. Active components like 40 Gbit/s modulators, pin and avalanche photodetectors on silicon have been demonstrated as well. These components demonstrated close and sometimes even better performances than the traditional optical technologies. However, there are many challenges and issues to be addressed before bringing photonics on CMOS to a mature industrial level.

The missing element among the building blocks for silicon photonics is a high performance, low cost, robust laser source. The realization of a laser directly on silicon is particularly difficult due to the silicon physical properties. The electronic band structure of silicon does not present a direct band gap, which is a fundamental requirement to efficiently obtain stimulated emission. To overcome this limitation the heterogeneous integration of III-V semiconductors on top of a Silicon-On-Insulator wafer has been proposed by several authors [4] [5] [6].

This thesis aims at demonstrating a horizontal cavity hybrid laser based on the bonding of III-V material on top of a Silicon-On-Insulator wafer, with performances compatible with access network communication requirements.

1.2 State of the art of silicon laser

1.2.1 Silicon and Germanium sources

A true monolithically fabricated injection type silicon laser would greatly simplify the photonic integration with the CMOS platform, and accelerate the development of silicon photonics. For this reason, a huge effort is directed to an all Si-based or silicon compatible light source.

Achieving a light source from silicon, or silicon compatible material such as germanium, represents a very challenging task, mainly for the indirect band-gap silicon electronic structure. An indirect band-gap implies low radiative recombination efficiency, as the radiative transition needs the assistance of a momentum conserving phonon. This means that electron-hole pairs have very long radiative lifetimes, in the ms range. With such a long lifetime the e-h pairs can move freely on an average distance of few μm . Thus, the probability to encounter a non radiative recombination center is high. As a consequence the non-radiative recombination lifetime is much shorter in silicon (a few nanoseconds) and most of the excited e-h pairs recombine non-radiatively. It has to be also noticed that population inversion (a mandatory condition to achieve laser action) it is difficult to be obtained in silicon. In fact fast non-radiative processes as Auger recombination or free carrier absorption become significant under high excitation, and deplete the excited population. [7]

Face to these limitations, several ways to improve silicon radiative properties have been proposed. In this section we try to give a picture of the actual state of the art.

Extremely thin p-n junctions [8] and extremely pure bulk silicon [9] have been used to achieve respectively stimulated emission and efficient silicon LED. Others solutions involved band structure

engineering [10] or implantation induced strain [11]. Others rely on quantum confinement effects in low dimensional silicon [12]. Electrically pumped Er-doped Si nanoclusters have recently shown an optical material gain of 1 dB/cm [13].

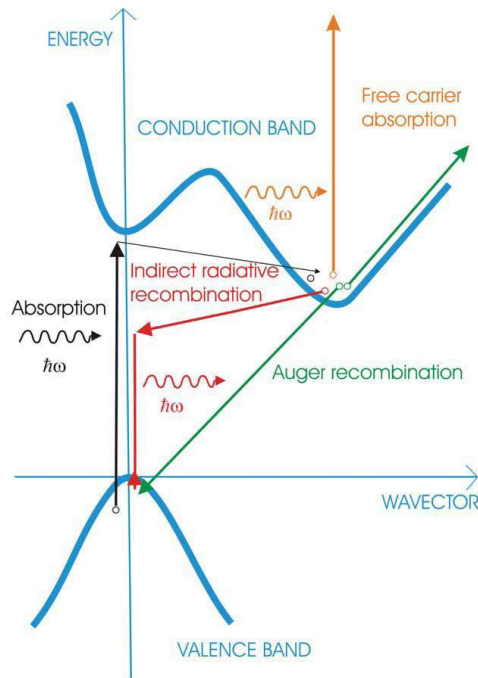


Figure 1.1: Simplified energy diagram of Si. The most relevant transitions are shown [14]

Another approach that is drawing increasing attention is based on strained germanium. It has been shown that Ge can become a direct band gap material under a strong tensile strain [15]. For example for a tensile strain of 2%, the band gap becomes direct, and the shifted bandgap gives an emission wavelength of 2.34 μm [16].

To maintain the emission wavelength around 1550 nm, a different approach that compensates for the energy difference between Γ and L valleys in germanium has been proposed recently [17]. Applying more tensile strain the energy difference between direct and indirect bandgap is reduced, at the same time n-doping the germanium partially fills the indirect conduction band. After these two steps the first empty level of the direct conduction band is at the same energy level that the first empty level in the indirect band; excess electrons injected in the structure will now be able to recombine via the direct transition that has much shorter lifetime. It has been shown by theoretical calculations that a net gain of 400 cm^{-1} could be achieved in 0.25% tensile-strained n+ Ge. Recently this approach has been demonstrated. Net optical gain [18] and lasing [19] at room temperature under optical pumping from its direct gap transition has been achieved. A gain of almost 50 cm^{-1} has been observed at 1605 nm.

In conclusion, several ways to achieve a monolithically integrated silicon based laser have been explored during the last ten years. Important results have been obtained, especially using Er-doped silicon nanoclusters and strained germanium. Very recently the first germanium laser on silicon has been demonstrated using optical pumping. However, these devices are obviously at a preliminary stage, and performances are still far from being sufficient. Electrical injection presents new

fabrication challenges related to the high germanium n-type and p-type doping [20]. It is hard to say if there is enough room for improvement, to meet the industrial applications needs.

1.2.2 III-V laser on silicon

III-V semiconductors are generally used to fabricate high-efficiency electrically injected lasers. Thanks to their direct bandgap and large gain value, they could be integrated with silicon to provide efficient lasers for silicon photonics. In the last ten years several configurations of hybrid III-V on silicon laser have been demonstrated, including microdisks, Fabry-Perot lasers, racetrack resonator lasers, distributed feedback (DFB) lasers and distributed Bragg reflector (DBR) lasers. The majority of the devices operate under continuous-wave electrical injection. The development of this research field is due to the maturation of silicon photonics, particularly through the work of European research teams (IMEC, LETI, III-V Lab, INL) supported by the European community, and American teams (UCSB, CALTECH, Intel) supported by grants from Intel Corp. and from the Defence Advanced Research Projects Agency (DARPA).

In this section we will summarize the different integrations techniques and laser designs that have been realized up to now.

1.2.3 Integration routes

Three main methods have been identified to integrate III-V material on silicon. The first one, the flip-chip technology, allows to directly bond individual lasers to a silicon-on-insulator (SOI) substrate by means of metal bumps [21]. The flip-chip is a mature technology but a precise alignment ($< 1 \mu\text{m}$) is needed to couple light from an active component into an on-chip waveguide. The time consuming process and the low integration density that it enables lead to high fabrication costs. This method has been used in the first silicon photonic product, the active cables designed and fabricated by Luxtera [22].

The second approach is the monolithic integration of III-V materials by hetero-epitaxial growth on a silicon substrate [23]. This technique could lead to highly integrated devices and to a real wafer scale process, but the large dislocation density measured in the deposited layers degrades the electro-optical properties and represents still a major limitation.

The last technique employed is the heterogeneous integration of III-V materials by die or wafer bonding. A III-V stack is transferred from its original growth substrate to a SOI wafer by means of bonding techniques. The III-V laser diodes are then fabricated on the SOI wafer using wafer-scale processing. This technique allows a high density of integration, collective processing and the use of high-quality III-V layers. The laser structure can be designed to ensure a direct coupling of the light into a silicon waveguide underneath. [5]

1.2.4 Bonding techniques

The III-V stack (dies or wafers) can be bonded on a SOI wafer without strict alignment tolerances. With die-to-wafer bonding we can further reduce the integration process costs since expensive III-V materials do not need to be bonded everywhere but they can be bonded only where they are

needed. We can mainly list three kinds of bonding that are employed in literature: molecular bonding, adhesive bonding and metal bonding.

Molecular bonding is based on the Van Der Waals interactions between two oxidized and hydrophilic surfaces. The bonding layer thickness can be reduced to less than ten nanometers. Therefore a very intimate contact between the surfaces is needed and the bonding quality is very sensitive to the surface roughness and particles [24]. The bonding layer thickness can vary between few nanometers and several hundred nanometers.

Adhesive bonding uses the thermosetting polymer divinylsiloxane benzocyclobutene (DVS-BCB) as a bonding agent. DVS-BCB can compensate for the surface roughness, therefore the bonding tolerances are relaxed compared to molecular bonding. However, the bonding layer thickness cannot be easily reduced below fifty nanometers and the thermal conductance is lower in DVS-BCB than in silica. [25]

Metal bonding is characterized by low bonding temperature, high thermal conductivity, no critical cleanliness requirements and a potentially conductive interface between silicon and bonded layers. However, due to its strong light absorption, the bonding metals have to be kept far from the light propagation area [26].

Hybrid silicon lasers have been achieved using all these techniques; anyhow, a large majority of the published works on this topic uses molecular bonding and DVS-BCB bonding to realize heterogeneous integration.

1.2.5 Fabry-Perot lasers

Fabry-Perot lasers are the starting point towards more complex laser designs. Several kind of electrically injected Fabry-Perot hybrid lasers have been developed during the last ten years. All the bonding techniques previously cited have been used. The performances achieved by the different research teams are shown in Table 1.1. In this section we briefly summarize the geometry of the employed designs.

The UCSB and INTEL groups, the pioneers of hybrid silicon lasers, have developed a laser structure based on evanescent coupling [4]. The III-V stack is integrated by molecular bonding. The bonding layer is extremely thin, around 5 nm. The optical mode is mainly confined on the silicon waveguide while there is just an evanescent tail overlapping the overlying III-V active material. As the III-V mesa is quite large, a H⁺ proton implantation on both sides of the mesa is necessary to prevent lateral current leakage. A schematic view of this laser structure is given in Figure 1.2. This solution has already given very interesting results. However, as the multi quantum well optical confinement is low, the lasing threshold of those devices is quite high and the power consumption is far from standard III-V lasers performances. Moreover, as the bonding layer is extremely thin, this technique is particularly sensitive to particles contamination, epitaxy roughness and wafer bow.

Other groups around the world have employed this design concept with minor adaptations (CALTEC group [6], Data Storage Institute Singapore [27], IMEC [28]).

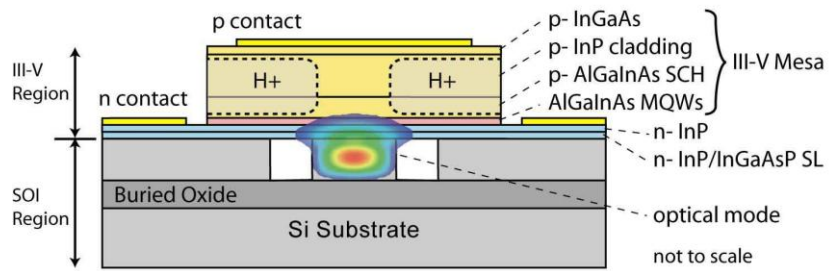


Figure 1.2: schematic drawing of the Fabry-Perot laser structure with the optical mode superimposed

A radically different concept was developed in parallel by IMEC, LETI and III-V lab. In this case the bonding layer is thicker, between 50 and 300 nm, the optical mode is confined by a III-V straight waveguide, at both ends of this waveguide an adiabatic coupler transfers the optical mode to an underlying silicon waveguide. The III-V waveguide is electrically pumped and provide gain to the structure while optical feedback is provided by silicon waveguide. The optical feedback is supplied by a cleaved or etched facet, or by a large optical bandwidth Bragg grating [29].

This architecture overcomes the low quantum wells overlap issue inherent in silicon evanescent lasers. The complete transfer results in a larger available gain for a smaller injection current and theoretically, a lower threshold and power consumption.

Different approaches have been investigated. In an IMEC configuration the laser diode is butt-coupled to a polymer waveguide after which the optical mode is gradually transformed into the SOI waveguide mode. This coupling layout is represented schematically in Figure 1.3 [30].

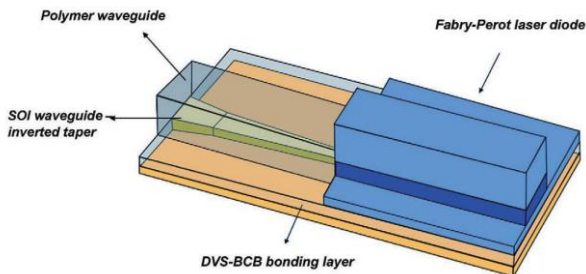


Figure 1.3: schematic of the layout of the optical coupling using an inverted adiabatic taper approach [30]

In a LETI configuration the adiabatic taper is located inside the silicon waveguide. As the width of the silicon waveguide is increased the optical mode is adiabatically transferred from one waveguide to the other as shown in Figure 1.4. [31]

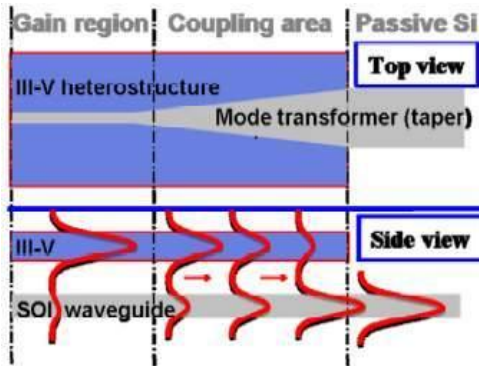


Figure 1.4: top and side views of a taper (mode transformer) showing the transfer of the supermode from the upper active waveguide to the lower silicon waveguide [31]

All Fabry-Perot hybrid lasers, and more generally all kinds of hybrid lasers on SOI, present a thermal behavior that is still far from the best performance achieved in pure III-V semiconductors. This is related to the high thermal resistance of the bonded laser diodes, arising from the low thermal conductivity of the bonding layer (both DVS-BCB and SiO_2) and the presence of the 2 μm thick buried oxide layer on the SOI waveguide substrate. [32]

Gold-based metallization layers made by lift-off are usually used to on InP technology. Nevertheless gold acts as a deep doping level in silicon and is therefore strictly forbidden in a microelectronics clean room. CMOS compatible gold free ohmic contacts on both n-InP and p-InGaAs layers were obtained with microelectronics standard. These developments led to the fabrication of a Fabry-Perot laser on silicon [33].

By incorporating an absorbing region in front of the lasing output, Fabry-Pérot mode-locked lasers on silicon with a repetition frequency up to 40 Ghz were also demonstrated. [34]

Finally, two main categories of Fabry-Perot laser have been presented, one, based on “evanescent” coupling between silicon and III-V which is already quite mature but presents performance and fabrication limitations. The other, based on complete transfer of the optical mode which is more recent but can potentially offer better results.

Bonding type	Coupling scheme	Characterisation	Remarks	Year	Ref.
Die-to-wafer adhesive DVS-BCB bonding (thickness=300 nm)	adiabatic taper butt joined to the active waveguide	Pumping regime: CW $\lambda \sim 1555 \text{ nm}$ $P_{\max} = 1,9 \text{ mW}$ (5°C)	Integrated photodetectors. Dry-etch facets.	2006	[30]
Wafer-to-wafer Molecular bonding (thickness < 5 nm)	Evanescence on SOI channel waveguide	Pumping regime: CW $\lambda = 1577 \text{ nm}$ (at 70 mA) $I_{\text{th}} = 65 \text{ mA}$ $T_{\max} = 40^\circ\text{C}$ $P_{\max} = 1,8 \text{ mW}$	H^+ implantation on both sides of the mesa	2006	[4]
Wafer-to-wafer Molecular bonding (thickness < 5 nm)	Evanescence on SOI rib waveguide	Pumping regime: CW $\lambda = 1326 \text{ nm}$ (at 100 mA) $I_{\text{th}} = 30 \text{ mA}$ $T_{\max} = 105^\circ\text{C}$ $P_{\max} = 5,5 \text{ mW}$	The second order transverse mode is lasing	2007	[35]

Wafer-to-wafer Molecular bonding (thickness < 5 nm)	Evanescence on SOI rib waveguide	Pumping regime: CW Mode locking with 4 ps pulses at 10 and 40 GHz	Integrated absorber for mode locking	2007	[34]
Wafer-to-wafer Molecular bonding (thickness < 5 nm)	Evanescence on SOI channel waveguide	Pumping regime: CW $\lambda = 1490 \text{ nm}$ $I_{th} = 60 \text{ mA}$ $T_{max} = 45^\circ\text{C}$ $P_{max} = 12.5 \text{ mW}$	Hybrid mode on the output	2009	[36]
Die-to-wafer Molecular bonding (thickness: 400 nm)	none	Pumping regime: CW $\lambda = 1565 \text{ nm}$ $I_{th} = 200 \text{ mA}$ $P_{max} = 1.5 \text{ mW}$	Contacts free of gold	2009	[33]
Die-to-wafer Molecular bonding (thickness: 100 nm)	Taper on silicon waveguide	Pumping regime: quasi-CW $\lambda = 1570 \text{ nm}$ $I_{th} = 100 \text{ mA}$ $P_{max} = 7.5 \text{ mW}$	Wide band DBR mirror reflector	2010	[31]
Die-to-wafer adhesive DVS-BCB (thickness: 45nm)	Evanescence on SOI rib waveguide	Pumping regime: CW $\lambda = 1310 \text{ nm}$ $I_{th} = 65 \text{ mA}$ $P_{max} = 3 \text{ mW}$	Hybrid mode on the output	2011	[28]

Table 1.1: state of the art of Fabry-Perot hybrid laser on silicon

1.2.6 Racetrack resonator lasers

Racetrack resonator lasers are a simple solution to define laser cavities without dicing and facet polishing. A hybrid version of racetrack resonator lasers have been demonstrated using the evanescent coupling scheme developed for Fabry-Pérot lasers [4]. A schematic view of the proposed device is shown in Figure 1.5 [37]. A directional coupler placed on the bottom arm is used to couple the light out of the racetrack region. Two integrated hybrid photodetectors measure the laser characteristics.

A mode-locked racetrack resonator laser (7 ps pulses at 30 GHz) based on the same cavity structure was also demonstrated [38].

Table 1.2 summarizes the principle characteristics of demonstrated racetrack resonators. Two main drawbacks characterize racetracks lasers. On the one hand the large footprint of the device reduces the integration possibilities, and, as the active waveguide is very long, we can achieve high output power but with an extremely high threshold and power consumption. On the other hand, the laser can oscillate on two counter propagating directions: clockwise and counterclockwise. This phenomenon leads to an unstable behavior of the L-I curve and of the optical spectrum.

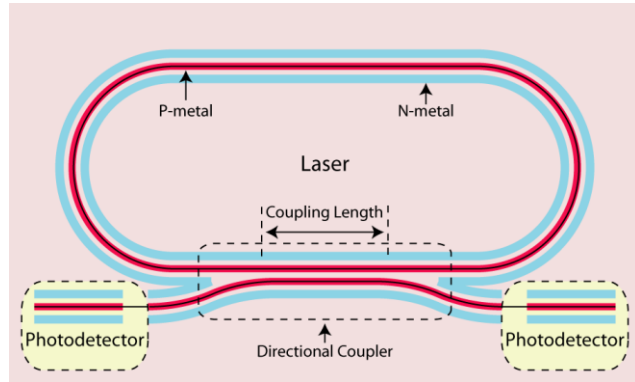


Figure 1.5: the racetrack resonator and the photodetectors layout (top view) [37]

Bonding type	Coupling scheme	Characterization	Remarks	Year	Ref.
Wafer-to-wafer Molecular bonding (thickness < 5 nm)	Evanescence on SOI rib waveguide	Pumping regime : CW $\lambda = 1592 \text{ nm}$ (at 240 mA) $I_{th} = 175 \text{ mA}$ $T_{max} = 60^\circ\text{C}$ $P_{max} = 29 \text{ mW}$	A directional coupler is used to extract the light from the laser region	2007	[37]
Wafer-to-wafer Molecular bonding (thickness < 5 nm)	Evanescence on SOI rib waveguide	Pumping regime : CW Mode locking with 7 ps pulses at 30 GHz	Same device as [37] with an integrated absorber for mode locking	2008	[38]

Table 1.2 : State of the art of racetrack resonators on silicon

1.2.7 Distributed Bragg reflector lasers

In DBR lasers the optical feedback is provided, at least at one side, by a distributed Bragg reflector located outside the gain section. The Bragg reflector is designed to achieve single wavelength laser emission. We can tune the emitted wavelength by carriers injection into the Bragg reflector or by temperature control. More details on DBR lasers are presented in chapter 3.1. The state of the art of DBR lasers on silicon is presented in Table 1.5.

The design of the first solution reported in literature [39] is presented in Figure 1.6. Light is generated and amplified in the hybrid section of the devices. Using a taper coupler on both side of the hybrid waveguide the evanescent part of the optical mode is coupled to the silicon waveguide. After the coupler a Bragg grating etched into the silicon waveguide provides the wavelength selective optical feedback. The laser is directly modulated; it shows open eye diagrams with extinction ratios of 8.7 dB and 6 dB for data rates of 2.5 Gb/s and 4 Gb/s, respectively. A tunable DBR laser fabricated using quantum well intermixing was also demonstrated [40]. The bandgap of the passive section is shifted from 1520 nm to 1440 nm by quantum wells intermixing. The tuning of the emitted wavelength is achieved by current injection into the passive regions. Tuning over 13 nm has been demonstrated. The DBR laser on silicon seems up to now the hardest way to achieve single mode lasing. There is a main fabrication limitation: as silicon and silica have a high refractive index contrast, it is quite complicated to obtain a narrow band grating reflector. Moreover, as the silicon refractive index changes slightly with temperature or carrier density, only a small tunability of the emitted wavelength is possible. Quantum well intermixing allows a better tunability but with a complex fabrication process.

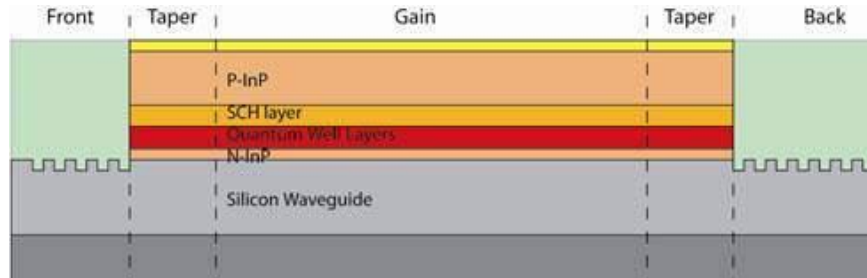


Figure 1.6: DBR silicon evanescent laser layout [39]

Bonding type	Coupling scheme	Characterization	Remarks	Year	Ref.
Wafer-to-wafer molecular bonding (thickness < 5 nm)	Evanescence on SOI rib waveguide, DBR grating in the Si region	Pumping regime : CW $I_{th} = 65 \text{ mA}$ $\lambda = 1597.6 \text{ nm}$ $T_{max} = 45^\circ\text{C}$ $P_{max} = 11 \text{ mW}$ $k = 80 \text{ cm}^{-1}$	Direct modulation: extinction ratios of 8.7 dB and 6 dB for data rates of 2.5 Gb/s and 4 GB/s	2008	[39]
Wafer-to-wafer molecular bonding (thickness < 5 nm)	Evanescence on SOI rib waveguide, DBR grating in the Si region	Pumping regime : CW $\lambda = 1506.5 \text{ nm}, 1501 \text{ nm}, 1514 \text{ nm}$ $I_{th} = 40 \text{ mA}$ $T_{max} = 40^\circ\text{C}$ $P_{max} > 2.5 \text{ mW}$ $k = 165 \text{ cm}^{-1}$	Quantum well intermixing is performed prior bonding. Tunable over 13 nm.	2008	[40]

Table 1.3 : state of the art of DBR lasers on silicon

1.2.8 Distributed feedback lasers

In DFB lasers a periodic structure is embedded inside the active waveguide and acts as a distributed reflector. The distributed reflector induces a selective optical feedback that can lead to single wavelength laser emission. More details on DFB laser devices are presented in chapter 3.3.

Several electrically pumped DFB hybrid lasers have been reported in the literature up to now. Their characteristics are summarized in Table 1.4.

UCSB group profited from the hybrid nature of the active waveguide in their structures to realize the distributed reflector on the silicon waveguide [41]. They achieved interesting performances; however as the index contrast between the guiding layer and the cladding is very high in SOI technology, high values of coupling coefficient k around 278 cm^{-1} (to be verified) have been reported leading to a low external efficiency.

In [42] and [43] the Bragg grating is located in the III-V waveguide. The distributed reflector is realized on the III-V wafer before wafer bonding and substrate removal. The entire fabrication process becomes more complex, e-beam lithography, etching and epitaxial re-growth are needed on the III-V wafer; accurate alignment between SOI wafer and III-V wafer is needed to align the Bragg grating with the silicon waveguides. These structures are represented schematically in Figure 1.7.

Recently a new concept based on exchange Bragg coupling has been presented by T. Dupont [44]. A Bragg grating is etched through the silicon waveguide before bonding. This grating is designed to

provide a selective optical feedback and also to optically couple the III-V waveguide mode to the silicon waveguide mode. Preliminary results have been achieved.

In conclusion, hybrid silicon DFB laser seems to be a viable solution to achieve single-mode laser sources on the silicon platform, when no tunability is needed. Many design solutions can be considered but the main issue to solve is related to the coupling coefficient value. It seems complicated to achieve an acceptably low coupling coefficient value in a repeatable way.

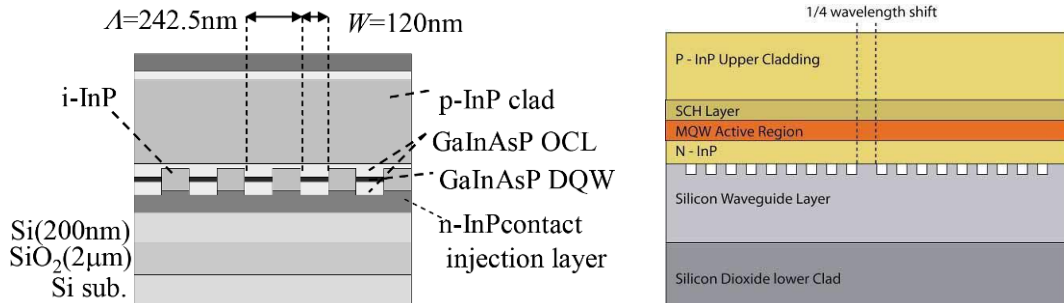


Figure 1.7. III-V DFB laser bonded on silicon. Left : the DFB grating is located in the active layer [43]. Right : the DFB grating is located in the silicon waveguide layer [41]

Bonding type	Coupling scheme	Characterization	Remarks	Year	Ref.
Wafer-to-wafer molecular bonding (thickness: few nanometers)	None	Pumping regime : pulsed $\lambda = 1542 \text{ nm}$ (at 135 mA) $I_{th} = 104 \text{ mA}$ $J_{th} = 400 \text{ A/cm}^2$ $k = 350 \text{ cm}^{-1}$	A DFB grating is included in the III-V epitaxy	2008	[42]
Wafer-to-wafer molecular bonding (thickness < 5 nm)	Evanescence on SOI corrugated rib waveguide	Pumping regime : CW $\lambda = 1599.3 \text{ nm}$ (at 90 mA) $I_{th} = 25 \text{ mA}$ $J_{th} = 1.4 \text{ kA/cm}^2$ $T_{max} = 50^\circ\text{C}$ $P_{max} = 5.4 \text{ mW}$ $k = 247 \text{ cm}^{-1}$	The DFB grating is located in the silicon region	2008	[41]
Wafer-to-wafer metal bonding	Evanescence on SOI strip waveguide	Pumping regime : pulsed $\lambda = 1542 \text{ nm}$ (at 200 mA) $I_{th} = 70 \text{ mA}$ $J_{th} = 2.9 \text{ kA/cm}^2$	A DFB grating is included in the III-V epitaxy	2009	[43]

Table 1.4 : state of the art of hybrid DFB lasers on Silicon

1.2.9 Array Waveguide Grating laser

Array Waveguide Grating (AWG) based lasers have been demonstrated so far on Indium Phosphate based technology [45]. Recently the first demonstration of AWG based laser on silicon has been achieved [46]. Compared to III-V technology, silicon based AWG lasers take the advantage of the small footprint of the silicon AWG.

The device layout is illustrated in Figure 1.8(a). It consists of 4 hybrid silicon SOAs that act as gain media in the four separate channels of the AWG. The AWG laser has been fabricated on the hybrid silicon platform as outlined in reference [47]. By biasing the amplifiers SOA1 – SOA4 above threshold, four lasing cavities are formed between the facets f1 – f4 and the common facet on the right

respectively. The AWG acts as a bandpass filter and determines the lasing wavelength. In this first demonstration the output power was very low (less than 50 μW for channel), with a SMSR between 25 and 35 dB and a threshold current of 113-120 mA.

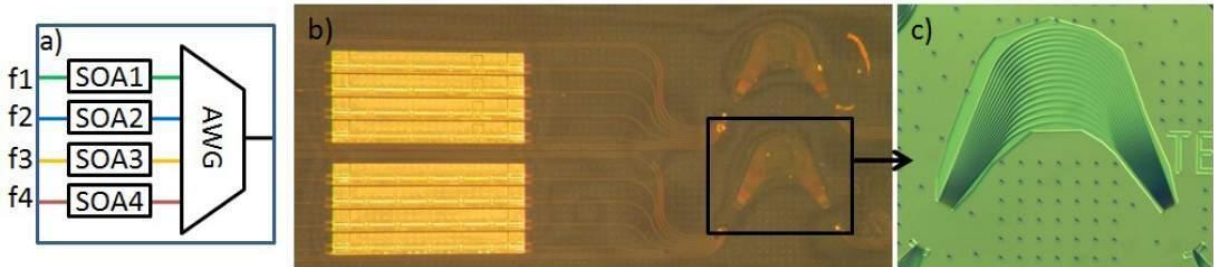


Figure 1.8 : (a) Schematic diagram of the hybrid silicon MWL; (b) Optical image of the fabricated device showing two separate MWLs; (c) Optical image of the AWG before III-V processing

This architecture seems to be the better candidate to achieve a multi-wavelength integrated laser on silicon. The small footprint of the SOI makes this solution extremely compact compared to every other actually available solution. Anyway performances need to be still significantly improved.

1.2.10 Microdisk lasers and hybrid microring lasers

Microdisk lasers present a great potential for intra-chip optical interconnects applications thanks to their low-power consumption and small footprint.

Micron-sized, electrically injected microdisks have been demonstrated [48] [49] [50] [51]. A schematic representation of a III-V microdisk integrated on a SOI wafer is given in Figure 1.9. After die-to-wafer molecular bonding of an InP-based epitaxial layer stack to a SOI-wafer, microdisks are etched into the III-V epitaxy and metallic contacts are deposited. Injecting an electrical current into the realized p-n junction allows to achieve stimulated emission and laser action in the microdisk. The fundamental optical resonances in this kind of structure are whispering gallery modes that are confined at the edges of the microdisk. A fraction of the light of the cavity is coupled to a silicon stripe waveguide (220 nm x 500 nm) located under the ring by evanescent coupling. To avoid absorption losses due to an overlap of the optical mode with the doped p-type contact layer, a tunnel junction in combination with another n-type contact is implemented. LETI has recently entirely manufactured microdisk lasers on a 200 mm microelectronics fabrication line.

By integrating four microdisks of different diameters on a single waveguide, a multi-wavelength laser was also obtained [52]. Indeed, microdisk lasers can yield single wavelength output and their wavelength selection is determined by the round trip cavity length. The multi-wavelength output spectrum contained four laser peaks, uniformly distributed by design within the free-spectral range of a single microdisk. At equal drive currents, the peak power of the channels varied up to 8 dB, due to loss caused by parasitic coupling to the higher order modes of the neighboring microdisks.

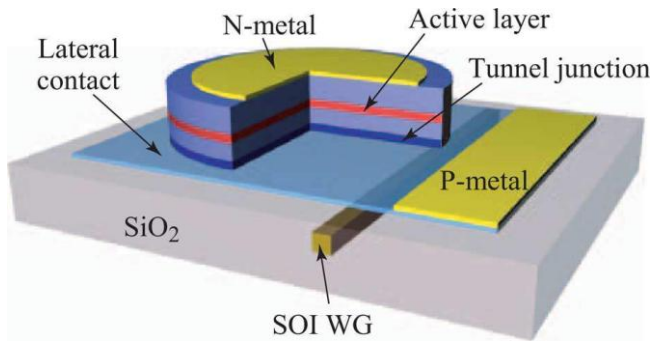


Figure 1.9. Layout of a single SOI-integrated microdisk laser [50]

Recently, hybrid microring lasers on silicon have been demonstrated [53]. Figure 1.10(a) shows a schematic view of the laser structure. An active InP-based ring resonator is located on top of a silicon disk with the same diameter, resulting in a hybrid ring resonator structure. The corresponding whispering-gallery mode profile is shown in Figure 1.10(a). A SOI waveguide hundreds of nanometers away from the resonator is used to extract the light from the hybrid resonator structure. Integrated photodetectors placed at both ends of the SOI bus waveguide are used to measure the laser light-current characteristics.

Principal results obtained with microdisk lasers on silicon are summarized in Table 1.5. As we have seen, many different designs have been explored. If the low power consumption and the small footprint makes of microring lasers a good candidate for in chip and intra-chip interconnect, the low emitted power is incompatible with telecommunication applications.

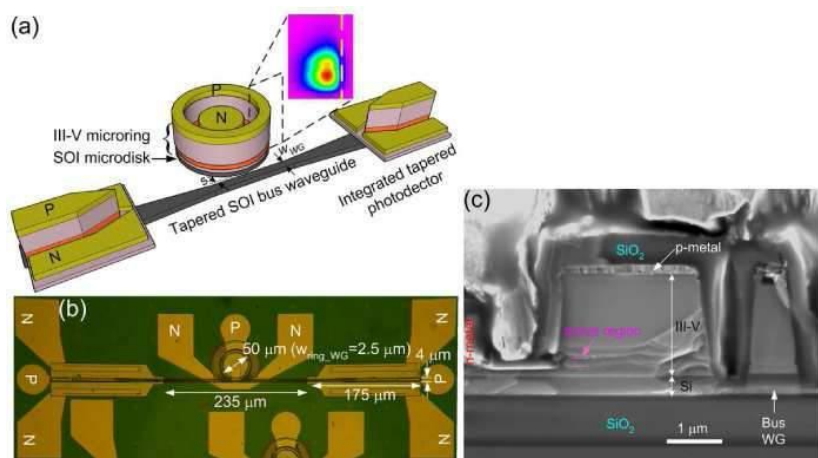


Figure 1.10: (a) Schematic of hybrid ring resonator laser with BPM mode profile and integrated photodetectors; (b) The microscopic image of a finished device with critical dimension labelled; (c) SEM cross-sectional image of the evanescent point coupler

Bonding type	Coupling scheme	Characterization	Remarks	Year	Ref.
Die-to-wafer molecular bonding (thickness: 130 nm)	Evanescence on SOI channel waveguide	Pumping regime: CW $\lambda = 1600 \text{ nm}$ (at 1.4 mA) $I_{th} = 0.5 \text{ mA}$ $J_{th} = 1,13 \text{ kA/cm}^2$ $P_{max} = 10 \mu\text{W}$	Multimode emission	2007	[50]
Die-to-wafer molecular bonding (thickness: 180 nm)	Evanescence on SOI channel waveguide	Pumping regime: CW $\lambda = 1585 \text{ nm}$ (at 2.8 mA) $I_{th} = 0.9 \text{ mA}$ $P_{max} = 12 \mu\text{W}$	Multi-wavelength transmitter	2007	[52]
Wafer-to-wafer molecular bonding (thickness: few nanometers)	Evanescence on SOI channel waveguide	Pumping regime: CW $\lambda = 1530 \text{ nm}$ (at 16 mA) $I_{th} = 5.97 \text{ mA}$ $P_{max} = 250 \mu\text{W}$	Integrated photodetectors	2009	[53]
Die-to-wafer molecular bonding	Evanescence on SOI channel waveguide	Pumping regime: CW $\lambda = 1580 \text{ nm} + 2\text{nm tuning}$ $I_{th} = 0.3 \text{ mA}$ $P_{max}=36\mu\text{W}$	Tunable	2010	[51]

Table 1.5 : State of the art of Microdisks lasers on silicon

1.3 Our approach to hybrid silicon laser

When I start this thesis the state of the art for hybrid lasers was represented by UCSB and INTEL with theirs “evanescent” laser design. Theirs design solution was not the only one in that moment, but it was surely the most known with the highest performances demonstrated. In Table 1.6 I present the state of the art at the beginning of this work.

UCSB obtained impressive results with several different laser configurations of their hybrid evanescent waveguides, but as the interest for the hybrid approach was increasing, some questions were arising about the evanescent configuration. For instance, a large III-V mesa seemed not truly optimized to achieve a low threshold current and a high efficiency; the necessity of an extremely thin bonding layer appeared as a big constraint; more generally many saw no practical reasons why the hybrid devices performances were that far from III-V standard devices.

Device type	Performances	Year
Fabry-Perot laser	Pumping regime: CW $\lambda = 1577 \text{ nm}$	$I_{th} = 65 \text{ mA}$ $T_{max} = 40^\circ\text{C}$ $P_{max} = 1,8 \text{ mW}$
DBR laser	Pumping regime: CW $\lambda=1597.6 \text{ nm}$	$I_{th} = 65 \text{ mA}$ $T_{max} = 45^\circ\text{C}$ $P_{max} = 11 \text{ mW}$
DFB laser	Pumping regime: CW $\lambda = 1599.3 \text{ nm}$	$I_{th} = 25 \text{ mA}$ $T_{max} = 50^\circ\text{C}$ $P_{max} = 5.4 \text{ mW}$

Table 1.6: state of the art at the beginning of the thesis

In partnership with IMEC and LETI we have tried to explore a new way in order to address the geometry and the issues of hybrid lasers. We chose an adiabatic transfer approach, in which a

standard III-V design suits very well for the gain region. Moreover this taper approach allows to pass from an extremely thin to a more tolerant bonding layer.

In this thesis we will report in detail all this development. In chapter 2 we described our approach to treat the coupling problem, by describing how we achieve an efficient coupling of light between III-V and silicon for several configurations. In chapter 3 is devoted to the single mode laser topic, describing the possible ways to obtain single mode emission. In chapter 4 we present our development on device fabrication. When I start this thesis we had no experience on III-V fabrication on heterogeneous integrated samples (i.e. III-V on silicon); the development of a reliable process needed a lot of effort that I tried to summarize in this chapter. Finally, in chapter 5 we introduce the characterization results we achieved.

1.4 Thesis context

The work presented in this thesis has been carried out inside the HELIOS project and some other French national projects. HELIOS (pHotonics EElectronics functional Integration on CMOS) is the biggest project funded by the European Commission (FP7-ICTprogram).

The mission of the project is to make CMOS photonics accessible to a broad circle of users. The HELIOS consortium is developing innovative means to combine a photonic layer with a CMOS circuit, using microelectronic fabrication processes. HELIOS gathers 19 partners among the major European CMOS Photonics and Electronics players and potential users. The project includes the development of essential building blocks such as efficient sources (Silicon-based and heterogeneous integration of III-V on silicon), fast modulators and, beyond, the combination and packaging of these building blocks for the demonstration of complex functions, addressing a variety of industrial needs:

- 40 Gb/s modulator on an Electronic IC
- 16x10 Gb/s transceiver for WDM-PON applications,
- Photonic QAM-10 Gb/s wireless transmission system
- Mixed analog and digital transceiver module for multifunction antennas

The results of HELIOS will pave the way for applications of CMOS photonics for other fields, eg sensors or optical processing. HELIOS will push integration technologies accessible for a broad circle of users in a foundry-like, fabless way [54]

The demonstrator I am focus on during my thesis is a semi-cooled WDM transceiver for metropolitan/access networks with 16 channels, 200 GHz channel spacing in the C-band, working at 10 Gbit/s for 10 km transmission distance. Semi-cooled operation means an operation temperature of 45°C.

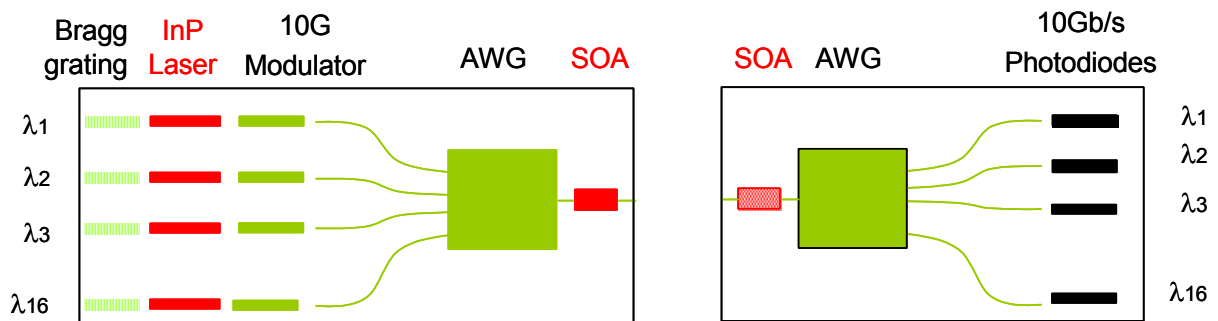


Figure 1.11: schematic view of HELIOS WP9 demonstrator [55]

Following this application scenario, let's specify the required performance for each building block.

The following specifications have been defined for the hybrid laser. The laser has to show single mode-operation, with side-mode suppression ratio > 30 dB, output power > 0 dBm and threshold current < 50 mA, at room temperature. The wavelength precision is also an important factor to be taken into account. For the semi-cooled operation of the demonstrator, the HELIOS consortium specifies the performances at 45°C as following:

Parameters	Requirements
Output power	> 0 dBm
Side-mode suppression ratio	> 30 dB
Threshold	< 50 mA
Channel spacing	200 GHz
Channel frequency accuracy	< 20 GHz
Drive current	< 150 mA
Drive voltage	< 1.8 V

1.5 Bibliography

- [1] T. Barwicz, H. Byun, F. Gan, C. W. Holzwarth, M. A. Popovic, P. T. Rakich, M. R. Watts, E. P. Ippen, F. X. Kärtner, H. I. Smith, J. S. Orcutt, R. J. Ram, V. Stojanovic, O. Olubuyide, J. L. Hoyt, S. Spector, M. Geis, M. Grein, T. Lyszczarz and J. U. Yo, "Silicon photonics for compact, energy-efficient interconnects," *Journal of Optical Networking*, vol. 6, no. 1, 2007.
- [2] M. Asghari, "Silicon Photonics: A Low Cost Integration Platform for Datacom and Telecom Applications," National Fiber Optic Engineers Conference, San Diego, 2008.
- [3] K. Wada, S. Park and Y. Ishikawa, "Si Photonics and Fiber to the Home," *Proceedings of the IEEE*, 2009.
- [4] A. Fang, H. Park, O. Cohen, R. Jones, M. Paniccia and J. Bowers, "Electrically pumped hybrid AlGaInAs-silicon evanescent laser," *Optics Express*, vol. 14, pp. 9203-9210, 2006.
- [5] G. Roelkens, Y. D. Koninck, S. Keyvaninia, S. Stankovic, M. Tassaert, M. Lamponi, G. Duan, D. V. Thourhout and R. Baets, "Hybrid Silicon Lasers," *SPIE*, 2011.
- [6] X. Sun, M. J. Shearn, A. Zadok, M. S. Leite, S. T. Steger, H. A. Atwater, A. Scherer and A. Yariv, "Electrically Pumped Supermode Si/InGaAsP Hybrid Lasers," in *Conference on Lasers and Electro-Optics*, San Jose, 2010.
- [7] Y. Zhizhong, A. Anopchenko, N. Daldosso, R. Guider, D. Navarro-Urrios, A. Pitanti, R. Spano and L. Pavesi, "Silicon Nanocrystals as an Enabling Material for Silicon Photonics," *Proceedings of the IEEE*, vol. 97, no. 7, 2009.
- [8] M. J. Chen, J. L. Yen, J. Y. Li, J. F. Chang, S. C. Tsai and C. S. Tsai, "Stimulated emission in a nanostructured silicon pn junction diode using current injection," *Applied Physics Letters*, vol. 84, 2004.
- [9] M. A. Green, J. Zhao, A. Wang, P. J. Reece and M. Gal, "Efficient silicon light-emitting diodes," *Nature*, vol. 412, 2001.
- [10] L. Pavesi and D. Lockwood, "Silicon Photonics," *Topics in Applied Physics*, vol. 94, 2004.
- [11] W. L. Ng, M. A. Lourenço, R. M. Gwilliam, S. Ledain, G. Shao and K. P. Homewood, "An efficient room-temperature silicon-based light-emitting diode," *Nature*, vol. 410, 2001.
- [12] L. Pavesi and R. Turan, *Silicon Nanocrystals: Fundamentals, Synthesis and Applications*, Berlin: Wiley-VCH Verlag GmbH, 2010.
- [13] A. Pitanti, D. Navarro-Urrios, R. Guider, N. Daldosso, F. Gourbilleau, L. Khomenkova, R. Rizk and L. Pavesi, "Further improvements in Er³⁺ coupled to Si nanoclusters rib waveguides," *Proceedings SPIE 6996*, 2008.
- [14] L. Pavesi, "Routes toward silicon-based lasers," *Materials today*, vol. 8, no. 1, 2009.
- [15] M. Fischetti and S. Laux, "Band structure, deformation potentials, and carrier mobility in strained Si, Ge, and SiGe alloys," *Journals of Applied Physics*, vol. 80, 1996.
- [16] M. E. Kurdi, G. Fishman, S. Sauvage and P. Boucaud, "Band structure and optical gain of tensile-strained germanium based on a 30 band kp formalism," *Journal of Applied Physics*, vol. 107,

2010.

- [17] J. Liu, X. Sun, D. Pan, X. Wang, L. Kimerling, T. L. Koch and J. Michel, "Tensile-strained, n-type Ge as a gain medium for monolithic laser integration on Si," *Optics Express*, vol. 15, 2007.
- [18] J. Liu, X. Sun, L. Kimerling and J. Michel, "Direct-gap optical gain of Ge on Si at room temperature," *Optics Letters*, vol. 34, pp. 1738-1740, 2009.
- [19] J. Liu, X. Sun, R. Camacho-Aguilera, L. Kimerling and J. Michel, "Ge-on-Si laser operating at room temperature," *Optics Letters*, vol. 35, pp. 679-681, 2010.
- [20] J. Michel, J. Liu, L. Kimerling, R. Camacho-Aguilera, J. Bessette and Y. Cai, "A germanium-on-silicon laser for on-chip applications," *CLEO*, 2011.
- [21] A. V. Krishnamoorthy, L. Chirovsky, W. Hobson, R. Leibengath, S. Hui, G. Zydzik, K. Goossen, J. Wynn, B. Tseng, J. Lopata, J. Walker, J. Cunningham and L. D'Asaro, "Vertical-cavity surface-emitting lasers flip-chip bonded to gigabit-per-second CMOS circuits," *Photonics Technology Letters*, vol. 11, no. 1, 1999.
- [22] T. Pinguet, B. Analui, E. Balmater, D. Guckenberger, M. Harrison, R. Koumans, D. Kucharski, Y. Liang, G. Masini, A. Mekis, S. Mirsaidi, A. Narasimha, M. Peterson, D. Rines, V. Sadagopan, S. Sahni, T. Slezoda, D. Song, Y. Wang and e. al., "Monolithically integrated high-speed CMOS photonic transceivers," *Group IV Photonics*, no. 2008.
- [23] J. Yang, P. Bhattacharya, G. Qin and Z. Ma, "On-chip integration of InGaAs/GaAs quantum dot lasers with waveguides and modulators on silicon," in *Novel In-Plane Semiconductor Lasers VII*, San Jose, 2008.
- [24] G. Roelkens, J. V. Campenhout, J. Brouckaert, D. V. Thourhout, R. Baets and P. R.-R. e. al., "III-V/Si photonics by die-to-wafer bonding," *Materials Today*, vol. 10, pp. 36-43, 2007.
- [25] G. Roelkens, D. Van Thourhout and R. Baets, "Ultra-thin benzocyclobutene bonding of III-V dies onto SOI substrate," *Electronics Letters*, vol. 41, no. 9, 2005.
- [26] T. Hong, G.-Z. Ran, T. Chen, J.-Q. Pan, W.-X. Chen, Y. Wang, Y.-B. Cheng, S. Liang, L.-J. Zhao, L.-Q. Yin, J.-H. Zhang, W. Wang and G.-G. Qin, "A Selective-Area Metal Bonding InGaAsP-Si Laser," *Photonics Technology Letters*, vol. 22, Aug. 2010.
- [27] Y. Zheng, Y. Huang, Y. Wang, Y. Wei, D. Ng, C. W. Lee, B. Liu, Y. Tu and S. Ho, "Heterogeneously Integrated Silicon/III-V Evanescent Lasers with Micro-loop Mirror (MLM) Reflector," *Proc. Frontiers in Optics, OSA Technical Digest*, 2010.
- [28] S. Stankovic, G. Roelkens, D. V. Thourhout, R. Jones, M. Sysak and J. Heck, "1310 nm Evanescent Hybrid III-V/Si Laser Based on DVS-BCB Bonding," *Integrated Photonics Research, Silicon and Nanophotonics, OSA Technical Digest*, 2011.
- [29] B. B. Bakir, A. Descos, N. Olivier, D. Bordel, P. Grosse, E. Augendre, L. Fulbert and J. M. Fedeli, "Electrically driven hybrid Si/III-V Fabry-Pérot lasers based on adiabatic mode transformers," *Optics Express*, vol. 19, 2011.
- [30] G. Roelkens, D. V. Thourhout, R. Baets, R. Nötzel and M. Smit, "Laser emission and photodetection in an InP/InGaAsP layer integrated on and coupled to a Silicon-on-Insulator waveguide circuit," *Optics Express*, vol. 14, 2006.

- [31] B. B. Bakir, N. Olivier, P. Grosse, S. Messaoudene, S. Brision, E. Augendre, P. Philippe, K. Gilbert, D. Bordel, J. Harduin and J.-M. Fedeli, "Electrically driven hybrid Si/III-V lasers based on adiabatic mode transformers," in *Proc. SPIE*, 2010.
- [32] M. N. Sysak, H. A. Fang, J. Bowers, R. Jones, O. Cohen, O. Raday and M. J. Paniccia, "Experimental and theoretical thermal analysis of a Hybrid Silicon Evanescent Laser," *Optics Express*, vol. 15, 2007.
- [33] L. Grenouillet, A. L. Bavencove, T. Dupont, J. Harduin, P. Philippe, P. Regreny, F. Lelarge, K. Gilbert, P. Grosse and J. M. Fedeli, "CMOS compatible contacts and etching for InP-on-silicon active devices," in *Proc. Group IV Photonics*, San Francisco, 2009.
- [34] B. Koch, A. Fang, O. Cohen and J. Bowers, "Mode-locked silicon evanescent lasers," *Optics Express*, vol. 15, pp. 11225-11233, 2007.
- [35] H.-H. Chang, A. Fang, M. Sysak, H. Park, R. Jones, O. Cohen, O. Raday, M. Paniccia and J. Bowers, "1310nm silicon evanescent laser," *Optics Express*, vol. 15, pp. 11466-11471, 2007.
- [36] X. Sun, A. Zadok, M. J. Shearn, K. A. Diest, A. Ghaffari, H. Atwater, A. Scherer and A. Yariv, "Electrically pumped hybrid evanescent Si/InGaAsP lasers," *Optical Letters*, vol. 34, 2009.
- [37] A. Fang, R. Jones, H. Park, O. Cohen, O. Raday, M. Paniccia and J. Bowers, "Integrated AlGaNAs-silicon evanescent race track laser and photodetector," *Optics Express*, vol. 15, 2007.
- [38] A. Fang, B. Koch, K.-G. Gan, H. Park, R. Jones, O. Cohen, M. Paniccia, D. Blumenthal and J. Bowers, "A racetrack mode-locked silicon evanescent laser," *Optics Express*, vol. 16, pp. 1393-1398, 2008.
- [39] A. Fang, E. Lively, Y.-H. Kuo, D. Liang and J. Bowers, "A distributed feedback silicon evanescent laser," *Optics Express*, vol. 16, pp. 4413-4419, 2008.
- [40] M. Sysak, J. Anthes, D. Liang, J. Bowers, O. Raday and R. Jones, "Hybrid Silicon Sampled Grating DBR Tunable Laser," in *Proc. Group IV photonics*, 2008.
- [41] A. W. Fang, B. R. Koch, R. Jones, E. Lively, D. Liang, Y.-H. Kuo and J. Bowers, "A Distributed Bragg Reflector Silicon Evanescent Laser," *Photonics Technology Letters*, vol. 20, pp. 1667-1669, 2008.
- [42] T. Okumura, T. Maruyama, H. Yonezawa, N. Nishiyama and S. Arai, "Injection type GaInAsP/InP/Si DFB lasers directly bonded on SOI substrate," in *Proc. IPRM*, 2008.
- [43] Chen-Ting, Hong-Tao, Pan-Jiao-Qing, Chen-Wei-Xi, Cheng-Yuan-Bing, Wang-Yang, Ma-Xiao-Bo, Liu-Wei-Li, Zhao-Ling-Juan, Ran-Guang-Zhao, Wang-Wei and Qin-Guo-Gang, "Electrically pumped room-temperature pulsed InGaAsP-Si hybrid lasers based on metal bonding," *Chinese Physics Letters*, vol. 26, no. 6, 2009.
- [44] T. Dupont, L. Grenouillet, A. Chelnokov, S. Messaoudene, J. Harduin, D. Bordel, J.-M. Fedeli, C. Seassal, P. Regreny and P. Viktorovitch, "A III-V on silicon distributed-feedback laser based on exchange-Bragg coupling," *Proc. Group IV Photonics*, 2010.
- [45] Y. Tachikawa and K. Okamoto, "32 wavelength tunable arrayed-waveguide grating laser based on special input/output arrangement," *Electronics Letters*, vol. 31, no. 19, 1995.
- [46] G. Kurczveil, M. J. Heck, J. D. Peters, J. Garcia and J. E. Bowers, "A Fully Integrated Hybrid Silicon AWG Based Multiwavelength Laser," in *Proc. IEEE International Semiconductor Laser*

Conference, 2010.

- [47] H. Park, A. Fang, D. Liang, Y.-H. Kuo, H.-H. Chang, B. R. Koch, H.-W. Chen, M. N. Sysak, R. Jones and J. E. Bowers, "Photonic Integration on the Hybrid Silicon Evanescent Device Platform," *Advances in Optical Technologies*, 2008.
- [48] H. Hattori, C. Seassal, E. Touraille, P. Rojo-Romeo, X. Letartre, G. Hollinger, P. Viktorovitch, L. D. Cioccio, M. Zussy and L. Melhaoui, "Heterogeneous integration of microdisk lasers on silicon strip waveguides for optical interconnects," *Photonics Technology Letters*, vol. 18, no. 1, 2006.
- [49] P. Romeo, J. V. Campenhout, P. Regreny, A. Kazmierczak, C. Seassal, X. Letartre, G. Hollinger, D. V. Thourhout, R. Baets, J. Fedeli and L. D. Cioccio, "InP on Silicon Electrically Driven Microdisk Lasers for Photonic ICs," *Optics Express*, vol. 14, pp. 3864-3871, 2006.
- [50] J. V. Campenhout, P. Romeo, P. Regreny, C. Seassal, D. V. Thourhout, S. Verstuyft, L. D. Cioccio, J.-M. Fedeli, C. Lagahe and R. Baets, "Electrically pumped InP-based microdisk lasers integrated with a nanophotonic silicon-on-insulator waveguide circuit," *Optics Express*, vol. 15, pp. 6744-6749, 2007.
- [51] L. Liu, T. Spuesens, G. Roelkens, D. V. Thourhout, P. Regreny and P. Rojo-Romeo, "A Thermally Tunable III-V Compound Semiconductor Microdisk Laser Integrated on Silicon-on-Insulator Circuits," *Photonics Technology Letters*, vol. 22, 2010.
- [52] J. V. Campenhout, L. Liu, P. Romeo, D. V. Thourhout, C. Seassal, P. Regreny, L. D. Cioccio, J.-M. Fedeli and R. Baets, "A Compact SOI-Integrated Multiwavelength Laser Source Based on Cascaded InP Microdisks," *Photonics Technology Letters*, vol. 20, pp. 1345-1347, 2008.
- [53] D. Liang, M. Fiorentino, T. Okumura, H.-H. Chang, D. T. Spencer, Y.-H. Kuo, A. W. Fang, D. Dai, R. G. Beausoleil and J. Bowers, "Electrically-pumped compact hybrid silicon microring lasers for optical interconnects," *Optics Express*, vol. 17, pp. 20355-20364, 2009.
- [54] 2011. [Online]. Available: <http://www.helios-project.eu/>.
- [55] L. Fulbert, "HELIOS presentation," 2008. [Online]. Available: <http://www.helios-project.eu/Download/Presentations>.

2 PRINCIPLE OF THE LIGHT COUPLING FROM III-V TO SILICON

By bonding together two different materials, we aim at developing new devices that could profit from both materials physical properties. In the case of guided opto-electronic components we need to ‘guide’ the light inside both materials, then from one to the other, to take advantage of their specific characteristics. The key design problem indeed is how to control the optical path and how to structure the two materials, to guide and to exchange light between them with minimum losses. In this chapter we will briefly introduce the basis of optical coupling between integrated waveguides, then we will detail the coupling designs used for our hybrid lasers, including their features, advantages and drawbacks.

2.1 Light coupling in hybrid lasers

A hybrid III/V on silicon laser is a device that provides a laser beam from a silicon output waveguide by electrical injection to the III-V region. A laser is based on two fundamental elements: an optical gain medium and an optical cavity.



Figure 2.1: two schematic representation of the hybrid III-V on SOI laser geometry, on the left the laser cavity is just on the III-V part, on the right we have an hybrid cavity

The overlying III-V stack provides the optical gain; it needs to be structured in order to electrically inject carriers inside the quantum wells region. If we want to fully profit from the optical gain, we need to have a high overlap between the optical mode and the quantum wells. To achieve a high overlap value the optical mode needs to be well confined inside the III-V waveguide. At the same time, in a hybrid laser, the light has to be confined in the silicon waveguide on the output of the laser, to efficiently extract the optical power.

The optical cavity is composed of a guided path between two mirrors (Figure 2.1). The cavity can contain only the III-V waveguide; in this case the light needs to be coupled somehow from the III-V cavity to the output silicon waveguide. Otherwise, the silicon waveguide can be part of the cavity; in this case the light needs to be coupled from the III-V waveguide to the silicon waveguide and vice versa, to allow a round-trip inside the hybrid cavity. In any case the role of the coupling between III-V waveguide and silicon waveguide is critical for the device.

2.2 Directional and adiabatic coupling

In guided optics we identify two classical ways to exchange power between waveguides: the directional coupler and the tapered coupler (Figure 2.2).

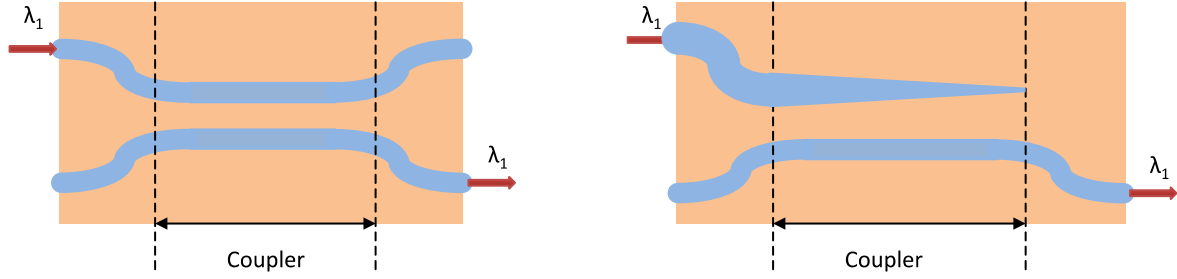


Figure 2.2: schematic representation of a directional coupler (on the left) and of an adiabatic coupler (on the right)

Directional coupler is based on coupled waveguide geometry. We define “coupled” two waveguides that exchange optical power. In the typical case if two waveguides are sufficiently close, such that their fields overlap, light can be transferred from one to the other [1]. Wave propagation in these composite waveguide structures can be described, for weak coupling, by a simplified approximate theory, known as coupled-mode theory. In the coupled mode analysis (or perturbation theory) the electric field is represented by a linear combination of the unperturbed normal modes of the isolated waveguides [2]. In the simpler form we can consider two parallel waveguides separated by a finite distance. The electrical field $E(x, y, z)$ can be written as:

$$E(x, y, z) = [au_1(x, y) + bu_2(x, y)] e^{-i\beta z} \quad (2.1)$$

Where u_1 and u_2 are the fundamental mode field distributions in the two waveguides, a and b are real coefficients, and β is the propagation constant. Coupling can be seen as a scattering effect. The field of the first waveguide (u_1) is scattered by the second one, creating a light source that modifies the amplitude of the second waveguide field (u_2). Similarly the second waveguide field has an effect on the first waveguide. An analysis of this mutual interaction leads to two coupled differential equations that describe the amplitude variations in the two waveguides. [2]

$$\frac{da}{dz} = -i\kappa_{12}b(z)e^{-i(\beta_2-\beta_1)z} \quad (2.2)$$

$$\frac{db}{dz} = -i\kappa_{21}a(z)e^{i(\beta_2-\beta_1)z} \quad (2.3)$$

Where κ_{12} and κ_{21} are coupling coefficient, β_1 and β_2 the propagation constants of the uncoupled waveguides.

In such kind of system the two waveguides will periodically exchange power; if the two waveguides have the same propagation constant ($\beta_1=\beta_2$), the exchange of power is complete, and the waveguides are said to be phase matched, as illustrated in Figure 2.3. If we inject a certain amount of power $P_1(0)$ on the first waveguide, after a propagation distance $L_0 = \frac{\pi}{2\kappa}$ (coupling length), all the power will be transferred to the second waveguide.

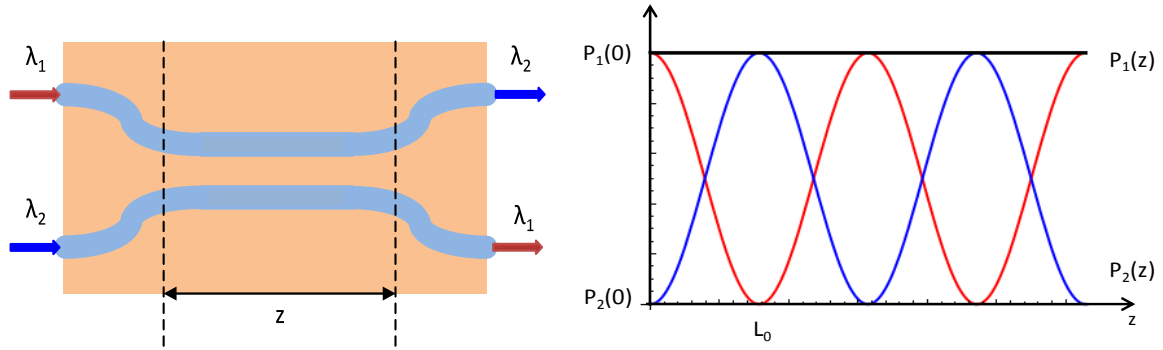


Figure 2.3: exchange of power between guides 1 and 2 in the phase-matched case

If the two waveguides are not phase matched, just a fraction of the light will be periodically exchanged. If we call F the fraction of power exchanged between the waveguides, and L_c the coupling length that insures the maximum coupling, we can deduce from previous equations:

$$F = \left(\frac{2L_c k}{\pi} \right)^2 \quad (2.4)$$

Tapered coupling has been introduced by J. S. Cook and A. G. Fox [3][4]. In this structure two waveguides separated by a finite distance have initially different propagation coefficients. If one or both of the propagation coefficients vary with distance, such that they become equal at some point within the length of the coupler, and cross over, complete transfer of power is possible under certain conditions [5]. Geometrically, in the simpler example, one waveguide is tapered down to a smaller dimension than the other one, as illustrated in Figure 2.4. If the waveguide dimensions vary slowly enough along the propagation direction we have what is generally called adiabatic tapering, no power exchange occurs between fundamental mode and higher order waveguide modes. A general analysis of this kind of structures is not easy to achieve, many model have been presented in literature for different configurations and applications. Taper structures have been applied to optical fibers [6], spot-size converter in laser diodes [7], modulators [8], arrayed-waveguide gratings [9], optical switches [10] and optical amplifiers [11]. Many geometries have been proposed, vertical taper, horizontal taper, 3D taper, double taper, etc... [12].

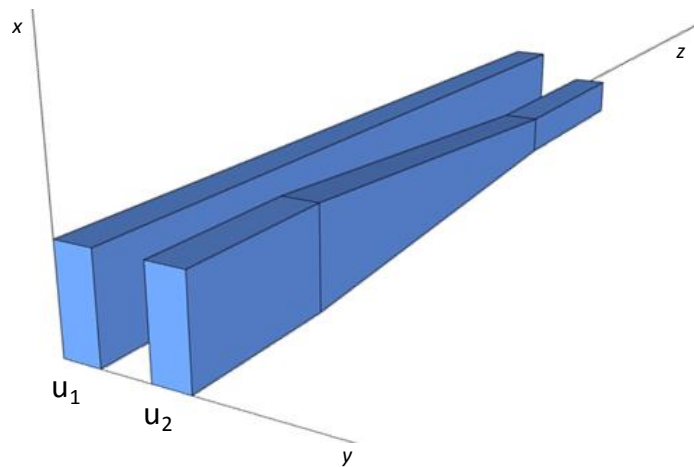


Figure 2.4: lateral taper geometry, the waveguide 2 changes its geometry along propagation direction

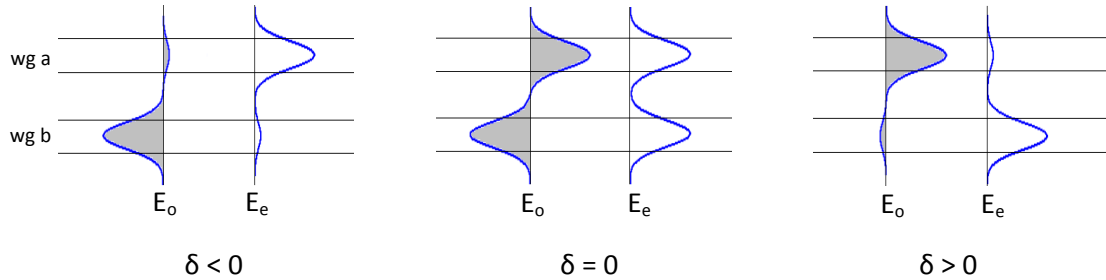


Figure 2.5: A schematic illustration of E_o and E_e supermodes for different values of the mismatch parameter

In recent works X. Sun, A. Yariv et al. presented an interesting model to analyze and design adiabatic mode transformers [13]. In their approach they introduce a mathematical model defining the optimum taper shape. “Optimum” means the shortest taper that can enable loss-less adiabatic coupling between two waveguides.

The model is based on supermodes formalism [14]. In this formalism the electrical field is decomposed in a combination of supermodes; “supermodes” stays for the eigenfunctions of the coupled waveguides system. The supermodes can be expressed as a linear combination of the optical modes of the isolated waveguides. Each supermode is determined by the ratio (a/b) and by a propagation constant β . These two values are determined by the phase mismatch δ and the amplitude spatial overlap κ between the modes of the uncoupled waveguides.

Neglecting the higher order modes we just consider the first even and odd supermodes, which we designate by the subscript o and e . These are given by [14]:

$$E_{o,e}(x, y, z) = [au_a(x, y) + bu_b(x, y)]e^{-i\beta z} \quad (2.5)$$

$$E_o(z) = [a_o + b_o]e^{-i\beta_0 z} = \left[\frac{ik^*}{(\delta + S)} + 1 \right] e^{-i(\bar{\beta} - S)z} \quad (2.6)$$

$$E_e(z) = [a_e + b_e]e^{-i\beta_e z} = \left[\frac{ik^*}{(\delta - S)} + 1 \right] e^{-i(\bar{\beta} + S)z} \quad (2.7)$$

Where

$$\delta = \frac{\beta_2 - \beta_1}{2} \quad S = \sqrt{\delta^2 + \kappa^2} \quad \bar{\beta} = \frac{\beta_1 + \beta_2}{2} \quad (2.8)$$

As we illustrate in Figure 2.5, we can distinguish three limiting values for the system. When $\delta < 0$ and $|\delta| \gg k$ the modes are substantially confined in one waveguide, and when $\delta > 0$ and $\delta \gg k$ the mode substantially resides on the other waveguide. At the phase matching point, $\delta = 0$, the modes are evenly distributed in both waveguides.

Starting from these equations, if we want to find the optimum taper, we need to find the coupled-system design that allows adiabatically transforming the even supermode by sweeping the δ value from a negative to a positive value in the shortest distance, while keeping the coupling to the other supermode below a certain level.

After some calculation steps, by defining ε as the power ratio coupled to the odd mode et z_0 the z position at which the taper reach the phase-matching condition, we arrive at the following *adiabaticity criterion* [13]:

$$\frac{\delta}{\kappa} = \frac{u}{\sqrt{1-u^2}} = \tan [\arcsin(u)] \quad (2.9)$$

where $u \equiv 2\kappa\varepsilon^{1/2}(z - z_0)$.

A taper that has been designed following this rule will be able to transfer the optical mode of the waveguide a to the waveguide b with an amount of power ε scattered to the odd mode for a taper length of $\frac{1}{\kappa\sqrt{\varepsilon}}$. As a general rule a longer taper will allow lower losses. Considering that a directional coupler has a minimal length of $L_0 = \frac{\pi}{2\kappa}$, an adiabatic coupler will be always longer of a $\frac{2}{\pi\sqrt{\varepsilon}}$ factor.

2.3 Hybrid III-V on SOI laser based on adiabatic taper

The hybrid III-V on SOI lasers we present in this work are based on a complete transfer of the optical mode between the III-V waveguide and the silicon waveguide. A schematic representation of the component geometry is illustrated in Figure 2.6. The structure can be divided into three parts. In the center of the device we have only a III-V waveguide where the optical mode is confined. In this section, that can range from 300 μm to 1 mm or more, the optical mode experiences a large overlap with the III-V quantum wells (more than 10%) that provide optical gain. The length of this section has a direct impact on laser performances, a shorter section will lead to a lower threshold and higher slope efficiency, while a longer section (within a certain limit) will lead to a higher threshold and lower slope efficiency. At both sides of this section there is an adiabatic taper coupling region that couples light from the III-V waveguide to the underlying silicon waveguide. This section is designed to be as short as possible, and to have a high coupling efficiency (higher than 95%). After the coupling region the light is guided by a silicon waveguide without III-V on top, the design of the silicon waveguide is important for the characteristics of the adiabatic coupler as we will see further on. In the Fabry-Perot configuration mirrors are provided by the cleaved facet of the silicon waveguide. The substrate is thinned before cleaving and no coating is used on cleaved facets.

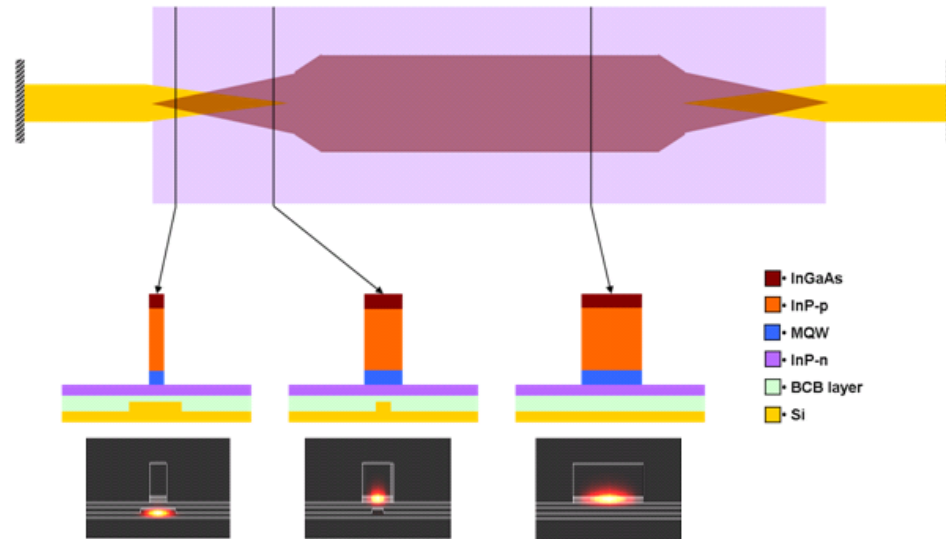


Figure 2.6: Top view, cross sections and calculated mode profiles of the III-V/SOI laser, the mode profiles have been evaluated using FIMMWAVE, the exact device geometry is defined in section 2.4 [15]

The hybrid nature of the device, and its peculiar fabrication process (SOI processing, bonding, III-V processing) gives de designer a lot of freedom in structure optimization. We can list several design parameters that have to be chosen: the silicon waveguide dimensions, the bonding layer thickness, the III-V epitaxial layer structure, the active waveguide dimensions, and the taper shape.

Optical, electrical and thermal criteria have to be taken into account and every design choice needs to be compatible with fabrication tolerances. In the following sections we will detail our choices for several designs.

2.3.1 III-V and SOI used wafers

The III-V epitaxial structure has been chosen following these criteria. It consists of a p-InGaAs contact layer, a p-InP cladding layer, 6 InGaAsP quantum wells surrounded by two InGaAsP separate confinement heterostructure (SCH) layers, and an n-InP layer as detailed in Table 2.1.

The structure has been grown by MBE (Molecular Beam Epitaxie). As the wafer needs to be bonded top-down, the layers are grown in a reverse order compared to standard III-V epitaxie. The wafer surface needs to be perfectly smooth to allow efficient bonding (surface roughness < 0.5 nm rms). The Multi Quantum Well (MQW) and Separate Confinement Heterostructure (SCH) layers design has been optimized in previous works made at III-V Lab [16].

layer nb.	layer type	nb. of periods	material	PL wavelength	thickness	carrier conc.	type	refractive index
8	cladding n		InP		200	10^{18}	n	3.16
7	SCH		InGaAsP	1,17	100		nid	3.33
6	MQW_w	6	InGaAsP	1,55	8		nid	3.56
5	MQW_b	5	InGaAsP	1,17	10		nid	3.33
4	SCH		InGaAsP	1,17	50		nid	3.33
3	cladding p		InP		1500	$5 \times 10^{17} \rightarrow 5 \times 10^{18}$	p	3.16
2	transition		InGaAsP	1,17	20	10^{19}	p	
1	contact p		InGaAs		300	3×10^{19}	p	
substrate			InP				N	

Table 2.1: III-V detailed epitaxial structure

The InGaAs layer is used as contact layer due to the higher solubility of dopants in this material and to the lower bandgap [17]. The InP-p thickness has been calculated to minimize the overlap between the optical mode and the InGaAs layer, as InGaAs strongly absorbs at 1.55 μm wavelength. The gradual doping of InP p-doped (from 5×10^{17} to 5×10^{18} cm³) layer is due to a compromise between reduction of series resistance and optical absorption in this region. InP n-doped layer thickness has been chosen to insure a sufficiently low n-side series resistance. As the thickness of this layer directly influences the coupling between III-V waveguide and silicon waveguide, this value has been chosen also to insure a sufficient coupling between both waveguides.

The SOI substrate (200 mm wafer manufactured by SOITEC) is composed of a mono-crystalline silicon layer on top of a 2 μm thick buried oxide layer on a silicon substrate. At the beginning of the thesis we used a 400 nm rib waveguides with an etch depth of 180 nm. This waveguide design was fixed by the HELIOS project consortium to be compatible with high-performance modulator and AWG designs. The better understanding of the coupling phenomenon leads us to use thicker silicon waveguides, which make easier the coupling with the III-V.

2.4 New concept on a double taper structure with deep ridge waveguide

2.4.1 Coupling section design

As we have previously explained the coupler between silicon and III-V waveguides is the fundamental element of the device structure. The design of the coupling section is determined by waveguides dimensions, taper length and shape, and bonding layer thickness. In this section we introduce a new hybrid laser coupler based on a double taper structure. This design is illustrated in Figure 2.10. It has been optimized for 400 nm silicon rib waveguide with an etch depth of 180 nm.

As we have previously seen, to have an efficient coupling between silicon and III-V waveguides, the parameter $|\delta|$ should be as big as possible at the end and at the beginning of the taper compared to the coupling coefficient κ [13]. The $|\delta|$ value is proportional to the refractive index differences between the two waveguides. To obtain the maximum variation of $|\delta|$ between the beginning and the end of the taper we use a double linear taper. In this way we can add to the $|\delta|$ the contribution coming from silicon waveguide tapering, and that coming from III-V waveguide tapering.

As we can see in Figure 2.8 the effective index of the fundamental mode for the shallow ridge waveguide changes slightly with the waveguide width. The value of $\Delta n/\Delta x$ (where n is the modal effective index and x the waveguide width) is much higher for a deep ridge waveguide. As a consequence a deep ridge III-V waveguide will be able to obtain a larger $|\delta|$, which in turn will lead to a shorter taper for the same coupling efficiency. This is the reason why we choose deep ridge geometry for our design. The refractive index values used in simulation are 3.56 and 1.44 respectively for silicon and silica. The refractive index used for BCB is 1.57. Deep ridge and shallow ridge structure are presented in Figure 2.7.

The exact design of the chosen geometry is shown in Figure 2.9. The design consists of two tapers. In the coupling region (Taper 2) the two waveguides are overlaid, and linearly tapered, while III-V waveguide width is reduced, silicon waveguide width increases and vice versa.

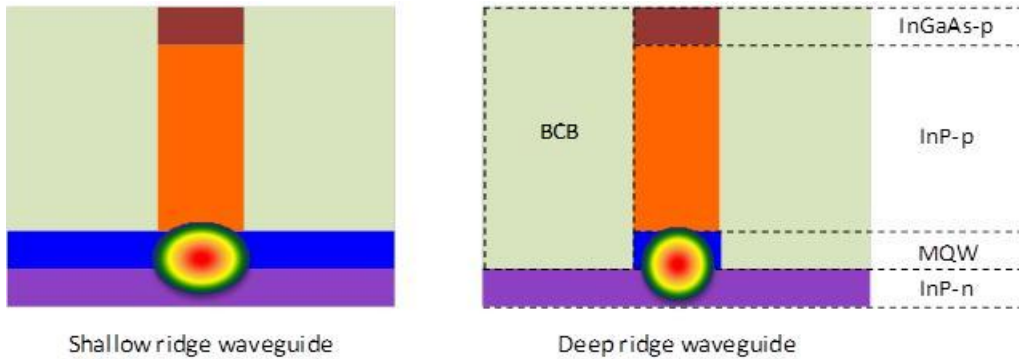


Figure 2.7: Shallow ridge and deep ridge III-V waveguide design

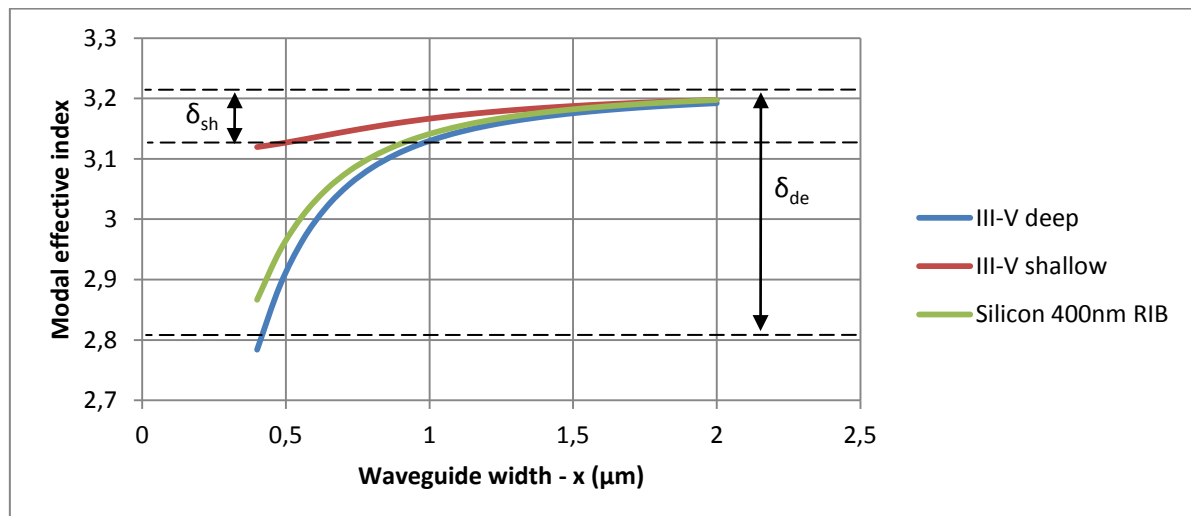


Figure 2.8: fundamental mode effective index as a function of waveguide width in III-V and silicon waveguide, bonding layer of 100 nm, simulation performed with FIMMWAVE

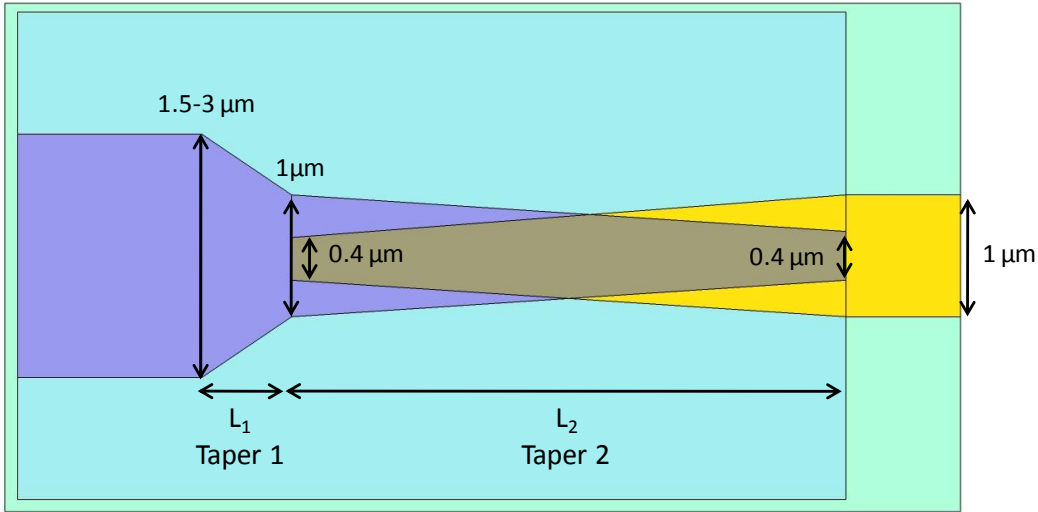


Figure 2.9: schematic top view of the double taper design

Both waveguides are tapered from 1 μm to 0.4 μm (Taper 2 in Figure 2.9) as they present the higher $\Delta n/\Delta x$ in this widths range; this ensures the higher value of $|\delta|$ at the beginning and at the end of the taper. Waveguide widths below 0.4 μm have not been considered due to fabrication complexity.

The straight III-V waveguide has a width varying from 1.5 μm to 3 μm on different designs (more details on straight waveguide optimization are given in 2.4.2.1). To connect the coupling region to the larger straight III-V waveguide avoiding scattering losses, another taper (Taper 1 in Figure 2.9) is needed. The Taper 1 adiabatically adapts the optical mode to pass from the wide to the narrow waveguide section avoiding optical losses. Figure 2.10 illustrates a 3D view of both taper and a cross section of the structure.

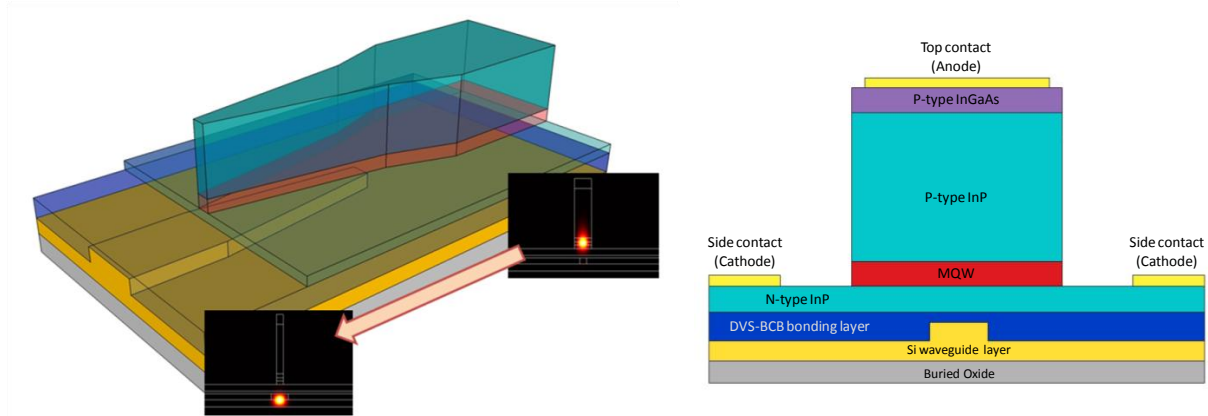


Figure 2.10: Deep etch design, (a) 3D view of the coupling structure of the hybrid laser with representative mode profiles in two cross-sections (b) the detailed cross-sectional view of the taper of the hybrid laser [18]

2.4.2 Optimization using Fimmwave

A fully vectorial mode finder software, FIMMWAVE, was used to optimize the modal properties of the device. The forward power of the fundamental mode (TE) was calculated for various taper lengths as well as different thicknesses of the bonding layer using FIMMPROP. Given that SiO_2 and

DVS-BCB have a similar refractive index (1.44 and 1.57 respectively) and that the bonding layer is thin (from 80 to 150 nm) the results are valid for both kinds of bonding layer.

2.4.2.1 Straight III-V waveguide optimization

The straight III-V section does not need to be single mode. The laser cannot lase on higher order modes as the taper coupler is designed to couple only the fundamental mode of the III-V waveguide, higher order modes experiment very high losses in the taper sections. However an optimum width should exist, it results from the optimization of the injection current, the roughness losses, the electrical leakage and the thermal dissipation. I try to get close to the optimum value by simulation looking for the width that would guarantee the higher overlap with quantum wells and the lower overlap with absorbing layers.

Figure 2.11 illustrates the calculated fundamental optical mode profile for a deeply etched waveguide of 2 μm width. The evolution of the confinement factor in the p-doped InP layer and in the QW layers as a function of waveguide width is shown in Figure 2.12. In the same figure we compare the confinement factor achieved for the same geometry on hybrid sample and on pure III-V wafers. We observe that for hybrid design the optical confinement factor does not change with waveguide widths ranging from 1 to 3 μm . We have more than 11% power confinement in QW layers. Also the p-doped InP layer confinement is really high, around 33%. These high values are mainly due to the refractive index geometry on hybrid samples. In III-V lasers we have a thick InP n-doped layer with a relatively high index (around 3.16) under the QWs layer, indeed the optical mode is located closer to the InP n region and less confined on MQW and on InP p-doped region. In hybrid sample the InP n-doped layer is thin (200nm), below which there is the bonding layer with a very low refractive index, this high index contrast strongly confines the optical mode on the layers above.

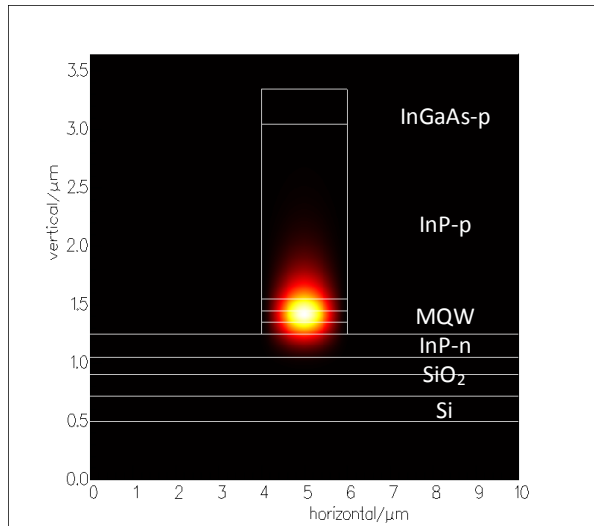


Figure 2.11: calculated power mode profile of a deeply etched 2 μm width III-V waveguide

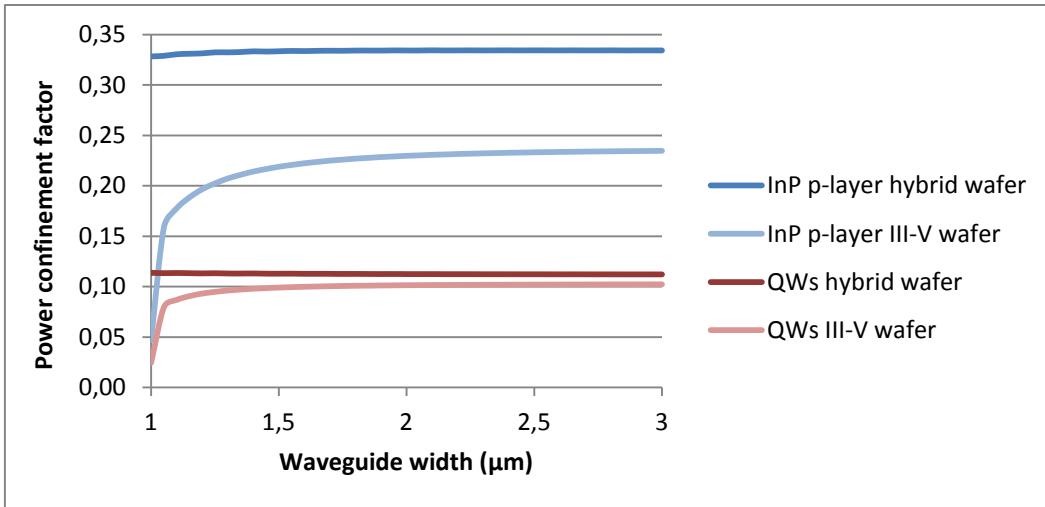


Figure 2.12: Fundamental mode power confinement factor in different layers for an hybrid laser or a full III-V laser with similar design, as a function of III-V waveguide width, FIMMWAVE

Figure 2.12 confirms this qualitative argument, the confinement factors QWs and InP p layers are lower on pure III-V structure for any width; for narrow waveguide the difference between hybrid and pure III-V increases, on III-V wafers as the waveguide is narrowed the optical mode spreads on the thick underlying InP n layer, while in the hybrid wafer it is forced to stay on the etched part of the waveguide, due to the low index bonding layer.

As the simulation results do not give the exact value of the optimal waveguide width, several laser configurations are designed on the lithographic masks with different widths ranging from 1.5 to 3 μm . A narrower waveguide would enhance the scattering losses from sidewalls roughness, a larger one would reduce the pumping efficiency.

2.4.2.2 Taper 1 optimization

Figure 2.13 shows power mode profile calculated at the beginning and at the end of the Taper 1. In Figure 2.14 the forward power of the fundamental mode is calculated as a function of taper length. A 25 μm length taper allows theoretically loss-less transition between 2 μm and 1 μm width deeply etched III-V waveguides.

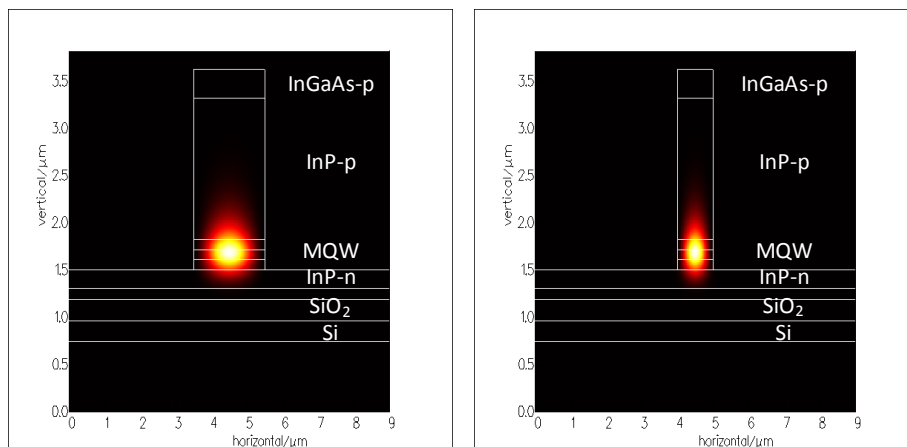


Figure 2.13: calculated power mode profile at the beginning and at the end of the Taper 1

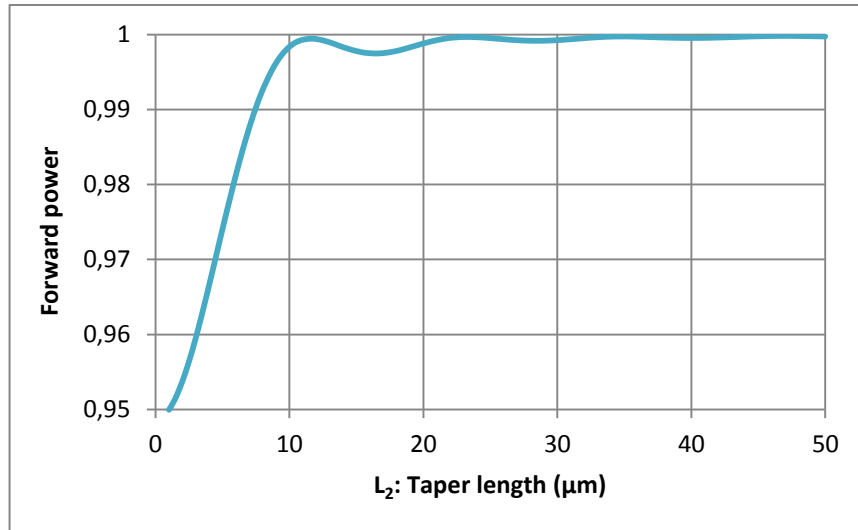


Figure 2.14: Forward power for the fundamental mode for different taper length, FIMMPROP

2.4.2.3 Taper 2 optimization

In order to find the optimum length for the double taper structure I perform several simulations of coupling efficiency as a function of taper length for different bonding layer thickness. The results of these simulations are shown in Figure 2.15. As we can see the bonding layer thickness has a major impact on coupling efficiency. The coupling efficiency rises as the bonding layer thickness decreases. It is quite easy to understand in a qualitative way, the coupling becomes more difficult as the separation between waveguide increases, especially because the separation layer has a low refractive index. In this simulation we use a silica bonding layer, but we achieve a very similar result for a BCB one, as the refractive indexes for these two materials are close.

Considering the maturity of bonding techniques that have been used on this thesis, we can assume to have a bonding layer thickness between 80 and 100 nm in a quite repeatable way, indeed a taper longer than 150 μm is able to allow a theoretically loss-less coupling between III-V and silicon waveguides.

For illustration, in Figure 2.16 we show the average power distribution along a 200 μm taper for an 80 nm bonding layer thickness, this figure clearly shows how the mode is adiabatically transferred from one waveguide to the other. In the same figure we can observe three calculated cross section mode profiles, at the beginning, after 80 μm and at the end of the taper. At the beginning of the taper the optical mode is entirely confined within the III-V waveguide. Along the taper the power comes adiabatically down to the silicon waveguide, after around 80 μm we have half of the power in the III-V waveguide and half in the silicon waveguide. At the end of the taper, the optical power is completely confined in the silicon waveguide.

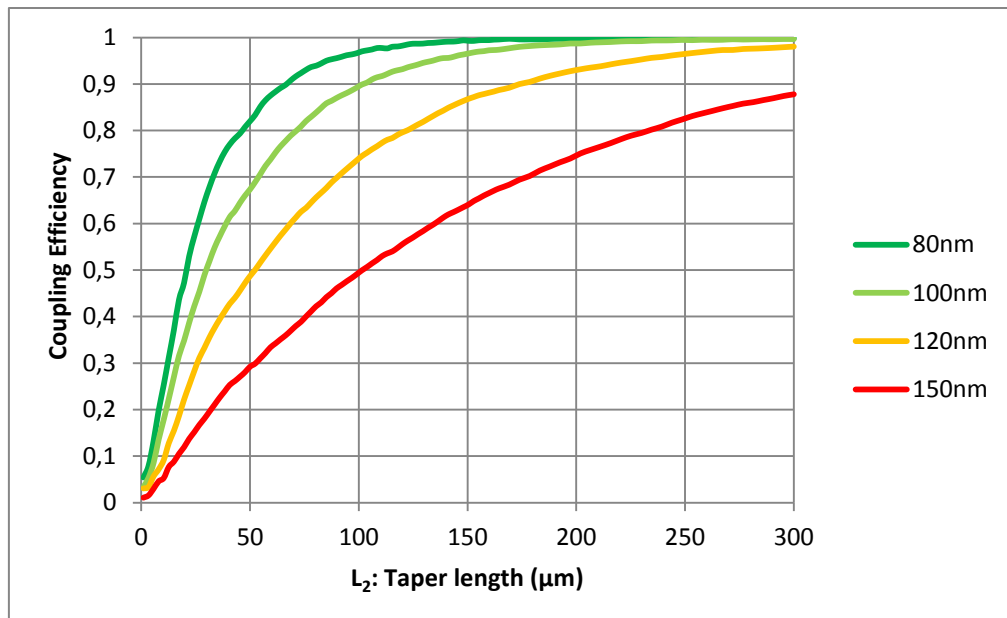


Figure 2.15: coupling efficiency as a function of taper length for different bonding layer thickness, FIMMPROP

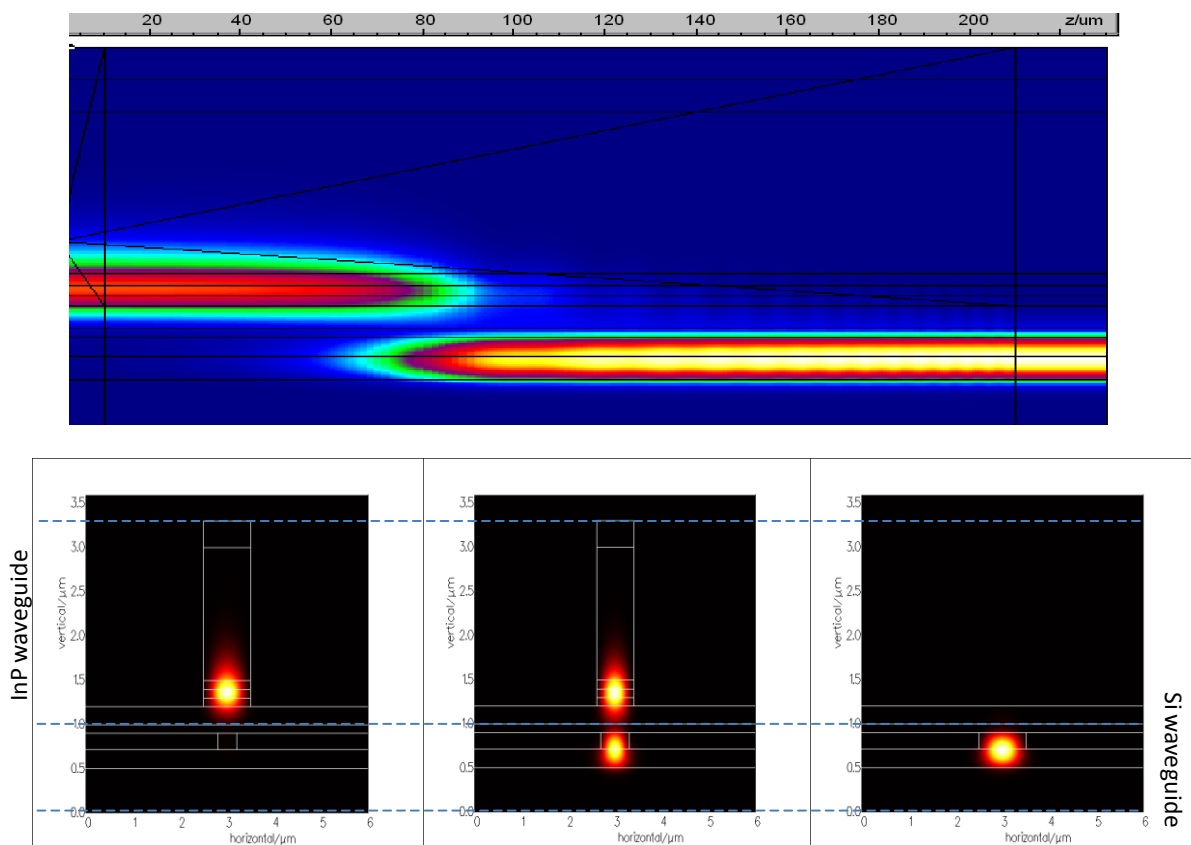


Figure 2.16: lateral view of average power distribution along a 200 μm taper with three cross section calculated optical mode profiles, FIMMPROP

2.4.3 Tolerance analysis

To insure the feasibility of our design I perform tolerance simulations. The study of lateral misalignment is particularly critical for our design. A lateral shift y of the III-V waveguide with respect to the silicon waveguide can result from the fabrication process; this shift strongly affects the coupling efficiency as we show in Figure 2.17.

For illustration, in Figure 2.18 we show the top view of average power distribution along a 200 μm taper, for an 80 nm bonding layer thickness and a lateral misalignment of 0.4 μm . The lateral misalignment modifies the coupling conditions, the taper is no more completely adiabatic but presents some coupled mode like power oscillation between III-V and silicon waveguide. From these simulations we deduce that we cannot tolerate a lateral misalignment of more than 0.3 μm , from a photolithographic point of view this represent a strong constraint.

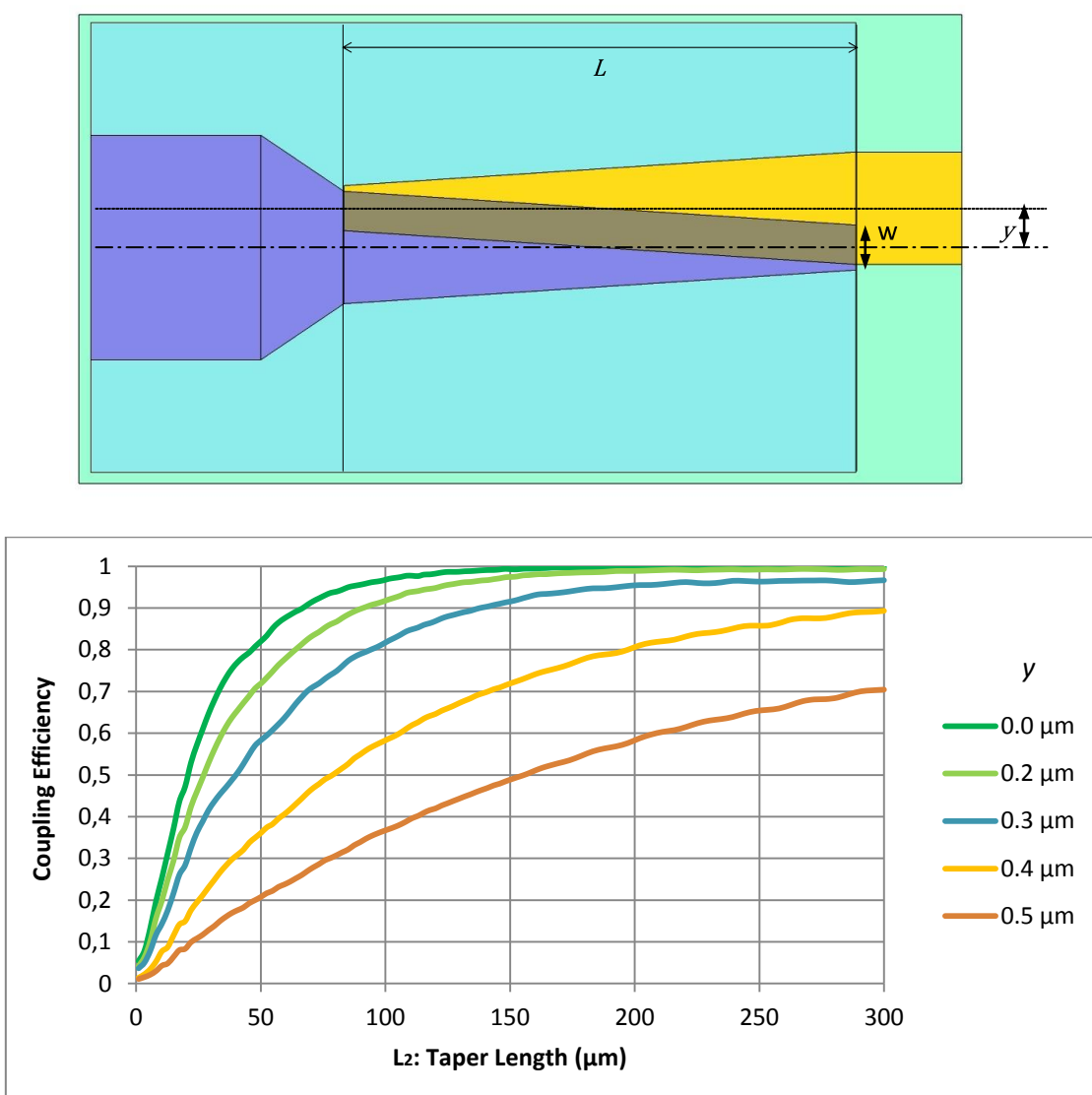


Figure 2.17: coupling efficiency as a function of taper length for different lateral misalignments y , bonding layer thickness is 100 nm, FIMMPROP

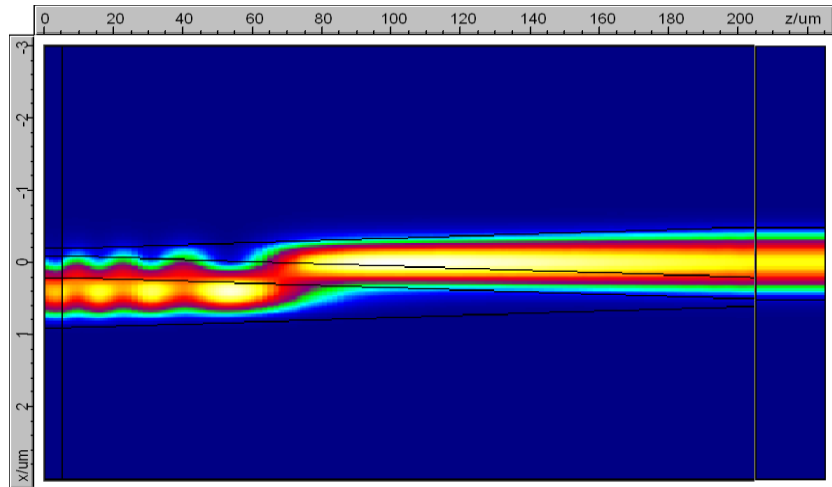


Figure 2.18: 200 μm taper top view, average power distribution with a lateral misalignment of 0.4 μm

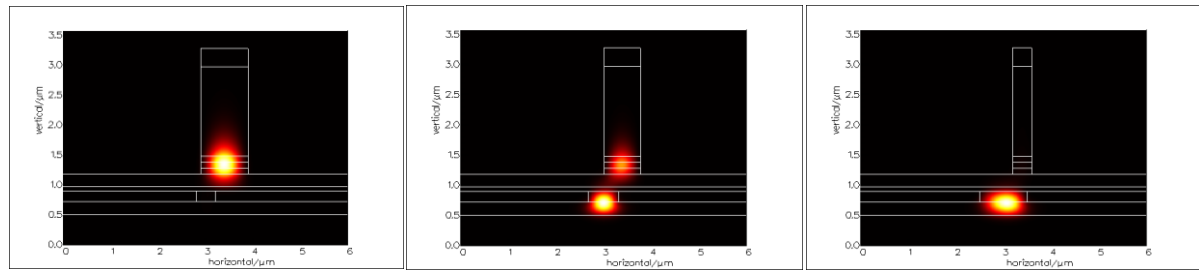


Figure 2.19: Cross section at the beginning, after 80 μm and at the end of the taper with a lateral misalignment of 0.4 μm , FIMMPROP

We also simulate the impact of III-V waveguide taper tip definition, as a 400 nm tip is not easy to achieve by contact lithography. In Figure 2.20 I present the simulated coupling efficiency as a function of taper length for different III-V taper tip widths, the bonding layer thickness is assumed to be 100 nm.

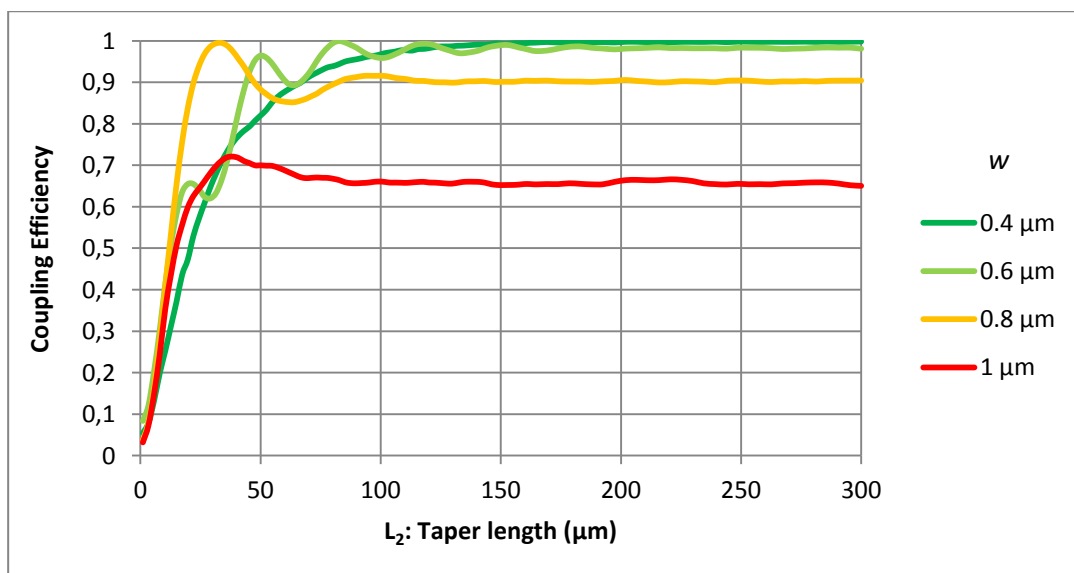


Figure 2.20: coupling efficiency as a function of taper length for different taper tip widths w , bonding layer thickness is 100 nm, FIMMPROP

With a larger III-V tip the taper loses some of its adiabatic behaviour, we observe some coupled mode like oscillations, to have more than 95% coupling efficiency the taper tip has to be narrower than 600 nm. We do not perform the same analysis on the silicon taper tip. The silicon waveguides are patterned on the SOI wafer by 193 nm stepper lithography, which can easily achieve smaller dimensions than 400 nm. In conclusion, this taper structure demonstrates efficient performances anyway, both the III-V thin taper tip and the precise alignment needed, introduce strong fabrication constraints.

Using these simulation results, I designed a set of masks with couplers length ranging from 150 to 250 μm , the straight III-V section width and length ranging respectively from 1.5 to 3 μm and from 300 to 800 μm . The thickness of the adhesive layer must be strictly less than 100 nm.

2.5 Structure with double taper with shallow/deep ridge transition

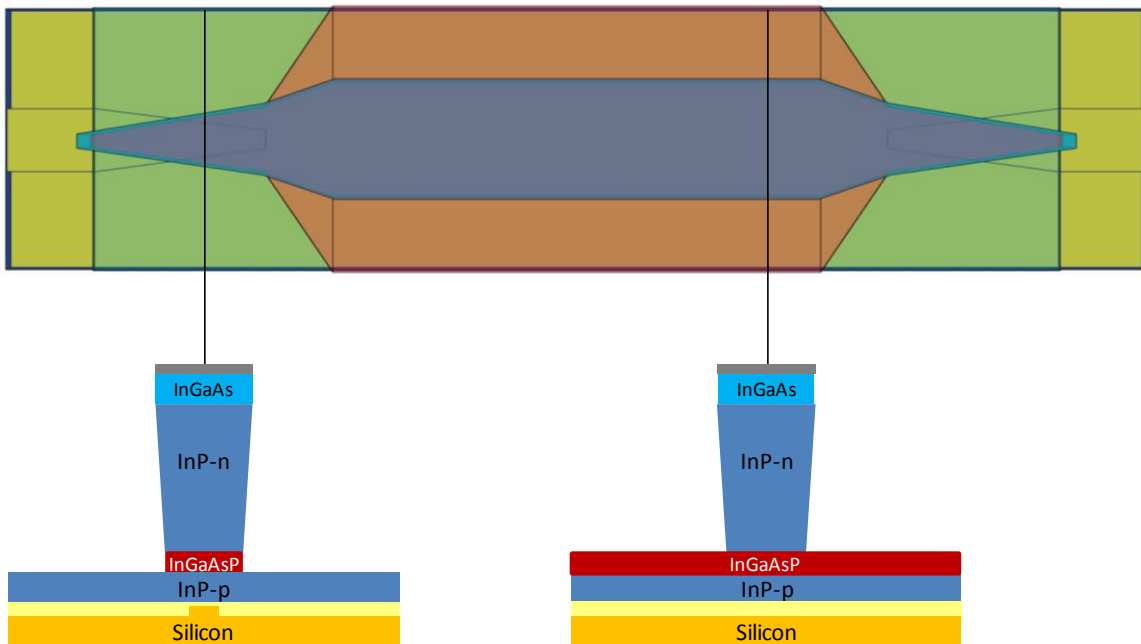


Figure 2.21: top view and cross section of the shallow/deep hybrid laser design

Deeply etched laser generally presents shorter lifetime, higher threshold and lower quantum efficiency compared to shallow etched and buried ridge lasers. Etching the active layer creates defects in the Multi Quantum Well layer, which induce non-radiative recombination leading to electrical losses. At the same time, we enhance scattering as we introduce sidewall roughness, leading to optical losses. [19]

The results achieved with the previous design (detailed on chapter 5.2.1) effectively showed high threshold and laser operation only in the pulsed regime. For these reasons I try to imagine a different configuration that could combine the superior performances of an active waveguide without MQW etching (a shallow etched waveguide), with the efficient coupling of deeply etched design. At the same time the new structure has to be realistic from a fabrication point of views. These considerations lead me to propose a new geometry that merges shallow and deeply etched active waveguides. This structure is illustrated in Figure 2.21.

I use a shallow etched waveguide on the entire straight section of the III-V waveguide, I leave untouched the adiabatic coupler section, and I modify the first taper to optically link these two sections without add losses. I introduce a new mask level to etch the MQW layer, I etch the MQW at a few μm distances from the ridge in the straight section, then, in the first taper, MQW etch is tapered to approach the ridge. The geometry will be better understood by observing Figure 2.22.

Such a design is relatively easy to fabricate, first we etched through contact and InP p-doped layers using an hard mask, we do not remove this mask and afterwards we define a second hard mask for the MQW etch. Using this process this mask does not need a precise alignment, $\pm 0.5 \mu\text{m}$ will be sufficient. In the Taper 2 region the first deposited hard mask will protect the semiconductor from being etched, leading to a deeply etched waveguide while, in the rest of device, the second mask will allow shallow etched geometry. This fabrication process and this innovative shallow/deep ridge design are patented. [20]

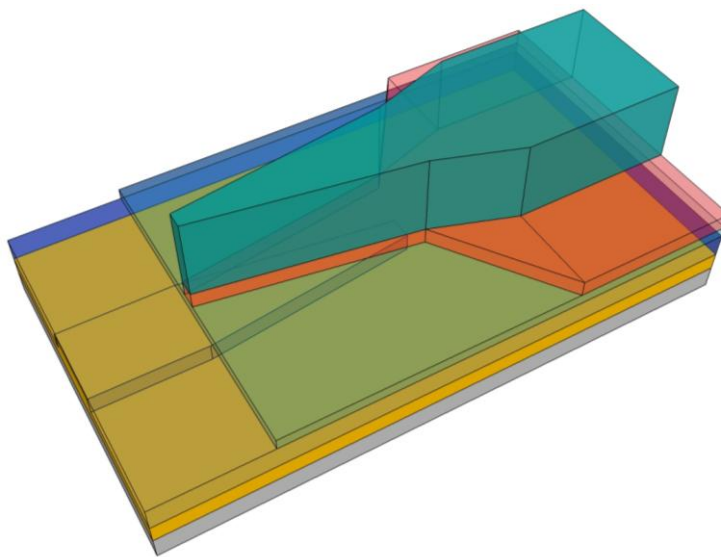


Figure 2.22: 3D view of the coupling section with shallow/deep etch design

2.5.1 Optimization using Fimmwave

The calculated mode profile of the straight shallow etched waveguide is shown in Figure 2.23. In Figure 2.24 we compare the InP p-doped and MQW layer confinement factor for deeply and shallow etched waveguides. We observe that the confinement factor in InP p-layer is lower for shallow ridge laser while the confinement in gain region is a bit higher; both factors have a positive impact on laser performances. In particular a narrow waveguide has a lower confinement factor in the InP p doped layer and therefore lower losses. As sidewall losses increase for narrower waveguides, it will exist an optimum value for the waveguide width, given by a compromise between InP-p layer losses and sidewall losses.

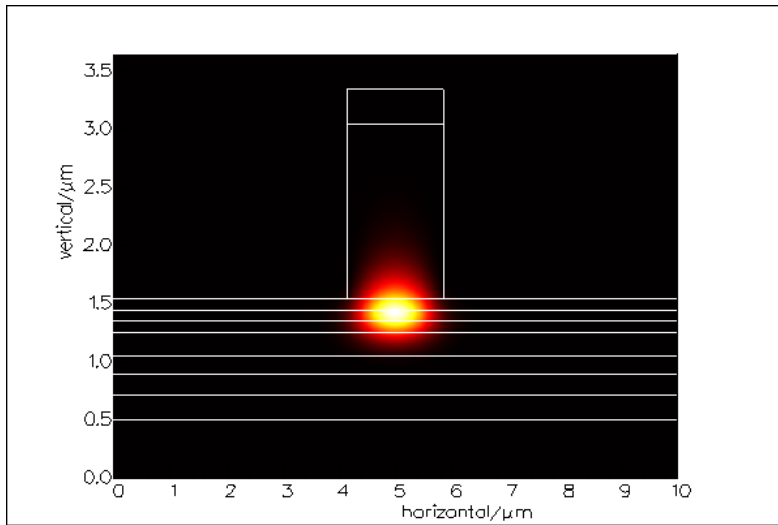


Figure 2.23: calculated power mode profile of a shallow etched 1.7 μm width III-V waveguide, bonding layer thickness is 100 nm, FIMMWAVE

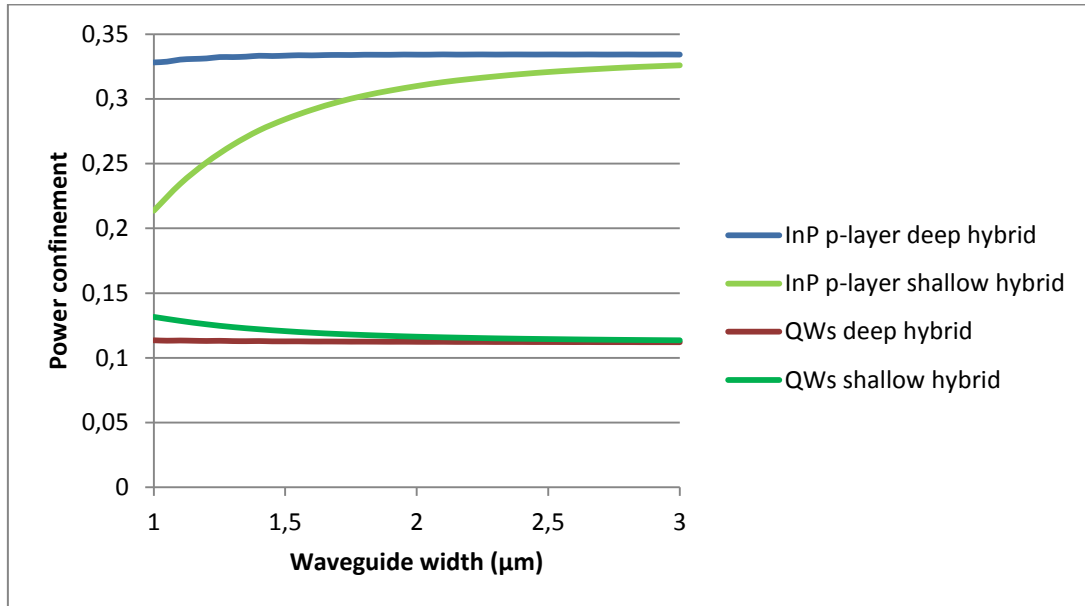


Figure 2.24: Power confinement in InP p-doped and MQW layer as a function of III-V waveguide width for deep and shallow etch design, bonding layer thickness 100nm, FIMMWAVE

The new configuration of Taper 1 has been simulated; in Figure 2.25 we present the simulated curves of the forward power on the first mode as a function of taper length. A 20 μm long taper can ensure almost loss-less transmission.

The results achieved with this design for respectively DVS-BCB and molecular bonding are described in sections 5.2.2 and 5.3.1. These results have revealed that components based on this design show much higher performances in terms of threshold current, output power and working temperature.

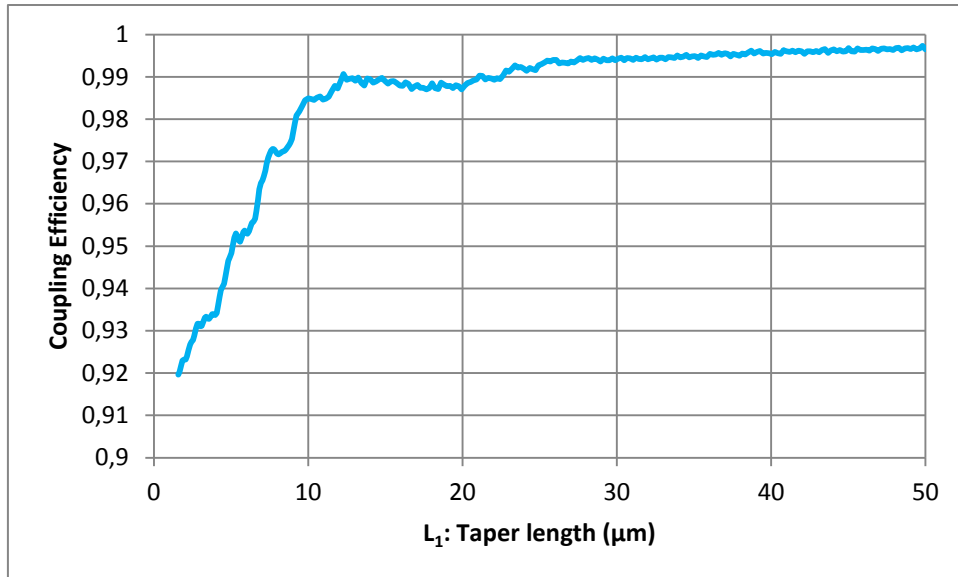


Figure 2.25: Forward power for the fundamental mode for different taper length

2.6 Optimized adiabatic taper

The lasers realized following previously described designs demonstrate good performances, anyway all the measured optical spectra present strong perturbations that reveal a multiple cavities effect. We explain this effect with a parasite reflection coming from the end of the taper.

If the tapers would work correctly, we should achieve a Fabry-Perot spectrum with a Free Spectral Range fixed by the distance between the two cleaved facets. But if the tapers coupling efficiency is lower than 100%, we will observe light reflection on the tapers tips; tapers behave like low reflection mirrors, and we do not have anymore a single cavity but many optical cavities. The spacing in wavelength between two transmitted maxima is not anymore defined by the FSR.

As we detail in chapter 5, it was impossible to respect the tolerances during fabrication and the achieved coupling efficiency was lower than 100%. To increase the coupling efficiency I try to improve the taper design to make it more tolerant and easier to fabricate. To improve the adiabatic coupler design I decide to use the theoretical model detailed on section 2.1 in a more practical way. The idea was to use the adiabaticity criterion to design an optimized taper, indeed the shortest taper for this coupled waveguide system. In this chapter we will detail how we go from the adiabaticity criterion to the taper design, and we will present the simulated performances and tolerances.

2.6.1 From the analytical model to the taper shape

The adiabaticity criterion describes the evolution along the coupler of the propagation constant difference between the two waveguides as a function of the coupling coefficient κ . To derive the taper shape I need to obtain the function describing the evolution of the waveguide width along the coupler. To reach this objective I first transform the equation (2.9) to explicit the refractive index of both waveguides (2.12). In the following section we will refer to silicon and III-V waveguides by the subscript *si* and *inp*.

$$\frac{\delta}{\kappa} = \frac{u}{\sqrt{1-u^2}} = \frac{2\kappa\varepsilon^{1/2}(z-z_0)}{\sqrt{1-[2\kappa\varepsilon^{1/2}(z-z_0)]^2}} \quad (2.10)$$

$$\delta = \frac{\pi}{\lambda} (n_{si} - n_{inp}) \quad (2.11)$$

$$n_{si} - n_{inp} = \frac{2\kappa^2\varepsilon^{1/2}(z-z_0)}{\pi\sqrt{1-[2\kappa\varepsilon^{1/2}(z-z_0)]^2}} \quad (2.12)$$

Once I found the equation (2.12) I can choose to use a double taper design, as in the preview linear configuration, or a single taper design; in that case the dimension of one waveguide does not change along the coupler. I chose this second possibility as the fabrication process is simpler letting the III-V waveguide straight and tapering the silicon waveguide. Therefore we consider n_{inp} as a constant as the III-V waveguide width will be constant.

$$n_{si} = \frac{2\kappa^2\varepsilon^{1/2}(z-z_0)}{\pi\sqrt{1-[2\kappa\varepsilon^{1/2}(z-z_0)]^2}} + n_{inp} = f(z-z_0) \quad (2.13)$$

We achieve a function f describing the evolution of the silicon waveguide index along the taper axe z .

Using a 2D mode solver we can obtain the function g relaying the silicon index at the waveguide width w as in Figure 2.8.

$$n_{si} = g(w) \quad (2.14)$$

$$w(z) = g^{-1}(n_{si}) = g^{-1}(f(z-z_0)) \quad (2.15)$$

$$w(z) = g^{-1} \left[\frac{2\kappa^2\varepsilon^{1/2}(z-z_0)}{\pi\sqrt{1-[2\kappa\varepsilon^{1/2}(z-z_0)]^2}} + n_{inp} \right] \quad (2.16)$$

Where g^{-1} denotes the inverse function of g . Inversing g and applying it to equation (2.13) allows to find a relation expressing the evolution of the optimized taper width along the z axe.

2.6.2 Coupling coefficient κ

Once I have found the previous relation I still need to evaluate the coupling coefficient κ between the waveguides. An exact calculation of κ is not easy to obtain in a real 3D system. To find an approximate value of κ one can profit from the properties of coupled waveguides.

I use Fimmprop to simulate the light propagation inside the coupled waveguide system. I choose a constant width for the silicon and the III-V waveguide, a defined bonding layer thickness, then I inject light on one waveguide, and I observe the amount of power exchanged with the other waveguide as a function of the system length (Figure 2.26). The coupled waveguides exchange power periodically with a defined spatial frequency. Measuring the period in space and the amount of power exchanged we can deduce κ (equation (2.4)).

In the model proposed by A. Yariv et al. the κ value is supposed to be constant along the optimized taper. This assumption is true only for weakly coupled waveguide systems and is partially true for our designs. As a matter of fact, changing the width of the waveguides in our simulations leads to variations of κ , especially, as it is obvious, for thin bonding layer thickness. In certain configurations κ can range from 50 to 200 mm^{-1} inside the same taper structure. However, as we will see in the next sections, the adiabaticity criterion validity is not strongly affected in those kind of systems in which κ evolves slightly along the coupler.

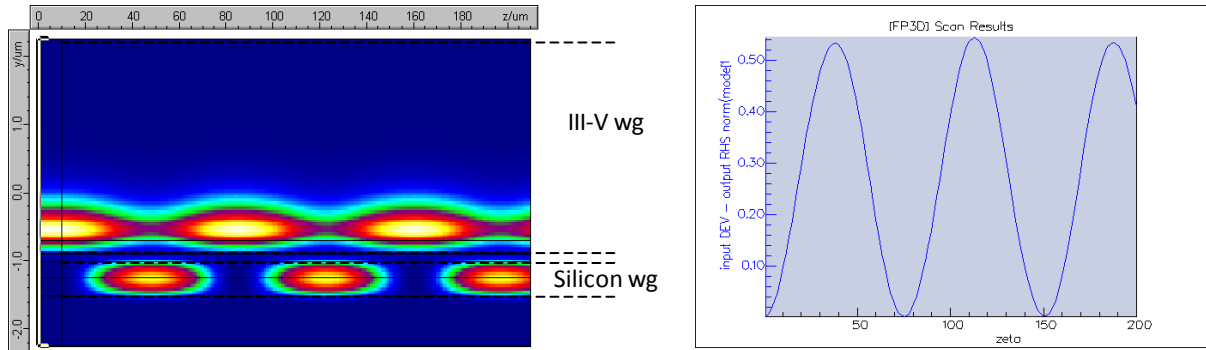


Figure 2.26: simulated power exchange between coupled waveguides, on the left the light propagation in the coupled system (200 μm length), on the right the fraction of power in the silicon waveguide as a function of the section length

2.6.3 Simulation results

Once I found the taper shape satisfying the adiabaticity criterion, I use Fimmprop and the eigenmodes expansion method to simulate the coupling efficiency achievable with the design.

To verify the accuracy of our simulation we first tried to reproduce the results described in [13]. In that paper a comparison between linear, cubic and optimized taper coupling efficiencies, calculated from the transfer-matrix method, is proposed. In Figure 2.27 we show the coupling efficiencies achieved for these three designs from Fimmwave eigenmodes expansion method. The geometry we simulate is slightly different from [13] due to the simulation software constraints. In the paper gamma value goes from -10 to +10, in our simulation gamma has to stay between -1 and +1 as we are forced to use realistic waveguide dimensions. However, the results are in very good agreement with the paper data. The optimized taper confirms to be potentially much shorter than linear or higher order tapers.

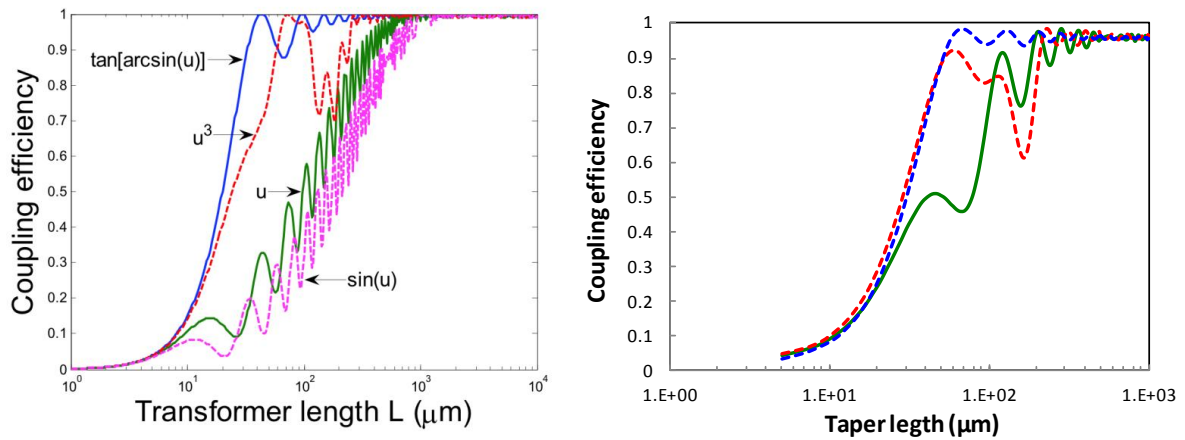


Figure 2.27: Comparison between linear, cubic and optimized taper performances presented in [13] on the left, and simulated with FIMMPROP on the right

2.6.4 Optimization for 400 and 500 nm thick silicon

I apply the optimized taper method to the design of hybrid III-V lasers on silicon. The laser geometry is the same described in 2.5, I only modify the coupler structure. I use this coupler in two configurations of silicon rib waveguide, 400 nm and 500 nm thick. As we will see thicker silicon makes the coupling with the III-V waveguide easier. In the following section I describe both designs and the simulated performances I achieved for these structures. Both designs are currently under fabrication.

2.6.4.1 400nm height silicon rib waveguide

As we have previously seen, for this thickness of the silicon waveguide it is hard to achieve a good coupling with a shallow ridge III-V waveguide, indeed we concentrate on deeply etched geometry for the coupler region. The main fabrication problem for the double taper design was related to the difficulty to achieve a narrow III-V taper tip. With this new design we do not taper anymore the III-V waveguide but we let its width constant to a reasonably achievable value.

To find the exact taper shape we use the method described in section 2.6. First we have to fix the value of the refractive index for the III-V waveguide (n_{inp}) as detailed by equation (2.10), that means that we have to choose a waveguide width. From a design point of view we would prefer a III-V refractive index value located exactly in the middle of the index variation range of the silicon waveguide, to have the maximum $|\delta|$ value on taper borders. But both from a fabrication and an electro/optics point of view, a too thin deeply etched III-V waveguide does not represent the best configuration. This is the reason why we opt for a 0.8 μm large III-V waveguide, which has a refractive index of 3.07 (Figure 2.28).

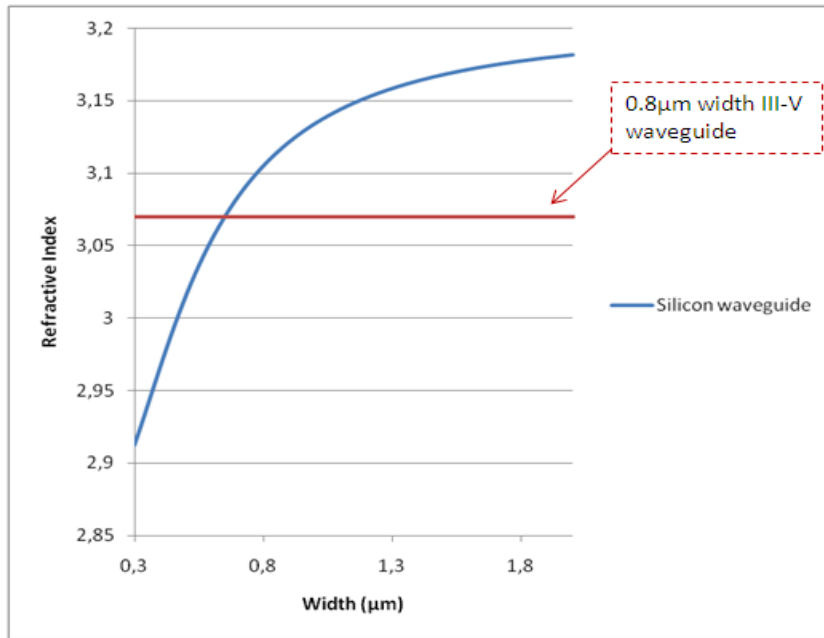


Figure 2.28: refractive index of silicon waveguide as a function of the width compared to the refractive index of a 0.8 μm large deeply etched III-V waveguide

Secondly, we need to evaluate the coupling coefficient value. With the method detailed in section 2.6.2 we found κ values ranging from 50 to 200 mm^{-1} . As κ is far from being constant the taper described by the adiabaticity criterion will not be perfectly adapted. Finally we use equation (2.16) to obtain the optimized taper shape presented in Figure 2.29. Looking for the ideal design we simulate the coupling efficiency as a function of the taper length for several tapers, every taper was designed for a different κ value. In Figure 2.30 we present two of the better designs, they are calculated for a κ value of 60 and 80 mm^{-1} . The bonding layer thickness is assumed to be of 100 nm.

Both tapers can be really short compared to the double linear design. The optimized taper calculated for a coupling coefficient of 80 mm^{-1} presents slightly better performances, we can have a 90% coupling efficiency for a taper length as short as 50 μm . Nevertheless both configurations present an imperfect adiabaticity; the coupling efficiency keeps oscillating between 100 and 90% over a length of 50 μm . This can be explained with the fact that the coupling coefficient κ is not constant along the structure. The adiabaticity criterion is deduced for a constant coupling coefficient, if this condition is not respected the criterion does not properly describe the light coupling anymore.

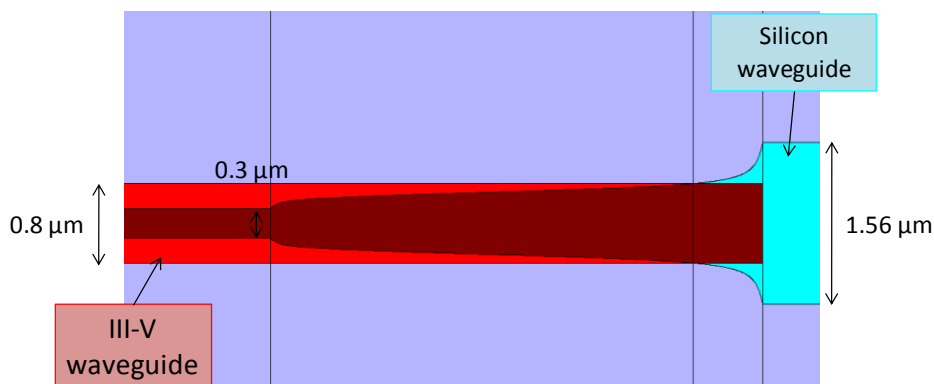


Figure 2.29: schematic top view of the optimized taper design for a 400 nm thick silicon rib waveguide

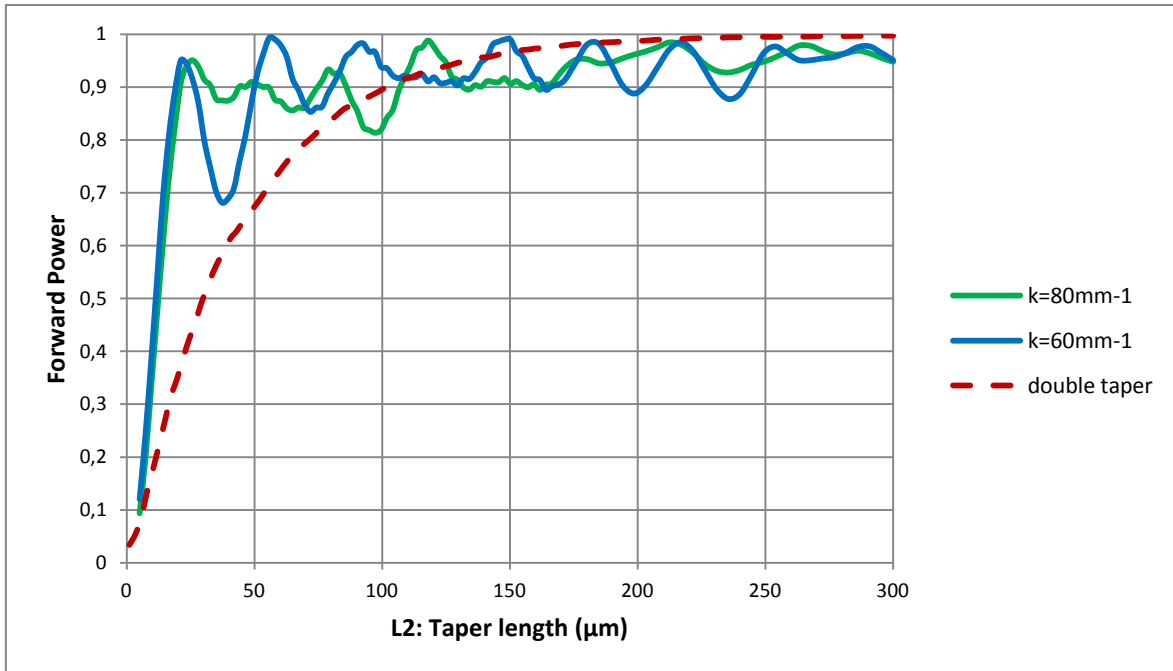


Figure 2.30: coupling efficiency of the optimized taper as a function of taper length for different k values

2.6.4.2 1.55 μm silicon 500nm height

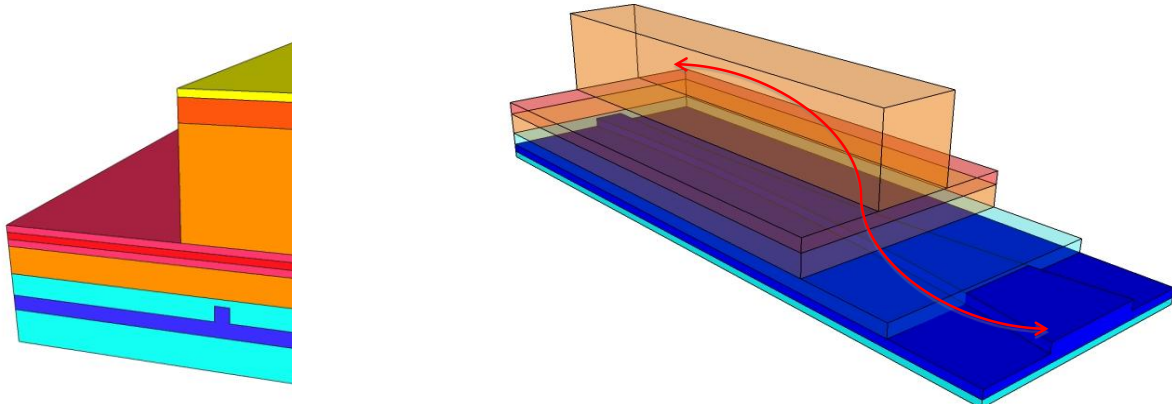


Figure 2.31: 3D views of the taper coupler for a 500 nm thick silicon waveguide

As we have seen with a 400 nm silicon waveguide the realization of an efficient coupler is far from being easy. Looking for a more efficient and shorter coupler we explored other geometries that could allow higher $|\delta|$ values. As we have previously seen, we do not need to reduce both the III-V and the silicon waveguide width in the taper, but we can fix the dimension of the III-V waveguide and vary just the silicon width. If the III-V waveguide width does not change along the taper, $|\delta|$ will be only related to $\Delta n_{Si}/\Delta w$ and to n_{inp} ; the more we will be able to change the refractive index of the silicon waveguide changing the waveguide width, the more we will be able to achieve a high $|\delta|$. A simple way to achieve a high $\Delta n_{Si}/\Delta w$ indeed is to use thicker silicon.

Moreover, we would like to profit from the higher performances of shallow ridge active waveguides also in the coupler region. Passing from thin to thick silicon, as we increase n_{Si} , we have the possibility to use a shallow etched III-V waveguide for the taper as for the straight section.

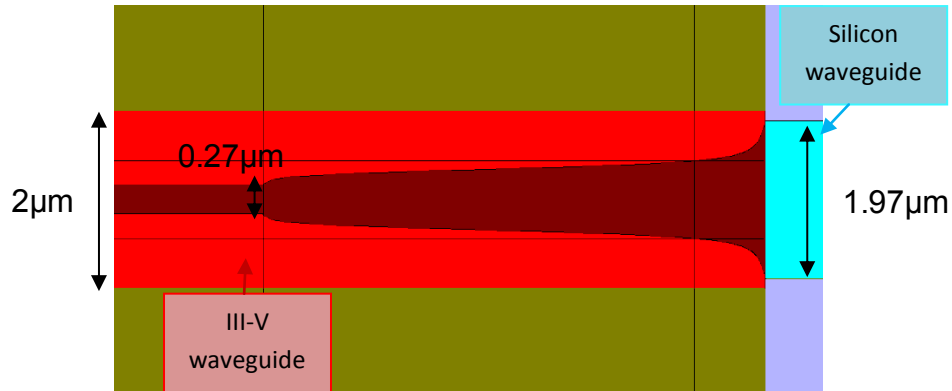


Figure 2.32: schematic top view of the optimized taper design for a 500 nm thick silicon rib waveguide

In this section we will review the design features of an optimized taper design for a 500 nm silicon rib waveguide with an etch depth of 250nm. We achieve a taper geometry described by Figure 2.31 and Figure 2.32.

As the silicon is thicker we can also allow a wider III-V waveguide on the taper part (Figure 2.23). We decide to use a 2 μm active waveguide in the taper section as in the central section, in this way we will never have to reduce or enlarge the waveguide width. We eliminate indeed the Taper 1 that we used in previous design. The III-V waveguide will be much simpler to realize as it will be composed by a shallow ridge waveguide of 2 μm width all over the laser structure.

By simulation we find a κ value between 60 and 90 mm^{-1} . κ is indeed quite stable along the coupler. Simulation results for tapers designed for different κ values are presented in Figure 2.34. The bonding layer thickness is assumed to be 100 nm. A 100 μm taper can ensure a really efficient coupling, moreover the power oscillation are reduced compared to 400 nm waveguide taper. Tolerance simulations have shown that this taper is less sensitive to bonding layer thickness variations and misalignment between silicon and III-V waveguides.

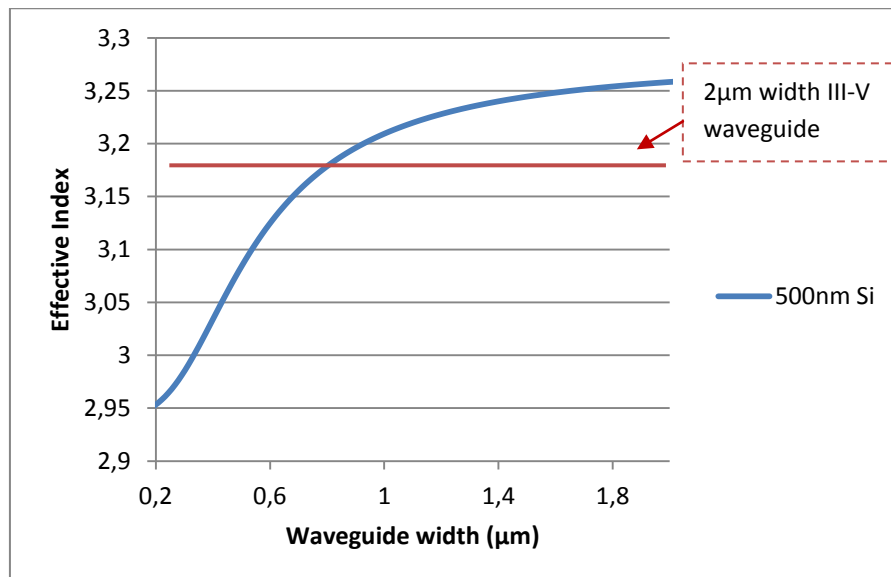


Figure 2.33: refractive index of silicon waveguide as a function of the width compared to the refractive index of a 2 μm large shallow etched III-V waveguide, bonding layer of 100 nm, FIMMWAVE

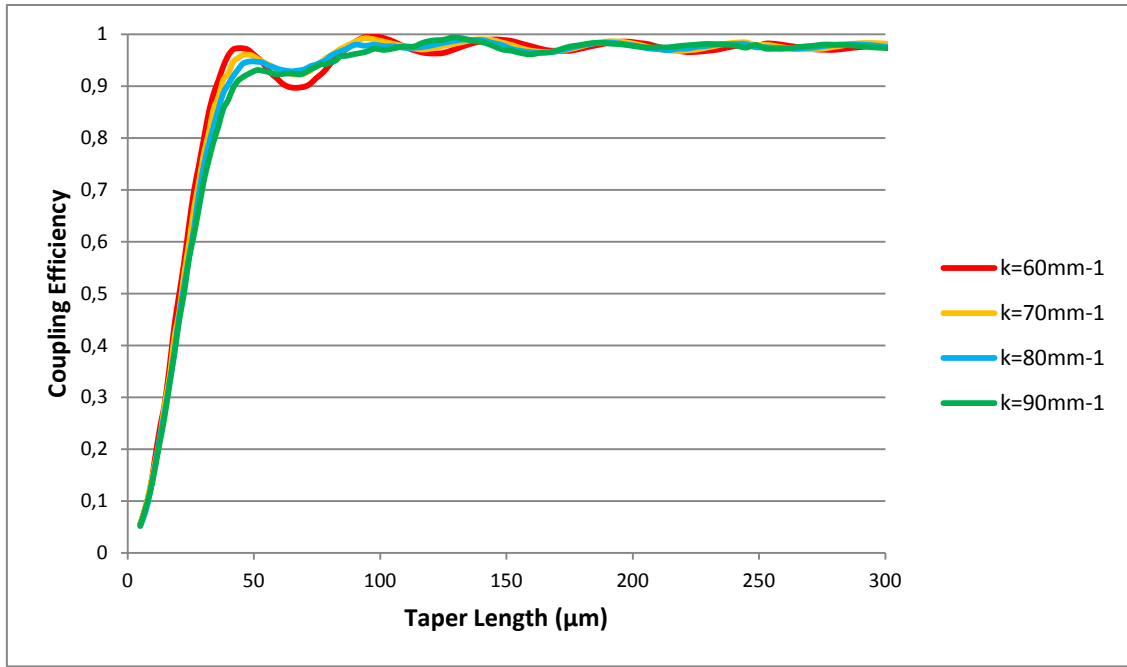


Figure 2.34: coupling efficiency of the optimized taper as a function of taper length for different k values

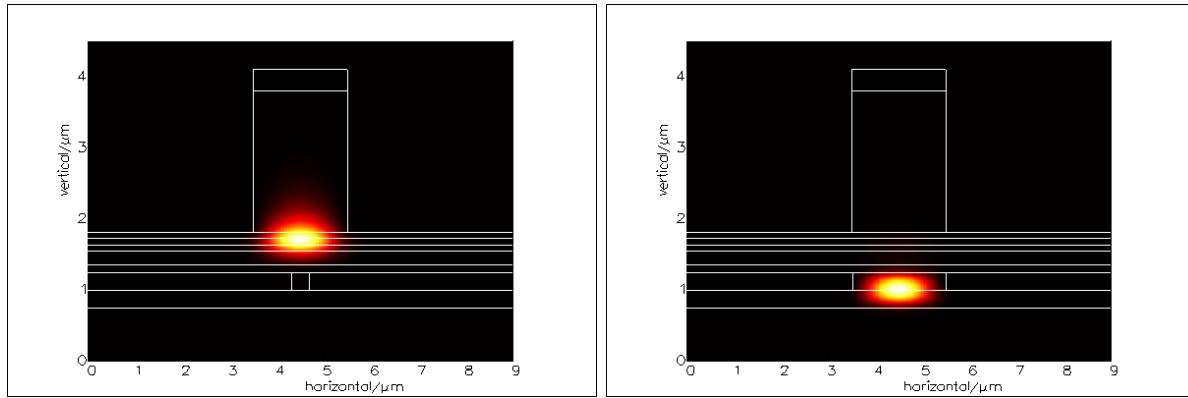


Figure 2.35: simulated optical power at the input and output of the taper

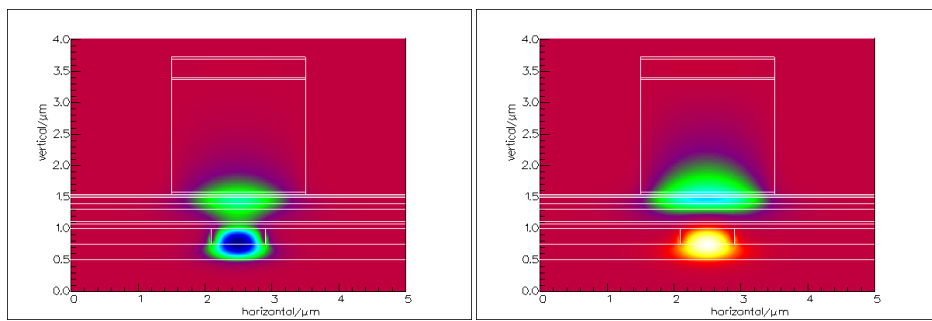


Figure 2.36: even and odd supermodes simulated electric field in the taper coupler

2.7 Conclusions

In this chapter we analyzed the light coupling between III-V and silicon waveguides in hybrid III-V on SOI lasers. We introduced a mathematical model to describe the adiabatic coupling and we derived an adiabaticity criterion. In Table 2.2 we resume the different taper designs reported in this chapter and theirs characteristics. We first designed a double taper based on a deep ridge III-V waveguide and on a 400 nm rib silicon waveguide. Beam propagation simulations of the structure revealed a correct adiabatic behavior but a low tolerance to fabrication constraints. Moreover, deeply etched lasers generally present lower performances compared to shallow etched and buried ridge lasers.

For these reasons we introduced two modifications to this design. First, we used a shallow etched waveguide for the straight III-V section, using the deeply etched waveguide only in the coupling sections. Shallow etched and deeply etched sections have been connected by adiabatically tapering the MQW layer. This configuration drastically improved the performances of our components.

Second, we introduced a different taper design that is more tolerant and efficient. We derived this design from the adiabaticity criterion. In this case only the silicon waveguide is tapered and the fabrication is much simpler. Thanks to this design we reduced the taper length of a factor two and we increased the tolerances to fabrication defects. A thicker silicon waveguide helps to achieve an even better taper behavior.

	III-V waveguide straight section	III-V waveguide coupler section	Taper geometry	Silicon waveguide	Taper length	Considerations
Double taper deep ridge	Deep ridge	Deep ridge	Double linear taper	400 nm rib	200 μm	Low tolerance, coupler adiabatic and long, high straight section losses
Double taper shallow/deep ridge	Shallow ridge	Deep ridge	Double linear taper	400 nm rib	200 μm	Low tolerance, coupler adiabatic and long, low straight section losses
Optimized taper 400 nm	Shallow ridge	Deep ridge	Optimized taper	400 nm rib	100 μm	Coupler short, not perfectly adiabatic, low straight section losses
Optimized taper 500 nm	Shallow ridge	Shallow ridge	Optimized taper	500 nm rib	100 μm	Tolerant, short and adiabatic, low straight section losses

Table 2.2: characteristics of the different designed tapers

2.8 Bibliography

- [1] B. Saleh and M. Teich, *Fundamentals of photonics*, Wiley, 1991.
- [2] P. Yeh, *Optical Waves in Layered Media*, Wiley, 1988.
- [3] J. Cook, "Tapered velocity couplers," *Bell Syst. Tech. Journals*, 1955.
- [4] A. G. Fox, "Wave coupling by warped normal modes," *Bell Syst. Tech. Journals*, 1955.
- [5] M. Wilson and G. Teh, "Improved tolerance in optical directional couplers," *Electronics Letters*, vol. 9, no. 19, 1973.
- [6] J. Love, W. Henry, W. Stewart, R. Black, S. Lacroix and F. Gonthier, "Tapered single-mode fibres and devices. I. Adiabaticity criteria," *Optoelectronics, IEE Proceedings J*, vol. 138, no. 5, 1991.
- [7] Y. Tohmori, Y. Suzuki, H. Fukano, M. Okamoto, Y. Sakai, O. Mitomi, S. Matsumoto, M. Yamamoto, M. Fukuda, M. Wada, Y. Itaya and T. Sugie, "Spot-size converted 1.3 μm laser with butt-jointed selectively grown vertically tapered waveguide," *Electronics Letters*, vol. 31, no. 13, 1995.
- [8] N. Yoshimoto, K. Kawano, Y. Hasumi, H. Takeuchi, S. Kondo and Y. Noguchi, "InGaAlAs/InAlAs multiple quantum well phase modulator integrated with spot size conversion structure," *Photonics Technology Letters*, vol. 6, no. 2, 1994.
- [9] A. Sugita, A. Kaneko, K. Okamoto, M. Itoh, A. Himeno and Y. Ohmori, "Very low insertion loss arrayed-waveguide grating with vertically tapered waveguides," *Photonics Technology Letters*, vol. 12, no. 9, 2000.
- [10] K. Kawano, M. Kohtoku, N. Yoshimoto, S. Sekine and Y. Noguchi, "2x2 InGaAlAs/InAlAs multiquantum well (MQW) directional coupler waveguide switch modules integrated with spotsize convertors," *Electronics Letters*, vol. 30, no. 4, 1994.
- [11] G. Valicourt, G. Duan, C. Ware, M. Lamponi and R. Brenot, "Experimental and theoretical investigation of mode size effects on tilted facet reflectivity," *Optoelectronics, IET*, vol. 5, no. 4, 2011.
- [12] I. Moerman, P. Van Daele and P. Demeester, "A review on fabrication technologies for the monolithic integration of tapers with III-V semiconductor devices," *Selected Topics in Quantum Electronics*, vol. 3, no. 6, 1998.
- [13] X. Sun, H.-C. Liu and A. Yariv, "Adiabaticity criterion and the shortest adiabatic mode transformer in a coupled-waveguide system," *Optics Letters*, vol. 34, no. 3, 2009.
- [14] A. Yariv, *Optical Electronics in Modern Communications*, New York: Oxford University Press, 1997.
- [15] M. Lamponi, S. Keyvaninia, F. Pommereau, R. Brenot, G. de Valicourt, F. Lelarge, G. Roelkens, D. Van Thourhout, S. Messaoudene, J.-M. Fedeli and G.-H. Duan, "Heterogeneously integrated InP/SOI laser using double tapered single-mode waveguides through adhesive die to wafer bonding," *Group IV Photonics (GFP), 2010 7th IEEE International Conference on*, 2010.
- [16] H. Debregeas-Sillard, A. Vuong, F. Delorme, J. David, V. Allard, A. Bodere, O. LeGouezigou, F.

- Gaborit, J. Rotte, M. Goix, V. Voiriot and J. Jacquet, "DBR module with 20-mW constant coupled output power, over 16 nm (40×50-GHz spaced channels)," *Photonics Technology Letters*, vol. 13, no. 1, 2001.
- [17] A. Katz, Indium Phosphide and related materials: processing, technology, and devices, Norwood: Artech House, 1992.
- [18] M. Lamponi, S. Keyvaninia, C. Jany, F. Poingt, F. Lelarge, G. d. Valicourt, G. Roelkens, D. V. Thourhout, S. Messaoudene, J.-M. Fedeli and G. Duan, "Low-threshold heterogeneously integrated InP/SOI laser with a double adiabtic taper coupler," *Photonics Technology Letters*, 2011.
- [19] B. J. Thibeault, T. A. Strand, T. Wipiejewski, M. G. Peters, D. B. Young, S. W. Corzine, L. A. Coldren and J. W. Scott, "Evaluating the effects of optical and carrier losses in etched-post vertical cavity lasers," *Journal of Applied Physics*, vol. 78, no. 10, 1995.
- [20] M. Lamponi, G.-H. Duan, G. De Valicourt, F. Point, G. Roelkens and D. Van Thourhout, "Hybrid III-V-silicon laser sources including transition from shallow ridge waveguide to deep ridge waveguide". 8 July 2011.
- [21] T. Koch, U. Koren and B. I. Miller, "High-performance tunable 1.5 μ m InGaAs/InGaAsP multiple quantum well distributed Bragg reflector lasers," *Applied Physics Letters*, vol. 53, 1988.
- [22] H. Kogelnik and C. V. Shank, "Stimulated emission in a periodic structure," *Applied Physics Letters*, vol. 18, no. 4, 1971.
- [23] T. Dupont, L. Grenouillet, A. Chelnokov, S. Messaoudene, J. Harduin, D. Bordel, J.-M. Fedeli, C. Seassal, P. Regreny and P. Viktorovitch, "A III-V on silicon distributed-feedback laser based on exchange-Bragg coupling," *Proc. Group IV Photonics*, 2010.
- [24] B. Liu, A. Shakouri and J. E. Bowers, "Passive microring-resonator-coupled lasers," *Applied Physics Letters*, vol. 79, 2001.
- [25] B. Liu, A. Shakouri and J. Bowers, "Wide Tunable Double Ring Resonator Coupled Lasers," *Photonics Technology Letters*, vol. 14, no. 5, 2002.
- [26] G. P. Agrawal and N. K. Dutta, Semiconductor Lasers, second edition, Kluwer Academic, 1993.
- [27] G. H. Duan, P. Gallion and G. Debarge, "Analysis of phase-amplitude coupling factor and spectral linewidth of distributed feedback and composite-cavity semiconductor lasers," *IEEE Journal of Quantum Electronics*, vol. 26, pp. 32-44, Jan. 1990.
- [28] H. Debrégeas-Sillard, A. Vuong, F. Delorme, J. David, V. Allarrd, A. Bodéré, O. L. Gouezigou, F. Gaborit, J. Rotte, M. Goix, V. Voiriot and J. Jacquet, "DBR module with 20mW constant coupled output power, over 16nm (40 channels 50 Ghz spaced)," *Photonics Technology Letters*, vol. 13, no. 1, 2001.
- [29] M. Zirngibl, C. H. Joyner, L. W. Stulz, U. Koren, M.-D. Chien, M. G. Young and B. I. Miller, "Digitally Tunable Laser Based on the Integration of a Waveguide Grating Multiplexer and an Optical Amplifier," *Photonics Technologie Letters*, vol. 6, no. 4, 1994.
- [30] R. Martin, S. Forouhar, S. Keo, R. Lang, R. Hunsperger, R. Tiberio and P. Chapman, "CW Performance of an InGaAs-GaAs-AlGaAs Laterally-Coupled Distributed Feedback (LC-DFB) Ridge

- Laser Diode," *Photonics Technology Letters*, vol. 7, no. 3, 1995.
- [31] S. Akiba, M. Usami and K. Utaka, "1.5- μm lamda/4-Shifted InGaAsP/InP DFB Lasers," *Journal of Ligthwave Technology*, vol. 5, no. 11, 1987.
- [32] H. Kogelnik and C. V. Shank, "Coupled-wave theory of distributed feedback lasers," *Journal of Applied Physics*, vol. 43, 1972.
- [33] V. Jayaraman, Z.-M. Chuang and L. Coldren, "Theory, design, and performance of extended tuning range semiconductor lasers with sampled gratings," *Journal of Quantum Electronics*, vol. 29, no. 6, 1993.

3 HOW TO ACHIEVE A SINGLE MODE LASER

High bandwidth optical links typically use wavelength division multiplexing (WDM), in which each wavelength of light acts as a separate data channel to produce high aggregate bandwidth links. Single wavelength lasers are needed to enable WDM. The hybrid architecture with III-V materials bonded to silicon demands an adaptation of the traditional structures employed to achieve single wavelength emission. In this chapter we describe the different approaches that can be used to realise single mode hybrid lasers, detailing the designs that we conceive, simulate and process. DBR, microring based, DFB and AWG laser solution are presented and analyzed. Theoretical model results for the evaluation of the performances of DFB exchange laser are proposed.

3.1 DBR laser

The Distributed Bragg Reflector laser (DBR) design has been proposed for the first time during the seventies, and it has been optimized later by different laboratories [1] [2]. A traditional DBR laser on III-V materials is composed of three sections, as illustrated in Figure 3.1. There are an active section, a phase section, and a Bragg section. The active section provides the optical gain, the DBR section provides the selective optical feedback and the phase section is used for fine tuning of the emitted wavelength. Wavelength tuning is achieved by modifying the refractive index of the Bragg and the phase section by carrier injection.

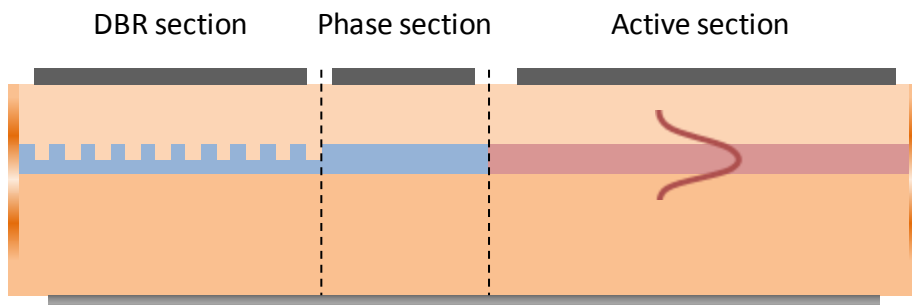


Figure 3.1: schematic view of a standard DBR laser structure

DBR hybrid lasers have already been proposed and fabricated as we have seen in chapter 1. All these solutions include a silicon passive part to realize the Bragg grating and the phase section, while the III-V part provides optical gain.

Because of the high index contrast between silica and silicon, it is not trivial to realize a narrow band DBR reflector on the SOI platform. In order to achieve desired narrow bandwidth, gratings with very shallow etching on the silicon waveguides (5 to 10 nm) are required. Moreover the etching depth should be precisely controlled to achieve reliable lasers performances. For those reasons the DBR geometry does not represent the better solution for single mode hybrid lasers.

3.1.1 Sampled Grating DBR

Sampled Grating DBR lasers are an interesting alternative to standard DBR grating [3]. Figure 3.2 schematically indicates the idea. A sampled grating is a conventional uniform grating with grating elements removed in a periodic fashion. This periodic modulation leads to periodic maxima in the reflection spectra. This behaviour can be used to obtain wide range tuning through the Vernier effect between two gratings on the cavity sides. As Figure 3.3 shows, the period of the two spectra is slightly mismatched, lasing will occur when a pair of maxima will be aligned. In standard III-V technology SG-DBR can achieve a tunability of 40 nm around 1.55 μm , while the standard tuning achievable for DBR laser is of 15 nm. The major drawback of the SG-DBR is the complex control for the different tuning sections and the large size; in fact the selective mirror length is of several hundred micrometers.

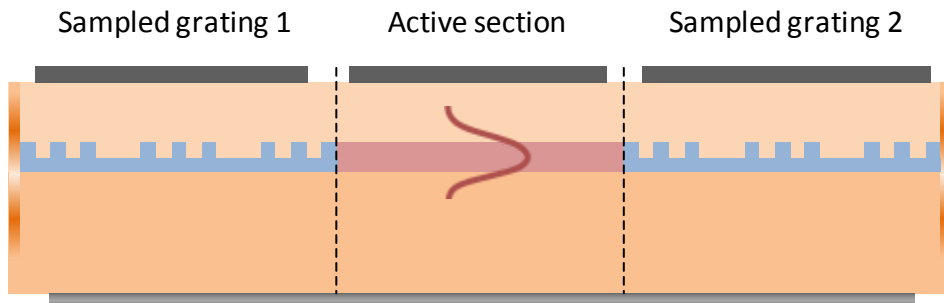


Figure 3.2: schematic view of a sample grating DBR laser

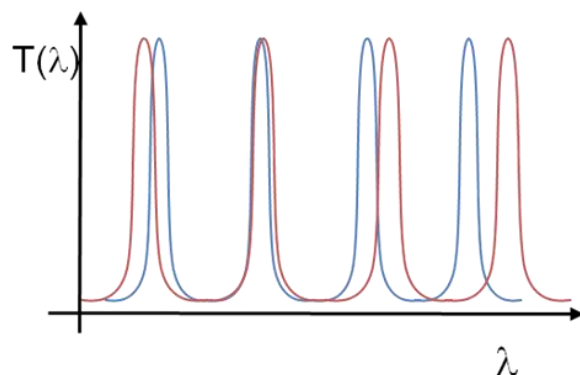


Figure 3.3: transmission spectrum of the sampled grating 1 and 2. With two comb like reflections a broad band tuneable laser can be realized using the Vernier effect

3.2 Rings resonator mirrors lasers

Ring resonators coupled lasers have been introduced by J. E. Bowers and al. in 2001 [4] [5] [6]. The structures presented offer several nice features such as narrow linewidth, large tuning range and large SMSR. The authors propose two laser configurations. The first one used a microring resonator based mirror to realize a single mode laser source. The device is divided into an active and a passive sections. The active section provides optical gain while the passive section, including a single microring resonator, filters the reflection spectra of a cleaved facet allowing single mode behavior. The second solution uses two ring resonators as mode selection filters to realize a tunable laser. The proposed structure is divided into three regions, one active and two passive regions. The active waveguide is on the center of the device and provide optical gain; on both sides a passive circuit provides a selective feedback exploiting a microring resonator and a cleaved waveguide. This structure behaves like the SG-DBR structure described by Figure 3.2, where the two sampled gratings are replaced by microring based reflectors. The two microring resonators have slightly different radii, generating indeed two combs with different free spectral range (FSR), as shown in Figure 3.3. The Vernier effect can be used to obtain wavelength tuning. We used both concepts to realize similar geometries for hybrid III-V on silicon lasers.

We design a single ring configuration that uses a microring and a large bandwidth DBR mirror. This structure allow a few nanometers wavelength tenability and single mode lasing. The second configuration uses a couple of microrings resonators. In this case we can tune the lasing wavelength through the Vernier effect by ring resonators heating. The tuning range in this case is of the order of 30 nm.

3.2.1 Microring resonator principle

Silicon microring resonators have been used for several applications due to their small size, high quality factor Q, transparency to off-resonance light, and no intrinsic reflection. Optical filters, electro-optical modulators, lasers and detectors exploiting this geometry have been fabricated so far.

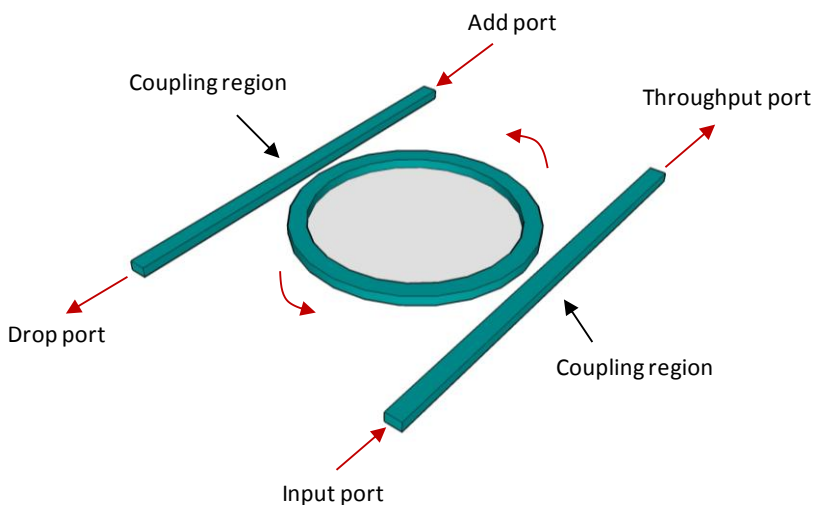


Figure 3.4: microring resonator filter configuration

The microring configuration used in our designs is schematically described in Figure 3.4. Two straight waveguides are optically coupled to a microring resonator. A fraction of the light injected in the input port, depending on the coupling efficiency of the coupling region, is injected into the microring. The injected wavelengths that fit the resonance condition of the ring are partially coupled to the second waveguide and pass through the drop port. The other wavelengths experience a destructive interference and are consequently filtered out.

The finesse of ring resonators can be set through the coupling efficiency of the coupling region. Racetrack resonators have been chosen because of the easier handling of the coupling coefficient between input or output waveguides and resonator itself. We choose 220 nm thick stripe waveguides, this geometry is commonly used in many passive silicon photonics devices and is fully compatible with silicon based modulators. A waveguide width of 450 nm has been chosen. We perform analytical simulations of the structure behaviour. Coupling simulation between the straight waveguide and the racetrack resonator have been performed as a function of the coupling region length using FIMMPROP, the separation distance between resonator and straight waveguide has been fixed at 350 nm, a value that is compatible with fabrication constraints. The simulation results are shown in Figure 3.5. Reflection coefficient (drop port on input port power ratio) for different T values (throughput port on input port power ratio) as a function of the injected wavelength as been simulated using an analytical model [7]. Simulation results are shown on Figure 3.6. The finesse and the maximum power reflectivity of the resonator have been simulated as well as a function of the T coefficient. As we can see in Figure 3.7 a high T value results in a sharp filter with high finesse but also low reflectivity. In our designs we use T values of 0.5, 0.8 and 0.9 as it will be detailed in the next sections.

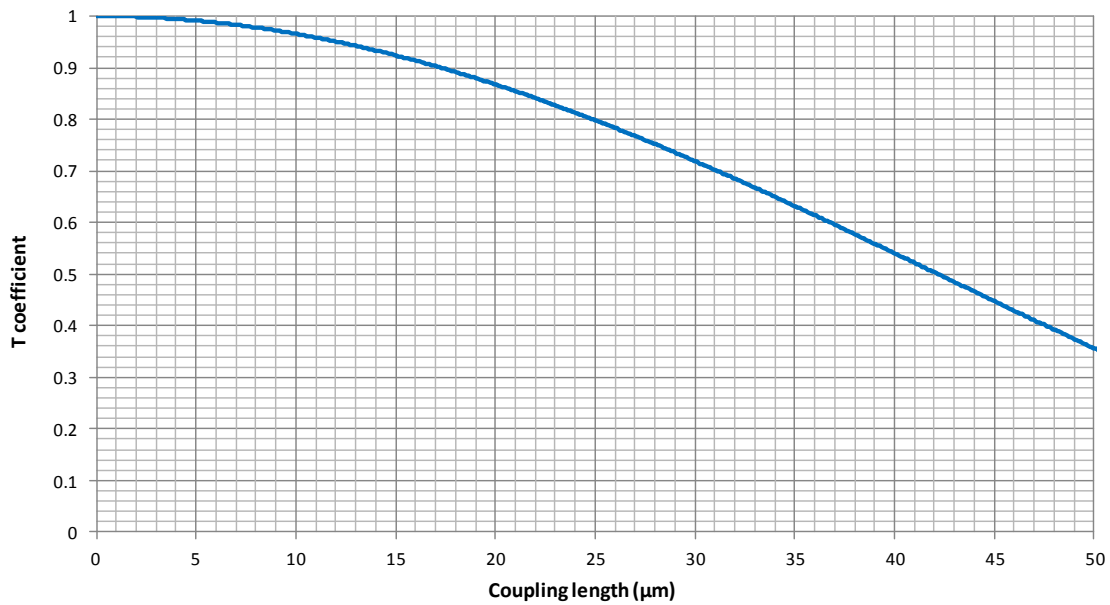


Figure 3.5: T coefficient (throughput port on input port power ratio) as a function of the coupling section length between resonator and straight waveguide, separation distance of 350 nm

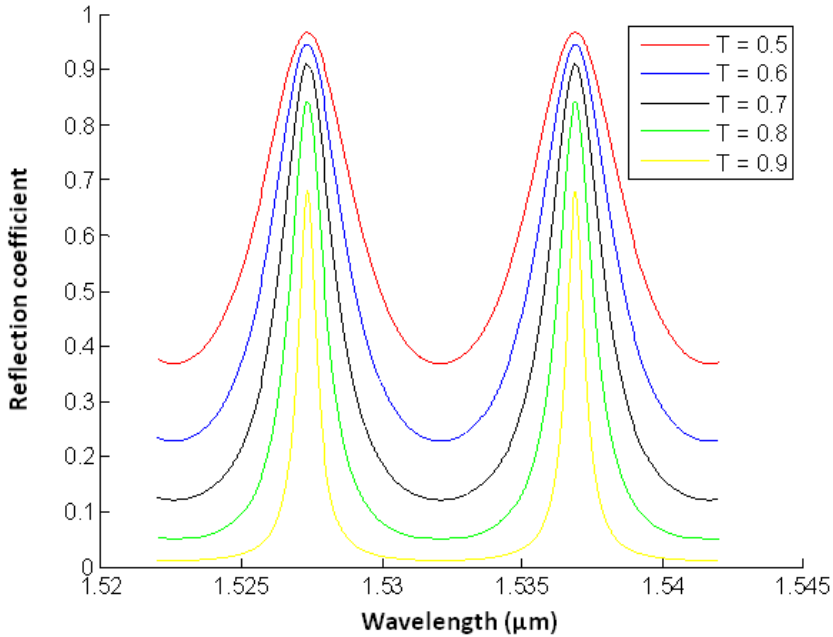


Figure 3.6: Reflection spectrum of a racetrack resonator, for various transmission coefficients, assuming 10% power losses per loop due to waveguide losses

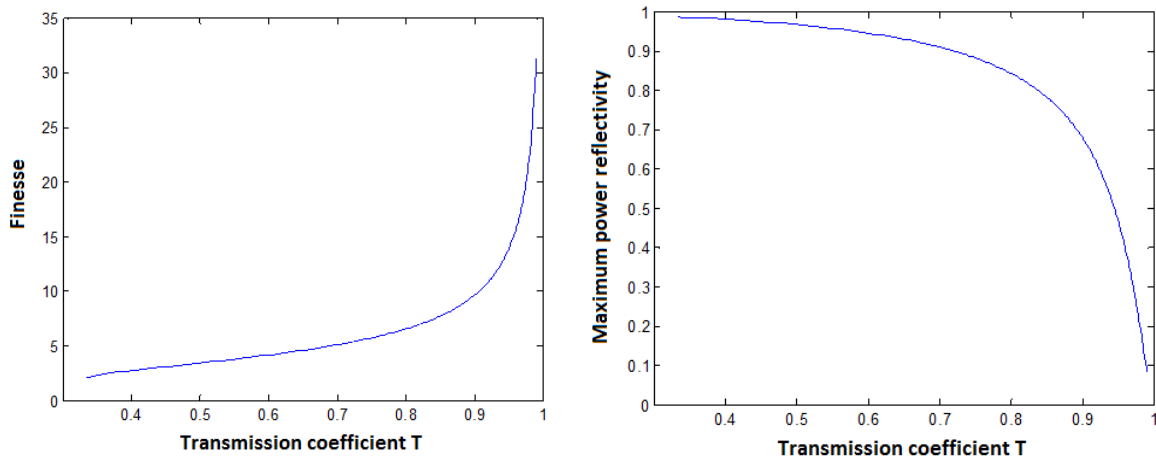


Figure 3.7: Finesse and maximum power reflectivity of a racetrack resonator for various transmission coefficients, assuming 10% power losses per loop due to waveguide losses

3.2.2 One ring resonator design

The laser cavity is built with two broad band Bragg gratings and a racetrack ring resonator for wavelength tuning and mode filtering. The wavelength selection can be achieved by thermal tuning of the racetrack ring resonator; a tunability of around 6 nm is theoretically achievable.

The proposed laser structure consists of a gain section in which light is mainly confined in the III-V waveguide with adiabatic tapers on both sides for coupling light to the silicon waveguide. Once in the silicon part, at one side the light meets a large bandwidth, high reflectivity Bragg reflector, on the other side it circulates through a racetrack ring resonator with a radius of about 3um and a free

spectral range of 25 nm, then it meets a large bandwidth Bragg reflector. The light that is not reflected passes through the grating and escapes from the output facet. The output facet needs to be treated to eliminate reflections. This structure is shown in Figure 3.8. The 25 nm FSR permits to select a single wavelength as we have an optical gain bandwidth of around 40 nm. We used a T coefficient

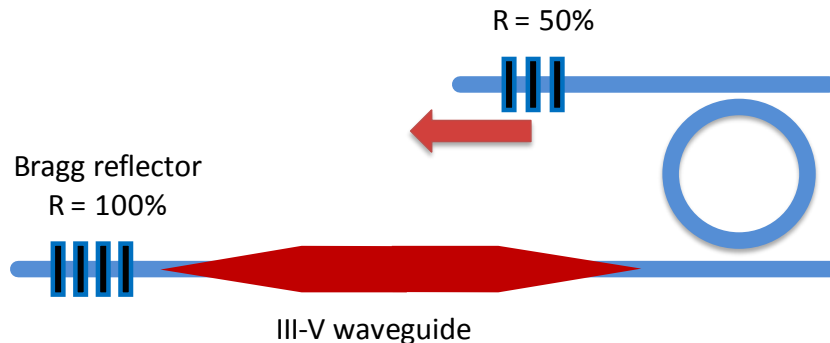


Figure 3.8: single wavelength microring based laser structure

3.2.3 Double ring based tunable laser designs

Two designs are possible, we call this two designs transmission type (Figure 3.9) and reflection type (Figure 3.11). These designs allow at the same time step by step wavelength tuning and very narrow linewidth.

In the transmission type design the laser cavity is built with a double racetrack ring resonator for wavelength tuning and mode filtering, and a broad band Bragg mirror (Figure 3.9).

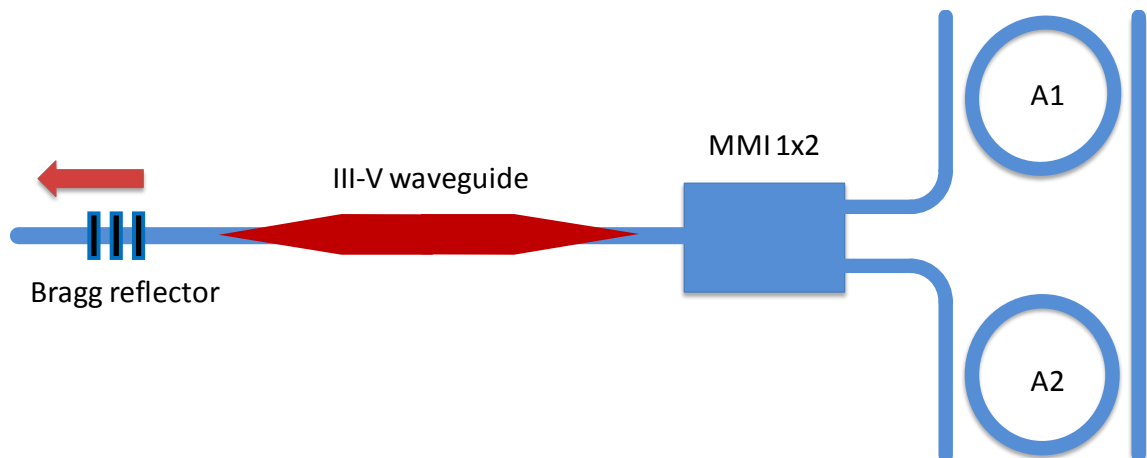


Figure 3.9: schematic view of the double ring based tunable laser structure, transmission type

In Figure 3.10 we show the optical path of the lasing wavelength from MMI output 2 to the output 1. As the MMI divides the optical power symmetrically on the two outputs we have an identical path in the opposite direction from the output 1 to the output 2. Only wavelengths that can resonate at the same time in both rings are able to complete these two paths. If the two rings are correctly designed with different radii, only one wavelength will be able to lase. We call this design “transmission type”, as the light pass only one time on both rings during a road trip inside the cavity.

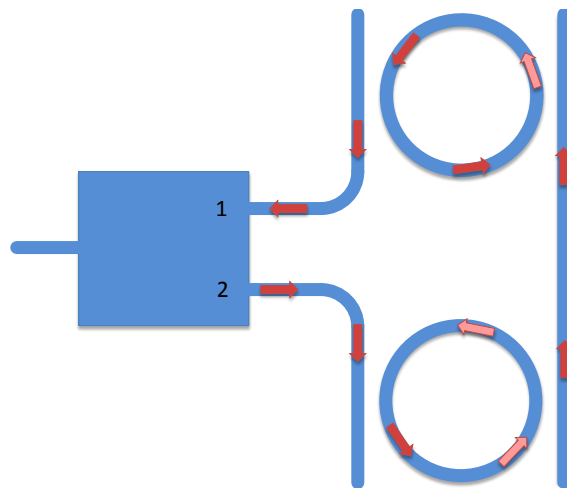


Figure 3.10: schematic representation of the lasing wavelength path from the MMI output 2 to the output 1

In the reflection type design the laser cavity is built with two racetrack ring resonators for wavelength tuning and mode filtering, and two broad band Bragg mirrors (Figure 3.11). We call this design “reflection type” as the light passes two times inside each ring during a road trip.

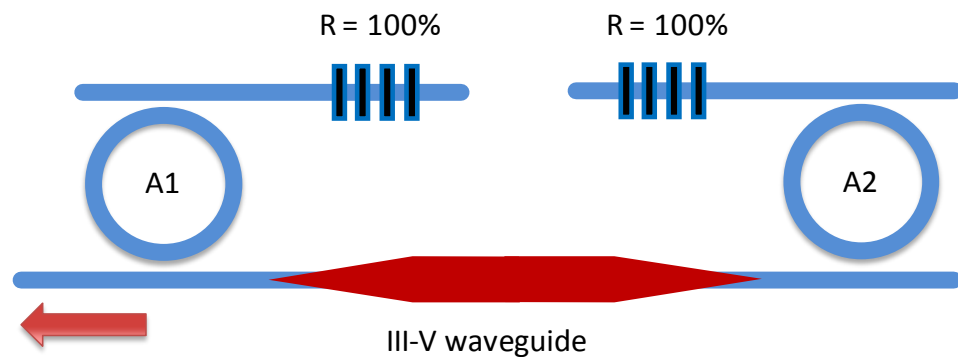


Figure 3.11: schematic view of the double ring based tunable laser structure, reflection type

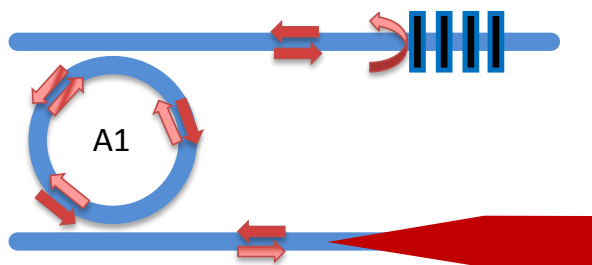


Figure 3.12: schematic representation of the lasing wavelength path in the reflection type design

3.2.3.1 Wavelength tuning

The purpose of the resonators is to provide a tunable narrow filtering function. The wavelength selection is achieved by thermal tuning of the racetrack ring resonators. To obtain Vernier effect, the FSR must be different for the two resonators: a 10% shift was chosen here. Two configurations have been employed:

A1: 610 Ghz / 4.89 nm, A2: 680 GHz / 5.45 nm

A1: 440 GHz / 3.52 nm, A2: 400 GHz / 3.2 nm

These FSRs were chosen because they roughly correspond to the thermal tunability range. The finesse of ring resonators can be set through the coupling coefficient between the input and output waveguides and the resonator itself. As shown on Figure 3.7, a high T coefficient gives a sharp filter with high finesse but also a lower reflection coefficient. Taking into account the tradeoff between the resonator finesse and the losses, T coefficients of 0.9 and 0.8 were chosen for the transmission type design, while T coefficient of 0.5 and 0.8 were chosen for the reflection type design. In the latter, the double filtering by each resonator is expected to compensate for the relative broadband filtering and benefit from fewer losses.

The couplers were designed with Fimmwave with $0.45 \mu\text{m}$ strip waveguides spaced by $0.35 \mu\text{m}$, and the length were calculated to be respectively $42.2 \mu\text{m}$, $24.8 \mu\text{m}$ and $17.2 \mu\text{m}$ to achieve transmission coefficient of $T=0.5$, $T=0.8$, $T=0.9$, respectively.

The wavelength tuning is achieved by thermal control of the rings. Refractive index change in the silicon induced by heating the ring makes the transmission peaks move. (Effective index change was calculated to be $-1.96 \times 10^{-4} / \text{K}$ giving a peak wavelength shift of $7.5 \times 10^{-5} \mu\text{m/K}$). When the spectrum on one of the two ring moves, according to Vernier design, the peaks corresponding to the next order then match (Figure 3.13). The maximum of the equivalent transmission jumps to another wavelength. For more accurate wavelength selection, the two rings can be tuned with temperature, allowing a step by step wavelength selection (Figure 3.14). By tuning both rings, as the tunability of one ring is of the order of one FSR, the laser is expected to cover the 40 nm range.

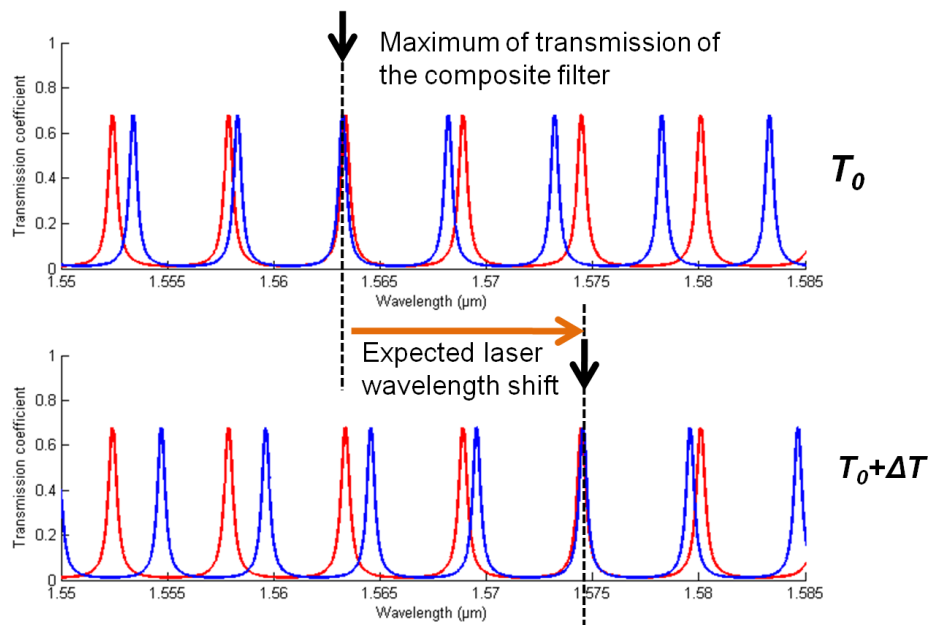


Figure 3.13: Transmission coefficient of the two 610 GHz (red) and 680GHz (blue) rings. Bottom graph is the transmission when the blue ring resonator is heated by 18° . The laser wavelength is shifted from $1.563 \mu\text{m}$ to $1.574 \mu\text{m}$

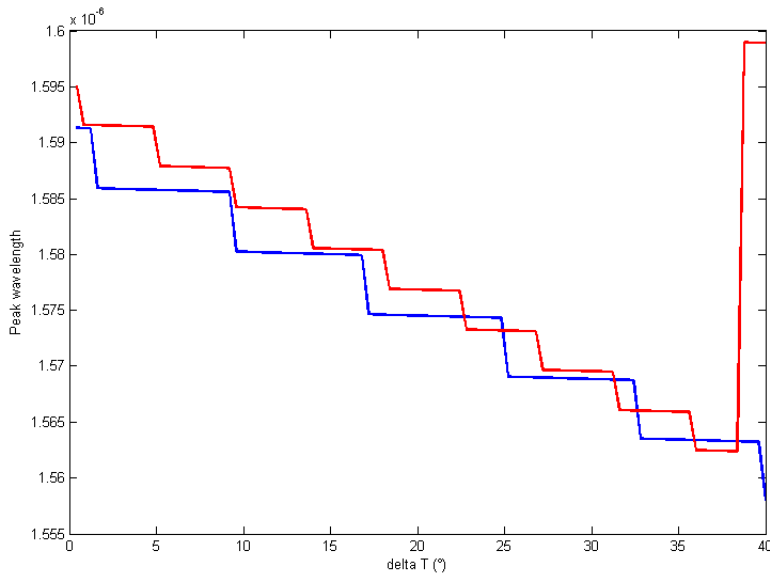


Figure 3.14: Expected laser wavelength with temperature variation on one ring for the two types of rings : 610/680 GHz (blue) and 440/400GHz (red). A jump in the laser wavelength occurs when the refractive index change make different ring resonator order match

3.2.3.2 Bragg grating design

Bragg reflectors are designed on wide ($2\mu\text{m}$) stripe waveguides to decrease effective index difference and thus provide a better control on the reflective coefficient. The grating has a period of 280 nm and a duty cycle of 0.5; it is realized through the periodic etching of 70 nm deep stripes on top of the waveguide, Figure 3.15. In Figure 3.16 we present an analytical simulation of the Bragg power reflectivity as a function of the grating length. The reflection bandwidth is close to 40 nm.

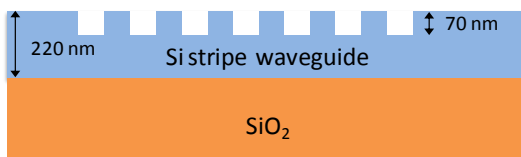


Figure 3.15: schematic view of the Bragg grating

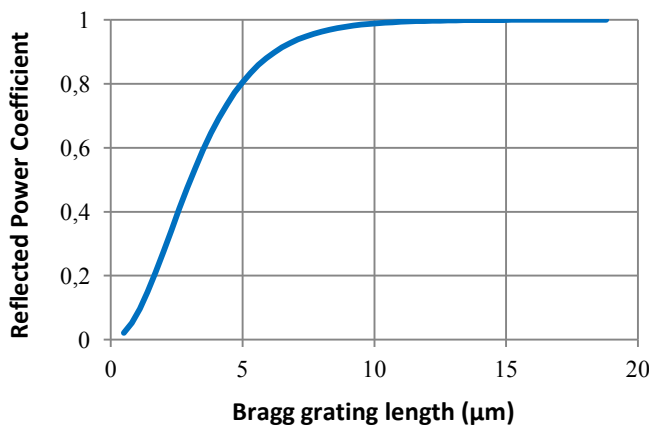


Figure 3.16: analytical simulation of Bragg reflectivity against length, period 280 nm, duty cycle 0.5

3.2.4 Spectral linewidth analysis

The linewidth is an important concern for many applications. In this section we detail our linewidth simulation results for ring resonator mirrors lasers. We used an analytical mode that is detailed in [8]. This model is well adapted for structure in which the active region is loaded by a separate passive region with a higher Q. In this case we can describe the cavity as a Fabry-Pérot cavity in which we consider the external resonator with a complex effective reflectivity: $r_{\text{eff}}(\omega) = r(\omega) \exp(j\phi\omega)$

We take as a reference the Fabry-Perot laser with two Bragg gratings. The linewidth – power product of the reference laser is in the range 20 – 100 MHz mW. Then we calculate the linewidth reduction due to the presence of the ring resonators through the use of an effective reflectivity. According to [8] the linewidth can be calculated as:

$$\Delta\nu = \frac{v_g^2 \hbar \omega_0 \alpha_m g n_{\text{sp}} K_0}{4\pi P_1} \frac{(1 + \alpha_H^2)}{[1 + A + \alpha_H(B + G_\omega/2)]^2} \frac{r(\omega_0)(1 - r_1^2)}{[r_1 + r(\omega_0)][1 - r_1 r(\omega_0)]} \quad (3.1)$$

Where α_H is the phase-amplitude coupling factor in the active region, and A and B are defined as:

$$A = \frac{1}{\tau} \frac{d\phi(\omega)}{d\omega} \Big|_{\omega_0} \quad B = \frac{1}{\tau} \frac{d \ln r(\omega)}{d\omega} \Big|_{\omega_0}$$

Figure 3.17 plots the linewidth reduction ratio as a function of the external cavity length for both reflection and transmission type ring resonators for a T value of 0.9. This value of T corresponds to a resonator finesse of 13 (Figure 3.7). The external cavity length means the distance between the Bragg grating and the ring resonators. We can see that the reflection type ring resonator structure results in a much larger reduction factor. This is due to the fact that the light propagates two times through each ring resonator for reflection type structures, while light travels only one time in the transmission type structures. Each time the light travels through a ring resonator, there is a filtering of the spontaneous emission and a reduction of the spectral linewidth. The linewidth reduction factor can be as large as 50 for an external cavity length of 1700 μm.

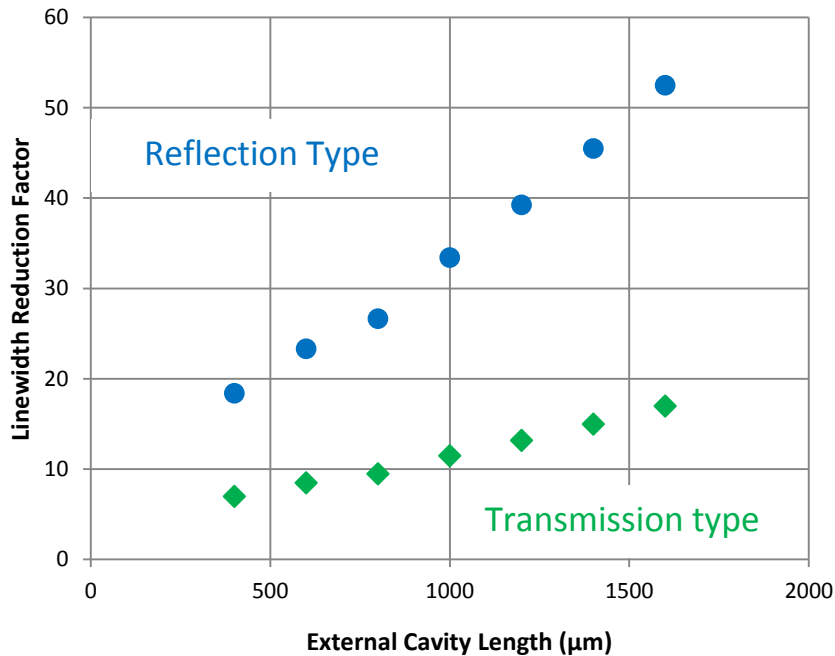


Figure 3.17: linewidth reduction ratio as a function of the external cavity length for both reflection and transmission type ring resonators for a resonator finesse of 13

Figure 3.18 plots the linewidth reduction ratio as a function of the finesse of the ring resonators for an external cavity length of 1000 μm . We can see again that the reflection type ring resonator structure results in a much larger reduction factor. We see also that the linewidth reduction ratio increases with the increase of the resonator finesse, due to the stronger filtering of the spontaneous emission. However, a very large finesse is not a good solution, as it would result in a low value of the effective reflectivity, leading to high threshold and thus large linewidth for the reference laser itself.

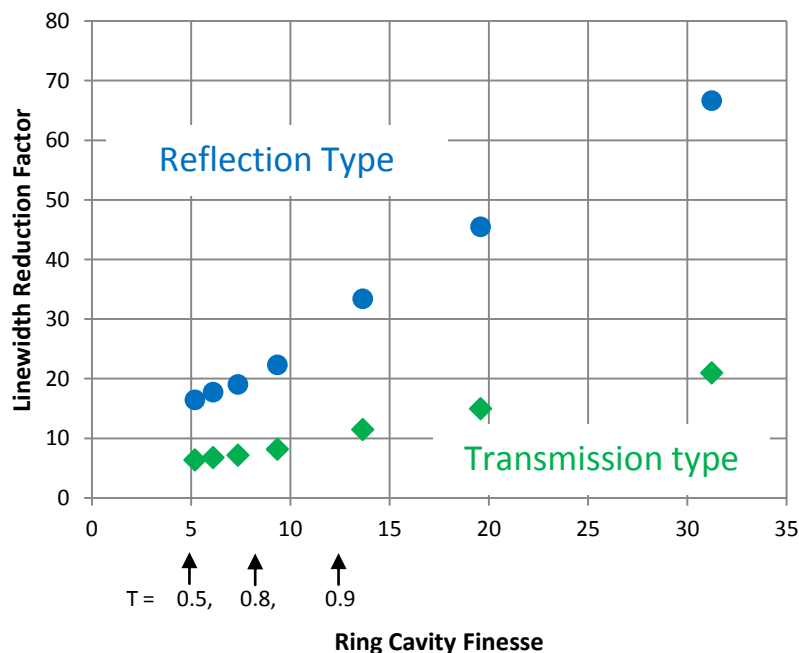


Figure 3.18: linewidth reduction ratio as a function of the finesse of the ring resonators for an external cavity length of 1000 μm

From Figure 3.17 and Figure 3.18, we can see that the linewidth reduction factor compared to a Fabry-Perot can reach 50. Thus the final linewidth would be in the range 400 kHz – 2 MHz mW.

It has to be noticed that these values are related to the filtering of the spontaneous emission. These devices like every tunable device, suffer also from fluctuations in the emitted wavelength due to tunable mechanism. In this case, micro fluctuations of the ring temperature can induce a wavelength broadening.

3.3 DFB laser

Distributed feedback (DFB) laser structure has been proposed for the first time in 1971 at Bell laboratories [9]. In DFB lasers a periodic structure is embedded inside the active waveguide and acts as a distributed reflector. In a hybrid III-V on silicon configuration DFB lasers can be realized following different schemes compared to standard III-V technology. The heterogeneous nature of the device opens more space for new concepts and designs. The distributed reflector can be realized in several ways. We can etch a Bragg grating through the silicon before bonding, or in the III-V before bonding, or finally in the III-V waveguides after bonding.

As we have seen in chapter 2, the main problem in hybrid lasers is the optical coupling between III-V waveguide and silicon waveguide. DFB structures offer an important advantage from this point of view. As the cavity is entirely defined by the active section, the coupler parts will be located outside the laser cavity. That means that the losses introduced by the couplers will impact in a much lighter way on laser performances.

To define a DFB laser design we mainly need three parameters: the coupling coefficient k , the laser length L , and the grating period Λ . The grating period is connected to the emission wavelength by the following equation (figure 3.19):

$$\lambda = 2 n \Lambda$$

To effectively achieve a single mode emission particular AR/HR coatings are needed and/or the inception of a $\lambda/4$ phase shift in the grating.

The coupling coefficient k between optical mode and Bragg grating, and the length L of the device have a strong impact on laser performances. A high value of the product kL will result in a higher confinement of the light inside the cavity, we will achieve a low threshold but also a lower external efficiency. An opposite effect will be achieved for a low kL value. In standard III-V technology DFB lasers kL varies between 1 and 3, these values permit to achieve the better compromises between laser threshold and slope efficiency [10].

The coupling coefficient can be estimated with a first order approximation as:

$$k = \frac{\pi(n_2 - n_1)}{2 \lambda} \tag{3.2}$$

In the following section we analyse the advantages and drawbacks of the different DFB solutions that we have studied and simulated.

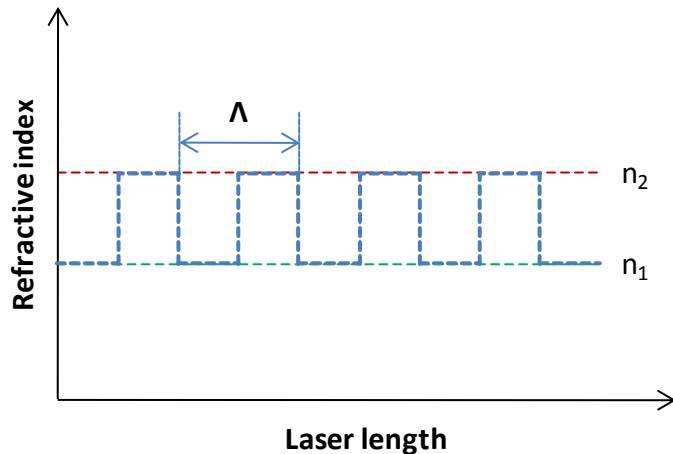


Figure 3.19: qualitative graphic of effective refractive index inside a DFB laser

3.3.1 Grating on the III-V

The Bragg grating can be realized on the III-V part of the device. In a standard III-V technology a Bragg grating is generally etched through a dedicated high index layer that is subsequently covered by epitaxial regrowth with a lower index material. Other designs have been investigated to simplify the technological process. Gratings have been etched through the entire ridge structure or through a dedicated layer during the ridge etching process without regrowth step [11]. All those approach can be used as well in hybrid devices. The optical mode needs to be confined in the III-V waveguide to experience the effect of the grating.

3.3.1.1 Full etched grating

This is definitely the simpler way to realize a DFB hybrid laser with grating inside III-V dies. The same epitaxy presented in Table 2.1 can be used. The III-V corrugated waveguide is defined after bonding by e-beam lithography; the InGaAs and the InP-p layer are subsequently etched like in Figure 3.20. The fabrication of this kind of waveguide presents a main technological challenge, the etching of a corrugated waveguide with a pitch of around 250 nm and an etching depth of 1.8 μm is far from being trivial.

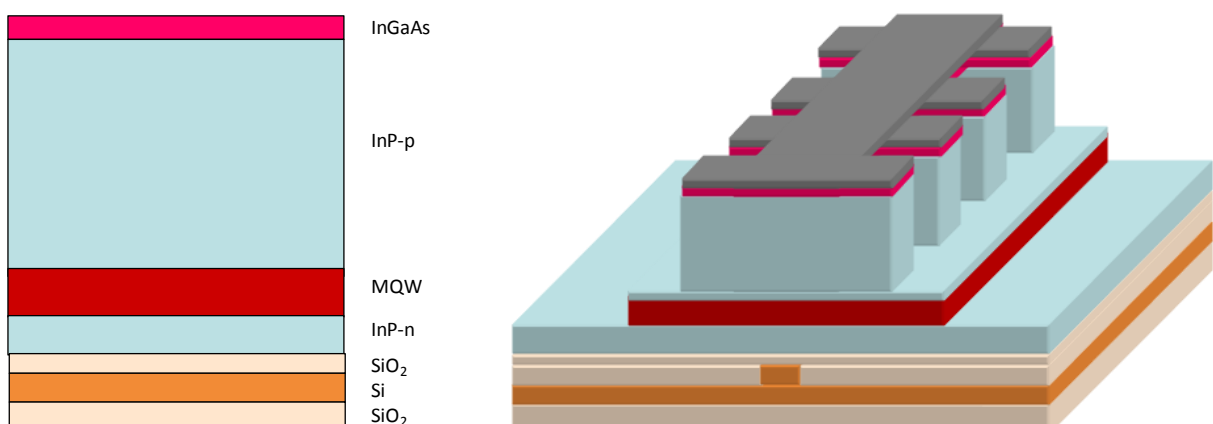


Figure 3.20: schematic view of a DFB full etched grating

3.3.1.1.1 Simulations

Mode profile simulations have been performed to evaluate the mode refractive index. Once the two refractive indices are known, we deduce the coupling coefficient k according to (3.2). In Figure 3.21 we present the 2D mode profile in the two different sections of one period of the corrugated waveguide. Figure 3.22 shows the coupling coefficient value for different width of the corrugated waveguide. We fix the minimal waveguide width to $1.4 \mu\text{m}$ and we evaluate k as a function of the maximum waveguide width named x . The coefficient increases with x as the mode effective index between both section increases.

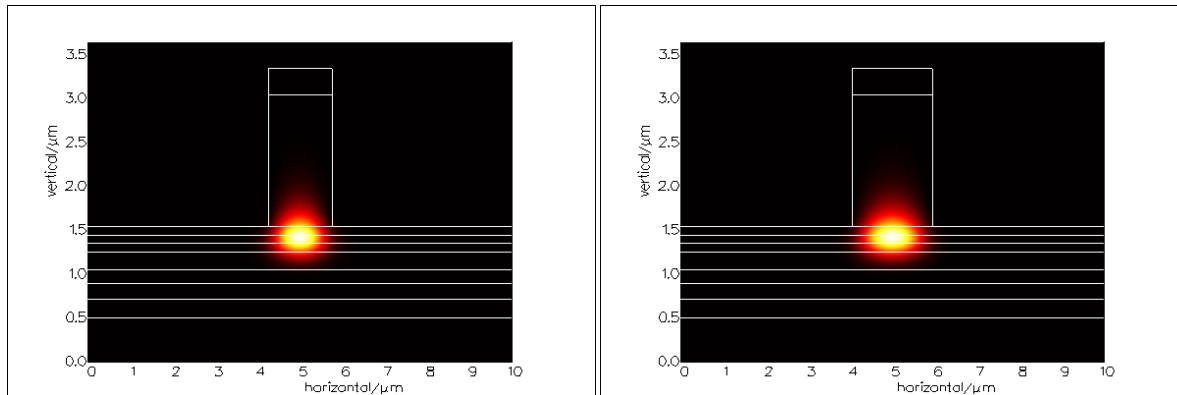


Figure 3.21: 2D mode profile simulation for a III-V shallow ridge waveguide width of 1.5 and $1.9 \mu\text{m}$

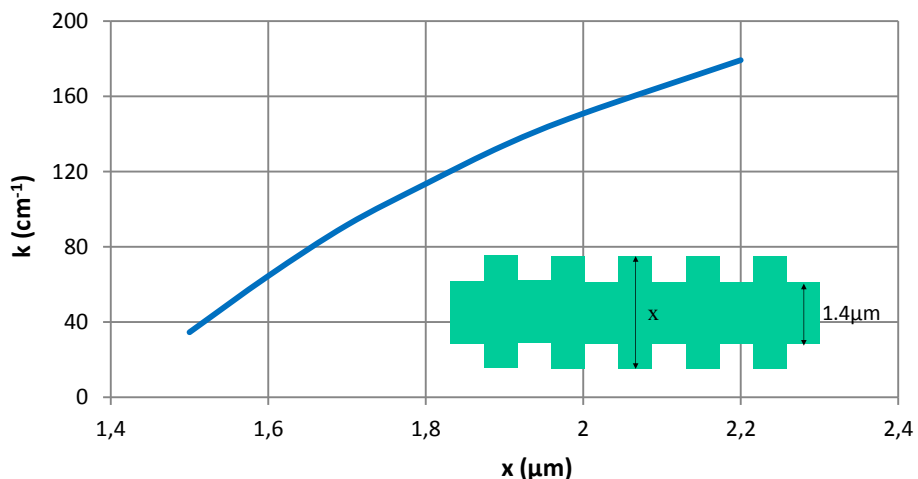


Figure 3.22: coupling coefficient evolution as a function of the x section width

3.3.1.1.2 Design

As we see in Figure 3.22 the coupling coefficient is strongly dependent on the corrugation of the waveguide. That means that a slight difference introduced by the fabrication in the geometry will have a strong impact on laser performances. The chosen design is based on a $1.4 \mu\text{m}$ waveguide with a 200 nm corrugation depth on both sides. This insures a coupling coefficient of around 100 cm^{-1} . To achieve laser action at $1.55 \mu\text{m}$ the pitch is set to 249 nm . A $\lambda/4$ phase shift located at the center of the waveguide has been used to allow a true single-mode operation.

This solution presents a main fabrication drawback. The grating needs to be etched through the entire InP-p layer, a layer that is often quite thick, around $1.5\text{ }\mu\text{m}$. As the pitch of the grating is around 250 nm it is difficult to etch a grating with such a high aspect ratio. If the grating is not correctly open, especially on the bottom, the coupling coefficient will become lower compared to the designed one and laser performances will be affected. In order to prevent this effect we use longer laser lengths such that the calculated values of kL are in the range between 2 and 4.

3.3.1.2 Dedicated grating layer

This structure, schematically presented in Figure 3.23, represents a valid alternative to the previous one. We add to the III-V stack a thin “grating” layer with InGaAsP ($\lambda g = 1.17\text{ }\mu\text{m}$ and $n=3.327$) and a “spacer” layer on InP. Compared to the previous structure the fabrication process needs one more step. A first etching defines the waveguide through the InGaAs and the InP p-layer. A second etching, with a mask defined by e-beam lithography, patterns the grating layer on the ridge borders. The etching step is simpler in this case as the grating etching depth is greatly reduced (between 30 and 100 nm).

The grating layer needs to be close to the quantum wells and to have a sufficient thickness to produce a relevant effective index difference. By using equation (3.2) we can calculate that a refractive index difference of the order of 8×10^{-3} is needed to achieve a coupling coefficient value of around 80 cm^{-1} . The introduction of the high index grating layer also modifies the optical confinement in MQW and p doped InP layers. The grating layer thickness has to be carefully chosen to allow high optical confinement on the quantum well and low confinement on the InP-p layer.

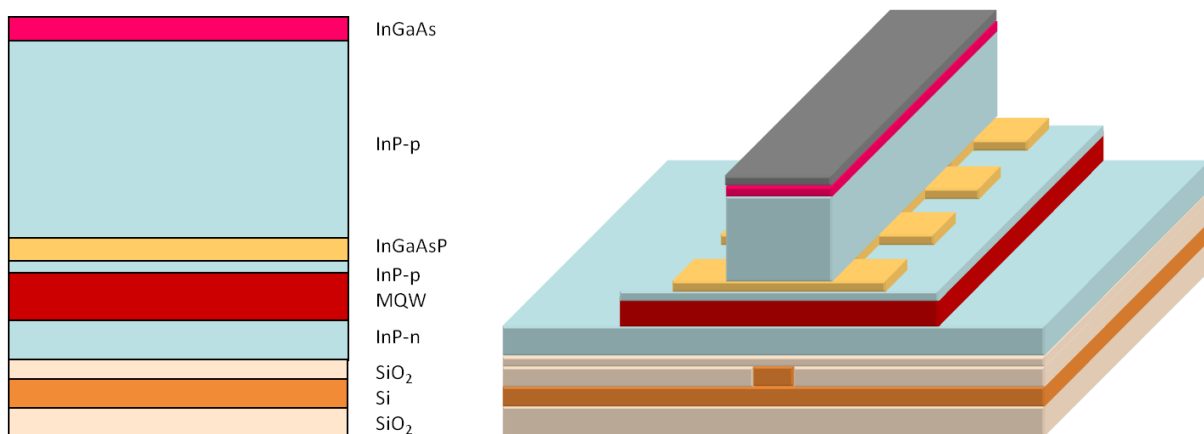


Figure 3.23: schematic view of a DFB with a laterally dedicated layer grating

3.3.1.2.1 Simulations

Mode profile simulations have been performed to evaluate the mode refractive index for different thickness and positions of the quaternary layer. The epitaxy that has been chosen is illustrated in Table 3.1. The spacer layer has been fixed to 30 nm to maximize the overlap between the grating and the optical mode, leaving at the same time a comfortable thickness to precisely stop the etching during the fabrication process. The waveguide width has been fixed to $1.5\text{ }\mu\text{m}$ to achieve a single mode structure. In Figure 3.24 we present the 2D mode profile in both sections for one pitch of the DFB waveguide.

How to achieve a single mode laser

Figure 3.25 shows the coupling coefficient and the InP-p layer confinement factor value for different quaternary grating layer thickness. MQW optical confinement is almost constant for all the plotted values (between 11% and 12%). To further reduce the InP-p confinement factor, thicker SCHs layer could be used.

layer nb	layer type	nb of periods	material	PL wavelength	thickness	carrier conc.	type
10	cladding n		InP		200	1,0E+18	n
9	SCH		InGaAsP	1,17	100		nid
8	MQW_w	6	InGaAsP	1,55	8		nid
7	MQW_b	5	InGaAsP	1,17	10		nid
6	SCH		InGaAsP	1,17	50		nid
5	spacer		InP		30		nid
4	grating layer		InGaAsP	1,17	x		nid
3	cladding p		InP		1500	1E18->5E18	p
2	transition		InGaAsP	1,17	20	1,0E+19	p
1	contact p		InGaAs		300	3,0E+19	p
substrate			InP				N

Table 3.1: III-V detailed epitaxial structure

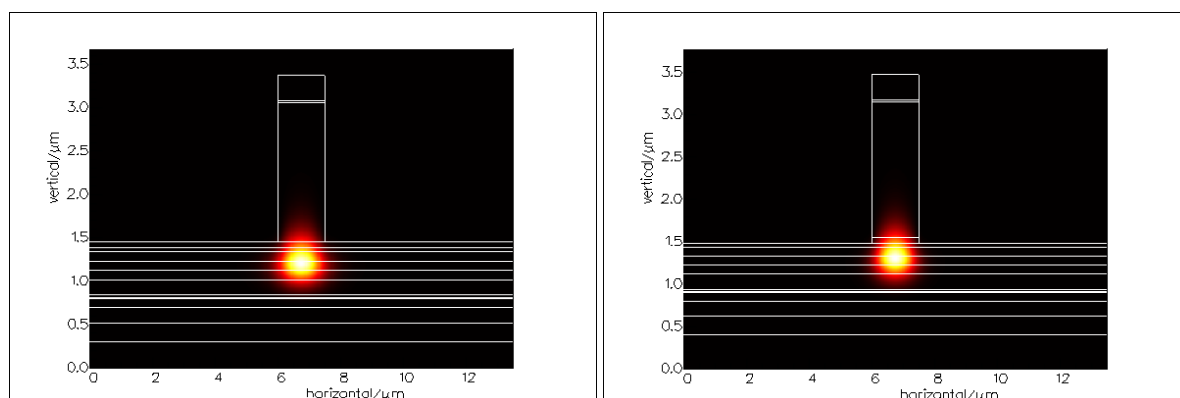


Figure 3.24: 2D mode profile simulation for a shallow ridge waveguide with a Bragg quaternary layer of 70nm and a InP spacer of 50nm, unetched on the left, etched on the right

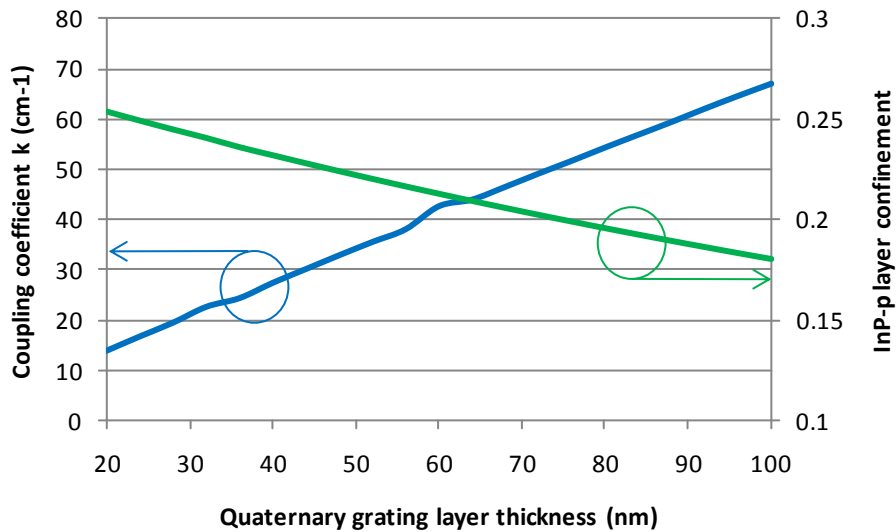


Figure 3.25: coupling coefficient value for different quaternary grating layer thickness

3.3.1.2.2 Design

From the performed simulation we know that a thicker grating layer allows higher coupling coefficient and lower InP p-doped layer confinement. Indeed we choose a thickness of 80 nm for our design, which insures a coupling coefficient of 55 cm^{-1} and InP-p confinement of less than 20%. The design that we have chosen is based on a $1.5 \mu\text{m}$ waveguide with spacer of 30 nm. The grating pitch is of 242 nm to achieve laser action around $1.55 \mu\text{m}$. A $\lambda/4$ phase shift located at the center of the waveguide has been used to obtain single wavelength operation. Different laser lengths have been designed to test several values of kL between 1 and 3.

3.3.2 Grating on silicon

The distributed feedback can be achieved with a grating etched in the silicon part of the device. We focused our attention on two solutions. The first one is based on the complete transfer of the optical mode from the III-V to the silicon waveguide that has already been described in this work. We pattern a grating in the silicon waveguide underlying the III-V straight active section, if the grating has a sufficient overlap with the optical mode guided by the III-V waveguide, DFB laser action can be achieved. In the next section we detail the characteristics of this structure and we propose a specific design.

A second solution using grating on underlying silicon waveguide has been recently proposed [12]. It is based on a contra-directional coupling between the III-V and the silicon waveguide eigenmodes. In this case no coupler is needed, the III-V and the silicon waveguide are superimposed, on the silicon waveguide we have a grating that allows at the same time a continuous power exchange between the waveguides and a wavelength selection. In section 3.3.2.2 we propose an analytical model to evaluate the performances of this kind of DFB laser in terms of modal gain, and threshold.



Figure 3.26: schematic top and side views of a DFB hybrid laser with silicon grating

3.3.2.1 Classical DFB configuration with a grating on silicon

The laser configuration is similar to the one described for a Fabry-Pérot laser. We have a straight III-V shallow ridge section in the center with two adiabatic couplers that transfer the optical power to the silicon on both sides. In this case, under the III-V straight waveguide we realize a silicon grating (Figure 3.26). The optical mode guided by the III-V waveguide will have an evanescent coupling with the silicon grating. If the overlap is strong enough to produce a sufficient effective index variation we will be able to achieve a DFB lasing.

There are two main issues to solve using the classical DFB configuration with silicon grating. First, the high refractive index contrast between silicon and silica can produce very high values of coupling coefficient k , which leads to a poor slope efficiency. To reduce this effect we need to reduce the overlap between the optical mode and the grating. Second, once we have defined the bonding layer thickness that insures the right k value, we need to reduce the impact of bonding thickness variation on laser performances. The thickness of the bonding layer is critical for the device as it has a direct effect on the coupling coefficient k of the laser. Modifying the bonding layer thickness we change the overlap between the optical mode and the grating, changing the laser characteristics in term of threshold and slope efficiency.

3.3.2.1.1 Simulations

Mode profile simulations have been performed to evaluate the mode refractive index for several thicknesses and shapes of the grating. We used a 400 nm RIB silicon waveguides with an etch depth of 180 nm. The III-V epitaxy is identical to the one described in Table 2.1. In Figure 3.27 we present the 2D active waveguide mode profile for the etched and the unetched part of the grating pitch. We decide to fix the III-V waveguide width to 3 μm , the silicon waveguide width to 1 μm and to further optimize the design by varying the bonding layer thickness.

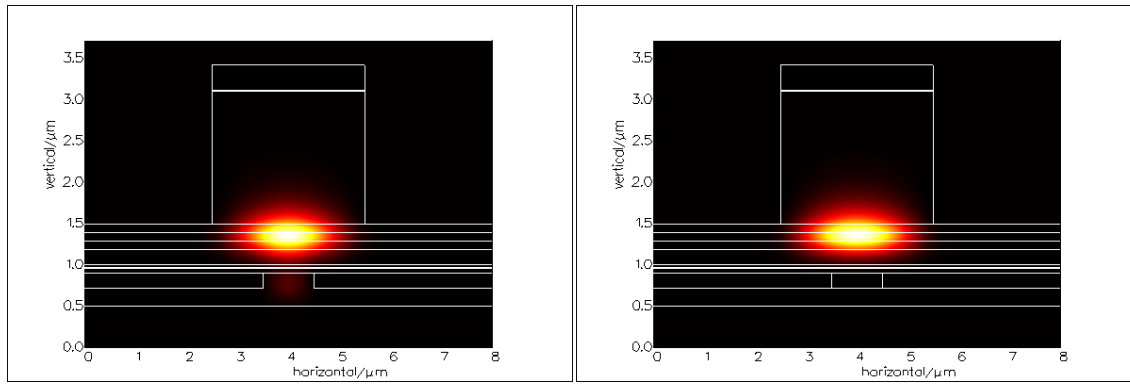


Figure 3.27: 2D mode profile simulation for DFB laser with Bragg grating on silicon on the full (left) and on the empty (right) part of the grating pitch

We simulate the effect of the bonding layer thickness variation on the DFB characteristics. The results are illustrated in Figure 3.28. We observe that the bonding layer thickness have a strong impact on laser performances. If we consider a 60 nm bonding layer thickness as the optimum value and a fabrication tolerance of ± 10 nm, we can estimate a 0.72 nm incertitude over the emitted wavelength, while the coupling coefficient can vary between 70 and 45 cm^{-1} . We do not perform specific calculations, but from literature results [10] we can evaluate a threshold current and a slope efficiency variation that can reach respectively 50% and 25%, depending on the laser length and internal losses.

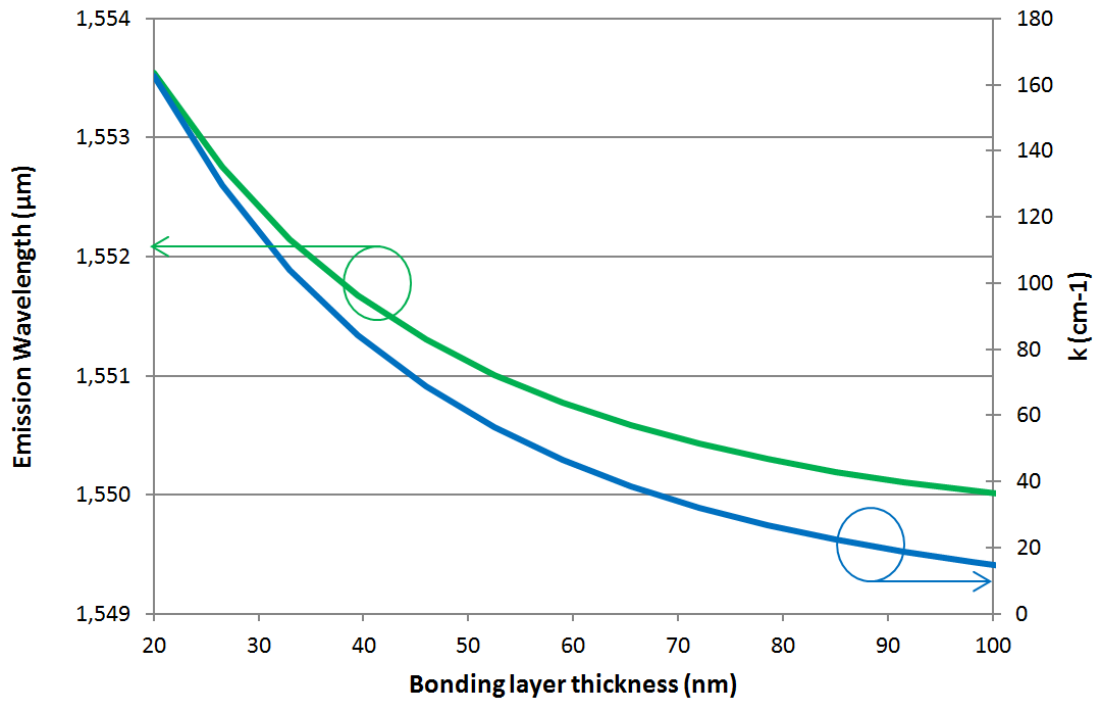


Figure 3.28: Simulated emission wavelength and coupling coefficient for a DFB laser with grating on silicon

3.3.2.1.2 Design

The design that we have chosen is based on a Bragg grating defined on a $1 \mu\text{m}$ wide, 400 nm thick silicon RIB waveguide with a shallow etch of 180 nm . The pitch is of 242 nm in order to have laser

emission around $1.55 \mu\text{m}$. A $\lambda/4$ phase shift located at the center of the grating has been used to achieve single mode lasing. Over the grating, a $3 \mu\text{m}$ wide III-V shallow ridge waveguide has been used, on both sides of the III-V waveguide an adiabatic taper insure the loss-less coupling of the light between both waveguides. The bonding layer thickness is chosen to be 60 nm . We calculate a coupling coefficient of 45 cm^{-1} for this structure. Different laser lengths have been designed to have several values of kL product. These devices are actually under fabrication.

3.3.2.2 Exchange DFB configuration with a grating on silicon

A novel type of DFB laser has been recently proposed by T. Dupont *et al.* [12]. The idea is to take advantage of contra-directional coupling between the III-V and the SOI eigenmodes (so called exchange Bragg coupling). This particular type of coupling enables distributed feedback as well as an equal share of the field between the III-V and SOI waveguides. Such a design is compatible with a bonding layer thickness as high as 200 nm , therefore relaxing the constraints toward the integration technology.

Exchange DFB uses a new concept by exploring the coupling between the III-V and the SOI modes created by the etched grating. However, to my best knowledge, no theoretical analysis has been performed so far on this kind of DFB lasers. The purpose of this section is to investigate quantitatively such a DFB laser using a coupled mode model. In particular, output emission spectrum and the slope efficiency are calculated from the model for both uniform and phase-shifted DFB lasers.

3.3.2.2.1 Model to analyse the exchange DFB lasers

Figure 3.29 shows the structure of an exchange DFB laser as proposed in [12]. It consists of a SOI waveguide partly etched. The silicon waveguide thickness is set to 260 nm and the grating depth to 40 nm . Above the silicon waveguide, there is a III-V waveguide obtained through wafer bonding between the SOI wafer and the III-V wafer. All other dimensional parameters of the hybrid laser can be found in [12], except that the grating period is now set such that the lasing wavelength is 1550 nm .

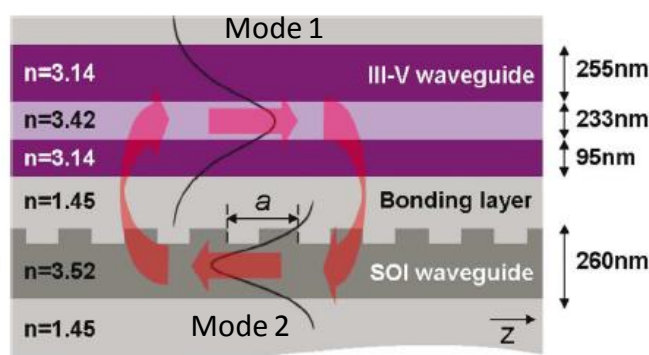


Figure 3.29: the structure of the exchange DFB laser

The Bragg grating creates a coupling between the forward mode (mode 1) propagating mainly in the III-V waveguide and the backward one (mode 2) that is mainly confined in the SOI waveguide. Coupled-mode theory was developed in 1970 to take into account the coupling between two counter-propagating modes with exactly the same transverse profile [13]. We adapt the coupled

mode theory developed for the classical DFB lasers to the exchange type DFB lasers by considering the coupling between those two counter-propagating modes with different transverse profiles. Those two modes experience different gain, losses and modal refractive index.

The values of main parameters used in our calculations are shown in the Table 3.2 below:

	Symbols	Values	Unit
Pitch of the grating	Λ	253.5	nm
Coupling coefficient	K		cm^{-1}
Length of the laser	L	400	μm
Losses for mode 1	α_{int1}	10	cm^{-1}
Gain for mode 2	g_2	0	
Losses for mode 2	α_{int2}	5	cm^{-1}
Effective index of mode 1	n_{eff1}	3.1648	
Effective index of mode 2	n_{eff2}	2.9508	

Table 3.2: Values of parameters used in the calculation

At both cavity ends, we assume that the end facet of III-V waveguide will not introduce any coupling from one mode to another. More detailed calculations show that the reflection coefficient in power from mode 1 to mode 2 and vice versa is in the range of 10^{-3} . Our assumption here is thus reasonably fair.

3.3.2.2.2 Calculation results for a DFB lasers with uniform grating

Figure 3.30 shows the emission spectrum for an exchange DFB laser with uniform grating. The coupling coefficient is assumed to be 123 cm^{-1} as that given in [12]. The gain used for this calculation is 45 cm^{-1} , just below the threshold gain. As in the case of a classical DFB lasers, there are always two modes symmetrical with respect to the Bragg wavelength.

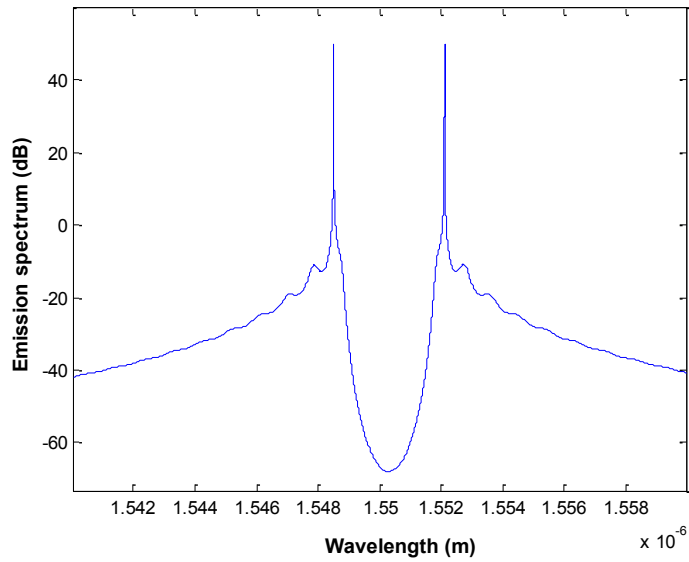


Figure 3.30: emission spectrum for an exchange DFB laser with uniform grating

Figure 3.31 shows the threshold gain as a function of the wavelength of the DFB modes. For the fundamental mode the threshold gain is around 45.9 cm^{-1} , comparable to that in a classical DFB laser with a coupling coefficient in the range of $40 - 80 \text{ cm}^{-1}$. The higher threshold gain compared to the classical DFB counterparts for the same coupling coefficient is due to the fact that only mode 1 benefits from optical amplification.

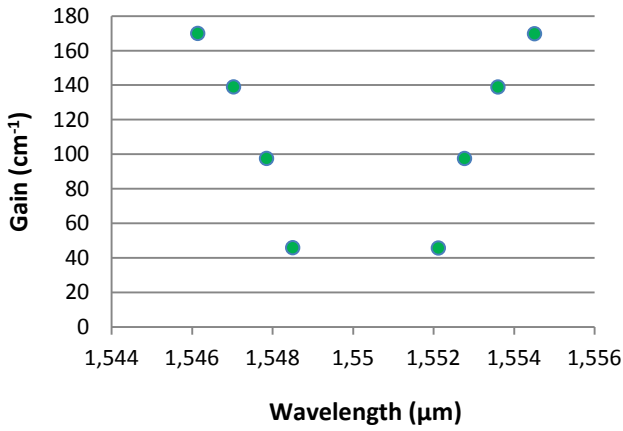


Figure 3.31: threshold gain for different modes in an exchange DFB laser with uniform grating

The output power coupled to the silicon waveguide (mode 2) and the output slope efficiency are also calculated using the coupled mode theory and the rate equation for the carrier density [14]. Figure 3.32 shows the slope efficiency as a function of the coupling coefficient for the DFB mode with the lowest threshold gain. In this calculation, we assume that the coupling coefficient changes due to the variation of grating depth, and other parameters are no affected by this variation. We can see that the output efficiency is in the range of $0.04-0.08 \text{ mW/mA}$ for the coupling coefficient in the range between 40 and 180 cm^{-1} . Such values are quite low compared to those of a classical DFB laser, mainly due to the larger threshold gain in exchange DFB lasers. We can also see that there is an

optimal value around 130 cm^{-1} for the coupling coefficient giving the maximum output efficiency. Those calculation results can be explained as follows. For low coupling coefficient the threshold gain is very high, implying high cavity losses. For high coupling coefficient, the threshold gain becomes reasonable. However the photons are confined inside the cavity, leading again to low output efficiency.

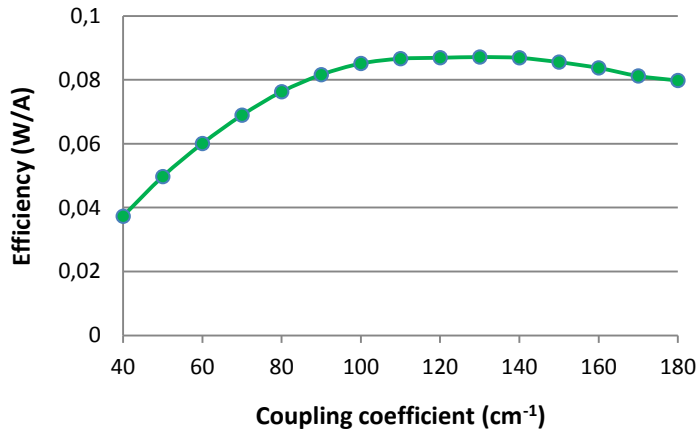


Figure 3.32: output slope efficiency as a function of the grating coupling coefficient for a exchange DFB laser with uniform grating

3.3.2.2.3 Calculation results for a DFB lasers with a $\lambda/2$ phase shift

As in the case of classical DFB lasers, a $\lambda/2$ phase shift introduced in the center of the cavity allows eliminating the bi-mode degeneracy in a DFB laser with uniform grating. A truly single wavelength operation is indeed observed on the emission spectrum shown in Figure 3.33 for a phase shifted DFB laser with a gain of 22.3 cm^{-1} . We assume again that the coupling coefficient is 123 cm^{-1} .

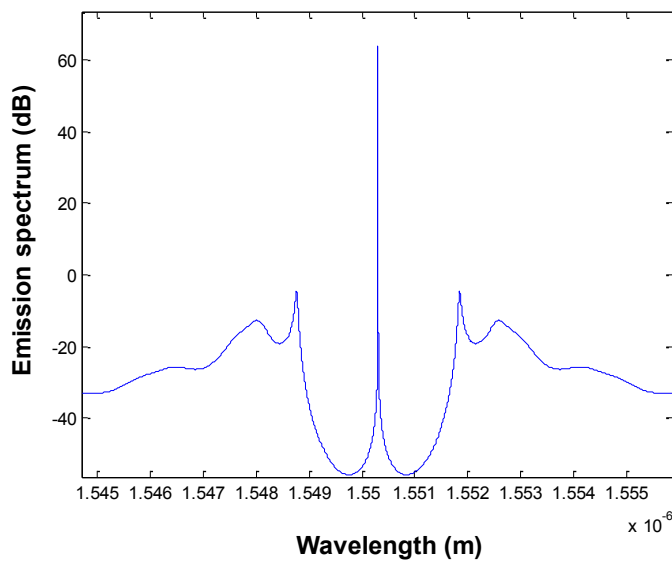


Figure 3.33: emission spectrum for an exchange DFB laser with phase shift

Figure 3.34 shows the threshold gain as a function of the wavelength of the phase shifted DFB modes. Indeed there is only one mode at exactly the Bragg wavelength which has the lowest threshold gain, as in the case of a classical phase-shifted DFB laser.

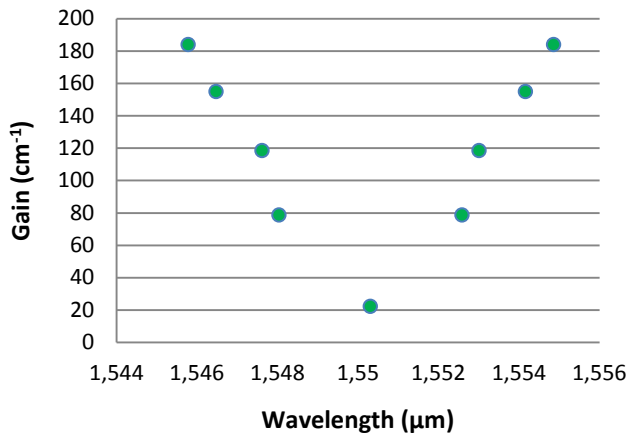


Figure 3.34: threshold gain for different modes in an exchange DFB laser with phase shift

Figure 3.35 shows the slope efficiency as a function of the coupling coefficient for the phase-shifted DFB mode with the lowest threshold gain. One can see that the output efficiency is in the range of 0.05-0.088 mW/mA for the coupling coefficient varying from 50 to 120 cm⁻¹. There is again an optimal value for the coupling coefficient, which is now around 80 cm⁻¹. We observe also a sharper decrease of the slope efficiency with the increasing coupling coefficient than that in a DFB laser with uniform grating. This is due to the fact that for high coupling coefficient, the photons are highly confined close to the point at which the phase-shift is located.

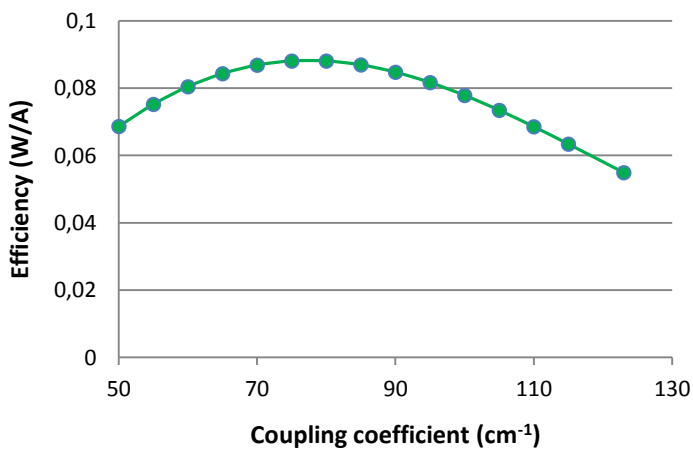


Figure 3.35: output slope efficiency as a function of the grating coupling coefficient for a exchange DFB laser with phase shift

3.3.2.2.4 Conclusions

The coupled mode theory is applied to exchange DFB lasers, in which the forward mode is mainly located inside the III-V waveguide, and the backward mode located inside the SOI waveguide. The calculations show that the exchange DFB lasers have similar modal characteristics as their classical

counterparts. More importantly we show that the exchange type DFB lasers have quite low slope efficiency, limited in one end by the high threshold gain and in the other end by the confinement of photons inside the laser cavity. We find that for both exchange DFB lasers with uniform grating and with a phase shift, there is an optimal value for the coupling coefficient giving maximum output slope efficiency.

3.4 AWG laser

Arrayed waveguide grating (AWG) laser has been introduced by M. Zirngibl et al in 1994 [15]. This kind of design allows the fabrication of monolithically integrated multi-wavelength and wavelength selective lasers. In hybrid technology this geometry is particularly interesting as the footprint of AWG on silicon is much smaller compared to that on III-V materials, indeed very compact multi-wavelength lasers could potentially be fabricated.

3.4.1 Principle

An AWG laser is based on the wavelength filter provided by an arrayed waveguide grating. As it is schematically shown in Figure 3.36 two designs can be used. These two designs are graphically similar but present strong differences. In the first a series of III-V amplifier sections are placed on several channels of the demultiplexed AWG side. Every III-V amplifiers is located inside a Fabry-Perot cavity formed between a low reflection (30%) broadband Bragg grating on the multiplexed side of the AWG, and a high reflection broadband Bragg grating on the other side. All the passive part of the device is realized on silicon, the III-V active section is formed by a straight section. Adiabatic couplers on both sides ensure a loss-less light path between silicon and III-V waveguide. The AWG works like a wavelength selective filter, able to select one mode of the Fabry-Perot cavity. As the AWG selects a different wavelength for each channel, electrically injecting one III-V section we can achieve lasing at a specific wavelength. This device can operate as a wavelength selectable source.

The second design, known as IFF (Integrated Filtered Feedback), is based on a Fabry-Perot laser, which is submitted to a filtered optical feedback provided by the AWG. Several hybrid RSOAs (Reflective Semiconductor Optical Amplifiers) are connected to the output channels of the demultiplexed side of an AWG. The Fabry-Perot cavity, formed by two broadband Bragg mirrors, is connected to the multiplexed side of the AWG.

Electrically injecting the Fabry-Perot III-V section we would achieve laser action with a classical Fabry-Perot spectrum. We can use the integrated circuit formed by the AWG and the RSOAs to modify the optical feedback coming from the left side of the Fabry-Perot cavity. If we electrically pump one of the hybrid RSOAs, we amplify and then re-inject in the Fabry-Perot the fraction of the transmitted light filtered by the AWG channel. Doing so we lock the laser emission to the wavelength filtered by the AWG channel of the pumped RSOA. Using an RSOA related to a different AWG channel, we can lock the laser emission on a different wavelength. In this way we do not achieve a tunable laser but a selective wavelength laser. This second solution provides better wavelength selectivity, and can, in principle, leads to more stable single mode operation of the laser. Compared to the microring tunable laser, we do not need a precise temperature control to select the emitted wavelength. However the laser structure is quite complex and the device footprint is large.

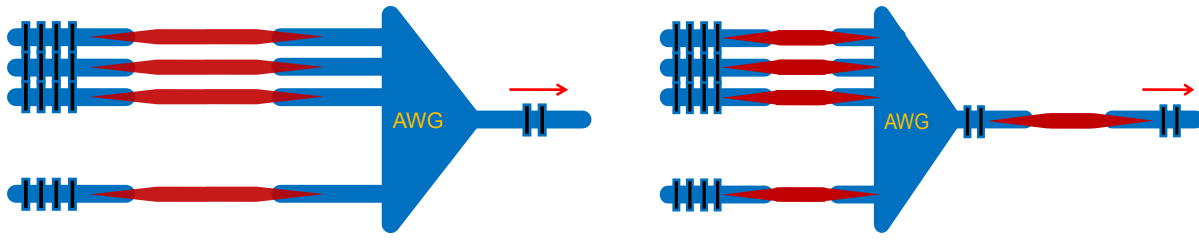


Figure 3.36: schematic diagram of the hybrid AWG laser on the left and of the hybrid IFF AWG laser on the right

Both configurations shown in Figure 3.36 have been designed in two ways. A first one based on a AWG with 5 channels and a channel spacing of 400 GHz, and a second one based on AWG with 16 channels and a channel spacing of 200 GHz. In all the configurations the left side Bragg gratings have a reflectivity of 100%, while the right side gratings has a reflectivity of 40%. All the III-V straight sections have a length of 500 μ m, adiabatic tapers length is 150 μ m.

3.5 Conclusions

In this chapter we describe the different design possibilities that can be used to realize an integrated single wavelength hybrid III-V on SOI laser. DBR, SG-DBR, micro ring based, DFB, and AWG lasers have been presented. A qualitative comparison of the proposed geometries in terms of SMSR, tunability, linewidth, fabrication tolerances and footprint, is presented in Table 3.3. It is impossible to identify a priori an optimum solution, as every design shows some advantages and some drawbacks.

DBR and SG-DBR designs present strong fabrication constraints on the hybrid platform due to the high index differences between silicon and silica. DBR lasers on silicon present an extremely low tunability. SG-DBR structures can allow a much higher tunability but need a large footprint.

Single ring resonator based laser are a valid solution to achieve single wavelength emission due to their compact footprint and easy fabrication, however they present a very narrow tunability. Double ring resonator based lasers can enhance the tunability up to more than 40 nm using the Vernier effect. A single and a double ring resonator based laser have been designed. An analysis of the spectral linewidth is presented. A very thin spectral linewidth is theoretically achievable, but temperature fluctuation can induce emitted wavelength broadening as for every tunable device.

DFB lasers designs for both III-V side and silicon side grating have been proposed. For this kind of devices the fabrication tolerances constitute a main drawback. We analysed several possible configurations. III-V side dedicate layer grating DFB design probably represents the better solution for the future, due to the theoretically higher tolerance to fabrication defects. As a result of the hybrid nature of these devices, a DFB laser based on a contra-directional coupling between III-V and SOI waveguide can be considered. An analytical mode to analyse DFB-exchange laser has been proposed. We applied the model to a recently published DFB exchange laser design; we obtained theoretical performances quite low compared to standard DFB lasers.

AWG hybrid lasers present several interesting features for access network applications. These structures have a very large footprint, but do not require a precise temperature control or complicate fabrication steps (like e-beam lithography). Two AWG laser geometries have been

How to achieve a single mode laser

designed. The first can be used to realize a multi-wavelength or a selective wavelength laser; the second defines a selective wavelength laser.

Up to know only the ring resonator based designs has been fabricated and characterized, all the other proposed design are actually under fabrication at III-V lab.

	SMSR	Tunability	$\Delta\nu$	Fabrication tolerances	Footprint
DBR laser	-	--	-	--	+
SG-DBR laser	+	++	--	--	-
Single ring resonator based laser	-	--	+	+	++
Double ring resonator based laser	+	++	-	+	+
DFB laser	++	--	++	--	++
AWG laser	+	+	+	++	--

Table 3.3 : comparative characteristics of the different single mode hybrid laser designs

3.6 Bibliography

- [1] T. Koch, U. Koren and B. I. Miller, "High-performance tunable $1.5\mu\text{m}$ InGaAs/InGaAsP multiple quantum well distributed Bragg reflector lasers," *Applied Physics Letters*, vol. 53, 1988.
- [2] H. Debrégeas-Sillard, A. Vuong, F. Delorme, J. David, V. Allarrd, A. Bodéré, O. L. Gouezigou, F. Gaborit, J. Rotte, M. Goix, V. Voiriot and J. Jacquet, "DBR module with 20mW constant coupled output power, over 16nm (40 channels 50 Ghz spaced)," *Photonics Technology Letters*, vol. 13, no. 1, 2001.
- [3] V. Jayaraman, Z.-M. Chuang and L. Coldren, "Theory, design, and performance of extended tuning range semiconductor lasers with sampled gratings," *Journal of Quantum Electronics*, vol. 29, no. 6, 1993.
- [4] B. Liu, A. Shakouri and J. E. Bowers, "Passive microring-resonator-coupled lasers," *Applied Physics Letters*, vol. 79, 2001.
- [5] B. Liu, A. Shakouri and J. Bowers, "Wide Tunable Double Ring Resonator Coupled Lasers," *Photonics Technology Letters*, vol. 14, no. 5, 2002.
- [6] S. Matsuo and T. Segawa, "Microring-Resonator-Based Widely Tunable Lasers," *IEEE Journal of Selected Topics in Quantum Electronics*, vol. 15, no. 3, p. 545, May 2009.
- [7] G. T. Reed, *Silicon Photonics*, Wiley, 2008.
- [8] G. H. Duan, P. Gallion and G. Debarge, "Analysis of phase-amplitude coupling factor and spectral linewidth of distributed feedback and composite-cavity semiconductor lasers," *IEEE Journal of Quantum Electronics*, vol. 26, pp. 32-44, Jan. 1990.
- [9] H. Kogelnik and C. V. Shank, "Stimulated emission in a periodic structure," *Applied Physics Letters*, vol. 18, no. 4, 1971.
- [10] S. Akiba, M. Usami and K. Utaka, "1.5- μm lamda/4-Shifted InGaAsP/InP DFB Lasers," *Journal of Lightwave Technology*, vol. 5, no. 11, 1987.
- [11] R. Martin, S. Forouhar, S. Keo, R. Lang, R. Hunsperger, R. Tiberio and P. Chapman, "CW Performance of an InGaAs-GaAs-AlGaAs Laterally-Coupled Distributed Feedback (LC-DFB) Ridge Laser Diode," *Photonics Technology Letters*, vol. 7, no. 3, 1995.
- [12] T. Dupont, L. Grenouillet, A. Chelnokov, S. Messaoudene, J. Harduin, D. Bordel, J.-M. Fedeli, C. Seassal, P. Regreny and P. Viktorovitch, "A III-V on silicon distributed-feedback laser based on exchange-Bragg coupling," *Proc. Group IV Photonics*, 2010.
- [13] H. Kogelnik and C. V. Shank, "Coupled-wave theory of distributed feedback lasers," *Journal of Applied Physics*, vol. 43, 1972.
- [14] G. P. Agrawal and N. K. Dutta, *Semiconductor Lasers*, second edition, Kluwer Academic, 1993.
- [15] M. Zirngibl, C. H. Joyner, L. W. Stulz, U. Koren, M.-D. Chien, M. G. Young and B. I. Miller, "Digitally Tunable Laser Based on the Integration of a Waveguide Grating Multiplexer and an Optical Amplifier," *Photonics Technologie Letters*, vol. 6, no. 4, 1994.

4 FABRICATION PROCESS

In this chapter we will discuss the development of a III-V technological process for the fabrication of hybrid InP/InGaAsP laser on SOI. When I started this thesis III-V Lab just did some very preliminary works on the process development. The development of a reliable process has been one of the important tasks during my thesis. In this chapter, I will describe the main techniques to realize a die-to wafer bonding process, comparing adhesive and molecular bonding. I will analyse the different solutions to etch III-V materials on SOI, summarizing their advantages and drawbacks. Lithographic issues will also be treated. Transmission Line Measurement results for the used semiconductor metal interface will be presented.

4.1 Fabrication steps

For a hybrid III-V on SOI device one can divide the fabrication into three main sections: SOI patterning, bonding, and III-V patterning.

The fabrication of the SOI structures has been realized at CEA-LETI, the process is summarized in Figure 4.1. The SOI substrates (200 mm wafer manufactured by SOITEC) used in this work are composed of a mono-crystalline silicon layer, of a thickness of 400 nm in most cases, on top of a 2 μm thick buried oxide layer on a silicon substrate. After a silica hard mask deposition, the waveguides are defined by means of a 193 nm deep-UV lithography followed by hard mask etching and photoresist stripping. The pattern is transferred to the silicon layer by means of a 180 nm HBr dry etching process. Afterward a thick silica layer is deposited on the wafer and is subsequently planarized by chemical-mechanical planarization (CMP).

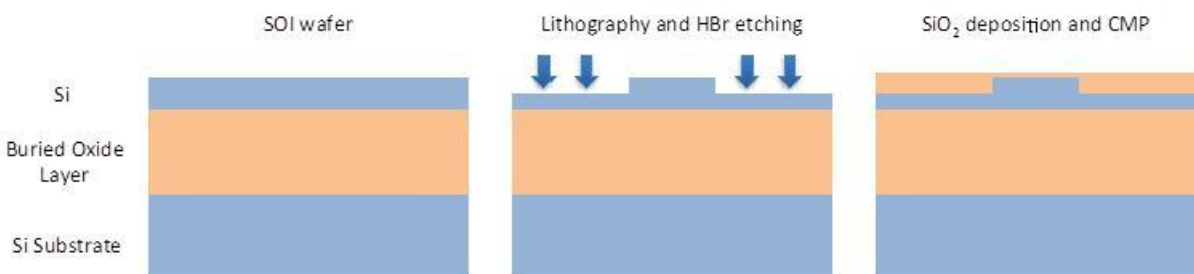


Figure 4.1: schematic description of the SOI fabrication

InP/InGaAsP wafers have been growth at III-V lab by MBE. We used both molecular bonding and adhesive BCB bonding. The first one has been performed at CEA-LETI, the second one at IMEC.

Once the hybrid vertical structure has been prepared, the patterning of the III-V part of the device can start. A series of technological steps are needed, they are schematically described in Figure 4.2: two or more etching steps define the active waveguide, a lift-off metallization step is used to define the n contact, BCB passivation and planarization allow isolating the active waveguide and finally one metallization on top of the structure ensures the p-contact.

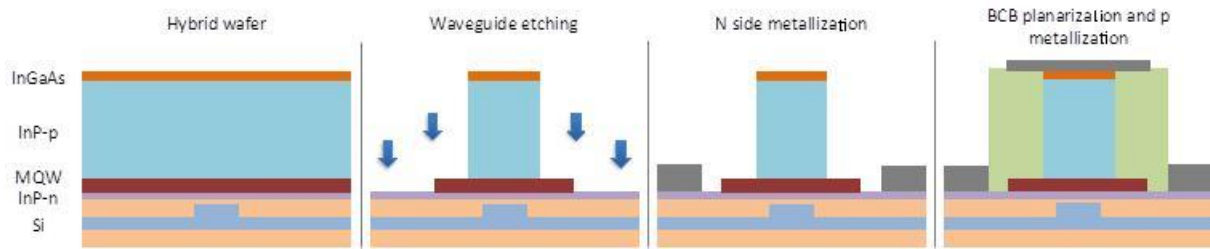


Figure 4.2: schematic description of the III-V technological process

Even though the processing steps are similar to those for standard III-V wafers, the process for the fabrication of hybrid lasers becomes challenging due to the peculiar kind of wafer employed. First, contact lithography is inherently more complicated on hybrid samples due to the peculiar topology of the samples. Second, all the etching processes, well defined for III-V materials, have to be readapted to this kind of hybrid III-V wafer with an isolating substrate, in particular dry etching processes can behave differently with a different substrate. Third, annealing treatments have to be modified to fit with limitations on temperatures due to the bonding layer.

To fabricate high performance lasers one needs to choose the optimum solution for every step. Three main technological issues had to be addressed: the definition of the narrow III-V taper tip from a lithographic and a etching point of view; the uniformity and the precision of the etching that has to be stopped on top of the thin InP n doped layer; the definition of a Ohmic p side metallization without the use of standard annealing treatments. In the following sections I will detail how I converge to the final process employed.

4.2 Bonding

High quality bonding of III-V epitaxy to SOI wafers is mandatory for heterogeneous integrated lasers. The bonding layer plays a key role on the device performance. Ideally, from a design point of view, we would like to have a thin bonding layer with a precise thickness. From a fabrication point of view, we aim to achieve a stable, mechanically robust, low cost, CMOS compatible, high yield and heat-resistant bonding. Practically, all these virtues are not achieved yet; different techniques have been developed and each of them presents some advantages and some drawbacks.

In this work we focused on the two main techniques reported in literature up to now: molecular bonding and DVS-BCB bonding. Comparing to a standard III-V wafer, the hybrid wafers obtained with these two technologies introduce several difficulties in the fabrication process: bonding defects, reduced tolerance to annealing treatments, inaccuracy of bonding layer thickness, need for adapted etching process.

4.2.1 Molecular bonding

Molecular bonding was performed at CEA LETI, which developed the process and bonded dies and entire wafer.

After the SOI fabrication and patterning, the entire waveguiding structure is covered by a 500-nm-thick cap layer of silica deposited by plasma-enhanced chemical vapor deposition (PECVD). A

chemical-mechanical polishing (CMP) step flattens the SOI surface, leaving only a silica capping layer of a desired thickness. The additional role of CMP is to adjust the thickness of the silicon dioxide cladding layer in order to satisfy the optical coupling conditions, the inhomogeneity of the process can lead to a thickness variation of ± 50 nm on the entire wafer. The control on the bonding layer thickness is indeed inaccurate. However the thickness of the cladding layer varies slowly along the wafer surface; it is possible to bond the III-V die only on the wafer zones that have approximately the desired cladding layer thickness. In Figure 4.3 (a) we show a bonded dice before substrate removal and in (b) a bonded dice after substrate removal.

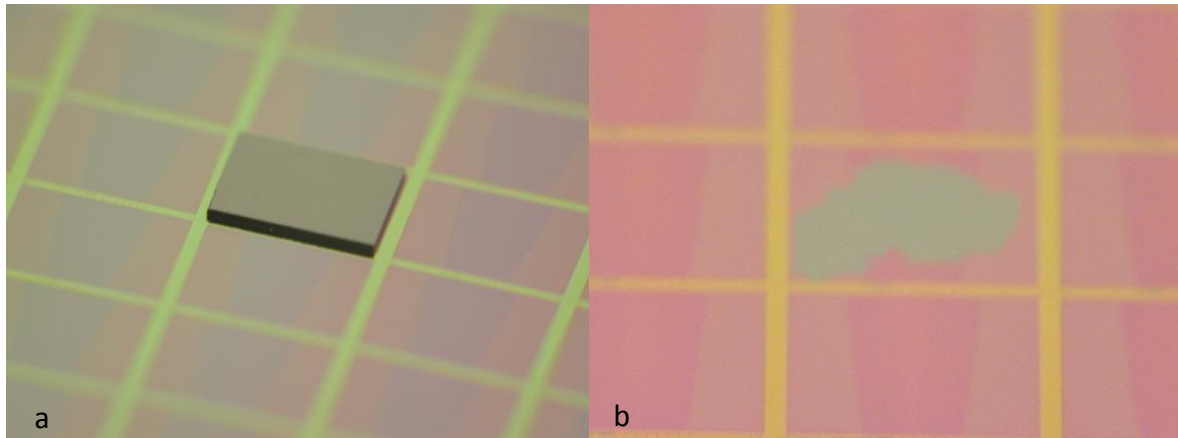


Figure 4.3: (a) III-V dice bonded to SOI before substrate removal, (b) after substrate removal

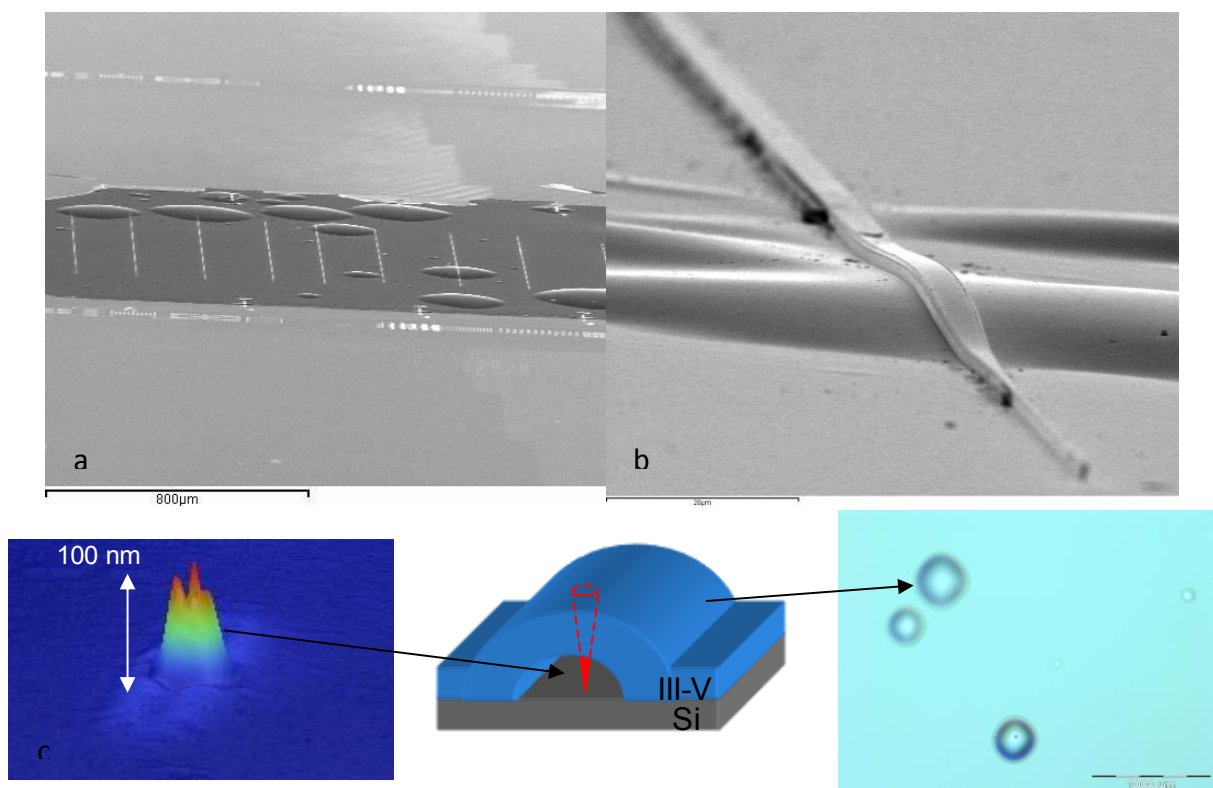
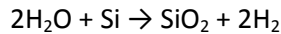


Figure 4.4 (a) SEM picture of a hybrid molecular bonded sample with many defects, (b) SEM picture of a hybrid laser patterned on a defect, (c) from epitaxial defects or particle to bonding defect

This technique is really sensitive to epitaxial defects and particles contamination on the surface and we observed sometimes several bonding defects. The defects look like gas bubbles between the silica dioxide layer and the thin stack of III-V. In Figure 4.4 (a) we can observe a bonded sample presenting several bonding defects; in (b) we show a laser ridge patterned on a bubble.

Bubbles come from the diffusion at the bonding interface of the hydrogen produced by the molecular wafer bonding reaction



When H_2 pressure exceeds the bonding energy, formation of bubbles occurs; as epitaxial defects or particle contaminations reduce locally the bonding energy, they act as nucleation centers for bonding defects as it schematically resumed in Figure 4.4 (c). Due to the strengths applied on bubbles during contact lithography and annealing treatments, defects normally enlarge during the process. The fabrication yield can be massively reduced. For small surface dices (from a few mm^2 up to a wafer quarter) the yield is around 30%. Thanks to LETI development the yield for entire wafer bonding has recently increased and it is now around 80%. To achieve high quality bonding the III-V wafers have to respect a few requirements: the wafer bow needs to be lower than $10 \mu\text{m}$, the surface roughness lower than 5\AA RMS , the defects density lower than 100 cm^{-2} and the defects height lower than 100 nm . In Figure 4.5 we show the bonding of 4 quarters wafer (a) and of an entire wafer (b). We observe that a large amount of the bonded III-V has been lost in (a) due to bonding defects; the bonding yield is much higher in (b), however we recognize some bonding defects in the center of the bonded wafer.

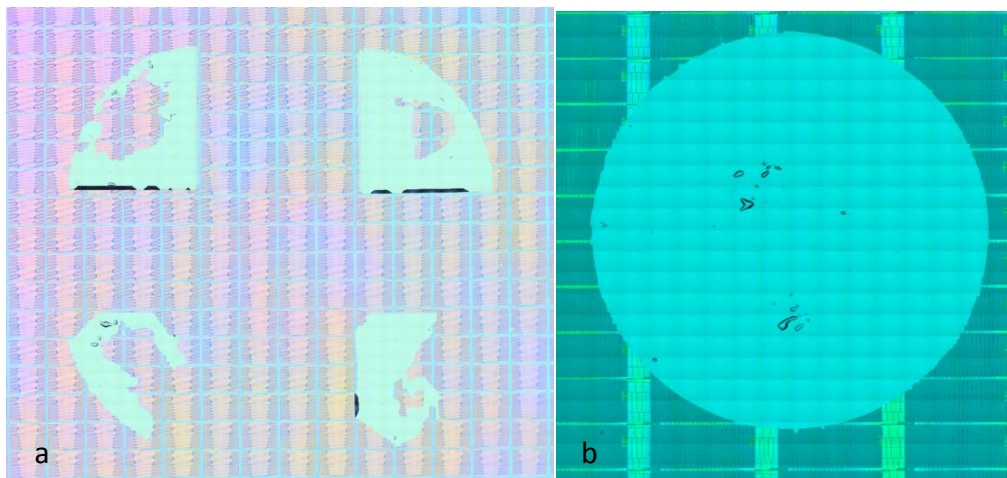


Figure 4.5: (a) four III-V wafer quarters bonded on SOI, (b) an entire III-V wafer bonded on SOI

4.2.2 DVS-BCB bonding

Ultra-thin DVS-BCB bonding for the heterogeneous integration of III-V material on SOI samples has been developed at IMEC. This technique allows bonding layers that are less than 500 nm thick. These layer thicknesses cannot be achieved using commercially available cyclotene and need to be formulated by dilution with mesitylene. Before bonding, the SOI waveguide substrate, is deepen in a cleaning solution ($1\text{NH}_3:4\text{H}_2\text{O}_2:20\text{H}_2\text{O}$) at 70°C . This chemical treatment helps to remove particles contaminations and renders the surface hydrophilic. Afterward a BCB adhesion promoter is applied. Mesitylene diluted Cyclotene 3022-35 is spin-coated on the SOI and partially cured (210°C for 40

min). A second layer is then spin-coated and undergoes a rapid thermal annealing at 250°C, this treatment increases the degree of polymerization into the optimal region for bonding.

The cleaved InP/InGaAsP dies are temporarily attached to a Pyrex carrier using a thermoplastic photoresist. The InP and InGaAs sacrificial layers are chemically removed to obtain a clean surface. This cleaning step removes the hydrocarbon contamination and all particles presents on the surface. To make the InP surface hydrophilic the sample is dippen on a diluted HF solution. The InP dies are bonded in a vacuum environment to avoid the inclusion of air at the bonding interface. The bonding is performed at 150°C to detach the InP dies from the Pyrex carrier. Afterward the stack is cured for 1 h at 250°C under a uniform pressure of 300 kPa in a nitrogen environment. The bonding sequence is graphically depicted in Figure 4.6 [1].

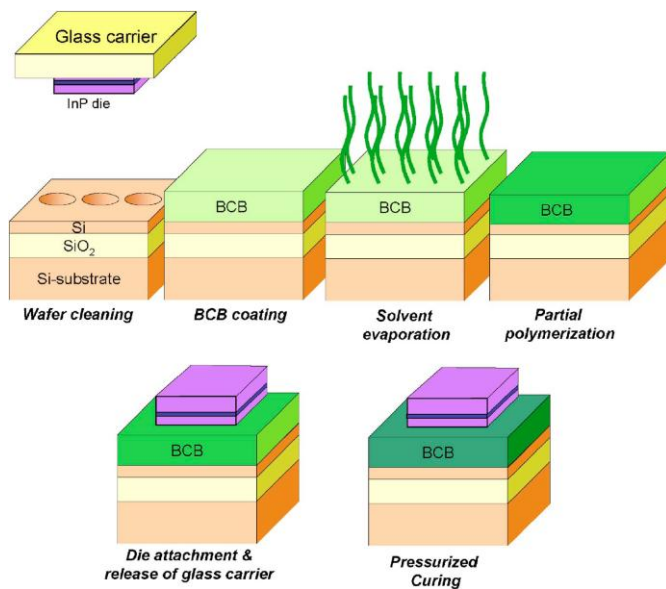


Figure 4.6: Overview of the InP/InGaAsP die to wafer bonding process [1].

We realized hybrid laser using DVS-BCB bonding for small bonded dices (4x6mm) and large dices (a quarter of III-V wafer). Two of these samples are shown in Figure 4.7.

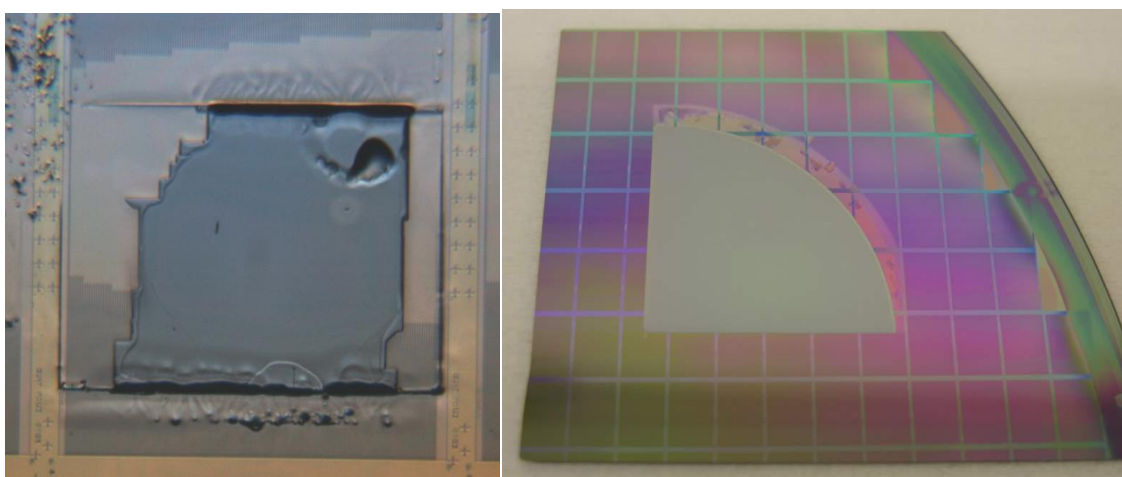


Figure 4.7: On the left a microscope image of a small bonded dice, on the right an image of a bonded wafer quarter

DVS-BCB samples demonstrated a better yield compared to molecular bonded samples. Generally a large part of the bonded surface (more than 80%) was free of macroscopic defects and could handle the entire process. However we often observe some thick (more than 10 μm) BCB bumps on the border of the bonded sample (left image of Figure 4.7). This kind of defect makes contact lithography impossible. Concerning the bonding layer thickness, thanks to recent IMEC development it has been reduced to less than 50 nm as shown in Figure 4.8. Anyway, as the process is still largely "handmade", it is not easy to achieve this thickness value in a repeatable way. DVS-BCB bonded samples are more tolerant to rapid thermal annealing as we will see in a following paragraph, but BCB cannot tolerate temperature higher than 400°C.

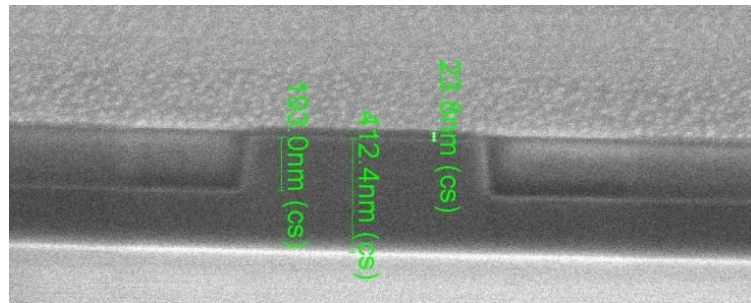


Figure 4.8: SEM cross section of the hybrid wafer, on the center the silicon waveguide, on top of it the III-V stack

4.3 Lithography

Two lithographic steps needed a specific development during this thesis. The first is related to the III-V narrow taper tip used in our design. To achieve an efficient light coupling we need to obtain a tip of 400 nm. On a standard III-V wafer this dimension can be achieved with a 405 nm UV contact lithography, as we will see in this section this is not true for hybrid III-V on SOI wafers. The second is connected to the definition of a grating on III-V material to realize a DFB laser. We need to pattern and etch 150 nm features, for this purpose e-beam lithography is mandatory.

4.3.1 Contact lithography

Contact lithography is mostly used for the definition of patterns in photoresist on III-V epitaxial structures due to the low cost of the lithography system.

Photolithography allows transferring a pattern from a photomask to a sample. The sample is spin-coated with a thin film of UV-sensitive photoresist and then placed underneath the photomask. A contact aligner is generally used to align and to press into "contact" the photomask and the sample. Once in contact condition the sample is "exposed" to UV light, which shines from the top side of the photomask. A photomask consists of opaque chrome patterns on a transparent glass plate. The sample surface lying underneath the opaque chrome patterns is protected from UV light while the rest of the surface is exposed. The UV light induces a chemical change in the photoresist; in a positive photoresist the exposed part becomes soluble to a chemical solution, generally called developer. Consequently we can transfer a pattern from the photomask to a substrate in the form of photo-sensitive resist. Afterwards the pattern can then be transferred from the photoresist into the wafer via microfabrication processes, like etching or lift-off.

The resolution in contact lithography is approximately the square root of the product of the wavelength and the gap distance. This resolution limit originates from the near-field diffraction of the light propagating through the photoresist. Diffraction causes the image to lose contrast with increasing depth into the photoresist.

Contact lithography is a complicated step on hybrid samples in two respects: the shape and the topology of the samples. SOI wafer diameter ranges from 150 mm to 300 mm, this dimension is not compatible with mask aligners typically used for III-V materials. Therefore we need to dice the SOI wafer to perform contact lithography. Normally we achieve irregular dice shapes that do not correctly fit with mask aligner supports. To solve this problem we send the SOI wafers to a company that cuts the SOI with a high power laser, to achieve 2" or 3" round shape samples as in Figure 4.9.

Hybrid samples often present an imperfect topology compared to standard III-V wafers. As we have previously seen, both BCB and molecular bonding can introduce defects that deteriorate the quality of samples surface. A hard defect is detrimental to contact lithography as it can widen the gap between the mask and the substrate, enhancing the diffraction.

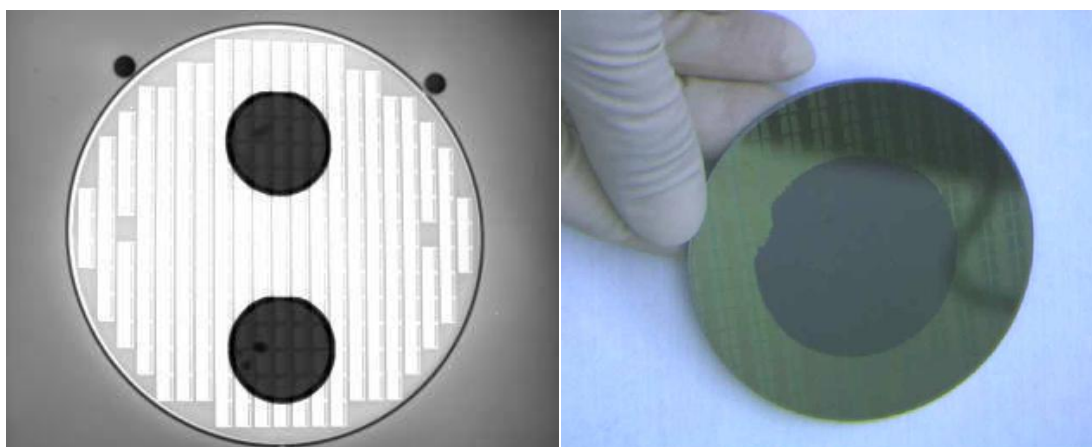


Figure 4.9: (a) 200mm SOI wafer with two III-V wafers bonded on top, (b) SOI wafer reduced to 3" by laser cut with a III-V wafer bonded in the center

4.3.1.1 UV 405 nm lithography

On standard III-V wafer we are able to pattern a tip as narrow as 300 nm with 405 nm UV contact lithography; on hybrid sample this was not possible. The lithography process is summarized in Figure 4.10. After surface cleaning, adhesion promoter AP-3000 is applied; a Lift-Off Resist 3A layer is spin-coated at 4000 rpm and undergoes a thermal annealing for 30 min at 200°C. The primary functions of the prebake process are to dry the LOR film and to fix the development and undercut rate. Subsequently, an AZ® nLOF 2070 negative photoresist diluted with EBR solvent is spin-coated at 4000 rpm and undergoes a thermal annealing for 1 min at 110°. The photoresist is diluted to achieve a 1.5 μm thick thin film. We expose to 405 nm UV light for 6 seconds (the UV lamp intensity is of 10 mW/cm²) using a binary quartz chrome photomask then the sample undergoes a post exposure bake for 1 minute at 110°C. We develop dipping in MF-CD-26 W for 150 seconds. The photomask holds several straight patterns ending with 400 nm tips. A 150 nm platinum layer is deposited by metal evaporation. The nLOF-platinum stack lift-off is achieved dipping in Acetone. The remaining LOR is

removed dipping in MF-CD-26 W for 3 minutes. The defined metal film is used as hard mask for the following etching performed by CH_4+H_2 RIE.

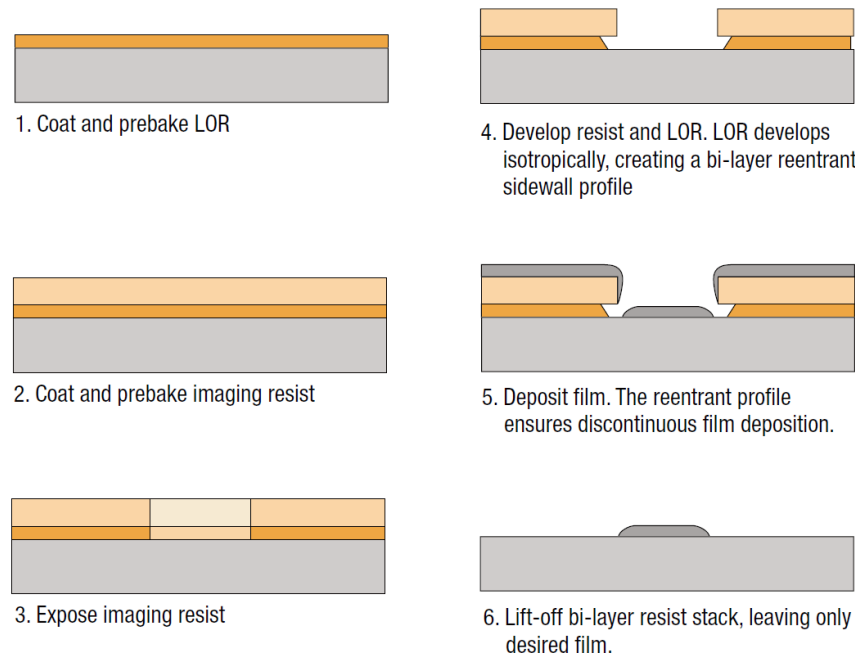


Figure 4.10: Lift-off process flow

In Figure 4.11 (a) we show an optical microscope picture of the tapered part of a laser ridge after deep ridge etching; we observe the platinum mask defined by lift-off in light grey, as the InP membrane is extremely thin we clearly perceive the silicon waveguides underneath in dark blue colour. A SEM picture of the cross-section of a laser ridge patterned with 405 nm contact lithography is shown in Figure 4.11 (b). With this process I achieved taper tips width ranging from 1 μm to 1.4 μm depending on the sample topology. Trying to improve the resolution I reduced both the exposure time and the nLOF layer thickness, going from 6 seconds exposure to 4 seconds and from 1.5 μm to 1 μm . With this slightly different process I achieved taper tips width between 0.6 μm and 1 μm .

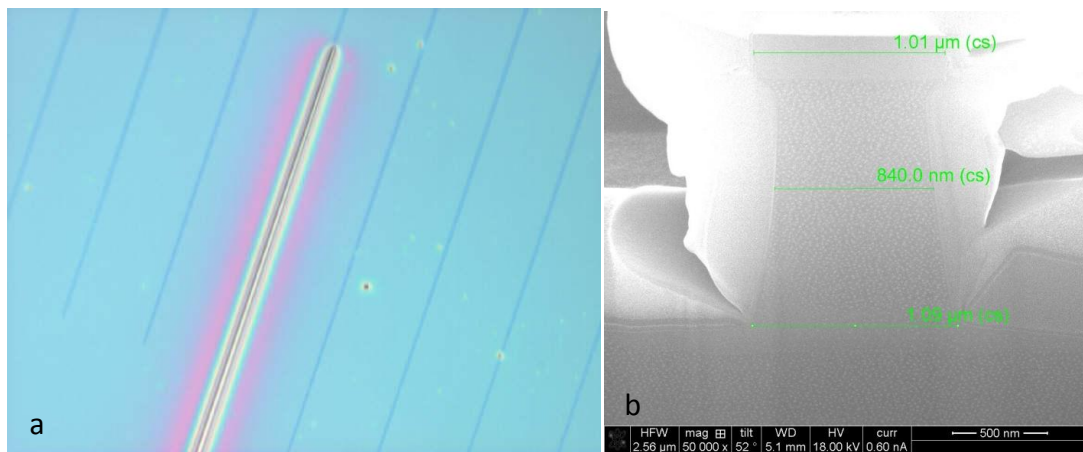


Figure 4.11: taper tips achieved with 405nm UV light contact lithography

4.3.1.2 UV 248 nm lithography

In order to improve the resolution of the lithography process we move from using 405 nm to 248 nm UV light. We have been forced to use a positive photoresist, as negative photoresists sensitive to this wavelength are not available. On a III-V wafer we can achieve a tip as narrow as 200 nm using this wavelength in contact lithography configuration.

The lithography process is the following. After surface cleaning we deposited a 50 nm thick titanium layer by Double Ion Beam Sputtering then a 300 nm silica thick dioxide layer by PECVD. Adhesion promoter AP-3000 is applied then a UVIII photoresist layer is spin-coated at 4000 rpm and undergoes a thermal annealing for 2 minutes at 135°C. We expose to 248 nm UV light for 18 seconds using a binary quartz chrome photomask, the UV lamp intensity is of 3 mW/cm². The sample undergoes a post exposure bake of 90 seconds at 105°C. We develop the photoresist dipping in MF-CD-26 W for 50 seconds. The photomask owns the same patterns that the 405 nm one but with reversed polarity.

After development we use the patterned photoresist as mask to etch the silica dioxide layer by CHF₃ RIE. The photoresist is removed by oxygen plasma and acetone. The patterned silica hard mask is used to etch trough the titanium and the InGaAs layer by ICP, subsequently the semiconductor is dipped into a selective etching solution of HCl and H₃PO₄ to etch the InP layer.

Using this process, taper tips ranging between 350 nm and 450 nm have been achieved. In Figure 4.12 we show two SEM pictures of the achieved tips.

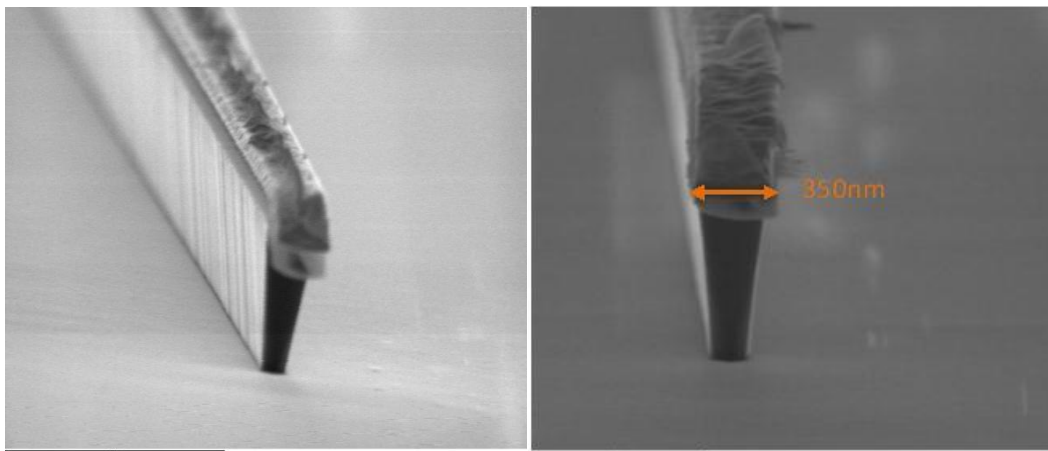


Figure 4.12: taper tips achieved with 248nm UV light contact lithography

4.3.2 Electron Beam lithography

Electron Beam Lithography (EBL) refers to a lithographic process that uses a focused beam of electrons to pattern a resist film and subsequently selectively removing either exposed or non-exposed regions of the resist. To realize Bragg gratings or nanophotonic devices electron beam lithography is extensively used in III-V processing.

The sample is spin-coated with a thin film of resist, commonly PMMA, then, under vacuum condition, a focused beam of electrons is scanned over the surface. Given the availability of technology that provides a small-diameter focused beam (around 10 nm), an EBL system does not need physical masks to perform its task anymore. An EBL system simply 'draws' the pattern over the resist layer

using the electron beam as its drawing pen. Once the sample has been written it can be developed, selectively removing either exposed or non-exposed regions of the resist (positive or negative resist). EBL systems produce the resist pattern in a 'serial' manner; it can take hours to write an entire wafer, it is an inherently slow writing process and cannot be used for mass fabrication. In Figure 4.13 we show some SEM pictures of very small features patterns transferred into III-V wafer by EBL, on the right a grating with a continuous variation of kappa, on the left a taper tip of around 100 nm.

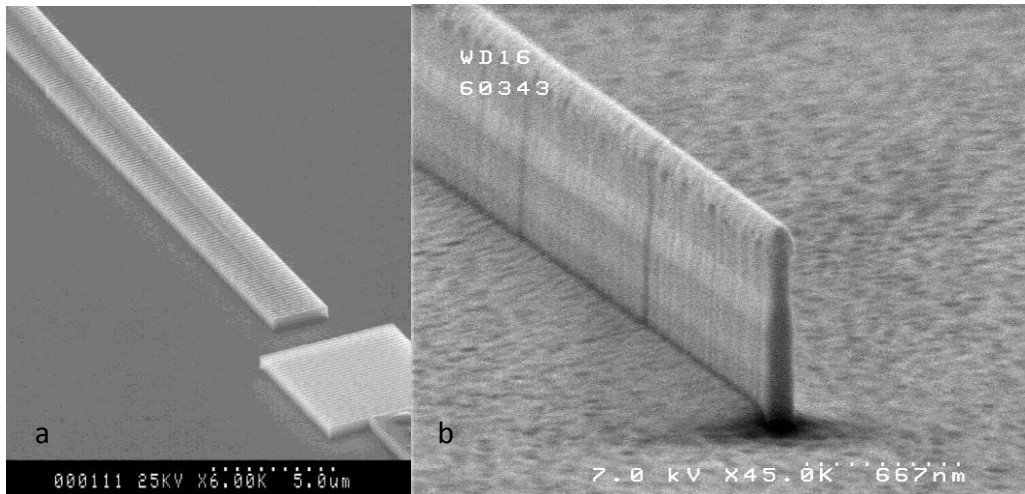


Figure 4.13: SEM pictures of (a) grating with a continuous variation of kappa and (b) a tip patterned by e-beam on a III-V wafer

Passing from III-V wafers to heterogeneous integrated hybrid samples, we need to adapt the electrons dose to fit with the different electronic properties of the substrate, but we especially need to manage the alignment marks configuration. EBL always needs alignment marks on the sample to have a frame of reference that allows EBL to focus the electron beam at the right horizontal and vertical position. In hybrid samples, as we need to align e-beam patterns on III-V with SOI waveguides, we must have alignment marks on top of the SOI. But, as we bonded the III-V stack on the SOI, not all the SOI surface is available to be identified by the EBL, because it is partially covered by III-V. Indeed the alignment marks have to be carefully designed to fit with the entire process, from SOI, through bonding, to III-V patterning.

We developed a reproducible process to pattern with EBL on hybrid samples. The main results are summarized on Figure 4.14 and Figure 4.15. 200nm taper tips have been achieved, the tips are well defined with vertical sidewalls. Vertical Bragg gratings for DFB laser has been written and etched, the grating is correctly defined and opened along the entire sidewall; on the right picture of Figure 4.15 we observe a $\lambda/4$ phase shift, it has to be noticed that the grating seems not correctly defined in this picture due to a strong edge charging effect of the SEM.

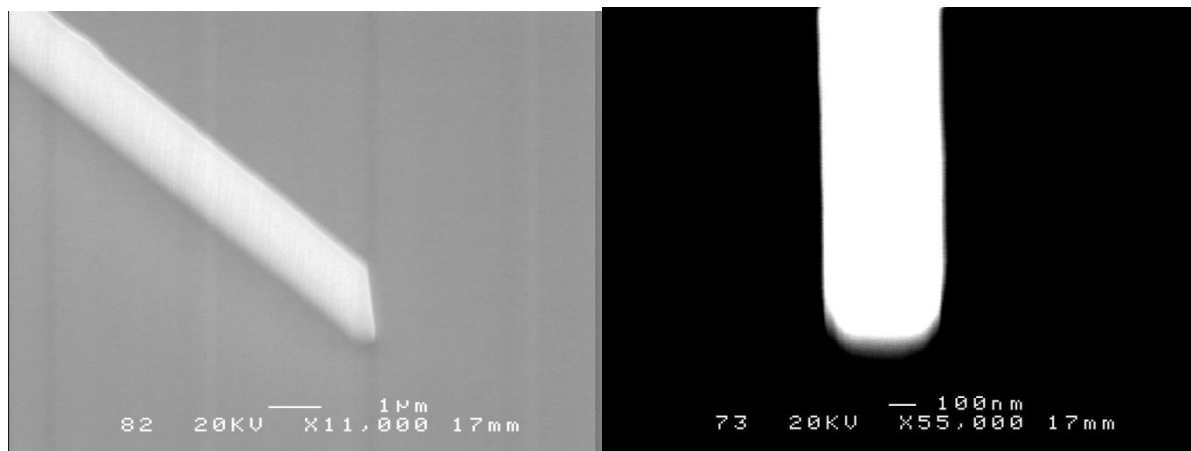


Figure 4.14: SEM pictures of taper tips patterned on hybrid samples by e-beam lithography and etched by RIE

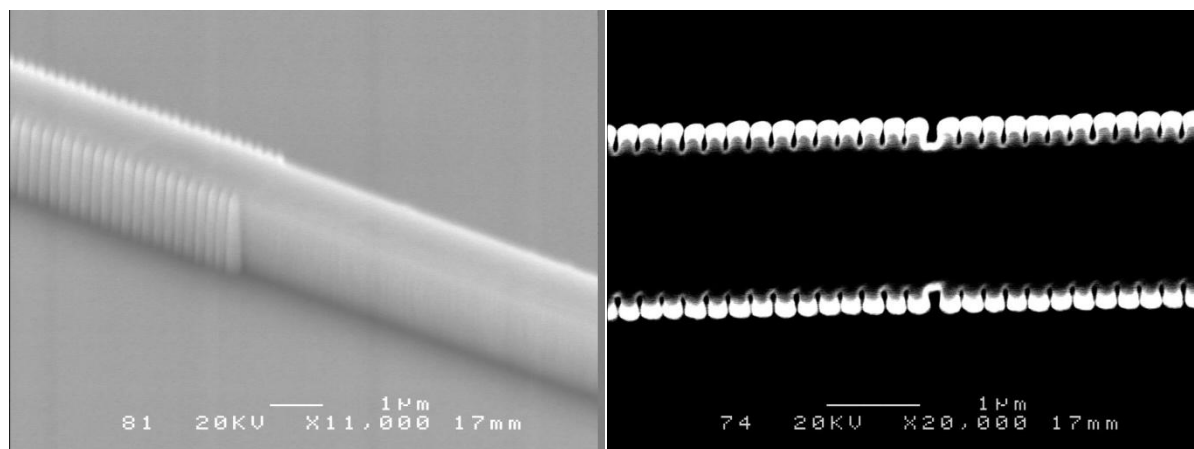


Figure 4.15: SEM picture of Bragg gratings on an hybrid sample written by e-beam and etched by RIE

4.3.3 Conclusions

	III-V wafer minimum feature size	Hybrid wafer minimum feature size	Alignment tolerance	Considerations
405 nm contact lithography	400 nm	600 nm	± 400 nm	Dependent on wafer topology, fast
248 nm contact lithography	200 nm	350 nm	± 400 nm	Dependent on wafer topology, fast
E-beam lithography	< 100 nm	100 nm	± 100 nm	Slow, alignment marks, high resolution, precise alignment

Table 4.1: lithography performances comparison

In Table 4.1 we compare the different lithographic solutions used. 405 nm UV contact lithography reveals to be unfit to the taper tip definition on hybrid samples. With this technique we never achieve a tip narrower than 600 nm due to enhanced diffraction effects on hybrid samples. 248 nm UV contact lithography presents a better definition, taper tips as narrow as 350 nm have been achieved thanks to the shorter wavelength and the thinner photoresist employed. However, the alignment, critical for a hybrid laser III-V waveguide, is still not precise enough for our designs. E-beam lithography surely represents the most efficient solution for both taper tip and grating definition. Once we solved the alignment marks issue we achieved extremely narrow features with a sufficient alignment tolerance. It has to be noticed that as e-beam lithography does not need a physical contact with the substrate, it is not sensitive to localized topology defects.

4.4 Etching on Hybrid III-V/SOI samples

Etching refers to the removal of material, typically a masked pattern of semiconductor material, by exposing the material to a chemical solution (wet etching), or to a bombardment of ions (dry etching) that dislodge portions of the material from the exposed surface. In this paragraph we present commonly used wet and dry etching techniques for III-V semiconductors technologies, investigating how these techniques can be adapted to hybrid samples.

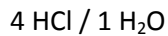
4.4.1 Chemical etching

In wet etching process the sample is dipped into an etching solution. The basic steps involved in wet chemical etching of III-V materials involve oxidation (or reduction) of the semiconductor surface and removal of a soluble reaction product. Wet etching is typically isotropic, however on crystalline materials etching rate is typically lower on the more densely packed surface than on the loosely

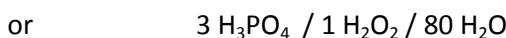
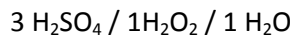
packed surface. This effect can allow very high anisotropy depending upon which crystal face is exposed to the etching solution.

For every material several etching solution are listed in literature, we summarize some of them for the used III-V materials in the following lines:

InP etching (selective):



InGaAs / InGaAsP (selective):



InP/InGaAsP/InGaAs (not selective):



Wet etching is also employed to remove hard masks, like silica dioxide masks or silica nitrate masks. Etching solutions used for this purpose are generally based on hydrofluoric acid. For a hybrid sample these kinds of solutions have to be used carefully, as they can etch through the SOI uncovered region damaging the SOI patterned devices (modulators, couplers, waveguides, AWG, etc...).

In the following section we will analyse in details the behaviour of two commonly used solutions for hybrid samples technology.

4.4.1.1 *Indium Phosphate wet etching*

To etch trough Indium Phosphate we used a solution of hydrochloric acid and phosphoric acid. This solution is extensively used in III-V technology, as it is not able to etch InGaAs/InGaAsP semiconductors the solution is “selective” [2]. At room temperature the etching rate is near to 1 $\mu\text{m}/\text{minute}$, and we observe a strong anisotropy. Passing from III-V wafers to hybrid samples we observe the following effect. By bonding the epitaxial structure to another wafer and then removing the InP substrate, we reverse the crystallographic orientation of the semiconductor. The surface of the III-V wafer before bonding, become the bottom of the III-V stack after bonding, the surface on top is not anymore (100) but (-100). Reversing the crystallographic axis we reverse the anisotropy properties of the etching.

On III-V wafer we have an etching profile like Figure 4.16(a) for an etching mask in the [011] direction, the etching reveals the (0-11) plane. For etching mask in the [0-11] direction we reveal the (111) plane as in Figure 4.16(b), on hybrid sample the solution etch in a radically different way.

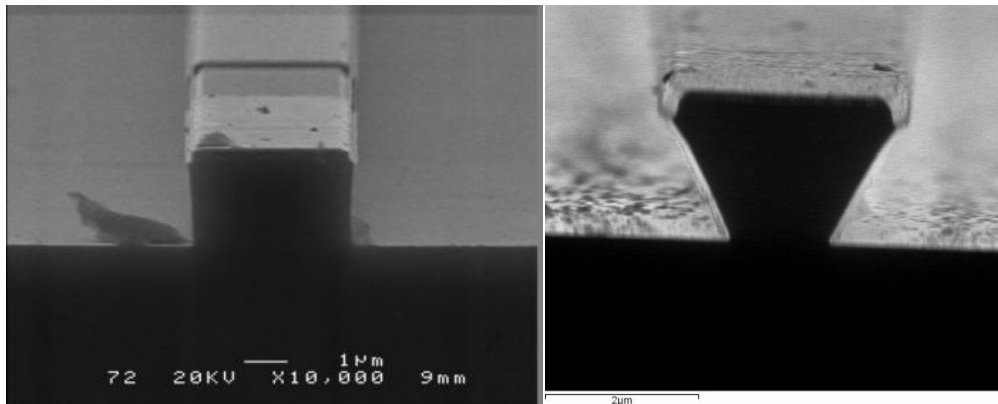


Figure 4.16: (a) wet etching on an InP wafer with stripe mask pattern following the [011] direction, (b) the [0-11] direction

In Figure 4.17 we can observe the etching profile for the hybrid sample case. In the first picture inside red circles we show the etching profile for a mask on the [011] direction, as we can observe in the picture the etching stops on the (1-11) plane. In the second picture we observe the etching profile achieved for a mask on the [01-1] direction, in this case the etching reveals the (011) plane.

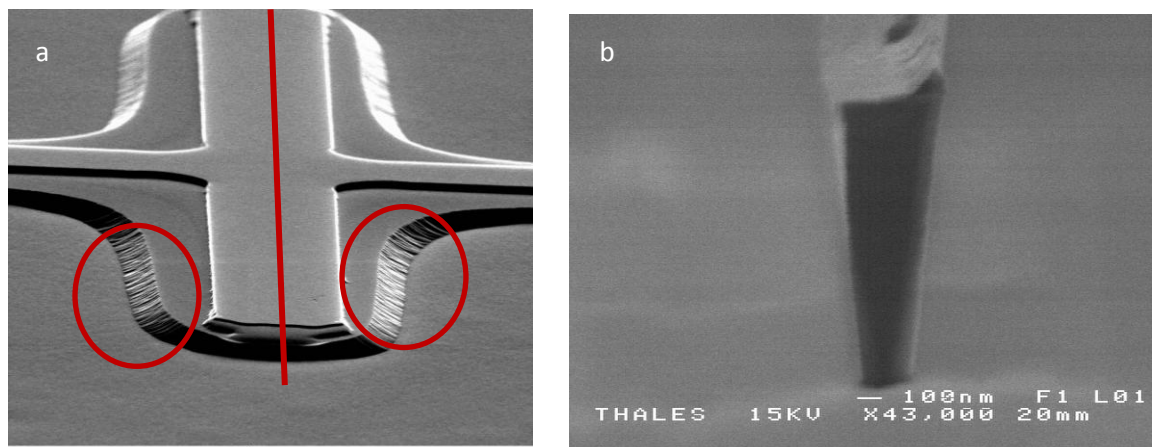


Figure 4.17: (a) wet etching on a hybrid sample with stripe mask pattern following the [011] direction, (b) the [0-11] direction

4.4.1.2 InGaAs wet etching

To etch InGaAs we used a phosphoric acid based solution ($3\text{ H}_3\text{PO}_4 / 1\text{ H}_2\text{O}_2 / 80\text{ H}_2\text{O}$). This solution is perfectly selective, as the etching rate for InGaAs (75 nm/min) is at least ten times higher than that for InGaAsP and InP, and almost isotropic. Isotropic etching solutions can reduce the etching roughness compared to anisotropic ones, as they do not follow a particular crystallographic plane, they can smooth the roughness coming from the mask. At the same time isotropic etching solutions are inadequate for defining feature size of less than 1 μm, as under masks etching is almost as fast as vertical etching, the solution would etch all the material under the mask destroying patterns. In Figure 4.18 we can observe, between yellow lines, a 300 nm thick InGaAs layer etched with this solution, we observe the isotropic profile and the undercut.

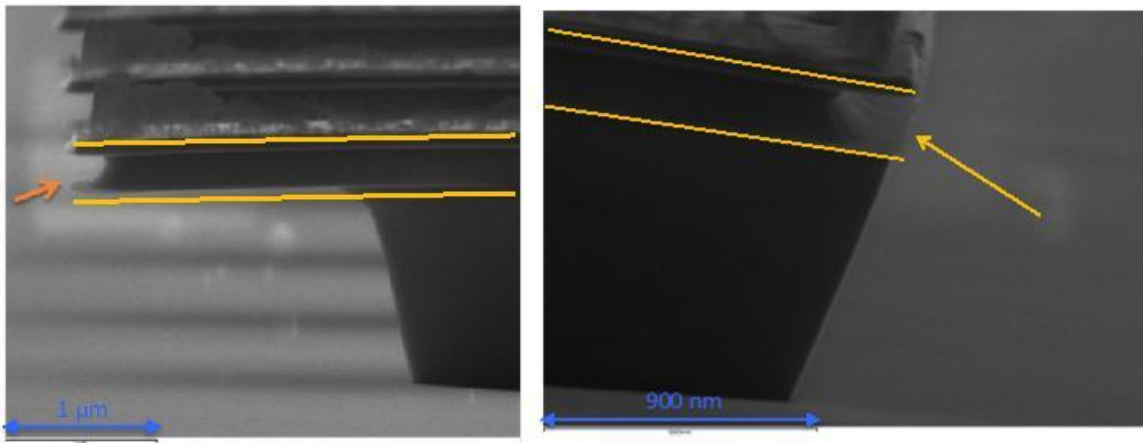


Figure 4.18: wet etched III-V stack, between yellow lines a InGaAs layer etched by $3\text{H}_3\text{PO}_4 / 1\text{H}_2\text{O}_2 / 80\text{H}_2\text{O}$

4.4.1.3 InGaAsP wet etching

To etch through passive quaternary layers and quantum wells we used the following sulfuric acid based solution at 0°C : $3\text{H}_2\text{SO}_4 / 1\text{H}_2\text{O}_2 / 1\text{H}_2\text{O}$. This solution is exothermic and needs to be cooled as it is too aggressive at room temperature. Partially selective, it does not etch indium phosphate but it has roughly the same etching rate for InGaAsP and InGaAs. As the solution can etch also ternary layers it has to be carefully employed, ternary layers need to be protected before dipping the sample in the solution. A method, commonly used in silicon technology, can be employed to protect the ternary layer (Figure 4.19). We deposit a thin layer of silica dioxide on the whole sample then we etch this layer on the whole sample by directive RIE. In this way, thanks to the isotropy of the deposit and to the anisotropy of the dry etching, we selectively deposit a thin layer of silica dioxide around InGaAs borders. In Figure 4.20 we observe a taper tip before and after this protection step. This solution is also isotropic and indeed inadequate to submicron size features etching.

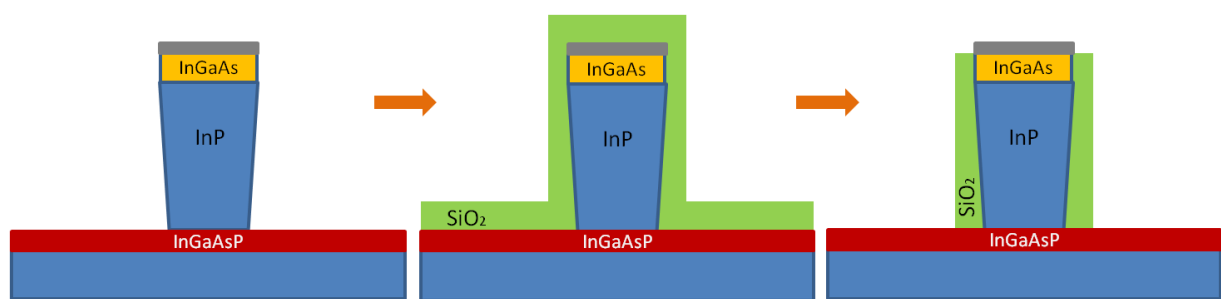


Figure 4.19: how to protect InGaAs from InGaAsP wet etching

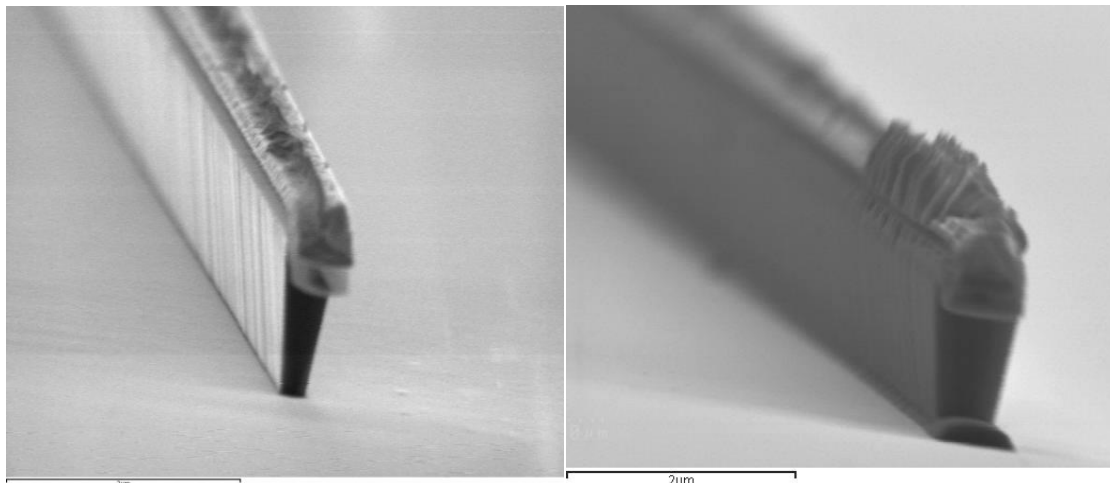


Figure 4.20: a taper tip before and after protection of the InGaAs layer by silica dioxide

4.4.2 Dry etching

Dry etching refers to the removal of material by exposing the substrate to a bombardment of ions that dislodge portions of the material from the exposed surface. [3]

4.4.2.1 Reactive Ion Etching

Reactive Ion Etching (RIE) is the most common dry etching method used in III-V technology. The term RIE is commonly applied to discharges contained between two parallel electrodes, one of which is powered at RF frequencies through a coupling capacitor. The much higher mobility of electrons in the discharge allows them to respond to the RF alternating field applied across the electrodes, while the movement of the much heavier ions is very little influenced. The electrons will travel through much longer distances than the ions, and in this way, they will much more frequently collide with the reactor walls and electrodes and consequently be removed from the plasma. This would leave the plasma positively charged. However, plasmas remain neutral. To guarantee this neutrality, a DC electric field has to be formed in such a way that the electrons are repelled from the electrodes. When one of the electrodes is smaller than the other, a large voltage is developed across the smaller sheath capacitance associated with the small electrode. Since the larger electrode is usually the chamber itself, most of the potential difference between plasma and electrode is dropped across the sheath region above the small powered electrode. The ions located near the edge of the sheath are accelerated across it and strike the small electrode at near-vertical incidence. The sample that has to be etched is placed on this electrode and is subject to this ion bombardment as well as a constant flux of neutral gas atoms and molecules [4].

For InP/InGaAsP semiconductors etching, a mixture of methane and hydrogen is generally used. The major drawback is the deposition of polymer within the reactor chamber and on the mask. Polymer can be removed by O₂ plasma cleaning after each etching run.

In Figure 4.21 we present a ridge waveguide etched by RIE on a hybrid sample, we used a platinum mask and we etched trough 0.3 μm InGaAs and 1.5 μm InP. On hybrid sample the etching rate, generally low for methane hydrogen RIE also on III-V wafers, decreases due to the insulating nature of the SOI substrate, as the process is longer we observe a lot of polymerization on top and on the

border of the mask. Polymers located on mask borders cover the underlying semiconductor, as they are deposited randomly they enhance the sidewalls roughness.

To reduce the impact of polymerization on sidewall roughness we alternate a CH₄ : H₂ plasma etching of 15 minutes with an oxygen plasma cleaning. In Figure 4.22 we show the etching profile achieved with this process, we observe a number of small steps in the InP etched sidewall, which have been generated during the etching due to polymers, cycle by cycle. The sidewalls roughness is much lower compared to Figure 4.21

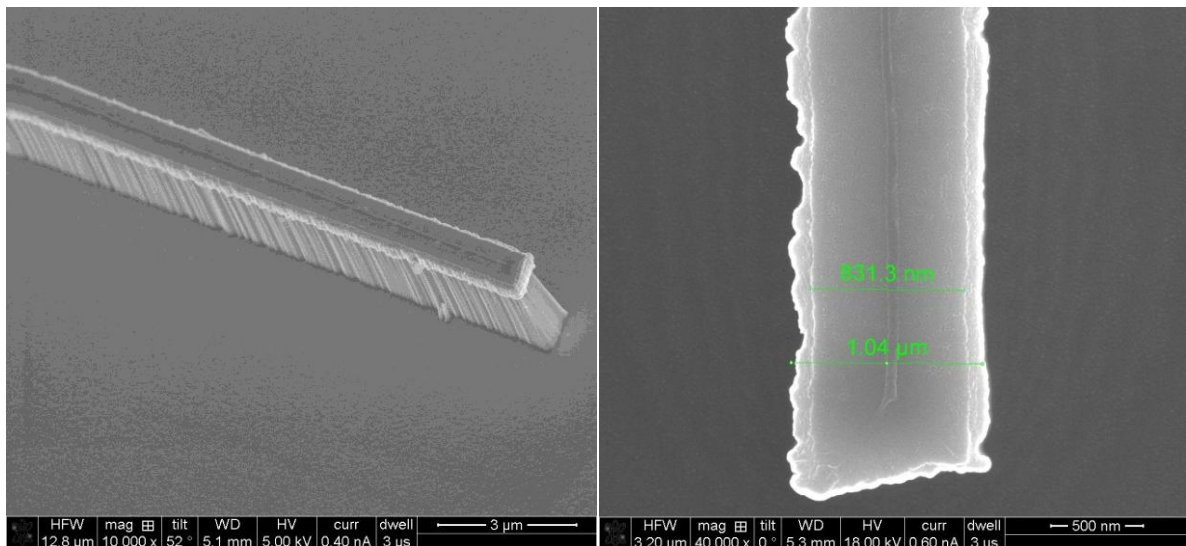


Figure 4.21: ridge waveguide etched by RIE etching

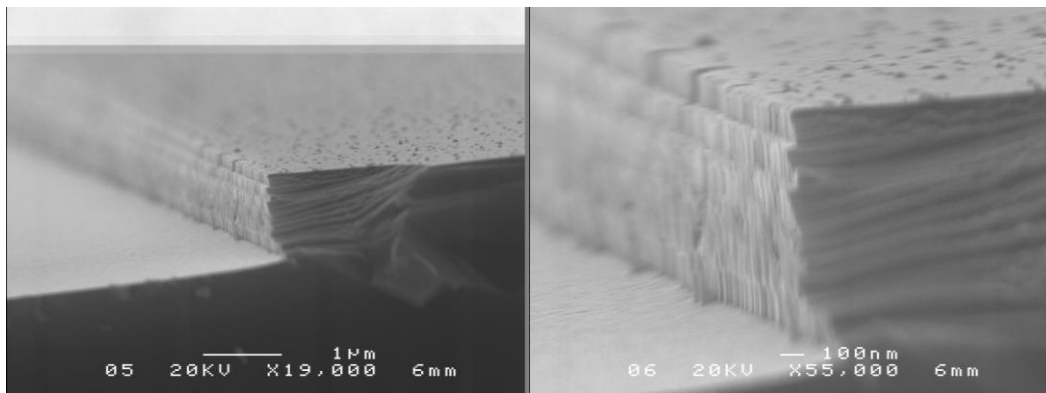


Figure 4.22: etching profile achieved by RIE CH₄:H₂ alternated with O₂ plasma

The second limit of RIE on hybrid sample comes from non-uniformity. The ion bombardment distribution on the sample changes due to the SOI insulating substrate. The etching rate is much faster on the border of the III-V stack than on the center, leading to a higher non-uniformity compared to standard III-V wafers with doped substrate. In Figure 4.23 we show an optical picture of a full III-V wafer bonded on SOI, after substrate removal there is a 2 μm thick InP/InGaAsP stack, we etch by RIE trough 1.5 μm of InP and 0.3 μm of InGaAsP, we stop the etching using a reflectometer to let just 200 nm of InP. The iridizations that we clearly see on the residual InP point out that the

etching has not been uniform. The large external circle in light blue is the residual trace of the bonded III-V wafer before etching, in this area the III-V is completely etched, in the internal blue/green circle we measure the desired InP thickness of 200 nm, in between those two areas the thickness linearly decreases from 200 nm to 0 nm. More than one half of the originally available surface has been lost due to the RIE process, we measured a non-uniformity of nearly 20%.

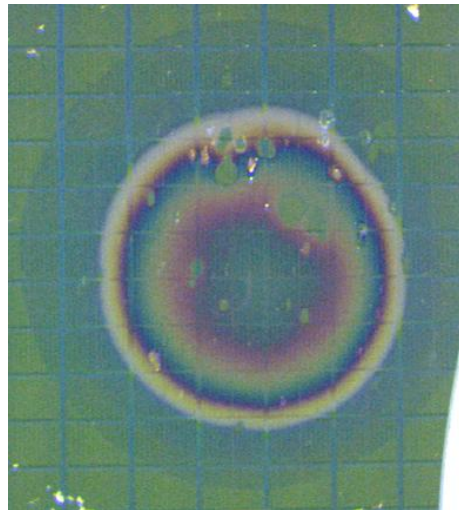


Figure 4.23: entire III-V 2 inches wafer bonded on SOI etched by RIE

The non-uniformity is proportional to the III-V area and to the etching time. Indeed RIE etching can be used for thin layer etching or for small bonded III-V dies, but it is not adapted to large III-V areas or thick layer etching, especially if we need to precisely stop the etching at a defined depth.

4.4.2.2 *Ion Beam Etching*

Ion Beam Etching (IBE) is extensively used to etch metals, oxides and semiconductors [5]. In this method, a plasma is generated in a separate source. This plasma source can be a conventional RF discharge of the type discussed previously. Ions generated in the plasma are accelerated from the source to the substrate to be etched through a set of dc-biased extraction grids. The voltage difference between the substrate and the last extraction grid determines the bombardment energy. [3]

Resists are commonly used as masks for IBE as the etching rate is lower for these materials. Ion Beam Etching introduces a large surface roughness; this is the reason why it is generally followed by a wet etching to flatten the semiconductor surface. In Figure 4.24 we present a taper tip etched by IBE on a hybrid sample, we deposit 50nm of titanium and 75nm of platinum, we define the resist mask by 248nm UV lithography. After 4' etching at 500eV, we etch through the metal layer and we stop inside InGaAs layer. We can observe the large surface roughness generated by IBE.

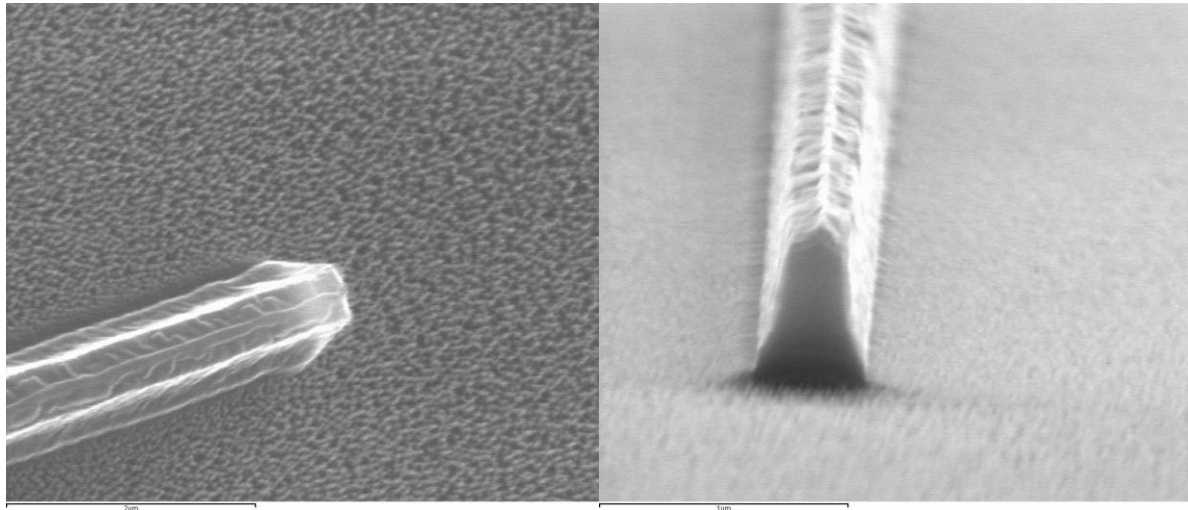


Figure 4.24: taper tip defined by 248nm lithography after 4' IBE etching

In Figure 4.25 the same epitaxial structure is etched for 10'. This time we etch trough the metals and trough the InGaAs layers, we stop inside InP layer. After the IBE we perform a 1 HCl / 3 H₃PO₄ wet etching to etch trough InP and selectively stop on top of the MQW stack. The process works properly, sidewalls are smooth and taper tips are well defined, anyway we observe a strange kind of deposit all over the surface. We performed several trials trying to clean the sample surface (oxygen plasma, solvents, and diluted etching solutions) but we did not succeed. To understand the physical origin of this contamination we carried out an Auger Scanning Electron Microscopy measurement (Figure 4.26). We found a small amount of platinum in the deposit. It was impossible to exactly establish the concentration of platinum just with this measurement, but we conclude that the contamination came from metal redeposit during the IBE.

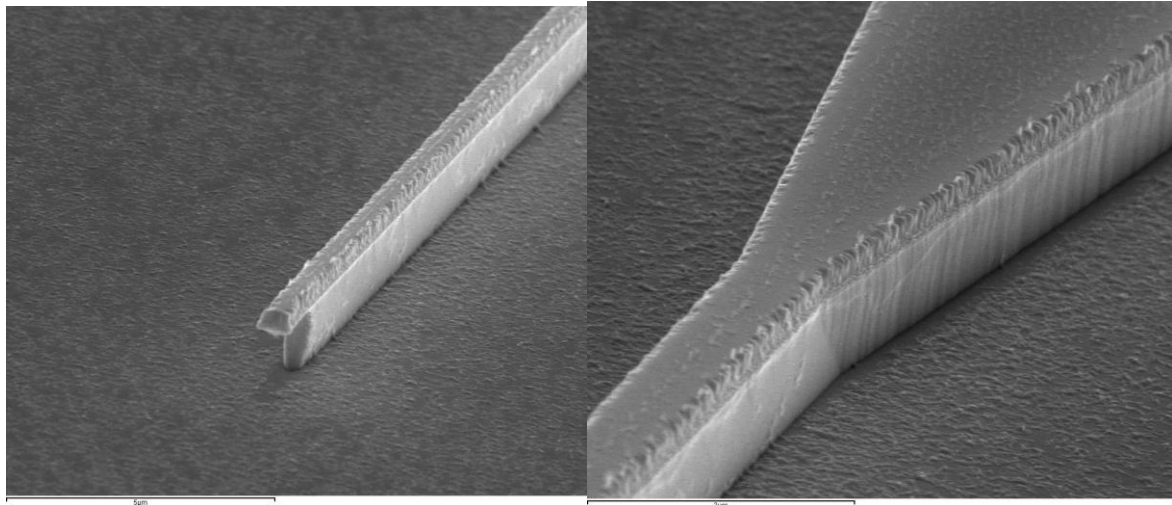


Figure 4.25: taper defined by 248nm lithography after 10' IBE etching and subsequent 1 HCl / 3 H₃PO₄ wet etch of the InP

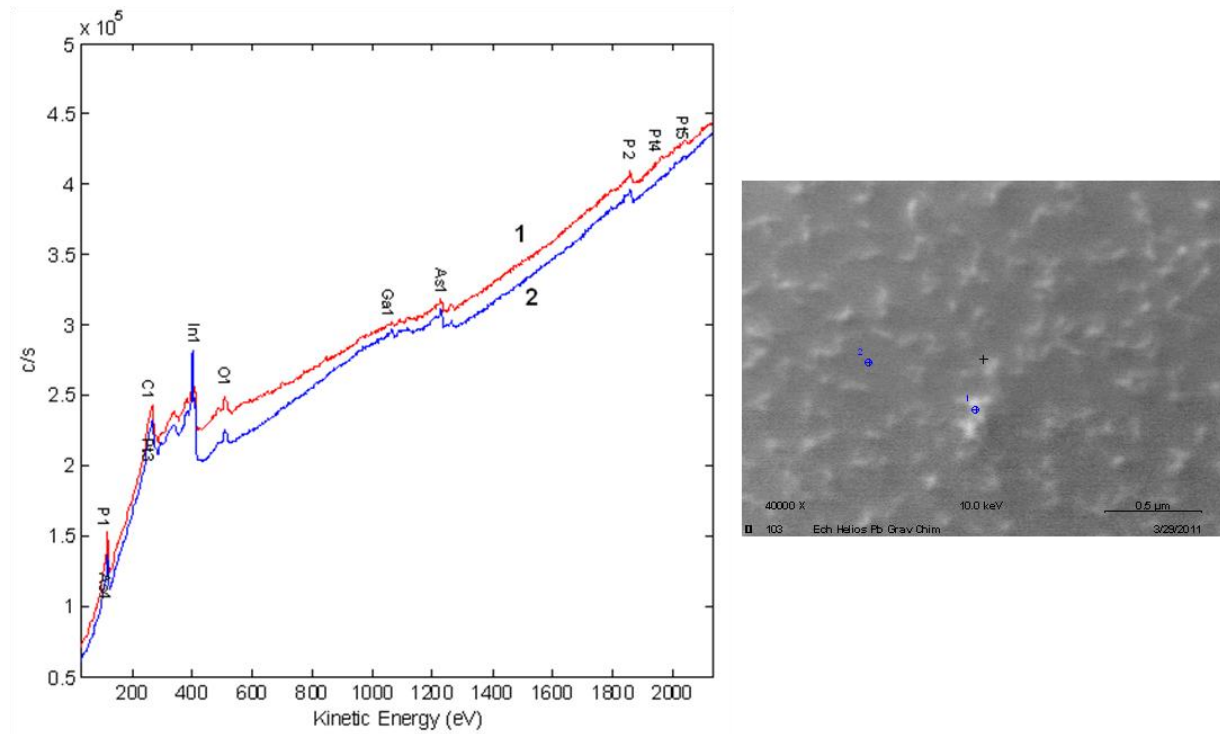


Figure 4.26: Auger SEM analysis of the Figure 4.25 deposit

Trying to eliminate the contamination deposit we slightly modify the IBE process. If the deposit come from re-deposit of platinum on Indium Phosphate, stopping the etch before to enter in the InP layer we should eliminate the contamination. Indeed we stop the etch on the InGaAs layer, then we complete the InGaAs etch by wet etching ($3\text{ H}_3\text{PO}_4 / 1\text{ H}_2\text{O}_2 / 80\text{ H}_2\text{O}$). Subsequently we etch trough the thin InGaAsP layer by a fast RIE and we etch the p-InP layer by wet etching ($1\text{ HCl} / 3\text{ H}_3\text{PO}_4$). We can observe in Figure 4.27 the etching profiles achieved with this process. We do not observe any contamination on the surface, sidewalls are smooth, the tips are well defined and present only a small undercut coming from InP wet etch.

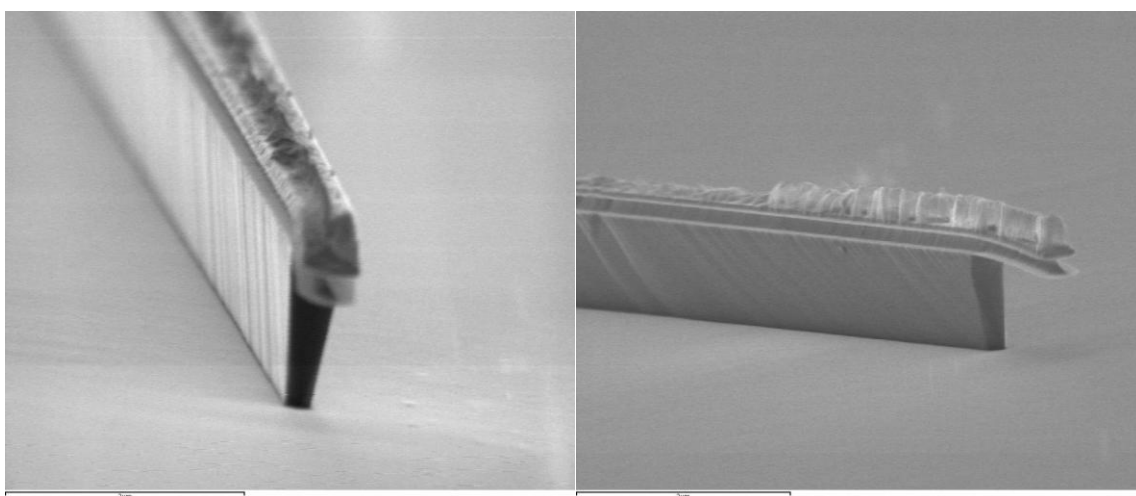


Figure 4.27: tapers etched by: IBE, InGaAs wet etch, InGaAsP RIE, InP wet etch

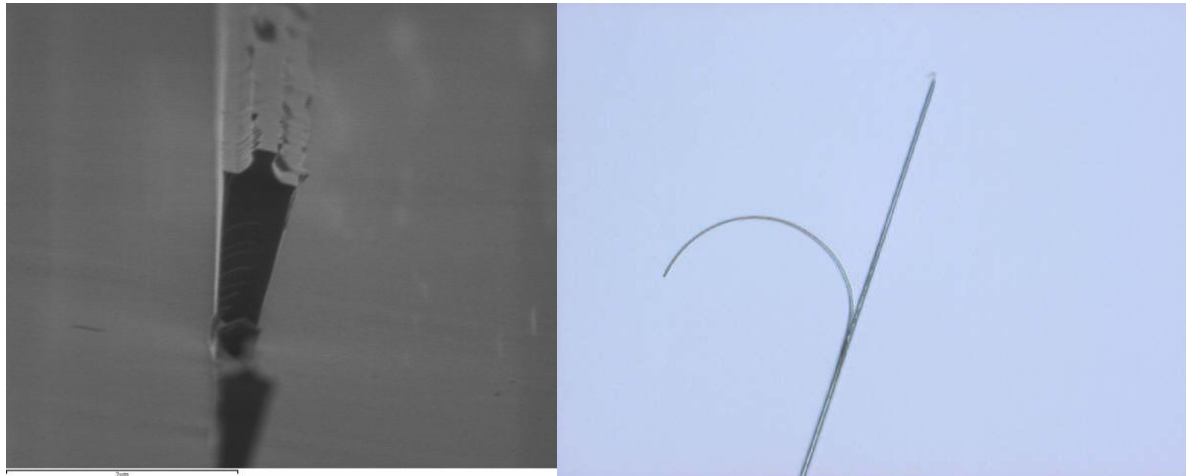


Figure 4.28: small feature defined by Figure 4.27 process, the metal lifts because the InGaAs undercut is too big

This process presents anyway a serious drawback. As we etch the InGaAs layer by wet etching with an isotropic solution, it is almost impossible to define small size feature in a repeatable way. If in Figure 4.27 the 400nm tip is well defined also if we can observe a small undercut in the InGaAs layer, in Figure 4.28, for the same process applied to another sample, we notice that the metal lifts from the semiconductor as the undercut is too big.

4.4.2.3 Inductively Coupled Plasma

Inductively Coupled Plasma (ICP) etching system can produce high density plasmas, which can be used to etch all kinds of semiconductors materials, such as indium phosphate, silicon, silicon-dioxide, silicon-nitride, etc. The plasma is contained inside a chamber that is surrounded by an inductive coil. The RF coils located in front of the RF transducer induce an alternating magnetic field, and this helps to produce high-density plasma due to confinement of electrons. It can therefore manufacture nano-scaled structures with high height-to-width ratio. [6]

In Figure 4.29 we present a taper tip etched by ICP etching on a hybrid substrate, we deposit 50 nm of titanium and a silicon oxide hard mask of 250 nm, the structure pattern is defined by means of a 248 nm lithography followed by hard mask etching and photoresist stripping. After 10' etching, we etch trough the titanium layer, InGaAs and InGaAsP layers, to stop inside InP layer for a total etching depth of 1.7 μm .

The surface is clean without visible roughness, however sidewalls are quite rough. The etching is perfectly homogeneous on the all sample. Caution is needed for SOI regions that are not covered by III-V material; the ICP etches trough silica and silicon, indeed uncovered silicon based devices or waveguides risk to be destroyed by this process if not correctly protected with a mask.

In Figure 4.30 we show the same structure after 1 HCl / 3 H_3PO_4 wet etch of the remaining InP. Sidewalls look smoother compared to the previous solution.

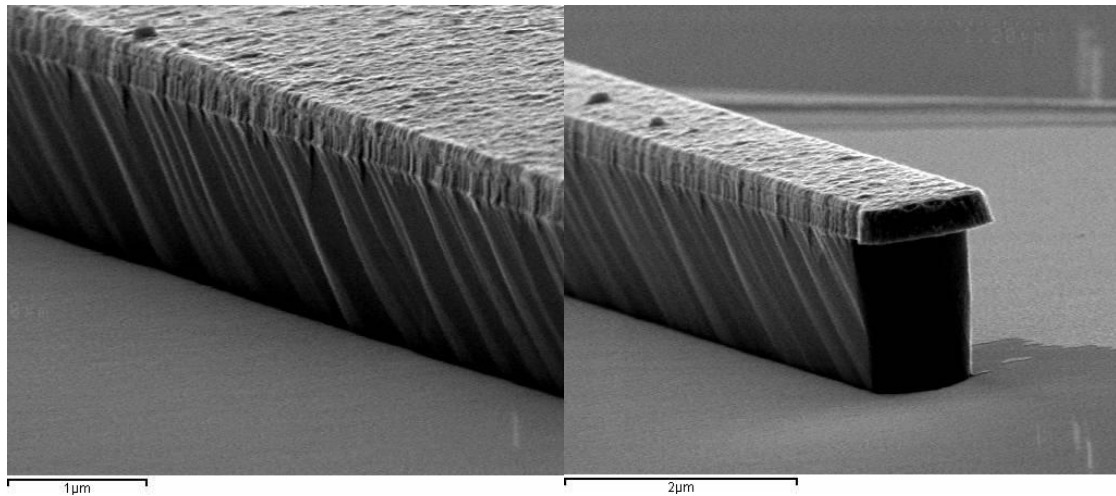


Figure 4.29: SEM images of an ICP etched taper tip

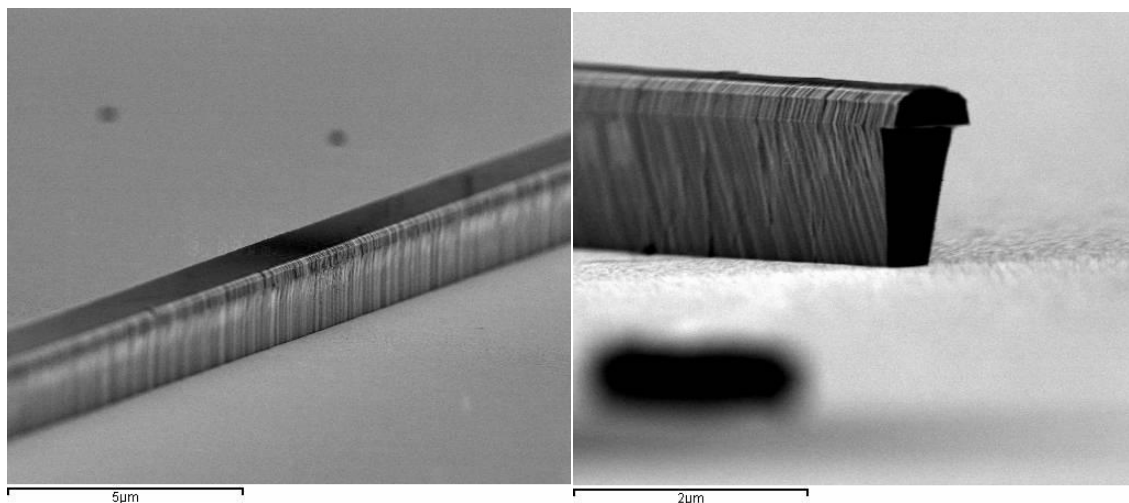


Figure 4.30: SEM images of a taper tip etched by ICP etching + 1 HCl / 3 H₃PO₄ wet etch of the InP

4.4.3 Conclusions

	Sidewall roughness	Under etch	Uniformity	Precise stop	Considerations
$3\text{H}_3\text{PO}_4 : 1\text{H}_2\text{O}_2 : 80\text{ H}_2\text{O}$	Good	Almost as fast as etching	High	$\pm 0\text{ nm}$	Selective for InGaAs, under etch not compatible with taper tip
$3\text{H}_3\text{PO}_4 : 1\text{ HCl}$	Dependent on mask roughness	None	High	$\pm 0\text{ nm}$	Selective for InP, no under etch
RIE	Bad due to polymerization	None	Extremely low	$\pm 20\text{ nm}$	Low uniformity and polymerization on long etching, precise etch stop
IBE	Bad	None	High	$\pm 100\text{ nm}$	Contaminations coming from metal mask etching hard to remove
ICP	Acceptable	None	High	$\pm 100\text{ nm}$	Uniform, quite smooth sidewalls, not precise etching stop

Table 4.2: etching techniques comparison

Table 4.2 presents a comparison of the different etching techniques studied during my thesis. Every technique presents advantages and drawbacks and only a combination of several of them permits to reach an optimized process. Finally we decide to do not use IBE, as we were unable to efficiently solve the contamination issue described in 4.4.2.2. We decide as well to do not use $3\text{H}_3\text{PO}_4 : 1\text{H}_2\text{O}_2 : 80\text{H}_2\text{O}$ solution as the under etch was not compatible with the thin taper tip fabrication. We go for a three step etching process. We used ICP to etch through the InGaAs and the InP-p layers, stopping the etching inside the InP-p layer. We finish the etching of the p doped InP by the selective $3\text{H}_3\text{PO}_4 : 1\text{HCl}$ wet etching. Thanks to the combination of these two steps we obtain a uniform, smooth etching that stopped on top of the MQW layer. Afterwards we deposite a hard mask and we etch through the MQW layer by RIE. As the MQW layer is thinner than 300 nm the RIE process inhomogeneity is $\pm 30\text{ nm}$, compatible with a precise stop on top of the InP n doped layer. Moreover, as this last etching step is short (a few minutes), we do not have an extremely high polymerization and the sidewalls are quite smooth. SEM picture of device etched following this process are showed in Figure 4.31.

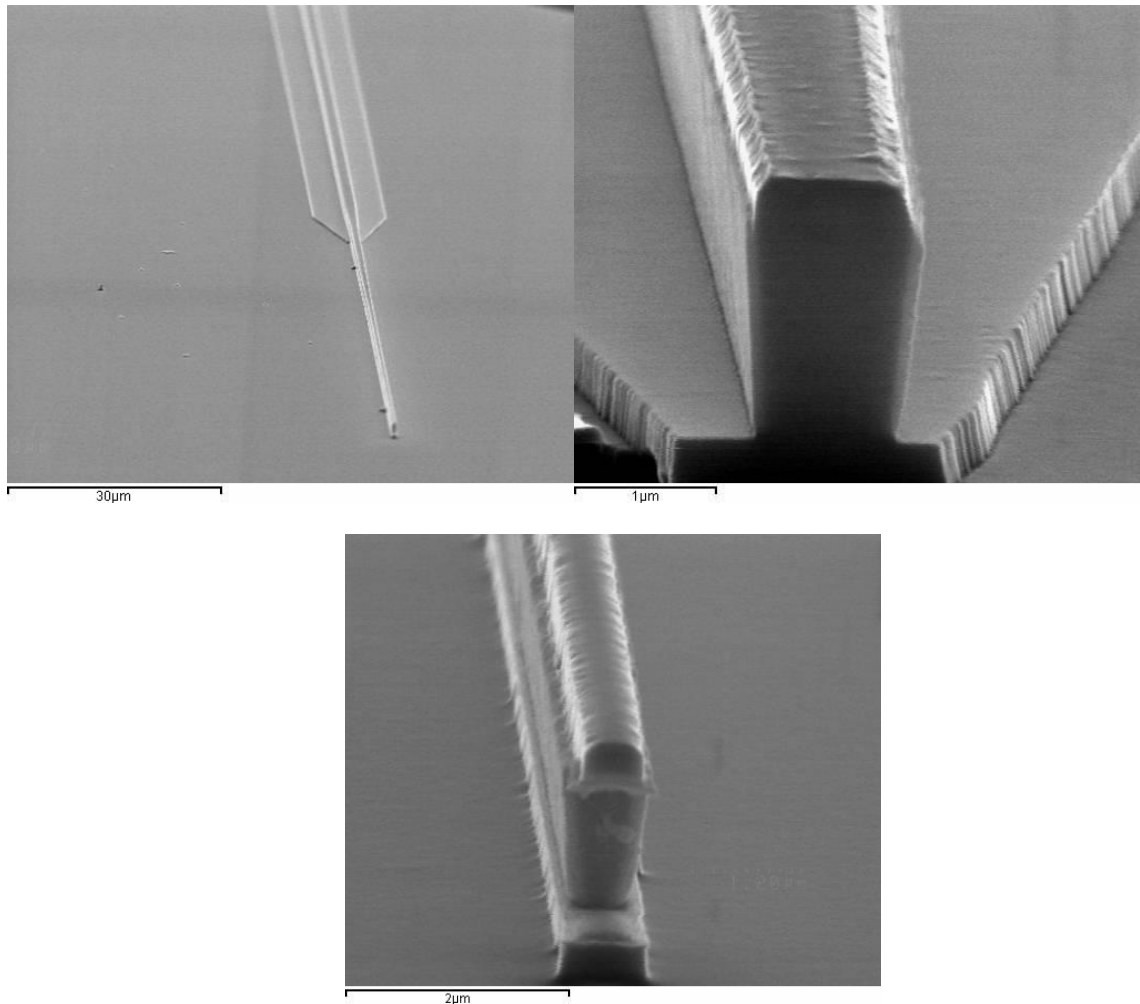


Figure 4.31: SEM images of a laser III-V taper realized with the optimized process

4.5 Metallization and annealing

Fabrication of high-quality ohmic contacts is essential for opto-electronics devices and, more specifically, for lasers. Low resistivity ohmic contacts are necessary to achieve high-speed operation and restriction of device heating effects. Due to the complicated nature of intermixed metallization and semiconductor materials, it is hard to understand all physical and chemical phenomena involved in metal-semiconductor interfaces. Ohmic contacts are basically Schottky barriers, through which a majority of the carriers can tunnel because of the narrow barrier width, enhanced by high dopant concentration in the interface region. These interfaces are characterized by very low Schottky barriers height, which is reflected in almost a linear relationship between the measured current and the voltage applied across the contact. The quality of the ohmic contact is frequently described in terms of contact resistivity ($\Omega \cdot \text{mm}$) or specific contact resistance ($\Omega \cdot \text{cm}^2$). [7]

To achieve metal-semiconductor contacts with ohmic characteristics and low contact resistance we can play on three factors: the dopants concentration of the semiconductor layer where the metal is deposited (a priori we want it to be as high as possible), the selected metals deposited on the semiconductor layer, the heat treatments carried out on the sample.

This problem has been extensively treated for III-V semiconductor devices, and for both n and p contacts the best solutions have been identified [8] [9]. For InP based semiconductors an highly doped InGaAs layer is used p side with Pt/Au and Ti/Pt/Au annealed alloys; n side Ti/Pt/Au alloys are generally employed. What does change with silicon photonics?

The long term goal of silicon photonics is the compatibility with CMOS technology to achieve VLSI. Gold is a forbidden material in most CMOS foundries as it can easily diffuse inside silicon and behave like a dopant. This is the reason why, in recent years, a few works have tried to find a gold free CMOS compatible metallization for InP based devices [10]. The results are encouraging but still far from gold based contact performances. We decided indeed to use classic metal alloys for this work to ensure better performances. We analyse traditionally used Ti/Pt/Au, Pt/Au alloys and we compared their performances with a Transmission Line Model (TLM) before and after rapid thermal annealing (RTA). For the p contact an InGaAs highly doped layer (10^{19} - 10^{20} cm $^{-3}$) has been used as a cap layer on top of InP. InGaAs offers the possibility of decreasing both the barrier height and width and it is typically used to achieve ohmic contacts on p-InP [7]. The results of our measurements are given in Table 4.3.

Metals have been deposited by Double Ion Beam Sputtering (DIBS), before metal deposition a low energy ion beam etching has been performed on semiconductor surface to remove surface oxide.

In a ridge laser the p contact surface will be equivalent to the ridge surface. For a standard InP based laser it will roughly be of 1000 μm 2 . Following this example, to have less than 1 Ω series resistance from p metallization we would need a specific contact resistance lower than $1 \cdot 10^{-5}$ Ω·cm 2 . Such a value is achievable only employing a RTA. But RTA presents a major drawback on bonded samples; a high temperature annealing can multiply the defects amount. This problem is particularly important on molecular bonded samples, while DVS-BCB bonded samples seem to be more resistant against annealing treatments. It is impossible anyway to obtain a quantitative analysis of bonded sample robustness to RTA for the moment. Different sample behaves differently as bonding techniques are still not repeatable. Figure 4.32 shows optical pictures of hybrid lasers on a molecular bonded sample after different kinds of RTAs. The defects number and dimension increase with higher temperatures and decrease for slower RTA.

	Ti/Pt/Au	Pt/Au
InGaAs p-doped ($3 \cdot 10^{19}$ cm $^{-3}$)	$5 \cdot 10^{-4}$ Ω·cm 2	$6 \cdot 10^{-4}$ Ω·cm 2
InGaAs p-doped ($3 \cdot 10^{19}$ cm $^{-3}$) RTA 320°C	$1 \cdot 10^{-5}$ Ω·cm 2	$1 \cdot 10^{-5}$ Ω·cm 2
InGaAs p-doped ($3 \cdot 10^{19}$ cm $^{-3}$) RTA 420°C	$4 \cdot 10^{-7}$ Ω·cm 2	$3 \cdot 10^{-7}$ Ω·cm 2
InP n-doped ($5 \cdot 10^{18}$ cm $^{-3}$)	$2 \cdot 10^{-6}$ Ω·cm 2	$3 \cdot 10^{-6}$ Ω·cm 2
InP n-doped ($5 \cdot 10^{18}$ cm $^{-3}$) RTA 420°C	$3 \cdot 10^{-4}$ Ω·cm 2	

Table 4.3: Contact resistances from different metal-semiconductor interfaces measured by TLM

The problem is unsolved for the moment. However a slow annealing process has shown to decrease the number of defects with an acceptable increase in the contact resistance. Two possibilities for future improvement can be identified. From the one hand the bonding quality can be improved, from

the other hand the use of a tunnel junction on the p-side can be considered. Using a tunnel junction we will have, both on the p and on the n side, an electrical contact between a metal and an n-doped semiconductor. As the n contact does not need a RTA, we would solve the problem.

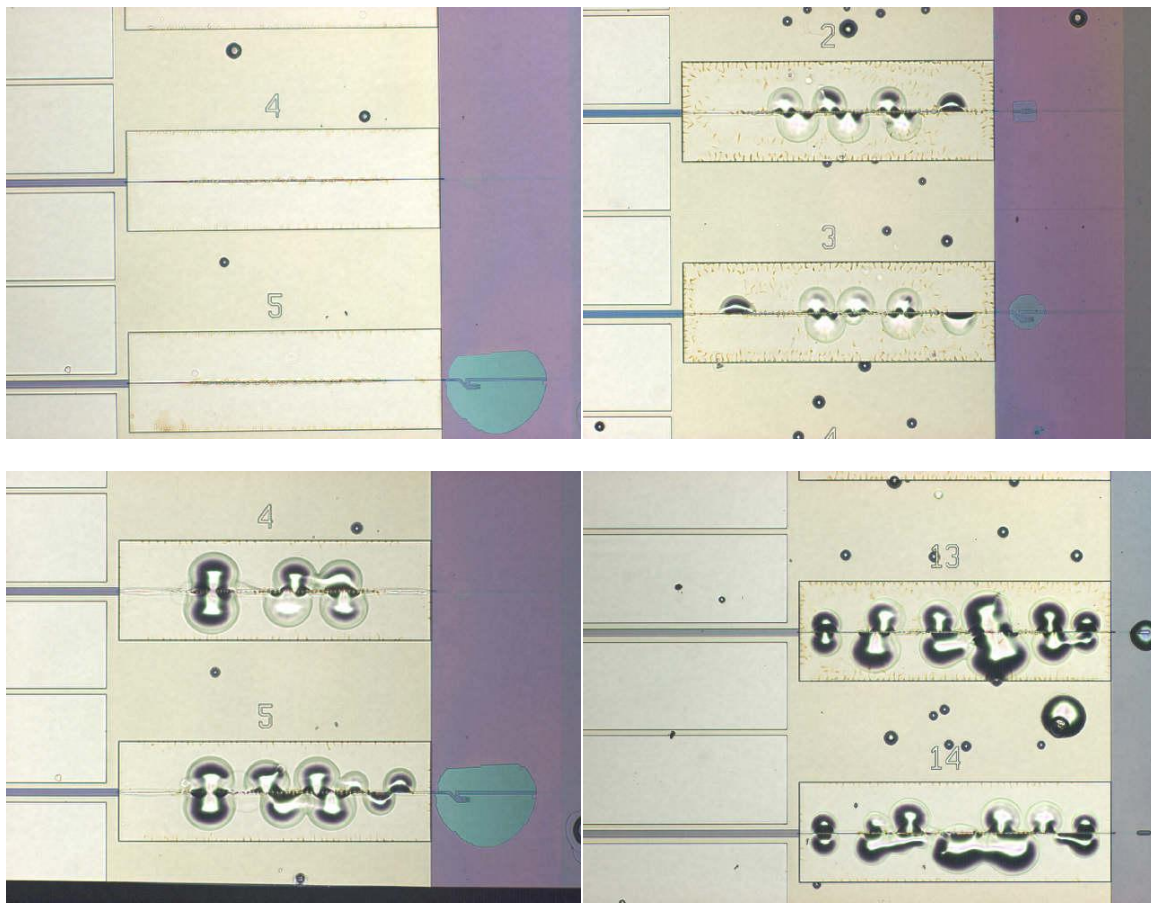


Figure 4.32: optical image of hybrid III-V on SOI laser based on molecular bonding: (a) before RTA; (b) after 350°C 90'' RTA; (c) after 400°C 60'' RTA; (d) after 400°C 30'' RTA

4.6 Conclusions – Final identified process steps

In this chapter we described the fundamental technological steps of III-V on SOI hybrid lasers fabrication. We introduced the SOI waveguides fabrication and the bonding techniques employed in this work, then we analysed more in details the issues related to III-V semiconductors manufacturing on hybrid samples. The hybrid nature of the sample introduces a number of difficulties related to lithography, etching, metallization, etc. We proposed and tested different ways to solve these problems and we finally converge to an optimized process for the fabrication of our devices.

The technological process that we finally identified and used for the devices presented in this work is summarized in Figure 4.33. We first deposit a 50 nm titanium layer and a silica hard mask; we perform 248 nm UV lithography to define the III-V ridge waveguide, then we etch through the silica by CHF₃ RIE. We used the silica mask to etch through the titanium and the InGaAs layer by ICP, stopping the etching inside the p doped InP layer.

Fabrication process

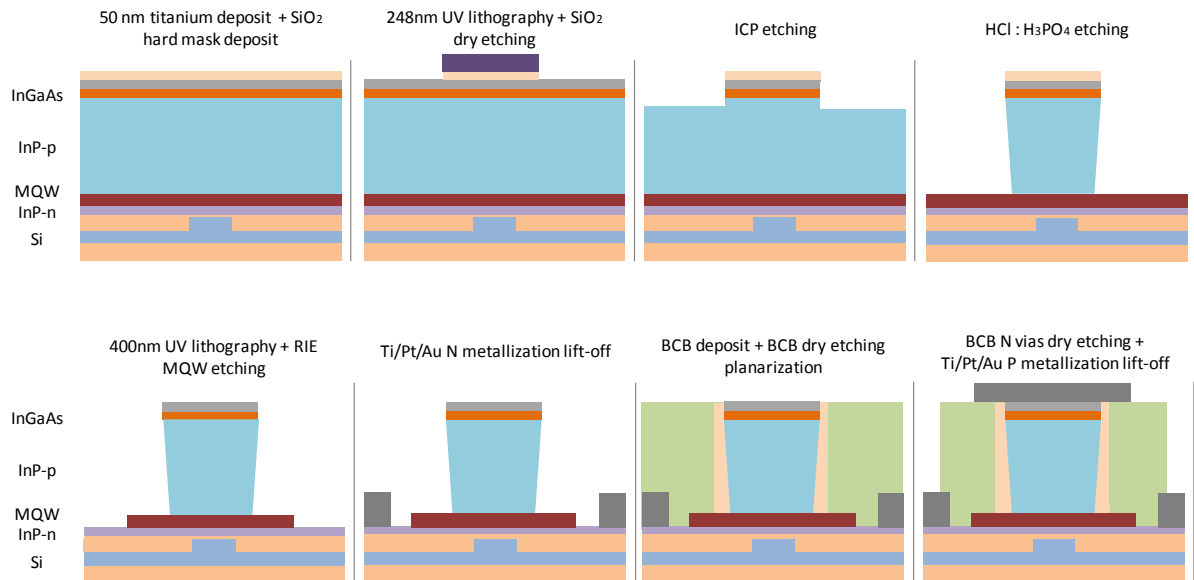


Figure 4.33: Overview of the hybrid laser process

We finish the etching of the InP by chemical selective etching that stops on top of the MQW layer. Subsequently we define the MQW etching mask and we etch by CH₄ : H₂ RIE, we stop the etching on top of the n doped InP layer. We deposit a thick Ti/Pt/Au n metallization by lift-off. We spin-coat a thick BCB layer then we etch it to the top of the titanium layer by RIE. We open vias in the BCB to reach the n contact, then we deposite a thick Ti/Pt/Au p metallization by lift-off and we perform a RTA. Finally the SOI is thinned down to 150 µm and diced.

4.7 Bibliography

- [1] G. Roelkens, J. Brouckaert, D. V. Thourhout, R. Baets, R. Notzel and M. Smit, "Adhesive Bonding of InP/InGaAsP Dies to Processed Silicon-On-Insulator Wafers using DVS-bis-Benzocyclobutene," *J. Electrochem. Soc.*, vol. 153, 2006.
- [2] N. Matine, M. Dvorak, J. Pelouard, F. Pardo and C. Bolognesi, "InP in HBTs by vertical and lateral wet etching," in *1998 International Conference on Indium Phosphide and Related Materials*.
- [3] A. v. Roosmalen, J. A. G. Baggerman and S. J. H. Brader, Dry Etching for VLSI, Plenum Press, 1991.
- [4] P. H. Holloway and G. E. McGuire, Handbook of compound semiconductors, Noyes Publications, 1995.
- [5] P. G. Gloersen, "Ion-beam etching," *Journal of Vacuum Science and Technology*, vol. 12, no. 1, 1975.
- [6] F. Pommereau, L. Legouezigou, S. Hubert, S. Sainson, J.-P. Chandouineau, S. Fabre, G.-H. Duan, B. Lombardet, R. Ferrini and R. Houdre, "Fabrication of low loss two-dimensional InP photonic crystals by inductively coupled plasma etching," *Journal of Applied Physics*, vol. 95, no. 5, 2004.
- [7] A. Katz, Indium Phosphide and related materials: processing, technology, and devices, Norwood: Artech House, 1992.
- [8] W. C. Dautremont-Smith, P. A. Barnes and J. W. Stayt, "A nonalloyed, low specific resistance Ohmic contact to n-InP," *Journal of Vacuum Science & Technology*, vol. 2, no. 4, 1984.
- [9] G. Stareev and A. Umbach, "A reliable fabrication technique for very low resistance ohmic contacts to p-InGaAs using low energy Ar+ ion beam sputtering," *Journal of Electronic Materials*, vol. 20, no. 12, 1991.
- [10] L. Grenouillet, A. Bavencove, T. Dupont, J. Harduin, P. Philippe, P. Regreny, F. Lelarge, K. Gilbert, P. Grosse and J. Fedeli, "CMOS compatible contacts and etching for InP-on-silicon active devices," *Group IV Photonics*, 2009.

5 EXPERIMENTAL RESULTS

In this chapter we present the measurement setups, the measurement results and some analysis on the achieved results on the fabricated devices. All the characterized devices have a coupling section based on the double adiabatic taper design. We compare deep ridge and shallow/deep ridge Fabry-Perot lasers, analyzing both molecular bonded and DVS-BCB bonded devices. We present also the first measurement of a single mode ring resonator mirrors based device. The other designs presented in section 2 and 3 are currently under fabrication.

5.1 Measurements setups

Figure 5.1(a) shows the measurement setup for electro-optical measurements, the lasers array (blue) is mounted on a temperature controller set (green) to determine the performances of our lasers for different temperatures. The laser output is collected by a lensed fiber (pink) located in front of the cleaved facet to measure the optical spectrum. Electrical probes are used to realize an electrical contact with p and n electrodes (yellow). A photodiode has replaced the lensed fiber to measure the optical output power without coupling losses.

Figure 5.1(b) shows a typical component under measurement. In blue we see the active waveguide surrounded by the n contact in green and the p contact in red. The violet stripe indicates the cleaved facet of the SOI while the lensed fiber is in orange color.

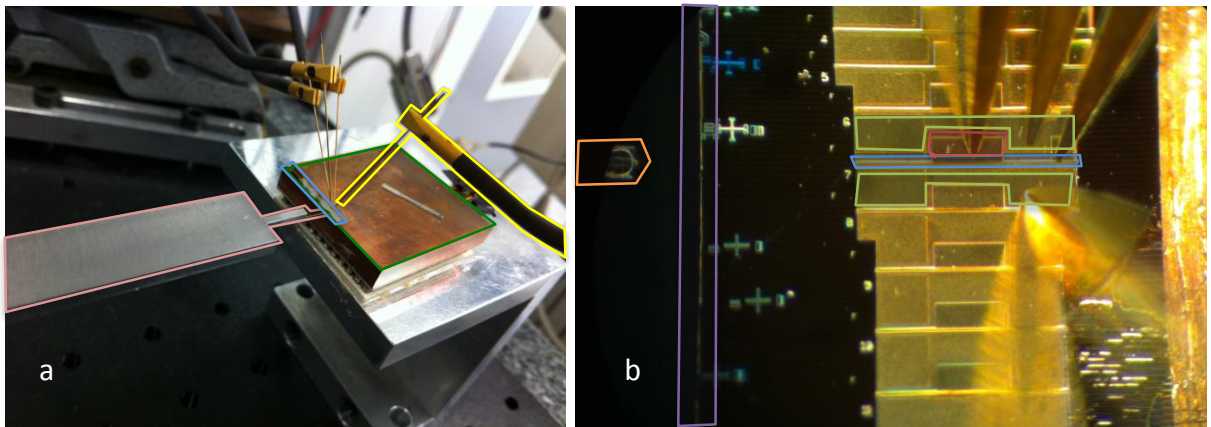


Figure 5.1: (a) measurement setup for electro-optical measurement, (b) optical microscope top view of a laser under measurement

5.2 Fabry-Perot hybrid lasers by DVS-BCB bonding

Fabry-Perot laser based on DVS-BCB bonding have been fabricated both in deep-ridge and in shallow/deep-ridge configurations. In this section we present and compare the best performances we achieved for these designs. These two designs have been fabricated in separate fabrication runs, for this reason it is difficult to have a fully fair comparison according to the possible process variations between two runs. However we can observe macroscopic performance differences that cannot be explained only by fabrication reasons.

5.2.1 Deep ridge design

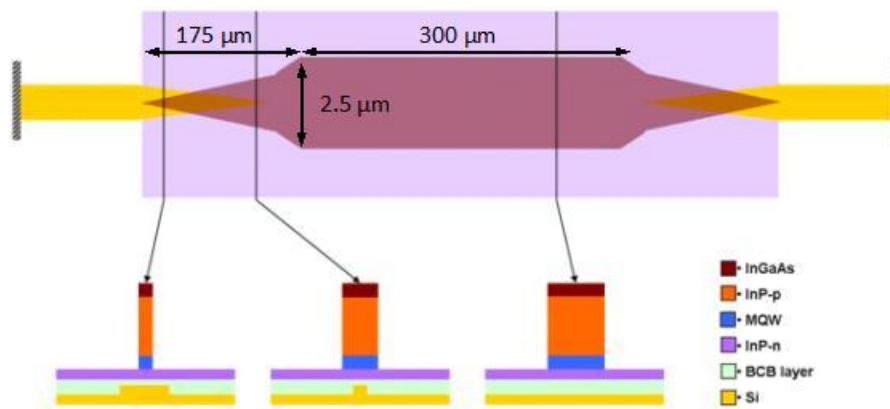


Figure 5.2: schematic design of the deep ridge hybrid III-V on SOI laser

In Figure 5.2 we detail the design of the fabricated laser. The device is mounted on a temperature controlled stage set adjusted at 20°C. The output laser beam is collected by a lensed fiber coupled to the silicon waveguide cleaved facet. The coupling losses are estimated to be higher than 8dB. The emission light intensity – current (L-I) curve is shown on Figure 5.3(a). The laser is electrically pulse-pumped up to 200 mA, with a pulse period and width of 10 μ s and 180 ns. The device has a lasing threshold of 45 mA and a maximum fiber coupled power of 0.75 mW at both sides. The series resistance is 12 Ohms.

The lasing spectrum is shown on Figure 5.3(b). A single wavelength operation regime is observed, due to parasite reflections at the ends of the InP taper tips. In fact, the taper tips have a width of around 0.8 μ m, much larger than the optimum value found by simulations. Therefore several percent of the power that is not coupled into the silicon waveguide is back reflected to the III-V waveguide, generating a multiple cavity effect. Moreover, the coupling efficiency between InP and silicon waveguides is strongly reduced, leading to a lower power efficiency of the fabricated devices. In Figure 5.4 we show an optical image of the measured device.

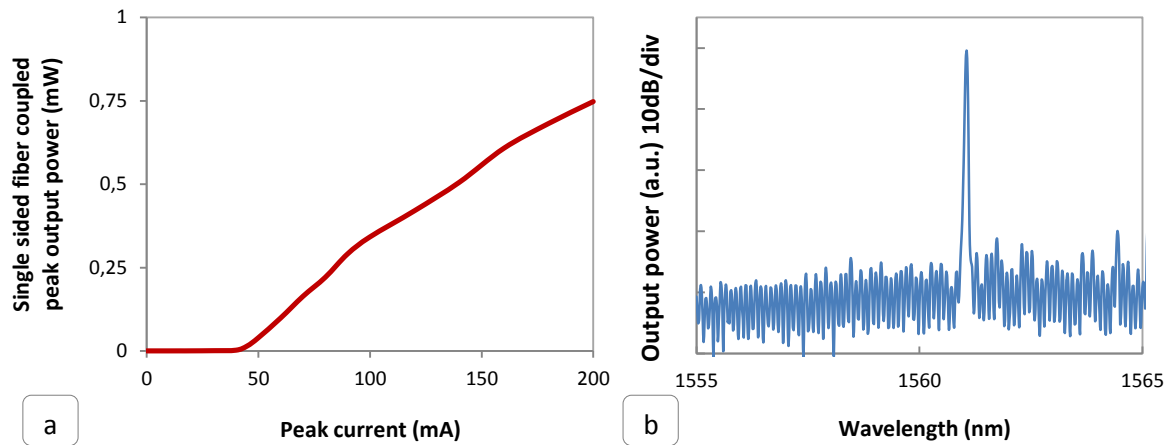


Figure 5.3: (a) fiber coupled laser power as a function of drive current (L-I curve) under pulsed operation at 20°C, (b) optical spectrum of the laser driven at 55 mA

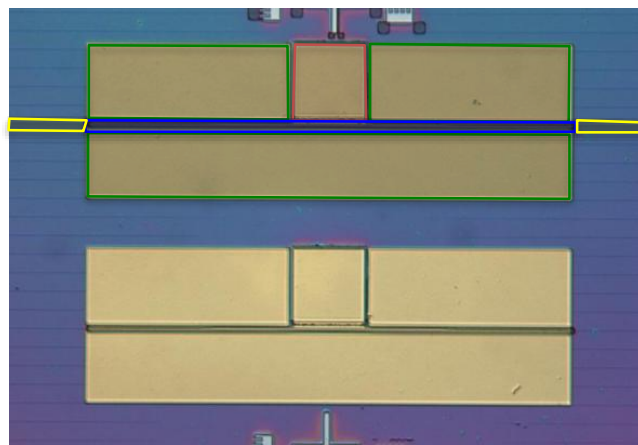


Figure 5.4: optical microscope top view of two Fabry-Perot hybrid laser with a deep ridge design, in blue the active waveguide, in yellow the silicon waveguide, in red and green the p and n contact respectively

5.2.2 Shallow/deep ridge design

The design of the measured laser is schematically shown in Figure 5.5. The L-I and V-I curves are presented in Figure 5.6. The output laser beam is collected by a photodiode located in front of the output facet. The length and the width of the straight III-V waveguide section are respectively of 490 μm and 1.7 μm . The coupling section length is 230 μm . The overall cavity length is 1700 μm , including the passive silicon waveguide. The device has a threshold current of 30 mA and a maximum single facet continuous wave output power of 4.5 mW at 20°C. In continuous wave regime at 60°C the laser still exhibits an output power of more than 1 mW. The series resistance is 5 Ohms, while the slope efficiency is 0.045 W/A. Based on these results we extract a characteristic temperature T_0 for the threshold of 69K and a characteristic temperature T_1 for the external efficiency of 94K. The kinks in the L-I characteristics are due to the jumps of the dominant lasing mode.

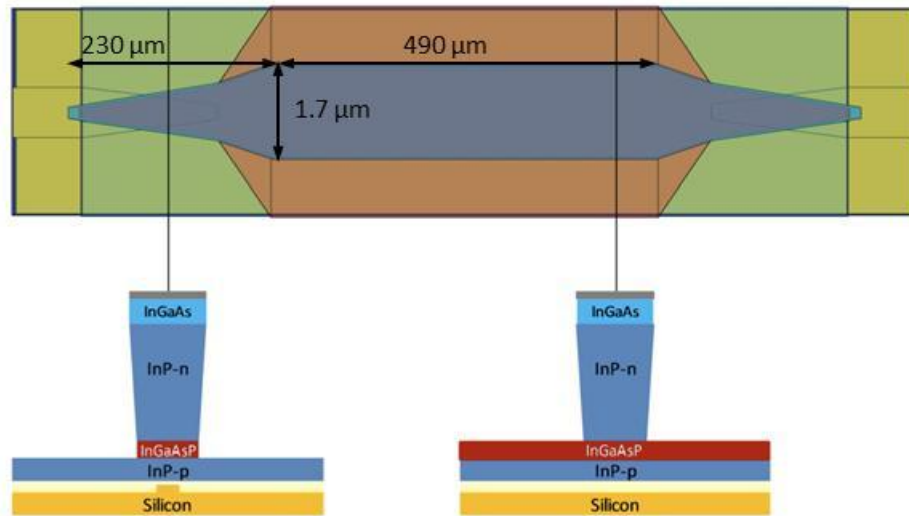


Figure 5.5: schematic design of the shallow/deep ridge hybrid III-V on SOI laser

Figure 5.7 shows the optical spectrum for an injection current of 100 mA. One can see the Fabry-Perot modes of the laser cavity. However, some perturbations are observed on the emission spectrum, due to parasitic reflections created by the taper tip. Considering the III-V tip width of 0.8 μm in our case, we estimate that the coupling efficiency between the III-V and silicon waveguides is between 70 and 80% and the power reflection coefficient due to the taper is around 3%. Such small fraction of power is sufficient to perturb the spectrum.

The performance of this device represents a big step forward compared to deep ridge design laser. Not only we achieved laser action in continuous regime up to 60°C, but we also measured the lower threshold (30 mA) ever measured for this kind of Fabry-Pérot lasers. It is clear that the shallow etched waveguide greatly reduce the optical and electrical losses coming from the straight section, allowing a much lower threshold. The low series resistance achieved in this fabrication run, allowing a lower power dissipation coming from the diode, has also an impact, especially concerning the high temperature CW behavior.

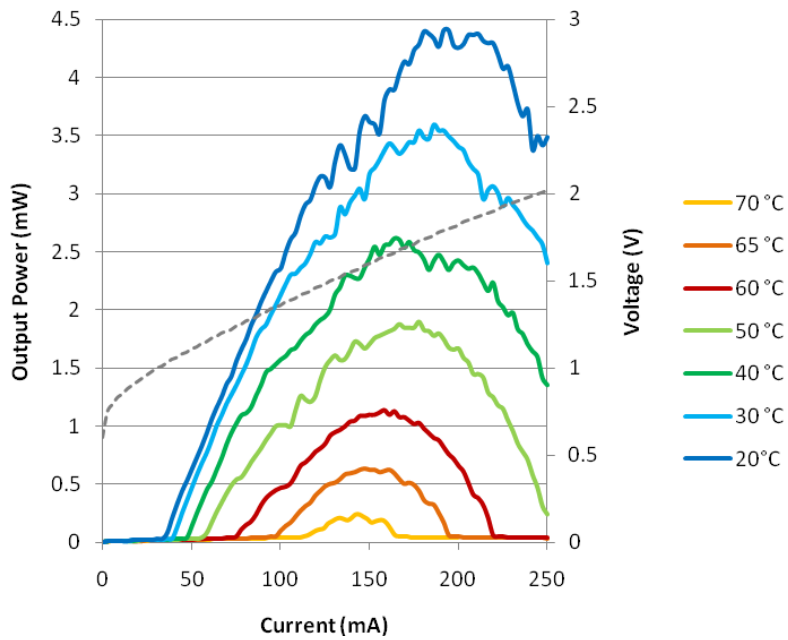


Figure 5.6: Continuous wave single facet laser power as a function of drive current at different stage temperatures and the (dotted) I-V curve of the laser.

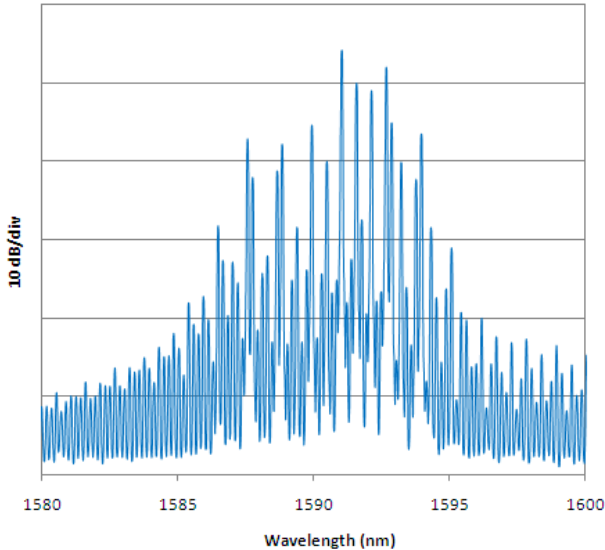


Figure 5.7: Lasing spectrum of the hybrid laser

5.2.3 Current threshold and slope efficiency simulations

To better understand the achieved results, we perform a series of analytical simulation to have a deeper idea on the impact of taper coupling efficiency on laser performances. In Figure 5.8 and Figure 5.9 we present the simulated values of threshold current and slope efficiency for the laser design described on Figure 5.5. Simulations have been performed for several values of internal cavity losses ranging from 0 to 100 cm^{-1} . The black line shows the achieved value for the fabricated device.

We can estimate an internal losses value between 10 and 25 cm^{-1} in our devices excluding the taper couplers. For these values of internal losses we find a good agreement between simulated and measured values, considering a taper efficiency between 70 and 80%.

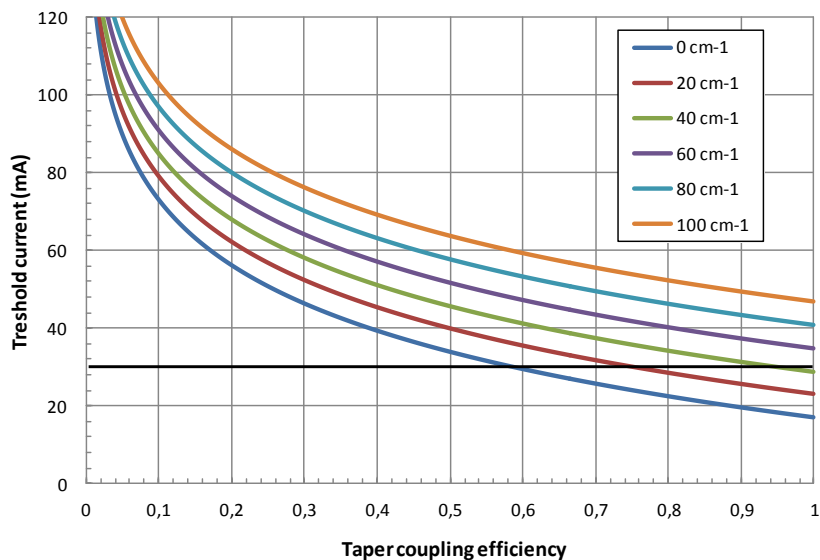


Figure 5.8: simulated hybrid laser threshold current as a function of the taper coupling efficiency for different values of internal losses

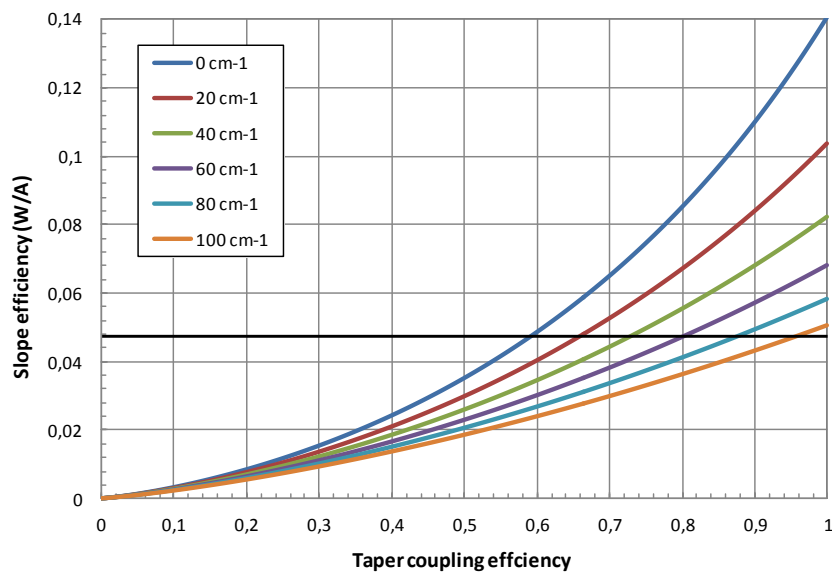


Figure 5.9: simulated hybrid laser slope efficiency as a function of the taper coupling efficiency for different values of internal losses

5.3 Fabry-Perot hybrid lasers by molecular bonding

5.3.1 Shallow ridge design

The employed design is the same that in Figure 5.5 but the bonding layer is silica in this case and not BCB. We measured lasers with different dimensions, in every section we will detail the exact dimensions of the measured component.

5.3.1.1 Continuous wave behaviour

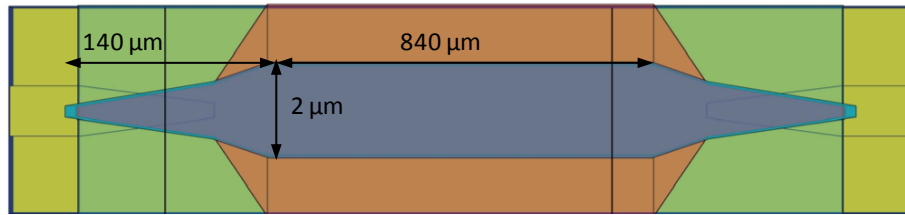


Figure 5.10: dimensions of the measured device

In Figure 5.11 we present the measured L-I and V-I curves for a Fabry-Perot hybrid laser silica bonded. A schematic description of the dimensions of the device is given in Figure 5.10. The III-V waveguide straight section has a width of 2 μm and a shallow etch design. The length of the straight III-V waveguide section is 840 μm . The coupling section length is 140 μm . The device has a threshold current of 60 mA and a maximum single facet continuous wave output power of 3 mW at 20°C. As previously shown, the kinks in the L-I characteristics are due to the jumps of the dominant lasing mode.

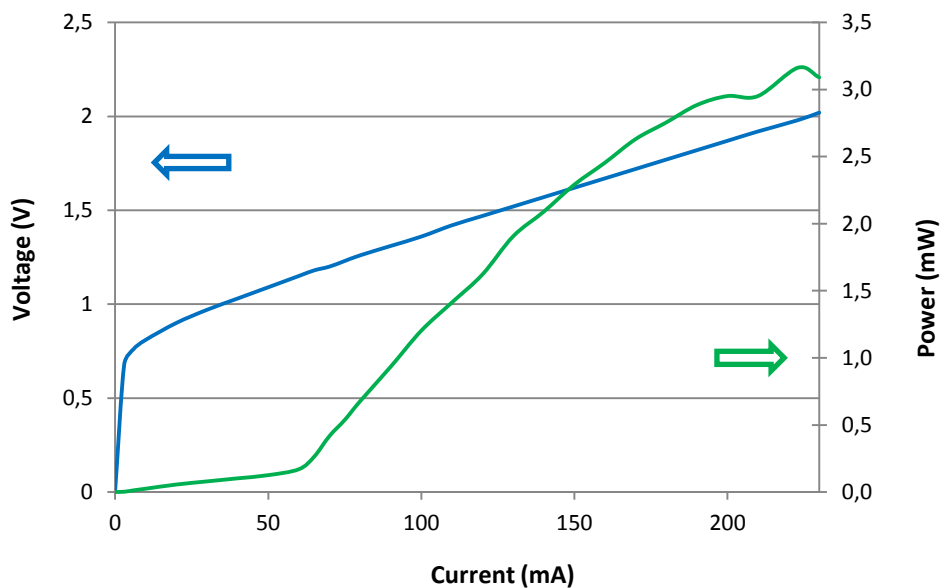


Figure 5.11: L-I and L-V curves of a silica bonded hybrid Fabry-Perot laser

Figure 5.12 shows the optical spectrum for an injection current of 100 mA. We observe that the optical spectrum is single mode in these conditions, but changing the injection current or the

temperature, the emitted wavelength can randomly jump to another wavelength, or other wavelengths can start lasing at the same time. As we have seen in the fabrication chapter, the taper tip is wider than the one designed (400 nm). The coupling efficiency of the adiabatic taper is then reduced. The uncoupled light in the III-V waveguide is back-reflected on the taper tip, creating a double cavity effect that perturbs the Fabry-Perot spectrum. Depending on the temperature and on the injected current, we can also achieve a phase matching condition between the different cavities leading to a single mode emission (Figure 5.12).

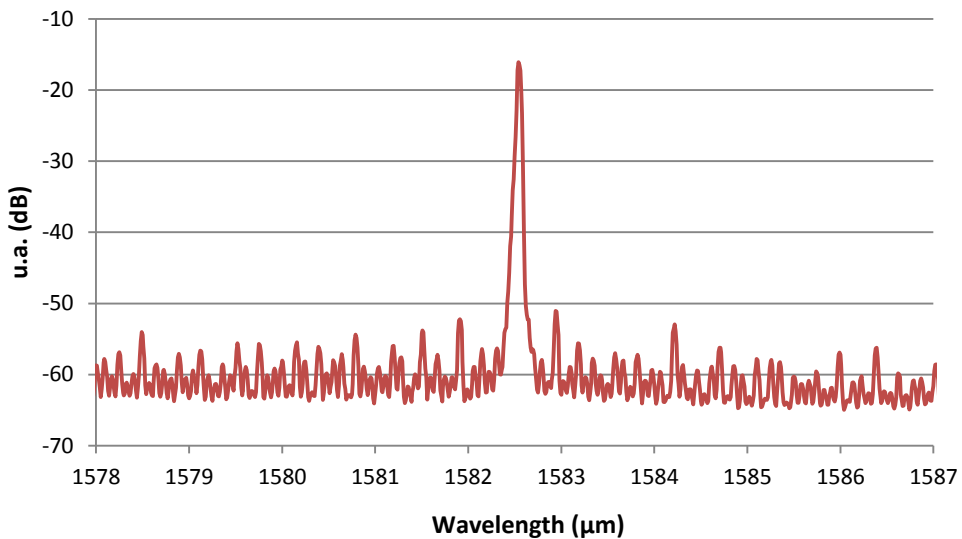


Figure 5.12: laser spectrum at 100mA 20°C CW

5.3.1.2 Thermal analysis

Thermal dissipation is a mainly concern for this kind of device. We investigate the thermal effects on laser performances. Figure 5.14 shows the L-I curves at room temperature of the device described in Figure 5.13 under CW and pulsed regimes. These measurements have been performed at different values of pulse duty cycle. The laser has a series resistance of 8 Ohms. One can see that the L-I curves exhibit a maximum output power, which increases with the decrease of the duty cycle. It is clear that the power roll-off at high injection current values is related to thermal effects.

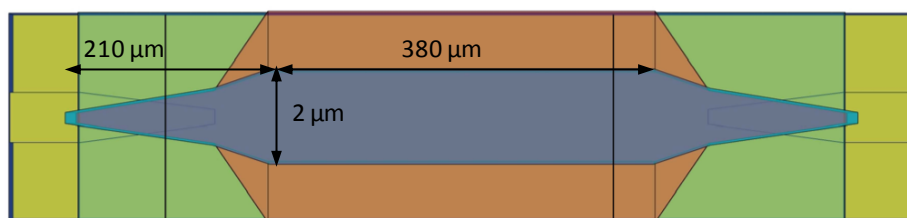


Figure 5.13: dimension of the measured device

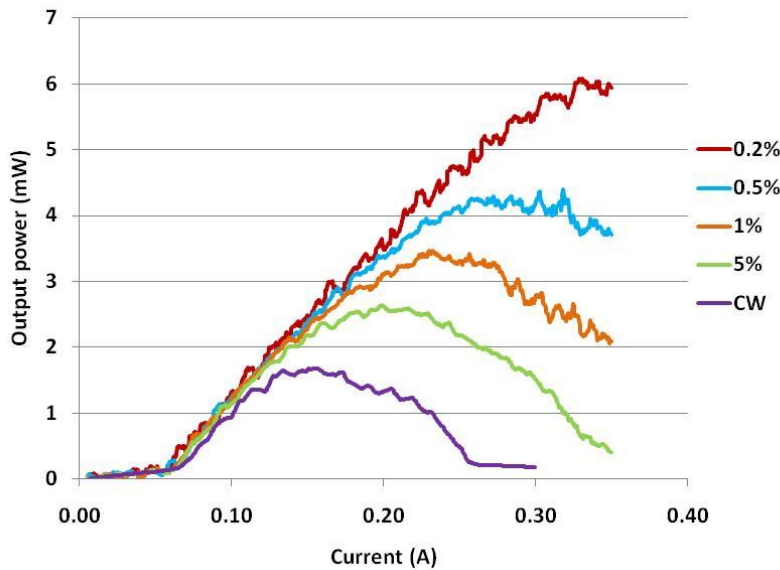


Figure 5.14: L-I curves of a Hybrid laser III-V on SOI measured with different duty cycles

In Figure 5.15 we plot the maximum output power of different lasers as a function of the series resistance. We can observe an almost linear dependence between series resistance and maximum output power. As the series resistance is the main heat source of the device, it is obvious that there is a strong relationship between maximum output power and heat dissipation.

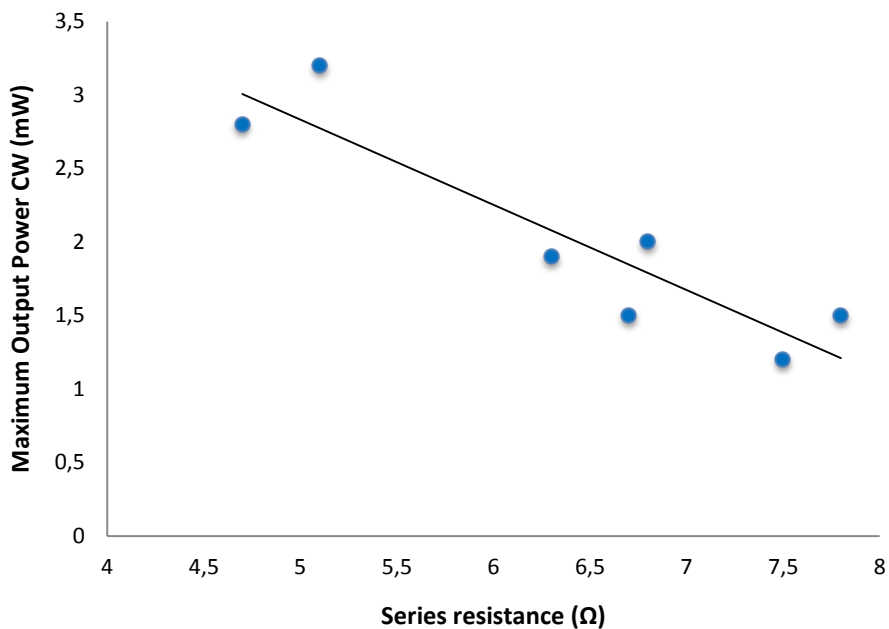


Figure 5.15: maximum output power as a function of series resistance

In the next figure we show CW L-I curves of a hybrid laser at different temperatures. As we can see it still exhibits laser action at 50°C with an output power of 0.5 mW

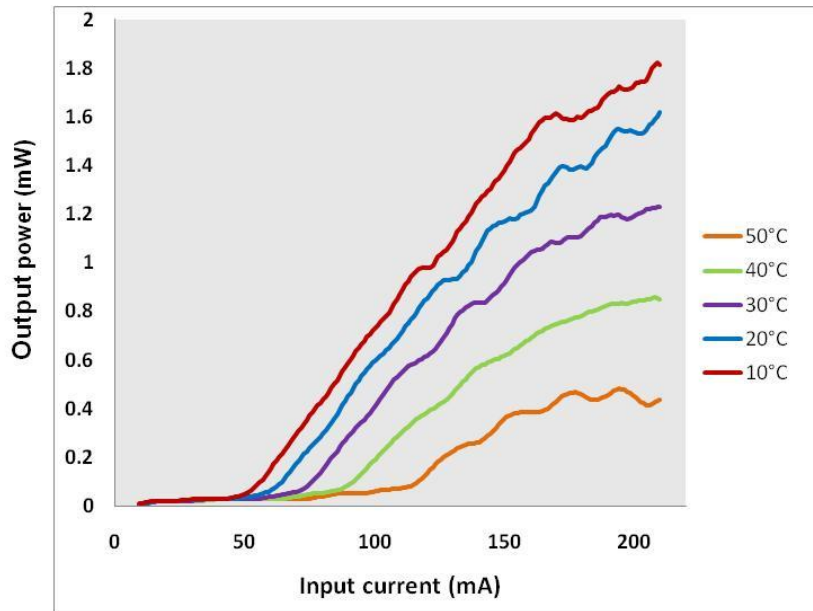


Figure 5.16 CW L-I curves of a Hybrid laser III-V on SOI at different temperatures

The threshold current and the external efficiency extracted from the above figure are plotted as a function of the temperature (Figure 5.17). These figures are then used to evaluate the characteristic temperatures T_0 and T_1 . We found a T_0 of 48K and a T_1 of 57K. T_0 is comparable with standard InGaAsP/InP lasers values (between 50 and 80K).

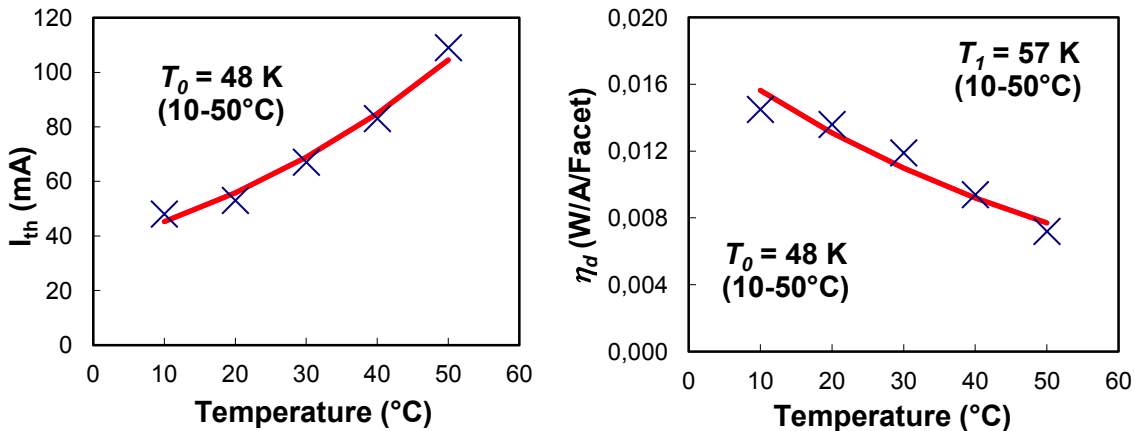


Figure 5.17: threshold and slope efficiency as a function of the stage temperature

5.3.2 Far field measurement

We also performed far field measurements on hybrid III-V/silicon lasers to verify that the output power was emitted from the silicon waveguide facet. The setup scheme is shown in Figure 5.18. A rotating photodiode is placed in front of the silicon waveguide; it measured the optical power for several angle θ , rotating both in the horizontal and in the vertical direction. An example of the measured far field is shown in Figure 5.19. We have a narrow far field in the horizontal direction with a FWHM of 10° and a large divergence in the vertical direction with a FWHM of 100°. Such an asymmetric far field distribution is due to the dimensions of the output silicon waveguide: 440 nm

thicknesses and 6 μm of width. Those measured values are in good agreement with the simulated values for this kind of output SOI waveguide: 13° in the horizontal direction, 104° in the vertical.

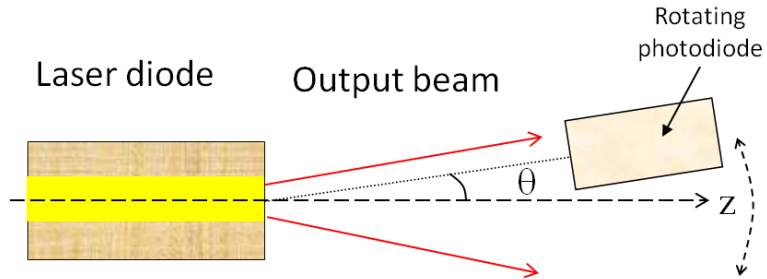


Figure 5.18: far field measurement setup scheme

We also measured the far field as function of the output power. No changes were observed in the far field properties, which is expected since the farfield is completely determined by the properties of the passive silicon waveguide.

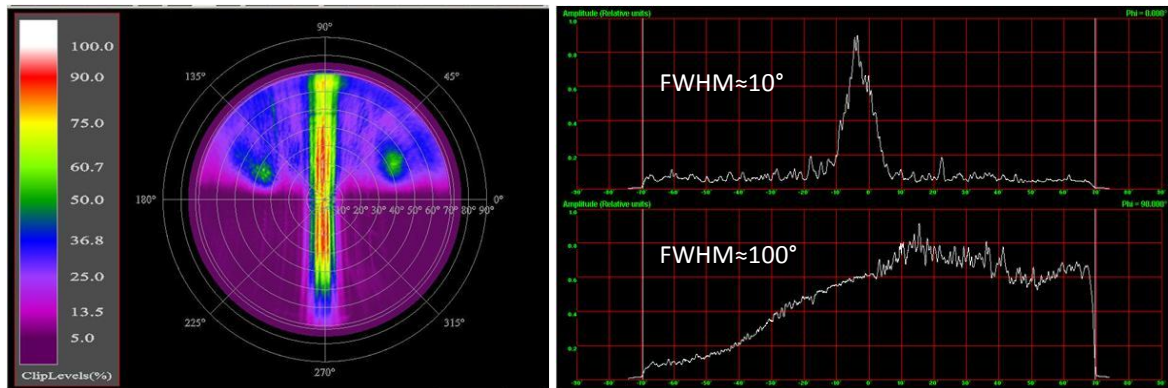


Figure 5.19: measured far field from silicon waveguide of hybrid lasers

5.3.3 Comparison with DVS-BCB bonded devices

Looking to the measurements we see that DVS-BCB devices present a much better threshold and a slightly better maximum output power and thermal behavior. However it is difficult to really compare the performances of molecular bonded and DVS-BCB bonded devices. The technological process (from the bonding itself, to the III-V process) introduces many differences between two different fabrication runs and it is hard to conclude if the performance variations are due to the kind of bonding or simply to some divergence in the fabrication process. Moreover, molecular bonded devices were fabricated starting from a small die (6 mm x 4 mm) bonded to the SOI wafer, while DVS-BCB lasers were obtained from an hybrid sample with a quarter InP wafer entirely bonded on the SOI. The fabrication onto small dices is intrinsically less uniform and reliable compared to bigger samples, as proximity of the die borders perturbs the process steps. What we can surely say is that the devices realized with both bonding technology present very interesting performances, close to the state of the art. The complete mode transfer demonstrates indeed to be a valuable solution for hybrid laser. Further improvement can be considered, both from a fabrication and a design point of view.

These devices present a major fabrication defects (the large taper tip) that strongly perturbs the laser behavior, reducing performances. A different design relaxing fabrication constraints, as the one described in chapter 2.6, would probably eliminate this issue. The thermal behavior needs also to be analyzed, these devices are not able to lase at more than 60°C; it represents a strong limitation for practical applications. This is mainly due to the buried oxide layer that avoids thermal dissipation from the substrate. New structure allowing a better heat dissipation could be used to reduce this effect.

5.4 Single ring resonator laser

Ring resonator mirror based lasers have been fabricated on a molecular bonded sample. This design aims at realizing a single-mode tunable laser source. In this section we detail the measurement results of our first fabrication run. The laser effectively presents single mode laser action and continuous wave behavior. However, due to fabrication defects, the output power is extremely low.

5.4.1 L-I-V characteristics

Figure 5.20 shows the single wavelength laser structure. It consists of a 500 μm long straight III-V waveguide, double taper both in the III-V and SOI waveguide, a back DBR mirror and a front micro-ring based reflector.

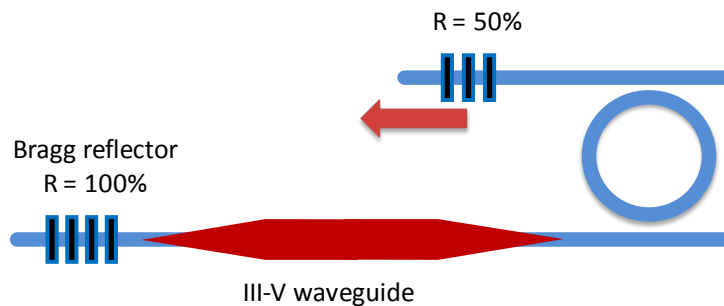


Figure 5.20: single wavelength microring based laser structure

Under the III-V waveguide, there is a RIB silicon waveguide. The total thickness of the silicon waveguide is 400 nm, partly etched to 180 nm to form the RIB waveguide. Then there is a transition between the RIB waveguide to the stripe waveguide with a thickness of 220 nm. The ring resonator is made with 220 nm thick waveguide and has a free spectral range of 25 nm. The DBRs are achieved by etching 50 nm of the 220 nm thick silicon waveguide. The sample has been thinned and diced; an AR coating has been deposited on the ring side output facet.

Figure 5.21 shows the L-I curve of the laser under CW operation regime at 20°C. We can see that the threshold CW current is around 75 mA and the output power coupled to the silicon waveguide is of around 150 μW for an injection current of 150 mA.

We achieve a continuous-wave behavior but the output power is extremely low and the threshold extremely high. Passing from CW to pulsed regime, differently from Fabry-Pérot devices, the performances do not increase significantly. The physical origins of these poor performances will be better understood reading the next section.

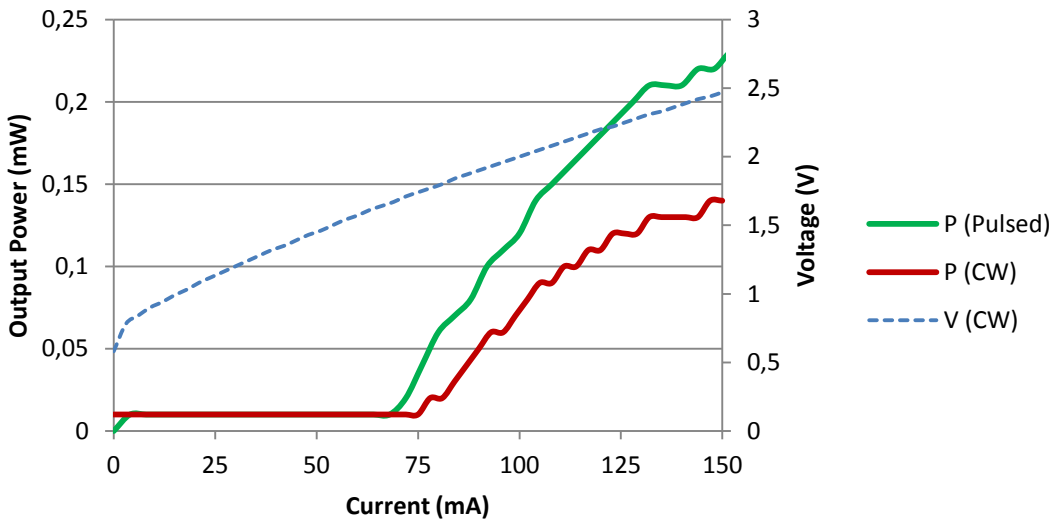


Figure 5.21: the L-I-V curve of the hybrid ring resonator based laser under pulsed and CW regime at 20°C

5.4.2 Spectral analysis

Figure 5.22 shows the emission spectrum of the hybrid laser measured for an injection current of 188 mA at a temperature of 11°C. Single wavelength operation is achieved with a side mode suppression ratio of 30 dB. However the SMSR is not stable and normally lower for other injection/temperature conditions. At the right of the lasing wavelength we can often recognize the transmission function of the ring resonator as is shown in Figure 5.23, which demonstrates that the laser follows the reflectivity of the ring resonator based mirror.

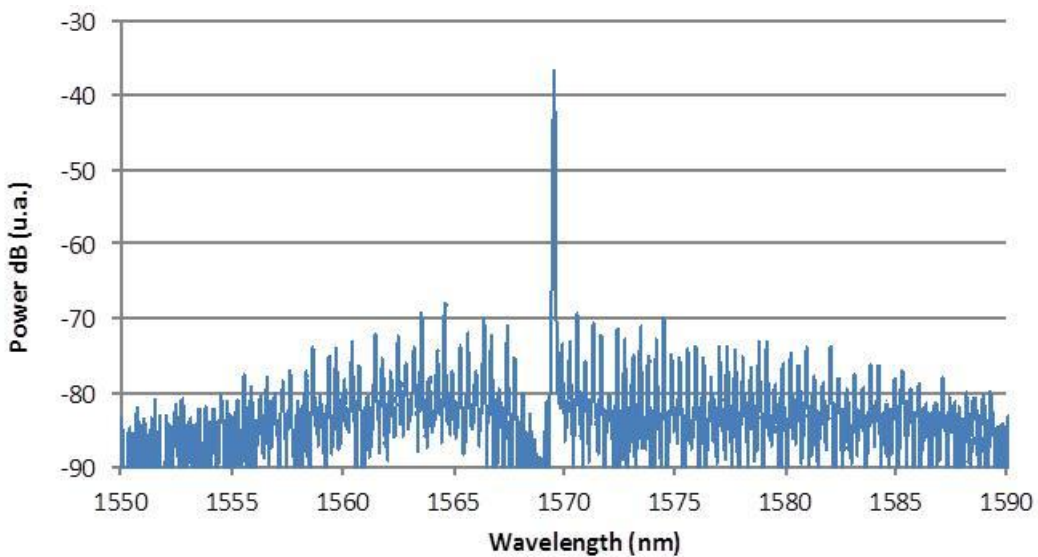


Figure 5.22: the emission spectrum of the hybrid laser

Further investigations make us believe that the device behaves as if the microring was outside and not inside the laser cavity. In Figure 5.24, we compare two measured spectrums; the first one is achieved coupling the lensed fiber to the silicon output waveguide, the second one moving the fiber far from the waveguide looking for a parasitic output where we could recuperate enough light to measure the optical spectrum. As we can see in the output from the silicon waveguide we recognize

the transmission function of the ring resonator with a minimum output power on the left of the lasing wavelength. But we don't obtain this behavior in the parasitic power. If the ring was inside the lasing cavity we would recognize its transmission function in both spectrums. As it is not so, the microring is surely outside the cavity. The measured free spectral range value confirms this hypothesis.

We do believe that the laser cavity is defined only by the III-V part, light propagates back and forth between the two III-V taper tips. Only a small fraction of light is coupled to the silicon waveguide and reflected by the microring based reflector. In Figure 5.25 we show an optical microscope picture of the taper tip. As we can observe the tip is at least three times larger than the designed values, due to an incorrect etching profile. A small amount of light reaches the ring and is filtered and back reflected into the cavity. This small reflection coming from outside the cavity is sufficient, in certain condition, to lock the laser emitted wavelength to the reflection function of the ring based mirror.

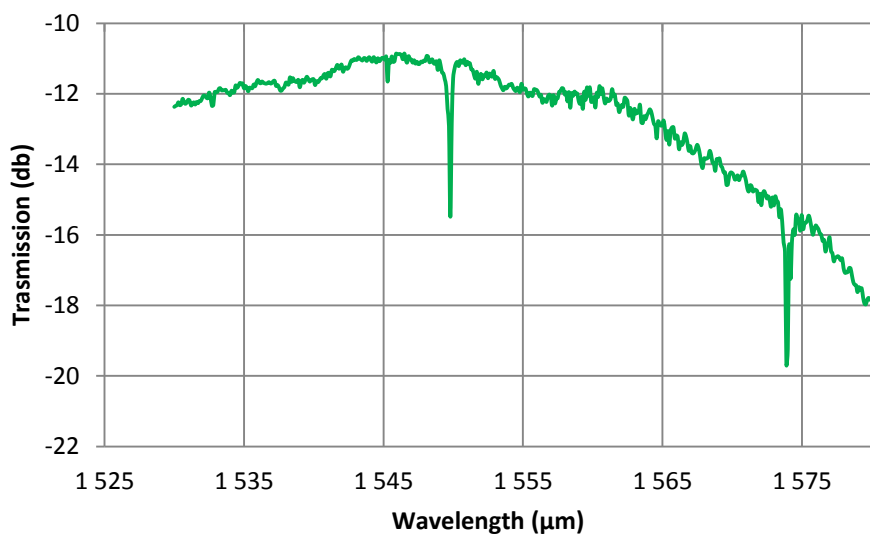


Figure 5.23: measured transmission for a ring resonator structure

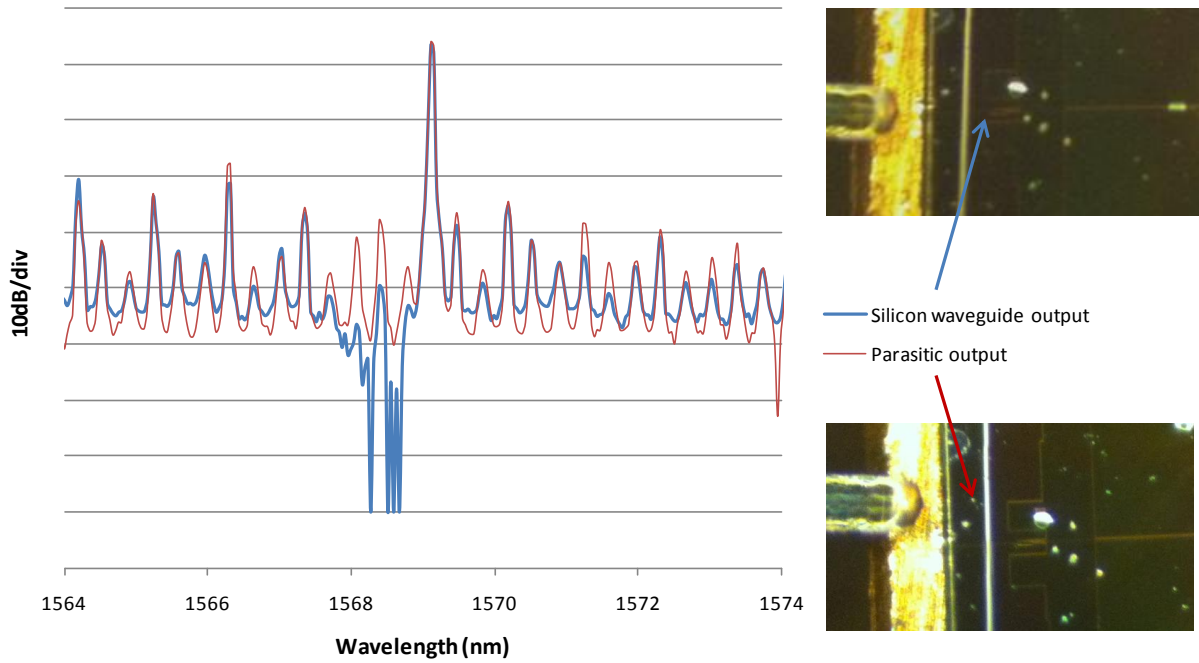


Figure 5.24: comparison between the silicon waveguide output spectrum and a parasitic output spectrum

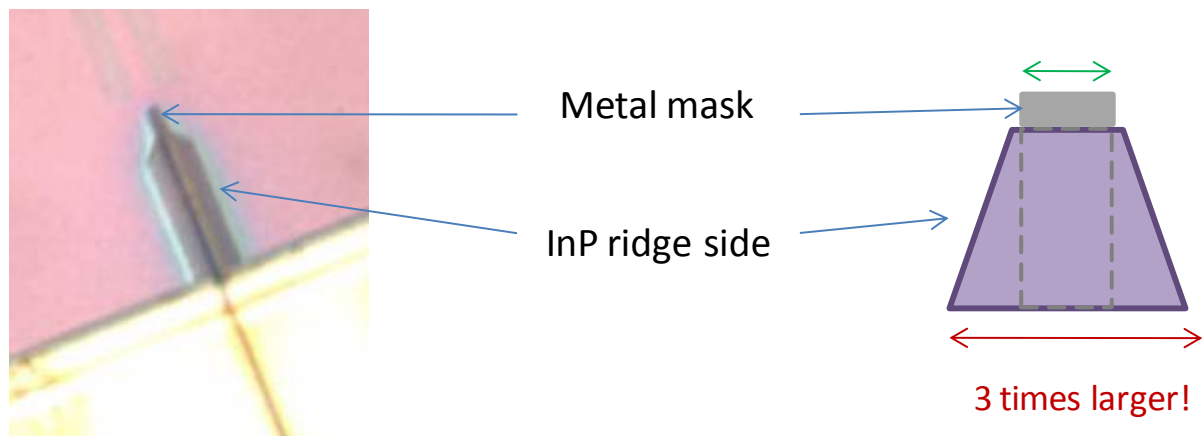


Figure 5.25: optical image of a laser taper tip, the etching profile enlarges the dimension of the tip

5.4.3 Thermal analysis

We studied the thermal behaviour of these devices. We measure the wavelength of one Fabry-Perot mode as a function of the injected current. In Figure 5.26 we present the result of this measurement. We see that the wavelength increases linearly with the injected current, the proportion factor is 0.027 nm/mA. The shift of the emitted wavelength is due to the heating of the active QW layers. In InP/InGaAsP QWs a wavelength shift of 0.107 nm corresponds to an increase of 1 K in the QWs temperature. Indeed we can deduce that for every injected mA the QWs temperature increases of 0.5 K.

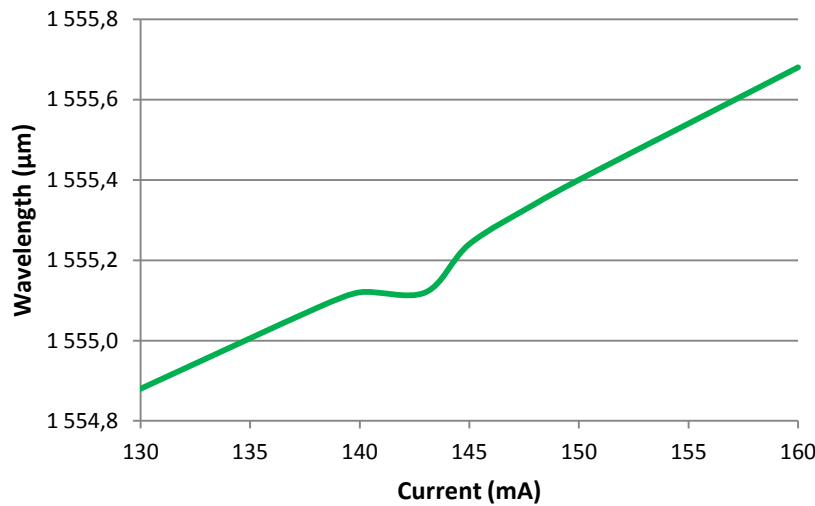


Figure 5.26: emitted wavelength as a function of the injected current

5.5 Double ring resonator laser

This design (Figure 5.27) aims at realizing a single-mode largely tunable laser source. The tunable laser consists of an InP based amplification section, tapers for the modal transfer between III-V and Si waveguides, two RRs for single mode selection, metal heaters on top of the rings for the thermal wavelength tuning and Bragg gratings providing reflection and output fibre coupling. The straight III-V waveguide has a width of 1.7 μm and a length of 500 μm . Both silicon and III-V waveguides are tapered over a length of 200 μm . In the silicon sections, ring resonators 1 (R1) and 2 (R2) have free spectral range (FSR) of 650 and 590 GHz, respectively. The Bragg reflectors are realized by partially etching the silicon waveguide. The two Bragg reflectors, each with a pitch of 290 nm and 60 periods, are designed to have a reflectivity of more than 90%, and a 3 dB bandwidth larger than 100 nm. The lasers are tested on wafers with vertical Bragg gratings coupling the output light into a cleaved single mode fiber. The coupling losses were measured to be around 10 dB.

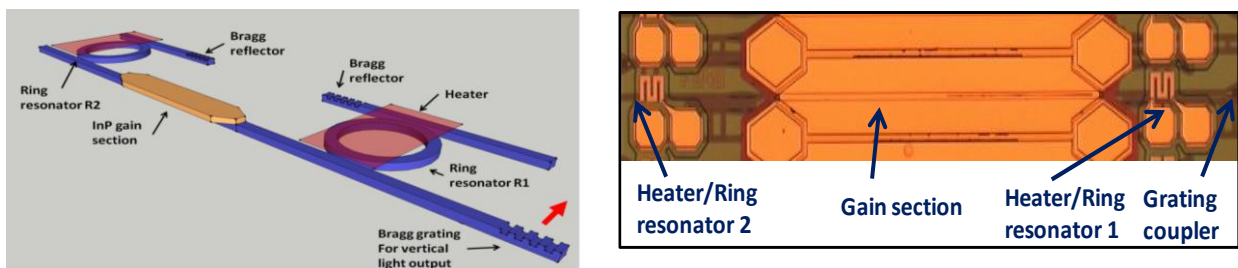


Figure 5.27: schematic view (left) and picture (right) of the widely tunable single mode hybrid laser

First the passive ring resonators are measured. In the left part of Figure 5.28 we show the transmission curves of the two ring resonators from the input port to the drop port. Two combs of resonance peaks are observed, corresponding to the two ring resonators with slightly different FSRs. It is remarkable that for each resonance peak, the full width at half minimum is estimated to be around 0.05 nm, which is one order of magnitude narrower than the one in InP based ring

resonators. Such narrow resonance peaks show the high quality of the fabricated silicon waveguides, and are the key to achieve large tuning range with high SMSR. It is to be noted that the amplitude variation in those curves is the limited resolution bandwidth (0.07 nm) of the optical spectrum analyzer used.

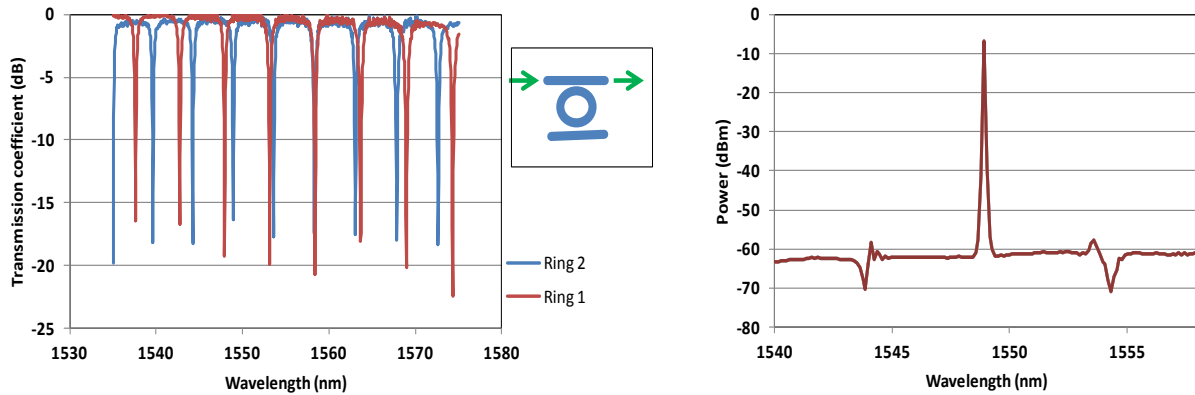


Figure 5.28: measured transmission spectra of the ring resonators (left) and laser emission spectrum at 80mA, 20°C (right)

At 20°, the laser has a threshold current of 21mA. The maximum power coupled to a single mode fibre is 1 mW at 20°C, for an output power from the laser itself of around 10 mW.

The right side of Figure 5.28 shows the laser spectra at 20° for 80 mA current, measured by heating the ring resonators. It shows clearly single mode operation with 50 dB SMSR. Such a large SMSR is attributed to the narrow bandwidth of the rings.

Figure 5.29 (left) shows the super-imposed laser emission spectra by changing heating power levels to the two ring resonators. On the backgrounds of those spectra curves, as well as on that of Figure 5.28, one can observe transmission peaks created by R2 and the transmission dips created by R1. This is due to the fact that the spontaneous emission generated by the active III-V waveguide is modulated by the drop transmission of R2 and by the through transmission of R1. Figure 5.29 (right) shows the wavelength tuning curves of the laser by heating simultaneously the two RRs with a laser injection current of 80 mA at 20°C. With less than 400mW of combined power in both heaters, a high SMSR (>40dB) wavelength range over 45 nm is achieved. For a given power P1 in ring 1, as the power P2 in heater 2 increases, the ring peak wavelengths shifts, and the laser wavelength jumps to the next ring interference order for which the two ring resonance peaks match. For wavelength setting, both ring power must be adjusted so that one transmission peak of R1 matches one of R2 at a desired wavelength. The wavelength tuning range is currently limited by the too large difference in the FSR between the two ring resonators. An optimized design should allow covering the whole gain bandwidth of the III-V active material.

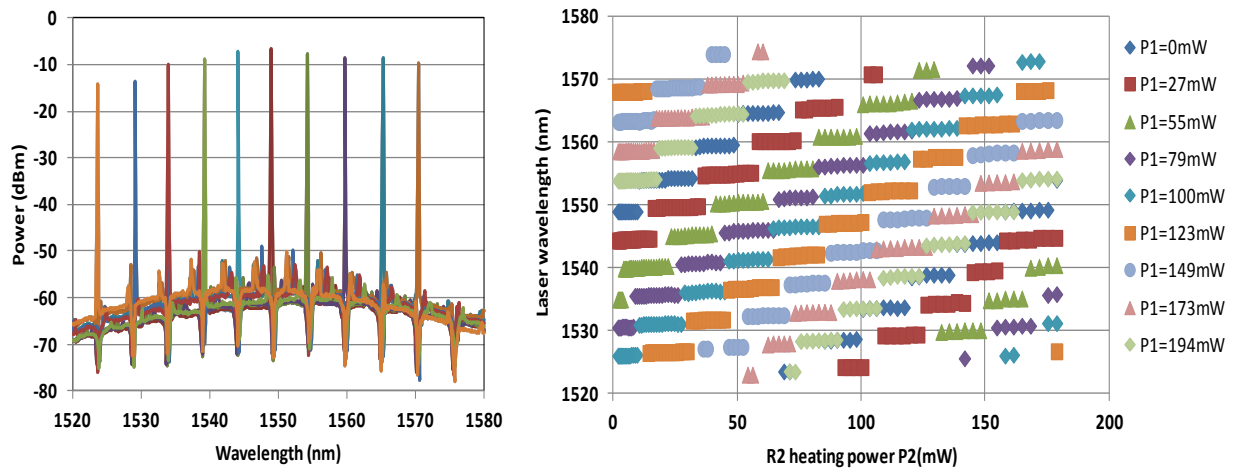


Figure 5.29: (left) super-imposed laser spectra, (right) laser wavelength as a function of the electrical power in the heater 1 and in the heater 2, at 20°C and laser injection current of 80mA

5.6 Conclusions

Five laser designs have been fabricated and characterized. All the realized structure used a double adiabatic taper to achieve a complete mode transfer between III-V and silicon waveguides. The first structured based on a III-V deep ridge waveguide and on DVS-BCB bonding presents lasing under pulsed electrical injection. The second and the third characterised structures have a shallow/deep ridge design, one is based on DVS-BCB bonding, the other on molecular bonding. Both solutions show laser action in continuous wave regime with output power between 3 and 4.5 mW. The DVS-BCB device presents a threshold of 30 mA that represents the state of the art for a Fabry-Perot hybrid III-V laser on SOI. All these devices present a perturbed Fabry-Perot spectrum due to parasite reflections from the III-V taper tip. This defect reduces the coupling efficiency of the adiabatic taper and in turns the devices performances in term of output power and threshold. A fourth geometry with a DBR mirror and a ring resonator based mirror realized in silicon has also been measured. The laser presents a single mode emission with a SMSR that can reach 30dB under continuous wave regime. The output power is however low and the threshold high. A fabrication defect that strongly reduces the performance of this device has been identified.

A fifth design with DBR mirrors and two ring resonators has been fabricated and measured. With this design we demonstrate for the first time a monolithically integrated widely tunable hybrid III-V/Si laser made by a wafer bonding technique. More than 45 nm wavelength tunability is achieved at a constant temperature and injection current into the gain section. Very large SMSR (>40dB) is maintained over the tuning range. A laser threshold of only 21 mA is measured.

Table 5.1 presents a comparison of our achieved performances with those reported by other research groups, maximum output power and slope efficiency are evaluated for both sides emission.

	III-V Lab		LETI	Intel/UCSB			Monolithic InP lasers
Type	Si FP	Si RRs	Si DBR	Si DBR	Si DFB	Si DBR	DFB, DBR
Silicon waveguide thickness (nm)	400	440	500	500	500	500	/
I _{th} (mA) at 20°C	30	21	40	45	25	65	< 20
η (mW/mA) at 20°C	0.1	/	0.1	0.1	0.05	0.15	> 0.25
P _{max} (mW) at 20°C	9	10	14	30	5.4	11	30
SMSR (dB)	/	45	>20	/	40	40	40
Tunability (nm)	/	45	/	/	/	/	/
T° max operation	60°C	/	60°C	90°C	50°C	45°C	90°C
Wavelength (μm)	1.55	1.55	1.55	1.3	1.55	1.55	1.3-1.55

Table 5.1: comparison of the achieved performances with those reported by other research groups

6 CONCLUSIONS AND OUTLOOK

Quod scripsi scripsi

Photonics is a rapidly growing sector in the global economy. Optical communications, optical storage, imaging, lighting, optical sensors or security are just a few examples. The penetration of photonics in many application fields is limited by the high cost of photonic components and their assembly. Silicon photonics aims at bringing the high level integration and the low costs of microelectronic fabrication to photonics. The long term goal is to achieve the fabrication of photonic integration circuits in a microelectronics production line. These chips could potentially integrate microelectronics and photonics functionality, enabling a large number of new and low cost applications.

Silicon photonics knew an impressive development in the last ten years. Almost all the fundamental building blocks have been demonstrated and reveal competitive performances. However, the lack of an efficient silicon integrated laser source has led the researchers to develop heterogeneous integration of III-V materials on silicon.

In this thesis we described and analyzed the design, the fabrication and the performances of these hybrid III-V on silicon lasers.

The heterogeneous integration of III-V materials on silicon is based on wafer-to-wafer or die-to-wafer bonding techniques, which allow bonding a III-V stack to a Silicon On Insulator wafer using a thin bonding layer. Passive waveguides are patterned on the SOI wafer while active waveguides are etched through the III-V stack after bonding. A key element for these devices is the coupler that allows a power exchange between the active and the passive section. In this thesis we propose the use of an adiabatic coupler that performs a total transfer of the optical mode between the III-V and the silicon waveguides. The active waveguide on III-V materials at the center of the device provides the optical gain, while, on both side, adiabatic couplers allow a loss-less transfer of the optical mode to the silicon waveguide. Optical feedback is provided by cleaved facets or resonators located in the silicon waveguides. A detailed theoretical analysis of adiabatic couplers was provided. An innovative geometry based on a double adiabatic taper is proposed and simulated. This structure allows a complete transfer of the optical mode within 150 micrometers through a 100 nanometers thick bonding layer.

The active waveguide geometry has also an important effect on laser properties. A new concept of III-V waveguide for heterogeneous integrated devices was proposed in this thesis. This waveguide consents to greatly reduce the optical and the electrical losses of the active section. We filed a patent covering this structure. Devices based on this idea and on adiabatic couplers have been fabricated and measured. They provided state of the art performances, the lasers threshold in particular are the lower ever measured for Fabry-Pérot hybrid III-V on SOI lasers. However, some fabrication defects perturb the spectrum of these devices and reduce the couplers efficiency. To improve the fabrication tolerances of this first design a second coupler derived from a theoretical adiabacity criterion was proposed and simulated. This adiabatic coupler reveals theoretically better performances compared to the double taper design; devices embedding this coupler are currently under fabrication.

Single wavelength emitting lasers are fundamental elements for high bandwidth optical links, as they enable wavelength division multiplexing. We reviewed all the effective solutions enabling single waveguide hybrid III-V on SOI lasers. DBR, microring based, DFB and AWG laser solutions were analysed. We proposed two microring resonator based designs. The tunability and the wavelength linewidth achievable with these designs were investigated. We completed and measured a first fabrication run with single and double ring based lasers. We effectively achieved single wavelength operation with a SMSR of 45dB. We measured a laser threshold of only 21 mA, an output power of more than 10 mW and tunability over 45 nm. This device represents the first demonstration of a monolithically integrated hybrid III-V/Si tunable laser made by a wafer bonding technique. The measured performances in terms of threshold, output power, tunability and SMSR set the state of the art for this kind of components.

DFB and AWG laser designs have also been proposed and are actually under fabrication. A theoretical model to evaluate the performances of DFB exchange lasers was proposed and the simulation results were discussed.

The fabrication technology development represented a large part of this thesis work. At the beginning of my thesis, III-V lab, had very limited experience on hybrid III-V on SOI fabrication. Lithography process needed to be adapted to fit with the design requirements. Wet and dry etching processes also behave differently onto a III-V stack bonded on SOI. Several tests were needed and specific processes have been developed to find the good compromise that could bring the best performances. Metal deposition and rapid thermal annealing have also needed a precise development in order to insure low ohmic resistance contacts between metal and semiconductor, without enhance the number and the dimension of bonding defects.

Unfortunately the long cycle of the entire manufacture process (SOI fabrication, bonding, III-V fabrication) did not allow terminating the fabrication of many of the designed structure during my PhD thesis. In the next six months, practically all the designed should be fabricated and measured. Important outcomes are expected. In particular the use of the optimized taper should guarantee the realization of devices that do not present the spectrum perturbation that affected all the lasers manufactured up to now. The improvement in the coupling efficiency should bring to even lower threshold and higher slope efficiencies. Significant results are expected also from single mode laser designs. The first fabrication run could tell us more about the potential of these structures and permit a comparison between the different kinds of laser. The DFB and the AWG lasers would represent the first demonstration of these devices based on the total transfer of the optical mode by adiabatic tapering. The future of these devices for practical applications is strongly related to the future of monolithically based lasers. If monolithically silicon or germanium lasers will demonstrate performances close to heterogeneous integrated laser outcomes in the next few years, hybrid laser will hardly be able to withstand the competition. If otherwise, monolithically integrated solutions will keep showing low performances unfit for real application, heterogeneous integrated lasers could know an extremely large commercial success. In a few years bonding techniques will be probably compatible with the high yield production standards of a CMOS fabrication line. Moreover the first commercial applications of silicon photonics will boost the development of a fully compatible CMOS laser process. There are no theoretical reasons why this devices should not reproduce, once correctly optimized, the performances of monolithically integrated lasers. III-V monolithically integrated devices days are numbered? Only the time will tell us.

7 RÉSUMÉ EN FRANÇAIS

Lasers InP sur circuits silicium pour applications en télécommunications

1	Introduction.....	143
2	Etat de l'art.....	145
3	Comment coupler efficacement la lumière du III-V au silicium.....	147
4	Comment obtenir un laser monomode	155
5	Fabrication.....	167
6	Caractérisation	172
7	Conclusion	176
	Bibliographie.....	178

7.1 Introduction

Ces dernières années la photonique du silicium a connu une accélération remarquable. Plusieurs entreprises leaders dans les marchés de la microélectronique et des télécommunications se sont investies dans le développement de cette technologie et d'ambitieux projets de recherche ont été lancés en partenariat avec de nombreuses universités et organismes de recherche publique.

Les raisons de cette accélération sont multiples et s'inscrivent dans différents horizons temporels. La photonique du silicium vise à établir une plateforme technologique qui permette la production sur large échelle de circuits intégrés photoniques, avec la possibilité d'intégration électronique.

A long terme le nombre d'applications que ces circuits pourraient couvrir dépasse largement la simple addition des deux domaines de départ. Dénormes marchés pourraient s'ouvrir, donnant lieu à de nouvelles occasions de développement entrepreneurial, industriel et économique. A court terme deux besoins immédiats, respectivement pour le marché microélectronique et le marché photonique, guident les investissements industriels dans ce domaine.

A cause de leur bande passante limitée, les interconnexions électriques sont considérées comme étant le prochain goulot d'étranglement des systèmes électroniques (1)(2). Face à ce problème, des acteurs comme INTEL et IBM ont proposé des architectures intégrant une couche de communication optique au circuit microélectronique, pour profiter des avantages offerts par la photonique en termes de bande passante et d'immunité au bruit électromagnétique.

Dans le domaine de la photonique, la croissance exponentielle du marché Fiber To The Home a relancé le besoin de circuits photoniques intégrés à très faible coût. Par rapport aux produits traditionnels du monde des télécommunications, caractérisés par des coûts élevés et de faibles volumes de production, les produits destinés au FTTH vont devoir assurer d'excellentes performances tout en gardant un prix extrêmement faible (quelques euros par composant) et des volumes de production élevés. L'adoption de standards de production du silicium pour des produits photoniques promet de satisfaire ces besoins apparemment inconciliables (1)(3). Alcatel-Lucent et NTT, Kotura et Calliopa, constituent des exemples de grandes et petites entreprises qui croient dans cette possibilité de développement, et qui vont probablement lancer des produits FTTH, basé sur la photonique du silicium, pour le marché télécom dans les années à venir.

La plupart des briques technologiques nécessaires pour réaliser de véritables circuits photoniques intégrés sur silicium ont été démontrées. Guides d'onde, coupleurs, modulateurs, photodiodes, multiplexeurs en silicium, etc., ont montré des performances souvent comparables et parfois meilleures par rapport aux technologies traditionnelles. Pour franchir le dernier pas qui sépare la photonique du silicium des véritables applications, il reste à trouver une source laser intégrée fiable, performante et à faible coût.

L'objectif de cette thèse est de réaliser des sources lasers à cavité horizontale oscillante, capable d'émettre des puissances optiques de l'ordre du milliwatt dans un guide silicium, en injection électrique continue, à température ambiante. La longueur d'onde émise doit être compatible avec la transmission sur fibre.

Cette thèse s'est déroulée dans le cadre du projet de recherche européen Helios, qui est financé par la Commission Européenne et qui réunit un large consortium d'entreprises et d'universités à la pointe en Europe dans ce domaine.

7.2 Etat de l'art

Le silicium n'est pas un matériau naturellement adapté à la génération de lumière. Ses propriétés physiques, notamment son gap indirect, ne permet pas d'obtenir un laser d'une façon simple.

Des études récentes, menées par le MIT, ont démontré la possibilité d'obtenir un laser basé sur une optimisation des bandes d'énergie dans des structures germanium (4). Les résultats obtenus, même s'ils sont prometteurs, sont pour l'instant très éloignés des besoins pour des véritables applications. Les études qui visaient la réalisation de laser III-V sur silicium par hétéro-épitaxie sont plus anciennes (5). La densité élevée de dislocations qu'on mesure à l'intérieur des couches déposées pose cependant de nombreuses limitations car elle dégrade les performances électro-optiques des matériaux.

La dernière technique employée est celle de l'intégration hétérogène de matériaux III-V par collage de vignette ou de wafers entiers. On obtient des empilements de couches hybrides III-V / silicium qu'on peut structurer en vue de subvenir au manque de gain optique du silicium. Une fois que l'épitaxie III-V a été transférée sur le wafer SOI, on peut fabriquer les lasers avec des procès à l'échelle de la plaque. (6)

Plusieurs types de lasers ont été fabriqués suivant cette technique par plusieurs laboratoires dans le monde. Des lasers ruban Fabry-Pérot (7), DBR (8), et DFB (9) ont été réalisés par INTEL et UCSB utilisant un guide d'onde dite « évanescante ». Dans ce genre de composants, dont la structure de base est illustrée en Figure 30, le mode optique est principalement confiné dans le guide silicium et seulement une partie évanescante du mode recouvre la partie active de la structure III-V. Les résultats obtenus ont été très intéressants : des puissances maximales de 11 mW et de 5.4 mW ont été mesurées respectivement sur des lasers DBR et DFB avec des seuils de 65 mA et 25 mA.

Cependant ces structures présentent un très faible recouvrement du mode optique avec les puits quantiques de l'épitaxie III-V, qui est d'ailleurs structurée avec une mesa très large. Dans ces conditions le seuil ne peut qu'être assez élevé et la consommation électrique bien plus importante que dans de laser III-V classiques. De plus, la couche de collage extrêmement fine (5 nm) rend cette technique sensible aux contaminations des surfaces, aux rugosités de l'épitaxie ou à la courbature de la plaque.

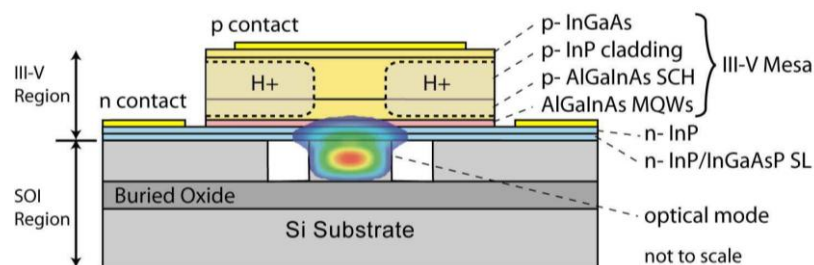


Figure 30: coupe verticale de la structure "évanescante" INTEL/UCSB avec le mode optique super imposé (7)

Pour dépasser ces limitations d'autres groupes de recherche, dont le nôtre, ont utilisé une géométrie différente. La couche collage est plus épaisse (entre 50 et 100 nm) pour rendre le collage plus robuste. Le collage peut être obtenu par collage moléculaire entre deux couches de silice (10)(11), ou être réalisé utilisant un polymère adhésif, le DVS-BCB (12). Au niveau du guidage optique le mode n'est pas guidé par le silicium mais il y a, des deux cotés du guide actif, un coupler adiabatique qui permet un transfert sans perte du mode optique entre le guide silicium et le guide III-V. Avec cette géométrie le laser peut profiter d'un fort couplage avec les puits quantiques ($\sim 10\%$) et donc, potentiellement, avoir un seuil plus faible et un rendement plus élevé. Ce concept est plus récent mais de bons résultats ont déjà été obtenus avec des lasers Fabry-Pérot qui émettent jusque à 7.5 mW en régime quasi-continue (13).

7.3 Comment coupler efficacement la lumière du III-V au silicium

La conception des composants issus du collage entre deux différentes plaques présentent des difficultés tout à fait différentes par rapport aux composants optoélectroniques à semi-conducteur standards. Dans le cas spécifique des lasers III-V sur silicium, le problème principal que nous sommes amenés à résoudre est celui du transfert (ou couplage) de la lumière entre un guide d'onde supérieur en III-V, et un guide d'onde inférieur en silicium. Pour maximiser les performances de nos composants nous voulons que dans la section active de notre laser le mode optique puisse profiter d'une amplification maximale. Pour ce faire nous voulons un transfert complet du mode optique entre le guide d'onde silicium et III-V, non pas un couplage évanescant. Avec un transfert complet du mode le confinement du mode optique dans les puits quantiques sera maximal.

En optique intégrée il existe deux solutions principales pour adresser le problème du couplage de la lumière. On peut employer des coupleurs directionnels (14) ou des coupleurs adiabatiques (15)(16). Les coupleurs directionnels ont l'avantage d'être plus compacts par rapport à des coupleurs adiabatiques, cependant ils présentent une faible robustesse vis-à-vis des imperfections de fabrication et une plus faible bande passante. Pour cette raison nous avons décidé de baser le design de nos composants sur des coupleurs de type adiabatique.

Dans ce type de coupleurs nous avons deux guides d'onde séparés par une distance finie. Les deux guides ont initialement deux différentes constantes de propagation. Si un ou les deux coefficients de propagation varient le long du coupleur pour devenir identiques et s'inverser ensuite, avec le plus grand qui devient le plus petit, un transfert complet de puissance entre les deux guides est possible sous certaines conditions. Pour comprendre le fonctionnement de ces coupleurs on peut utiliser un modèle dit à supermodes. Un supermode est une solution pour le champ électrique dans le système couplé formé par les deux guides. Les supermodes peuvent être exprimés comme une combinaison des modes optiques dans les deux guides isolés. Yariv et al. (17), en partant de ce modèle mathématique, ont proposé un critère d'adiabaticité qui nous donne l'évolution idéale de la différence de constante de propagation entre les deux guides le long du coupleur. Le coupleur adiabatique qui suit cette règle de design permet d'obtenir théoriquement un transfert total de puissance sur une distance plus courte.

7.3.1 Laser hybride III-V on SOI basé sur un taper adiabatique

Dans ce travail nous employons un coupleur adiabatique pour réaliser un laser hybride III-V sur silicium. Une représentation schématique du composant est présenté en Figure 31. La structure peut être divisée en trois parties. Au centre du composant la lumière est confinée à l'intérieur du guide d'onde III-V qui fournit le gain optique. Des deux cotés de cette section deux coupleurs adiabatiques transfèrent la lumière du guide III-V au guide silicium qui se trouve en bas. Après le couplage, la lumière se trouve dans les guides silicium qui n'ont plus du III-V au dessus. Dans une configuration Fabry-Pérot les miroirs qui forment la cavité sont réalisés dans le silicium par clivage.

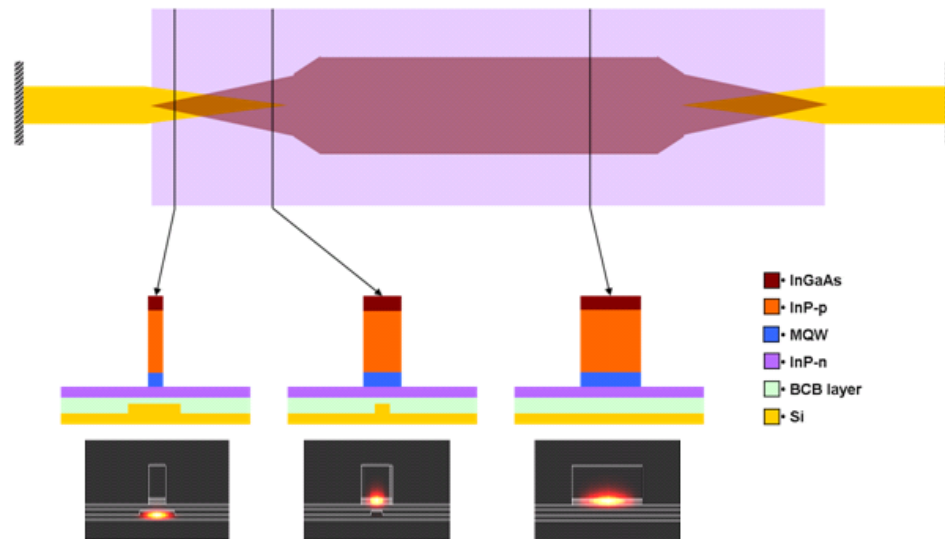


Figure 31: vue de dessus, coupes verticales et mode optique simulés du laser III-V/SOI

L'épitaxie III-V employée (Figure 32) a été réalisée par MBE (épitaxie par jet moléculaire). Vu que la plaque est collée avec la surface déposée en bas et le substrat en haut, les différentes couches ont été épitaxierées dans un ordre opposé par rapport aux épitaxies standards.

Les substrats SOI utilisés ont une taille de 200 mm et ont été produits par SOITEC, ils sont composés d'une couche monocristalline de silicium au dessus d'une couche de 2 µm de oxyde de silicium sur un substrat silicium.

Dans la suite nous détaillerons les différents designs des coupleurs que nous avons conçus pendant la thèse. Pour chaque design nous donnerons la structure du guide III-V et du guide silicium dans les sections non couplés, la forme et les caractéristiques du coupleur adiabatique.

Toutes les structures ont été optimisées en utilisant FIMMWAVE, un logiciel commercial de simulation vectorielle de mode et propagation optique.

layer nb	layer type	nb of periods	material	PL wavelength	thickness	carrier conc.	type
8	cladding n		InP		200	1,0E+18	n
7	SCH		InGaAsP	1,17	100		nid
6	MQW_w	6	InGaAsP	1,55	8		nid
5	MQW_b	5	InGaAsP	1,17	10		nid
4	SCH		InGaAsP	1,17	100		nid
3	cladding p		InP		1500	1E18->5E18	p
2	transition		InGaAsP	1,17	20	1,0E+19	p
1	contact p		InGaAs		300	3,0E+19	p
substrate			InP				N

Figure 32: structure détaillée de l'épitaxie III-V employée

7.3.2 Premier design : structure a double adaptateur de mode avec gravure de la couche active

Ce design a été optimisé pour un guide d'onde silicium en arête, la hauteur du guide est de 400 nm avec une gravure de 180 nm. Ce type de guide silicium a été réalisé par le consortium d'Helios pour pouvoir mieux intégrer au laser des modulateurs, des photodiodes, des multiplexeurs et de coupleurs verticaux. Pour le guide d'onde actif on a choisi un guide d'onde avec gravure de la couche active et des largeurs de ruban comprises entre 1.5 et 3 μm . Ces valeurs de largeur permettent d'avoir un guide suffisamment large pour réduire les pertes optiques liées aux rugosités de surface et suffisamment étroite pour ne pas réduire l'efficacité de pompage. Avec cette géométrie nous calculons un recouvrement du mode de l'ordre du 11% dans les puits quantiques, et de l'ordre du 33% dans la couche de InP dopé p.

La forme du coupleur adiabatique est montrée en Figure 2.9. Il est composé de deux sections, une première section de longueur L_1 (à gauche dans la figure) sans couplage avec le silicium. Une seconde section où l'échange de puissance optique entre III-V et silicium a lieu. Comme nous le voyons sur la Figure 2.9 le guide d'onde III-V se rétrécit dans la deuxième section en passant de 1 μm à 400 nm, lorsque le silicium s'élargit en passant de 500 nm à 1 μm . Une vue 3D du coupleur est montrée en Figure 34.

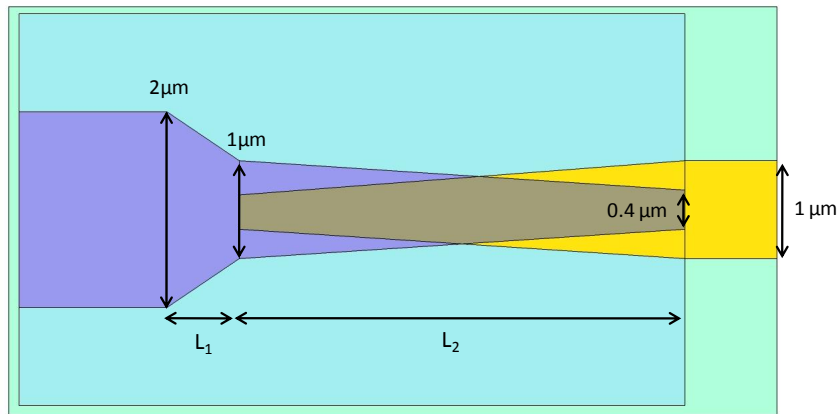


Figure 4 : vue du dessus schématique du design du double adaptateur de mode

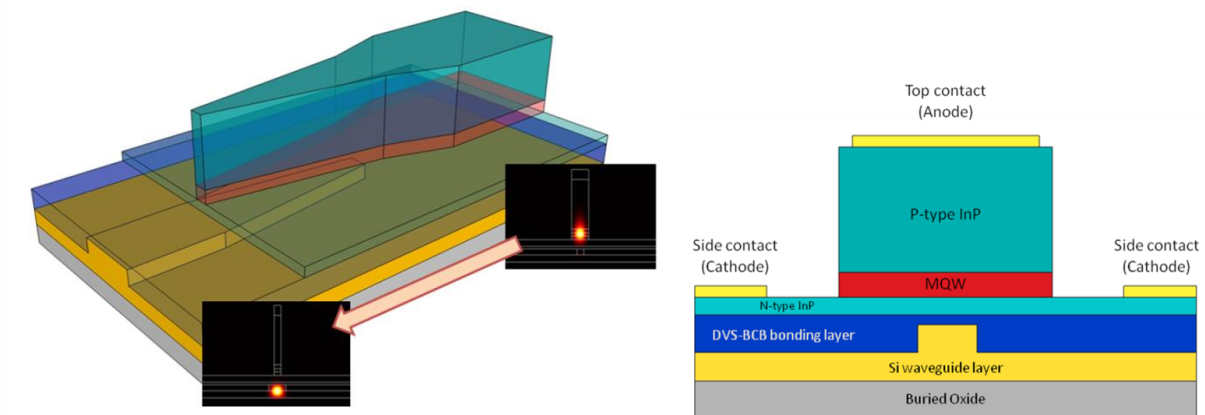


Figure 34 : structure avec gravure de la couche active, à gauche une vue 3D du double adaptateur de mode avec deux profils de mode représentatives, à droite une coupe verticale du coupleur

Des simulations ont montré qu'une longueur de 25μm de la première section (L_1) du coupleur assure une adaptation sans perte du mode. Concernant la deuxième section (L_2), l'efficacité du couplage a été simulée en fonction de la longueur du coupleur pour différentes épaisseurs de la couche de collage avec le logiciel FIMMPROP, les résultats sont montrés en Figure 2.15. Ces simulations nous montrent qu'une épaisseur de collage inférieure à 100 nm associée à des coupleurs de plus de 150 μm permet d'obtenir une efficacité de couplage supérieure à 95%.

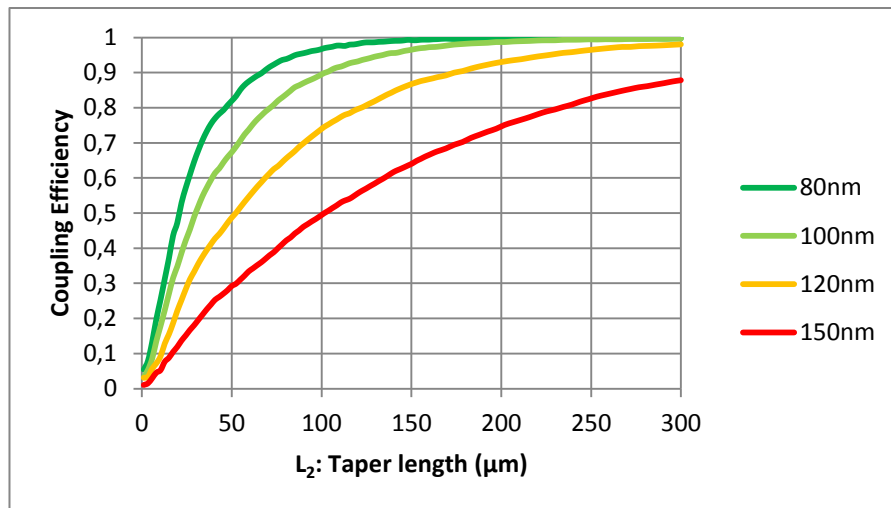


Figure 6: efficience de couplage en fonction de la longueur du taper pour différents épaisseurs de la couche de collage

Les tolérances de fabrication ont également été prises en compte. En Figure 2.17 sont présentées les valeurs d'efficience de couplage simulé dans le cas d'un désalignement entre le guide d'onde III-V et silicium. La Figure 2.20 montre l'efficience de couplage dans le cas où la taille de la pointe III-V du coupleur est supérieure à 400 nm.

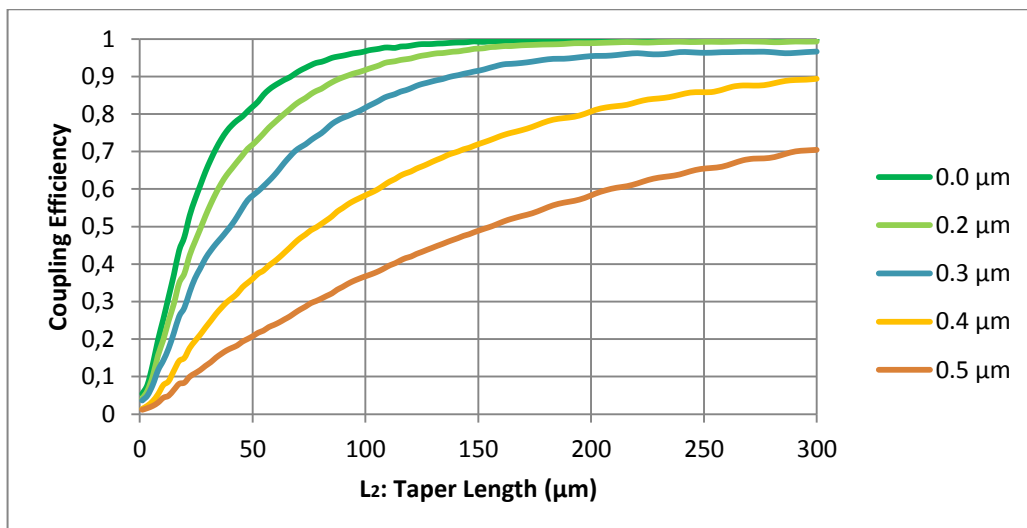
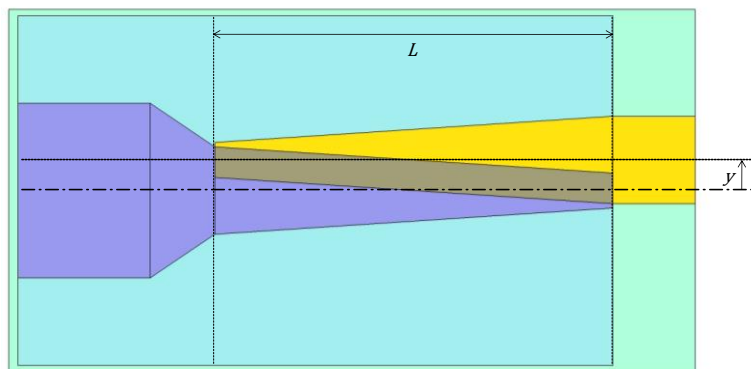


Figure 7: efficience de couplage en fonction de la longueur du taper pour différents valeurs de y

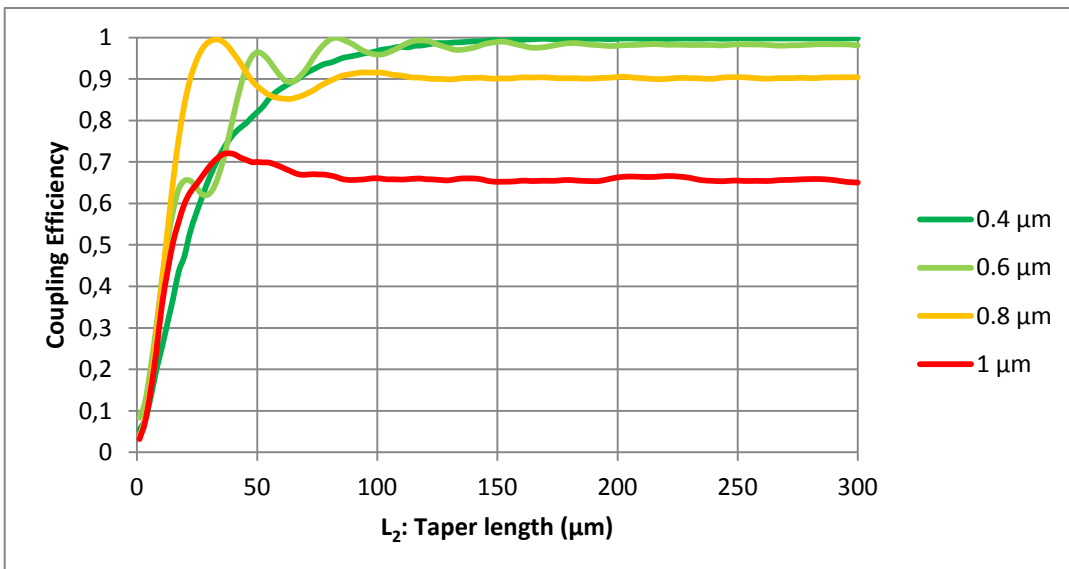


Figure 8: efficience de couplage en fonction de la longueur du coupleur pour différentes valeurs de largeur de la pointe III-V du coupleur

Comme on verra dans la section fabrication, une tolérance d'alignement de 0.2 μm et une pointe de 0.4 μm de largeur ne sont pas simples à réaliser par lithographie optique de contact. Ce design n'est donc pas extrêmement tolérant, une épaisseur réduite de la couche de collage peut cependant relâcher ces contraintes de fabrication.

Vus les résultats de ces simulations, les masques que nous avons codés prévoient des coupleurs d'une longueur qui va de 150 à 250 μm. L'épaisseur de la couche de collage doit être impérativement inférieure à 100 nm.

7.3.3 Structure à double adaptateur de mode sans gravure de la couche active dans la région de gain

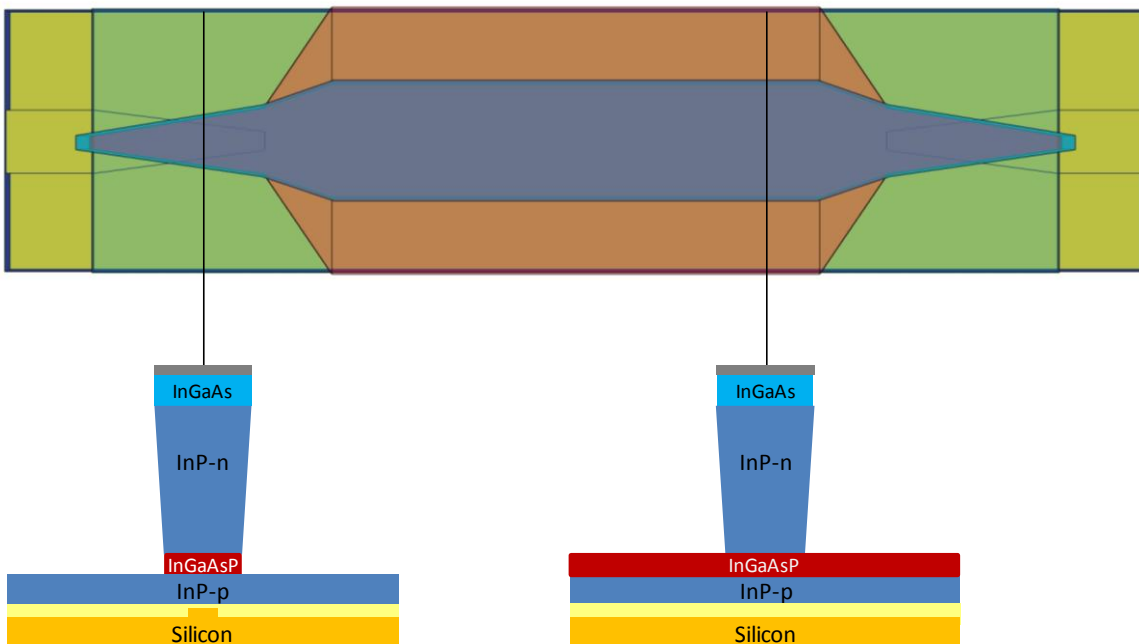


Figure 9: vue de dessus et coupes verticales du laser III-V/SOI sans gravure de la couche active

Les lasers à semi-conducteur sans gravure de la couche active présentent une durée de vie plus élevée, un seuil plus faible et une efficacité quantique plus élevée par rapport aux lasers avec gravure de la couche active. Pour ces raisons nous avons développé un design du guide III-V compatible avec la technologie hybride et sans gravure de la couche active dans la section droite du guide d'onde. Ce design est présenté en Figure 2.21. Il s'agit d'utiliser un guide d'onde sans gravure de la couche active dans la section III-V droit du composant et un guide d'onde avec gravure de la couche active dans la section de couplage pour aider le transfert de la lumière. On va raccorder ces deux sections rétrécissant progressivement la largeur de gravure de la couche active. Si cette section de raccord est plus longue que 20 µm les pertes optiques introduites sont négligeables.

On a choisi une largeur du guide III-V de 1.7 µm que nous permet d'avoir un confinement du 12% dans les puits quantiques. Le confinement dans le InP dopé p se réduit à environ 29%.

7.3.4 Coupleur adiabatique optimisé

Comme nous l'avons vu dans la section 7.3.2, le design du coupleur adiabatique précédent n'était pas tolérant. En plus, avec un guide silicium de 400 nm nous devons utiliser un guide III-V avec gravure de la couche active dans la section de couplage et avec une pointe extrêmement fine.

Pour contourner ces problèmes nous avons essayé de développer un design de coupleur adiabatique plus performant. Pour atteindre cet objectif nous avons conçu un coupleur adiabatique qui reproduit

exactement la condition d'adiabaticité présentée précédemment. Il s'agit de dessiner un coupleur adiabatique optimisé ou, en d'autres termes, le coupleur le plus court possible qui puisse permettre une transition adiabatique sans pertes entre les guides d'onde.

Du point de vue technologique une structuration de la forme du guide d'onde III-V est complexe, nous avons décidé de laisser constante la largeur du guide d'onde III-V. La transition entre les deux guides est ainsi obtenue seulement grâce à la variation de la largeur du guide silicium.

En Figure 2.32 nous montrons les caractéristiques d'un design de ce type. Le guide silicium est en arête avec une épaisseur de 500 nm et une profondeur de gravure de 250 nm. L'épaisseur plus importante du guide silicium est fondamentale pour obtenir un bon couplage optique tout en gardant un guide III-V large et sans gravure de la couche active. Le guide III-V a une structure ruban sans gravure des puits quantiques et une largeur de 2 μm sur toute la longueur du composant. Le guide silicium passe, dans la section de couplage, d'une largeur de 270 nm à une largeur de 1.97 μm . Cette transition de largeur se fait suivant le critère d'adiabaticité, la forme obtenue rappelle en partie celle d'une courbe Gaussienne. Comme on peut constater en Figure 2.34 cette structure permet de rejoindre des efficacités de couplage qui dépassent 90% avec un coupleur de seulement 50 μm .

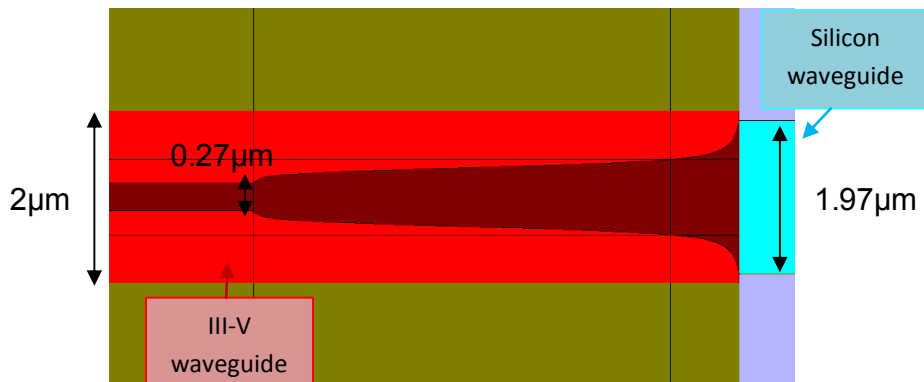


Figure 10: vue de dessus schématique du coupleur optimisé dans le cas d'un guide silicium de 500 nm d'épaisseur

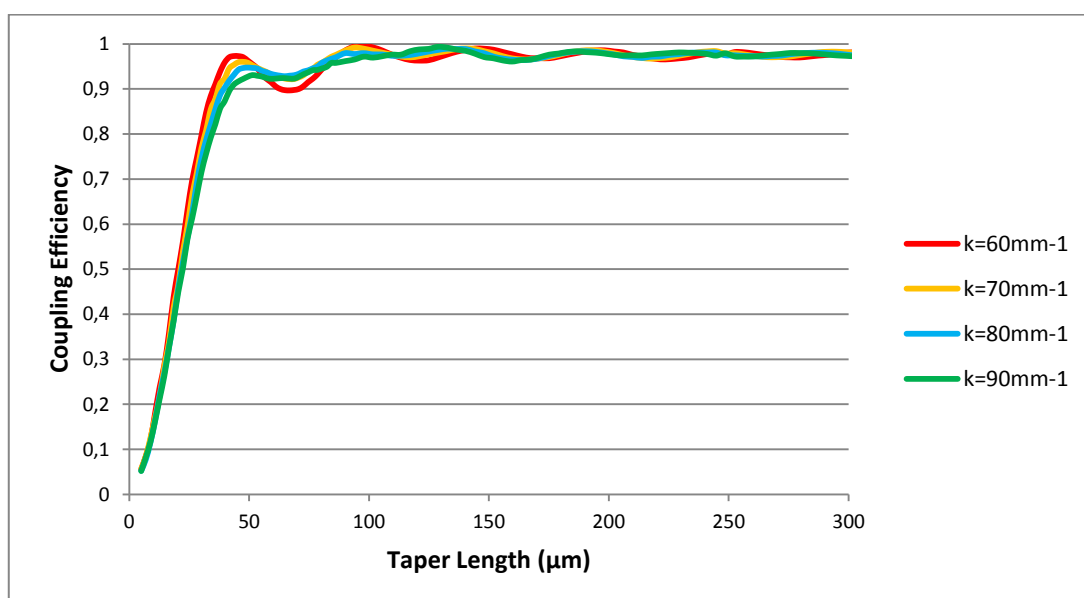


Figure 11: efficacité de couplage d'un coupleur optimisé pour différent valeur du coefficient de couplage

7.4 Comment obtenir un laser monomode

Les systèmes de communication qui permettent d'obtenir de grandes bandes passantes emploient le multiplexage en longueur d'onde. Pour permettre ce type de transmission des lasers mono longueur d'onde sont nécessaires. Plusieurs solutions peuvent être adoptées pour réaliser un laser mono longueur d'onde avec une architecture hybride III-V sur silicium.

7.4.1 Laser DBR

Un laser DBR (18) (à miroir de Bragg distribué) peut être schématiquement représenté en Figure 3.1. Il contient une section active qui fournit le gain optique, une section de Bragg qui se comporte comme un miroir sélectif en longueur d'onde, et une section de phase nécessaire pour obtenir un accord fin en longueur d'onde. On obtient un accord en longueur d'onde du laser en modifiant l'indice de réfraction dans la section de phase et dans la section de Bragg par injection de porteurs.

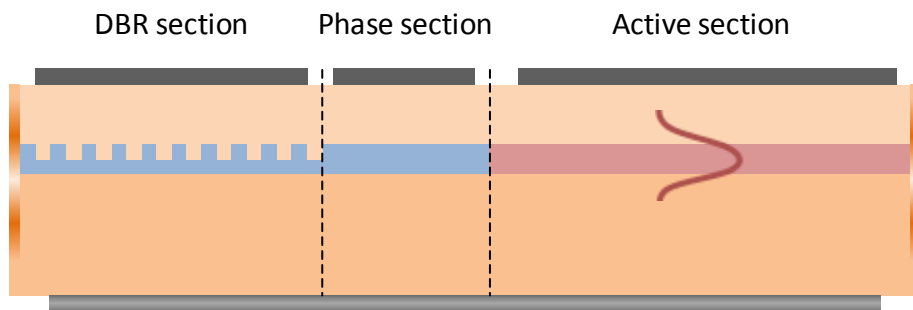


Figure 12: vue schématique d'une structure DBR standard

Ce type de laser a déjà été démontré en technologie hybride III-V sur silicium. Le miroir de Bragg et la section de phase sont réalisés dans des guides d'onde silicium alors que le gain optique est fourni par le guide III-V, les deux sections sont reliées par un coupleur adiabatique. Compte tenu de la variation d'indice qu'on peut obtenir dans le silicium par variation de température locale, ou par injection de porteurs, nous déduisons que l'accordabilité maximale dans ces structures est de l'ordre de quelque nanomètre.

Des structures laser de Bragg avec réseau échantillonné peuvent également être envisagées. Ces structures permettent d'obtenir une accordabilité plus importante (environ 40 nm), mais se caractérisent aussi par une taille plus grande du composant.

7.4.2 Laser avec miroirs en anneau résonateur

Les lasers avec miroirs en anneau résonateur ont été introduits en 2001 par J.E. Bowers (19). Ce genre de structure peut profiter d'une structure hybride car les anneaux résonateurs en silicium ont une taille bien plus petite que dans les technologies III-V.

Nous proposons d'utiliser des structures basées sur un design à deux anneaux résonateurs. Chaque anneau, inséré dans une configuration opportune, introduira un peigne de piques de transmission qui filtrera la lumière émise par la section III-V. En utilisant l'effet Vernier entre ces deux peignes qui ont des différentes valeurs d'intervalle spectral libre nous pouvons sélectionner la longueur d'onde d'émission du laser. Nous pouvons ensuite accorder la longueur d'onde du laser en chauffant localement les anneaux, nous avons calculé une accordabilité de 30 nm (Figure 14).

Les détails des designs employés sont résumés en Figure 13.

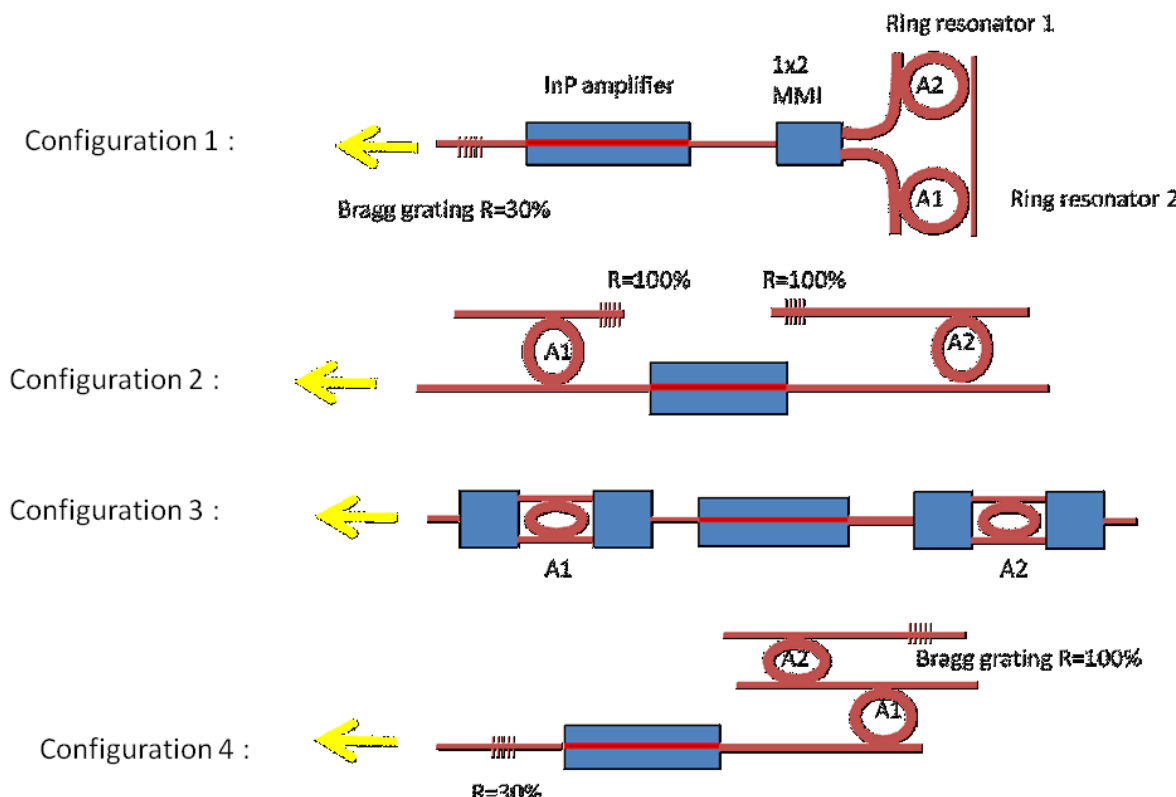


Figure 13: designs conçus pour des structures à double anneau résonateur

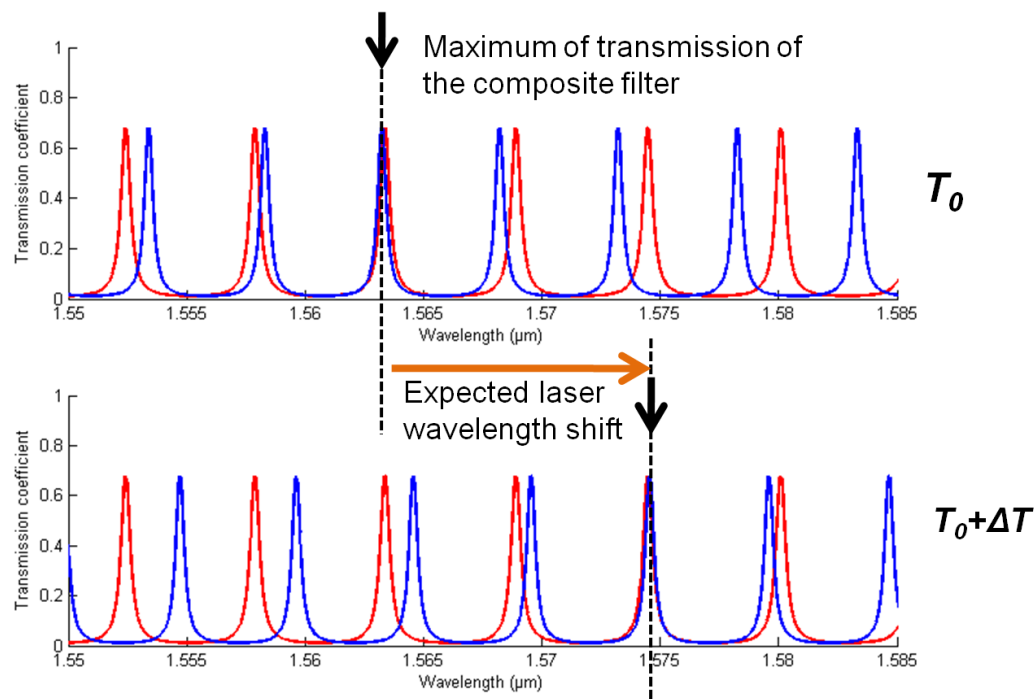


Figure 14: coefficient de transmission des deux anneaux résonateurs avec ISL de 610 Ghz (rouge) et 680 Ghz (bleu). Le graphique en bas montre la transmission du premier anneau lorsque il est chauffé de 18° ; la longueur d'onde du laser passe de 1.563 μm à 1.574 μm

La largeur spectrale d'émission est un paramètre important pour beaucoup d'applications. Nous avons effectué de calculs de largeur spectrale pour nos structures à anneaux résonateurs. Nous avons pris comme référence un laser Fabry-Perot avec deux miroirs de Bragg large bande. Le produit largeur spectral - puissance du laser de référence est dans la plage 20-100 MHz mW. Ensuite nous avons calculé la réduction de la largeur spectrale due à la présence des anneaux résonateurs en utilisant un modèle de réflectivité effective. En Figure 3.17 nous présentons la réduction de la largeur spectrale obtenue avec des résonateurs en configuration de transmission ou réflexion, pour une finesse des résonateurs égale à 13.

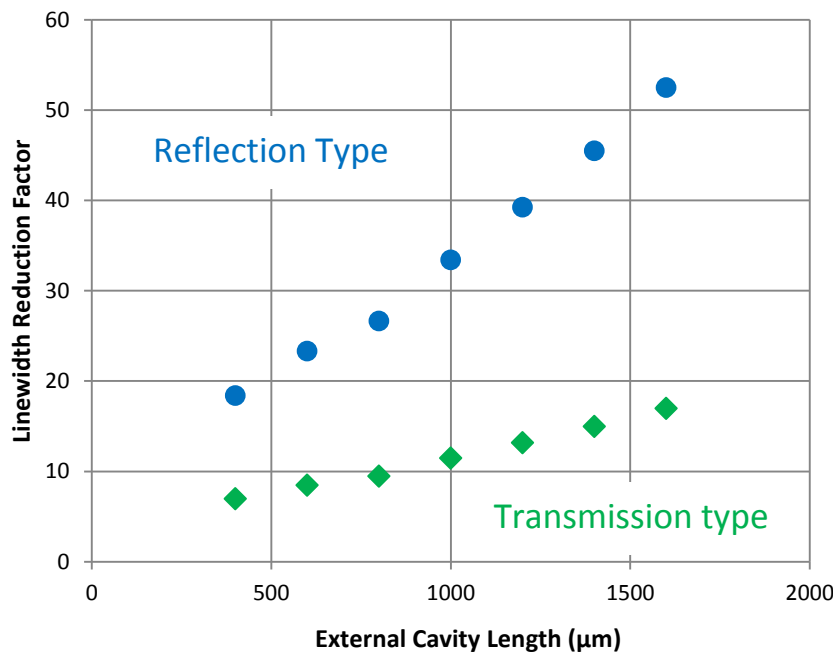


Figure 15: réduction de la largeur spectrale en fonction de la longueur de la cavité externe avec des résonateurs en configuration de transmission ou réflexion, pour une finesse des résonateurs égale à 13.

En Figure 3.18 nous présentons le facteur de réduction de la largeur spectrale d'émission en fonction de la finesse des résonateurs pour une cavité externe de 1000 μm de longueur. Nous en déduisons donc que le facteur de réduction de la largeur spectrale peut arriver à 50, le produit largeur spectrale – puissance sera donc dans la plage : 400 kHz – 2 Mhz mW.

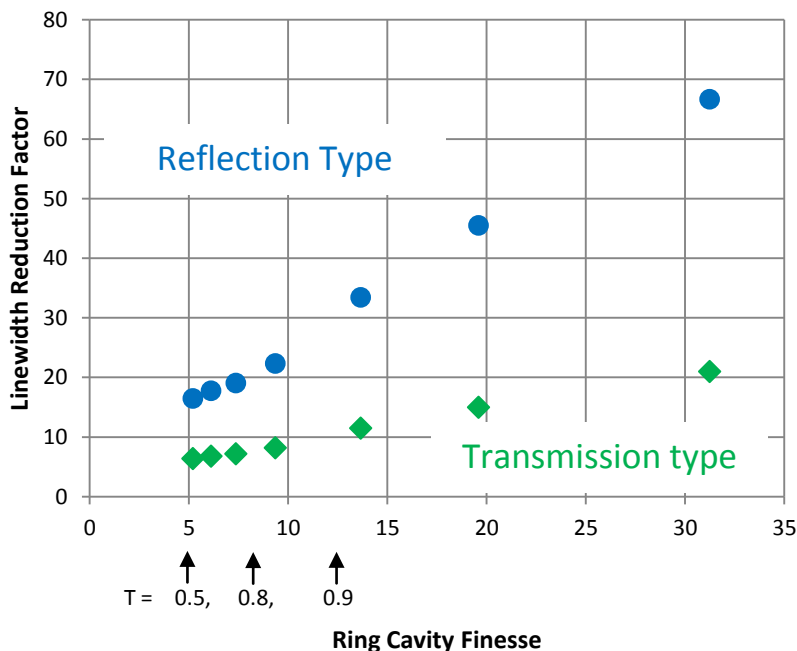


Figure 16: réduction de la longueur d'onde en fonction de la finesse des résonateurs pour une longueur de la cavité externe de 1000 μm

7.4.3 Laser DFB

Les lasers DFB ou à rétroaction distribuée représentent une solution très efficace au problème de l'émission monomode (20). Dans un laser DFB une structure périodique est embarquée dans le guide d'onde actif et se comporte comme un miroir distribué. Le miroir distribué peut permettre de verrouiller la longueur d'onde d'émission du laser à la longueur d'onde résonante avec la période du réseau. Un laser DFB peut être réalisé suivant différents schémas. Une structure hybride multiplie les solutions possibles pour le design. Dans la suite nous allons lister les configurations DFB possibles dans le cas d'une structure hybride et nous détaillerons les designs que nous avons conçus.

7.4.3.1 Laser DFB avec corrugation du guide d'onde actif

La structure de ce type de composant est montrée en Figure 3.20. Il s'agit d'utiliser un guide actif corrugé le long son hauteur. La forme du guide d'onde est définie par lithographie électronique avec une seule étape, la couche contact et la couche de InP dopé p sont ensuite gravé jusqu'aux puits quantiques. Cette structure est probablement la plus simple, mais présente un certain nombre de difficultés technologiques. La gravure d'un guide d'onde corrugé avec des dois d'environ 120 nm de longueur et 1.8 µm de profondeur n'est pas une opération triviale. En Figure 3.22 nous présentons nos résultats de simulation pour le coefficient de couplage en fonction de la largeur de corrugation du guide d'onde III-V.

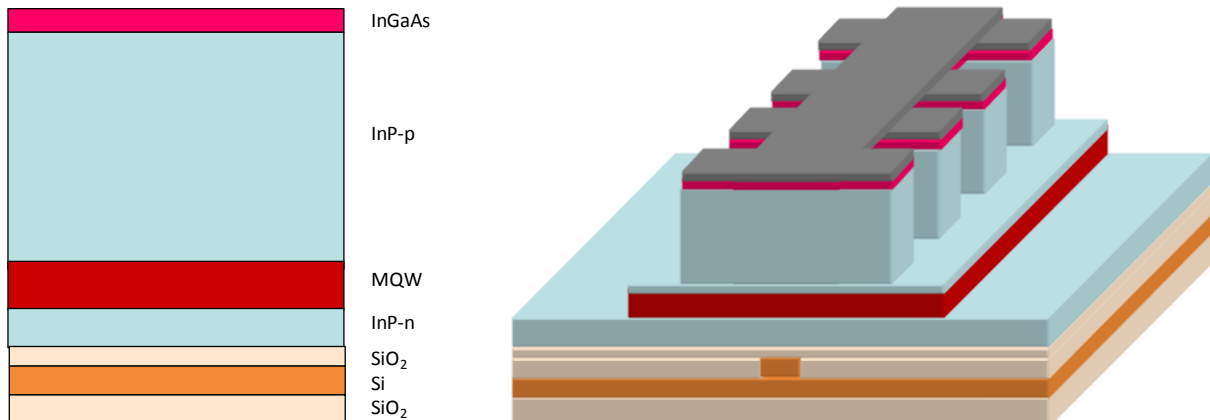


Figure 17: vision schématique d'un laser DFB avec corrugation du guide actif

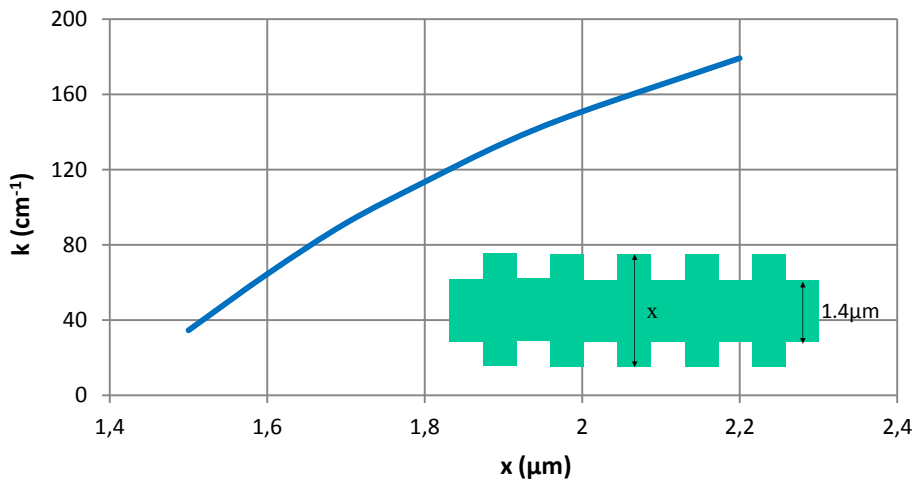


Figure 18: évolution du coefficient de couplage en fonction de la largeur x du réseau

7.4.3.2 Laser DFB avec couche réseau gravée au tour du guide d'onde actif

La structure de ce type de composant est montrée en Figure 3.23. Nous introduisons dans l'empilement des couches III-V une couche InP dite « spacer » et une couche réseau en InGaAsP. Par rapport à la structure précédente la fabrication prévoit deux étapes. Une première gravure des couches dopées p qui définit un ruban droit et qui s'arrête sur le couche réseau. Une deuxième gravure, avec un masque défini par lithographie électronique, qui grave le couche réseau en définissant le miroir distribué. La fabrication est plus simple car la gravure du réseau n'est pas profonde (entre 30 et 100 nm). En Figure 21 nous présentons nos résultats de simulation pour le coefficient de couplage et le confinement dans la couche d'InP dopé p en fonction de l'épaisseur de la couche réseau. En Figure 20 est détaillée l'épitaxie employée dans nos simulations.

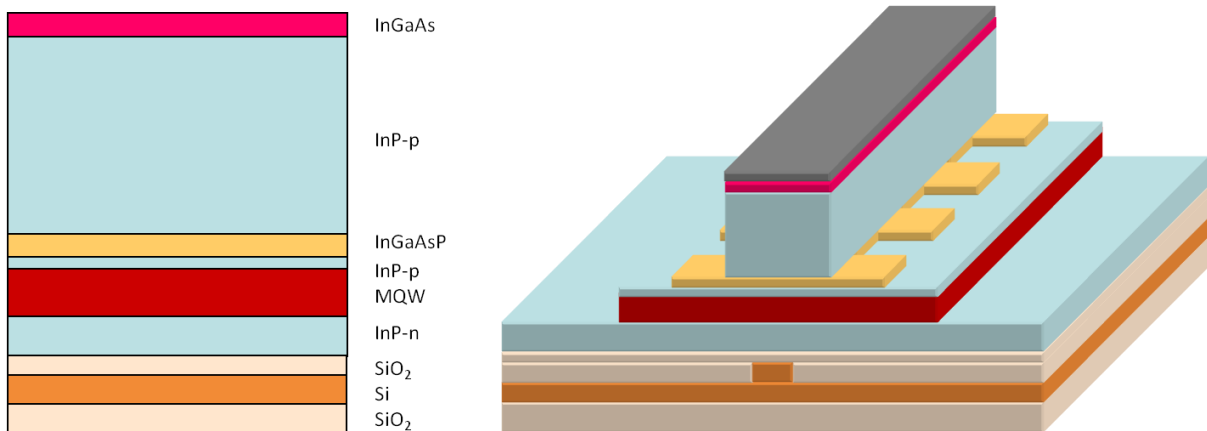
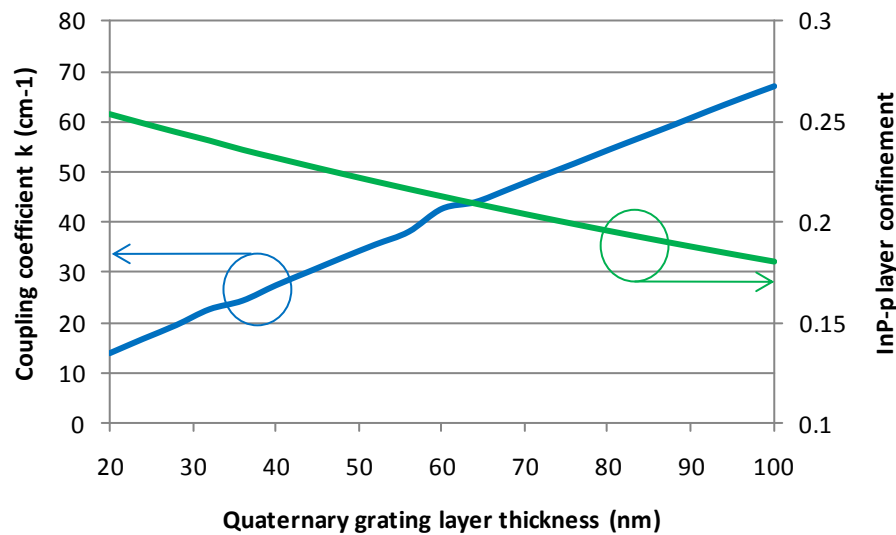


Figure 19: vue schématique du laser DFB avec couche réseau gravé au tour du guide actif

layer nb	layer type	nb of periods	material	PL wavelength	thickness	carrier conc.	type
10	cladding n		InP		200	1,0E+18	n
9	SCH		InGaAsP	1,17	100		nid
8	MQW_w	6	InGaAsP	1,55	8		nid
7	MQW_b	5	InGaAsP	1,17	10		nid
6	SCH		InGaAsP	1,17	50		nid
5	spacer		InP		30		nid
4	grating layer		InGaAsP	1,17	x		nid
3	cladding p		InP		1500	1E18->5E18	p
2	transition		InGaAsP	1,17	20	1,0E+19	p
1	contact p		InGaAs		300	3,0E+19	p
substrate			InP				N

Figure 20: structure détaillé de l'épitaxie III-V employé**Figure 21:** coefficient de couplage et confinement dans la couche InP-p pour différents épaisseur de la couche réseau

7.4.3.3 Laser DFB avec couche réseau gravée avant collage

La structure de ce type de composant est montrée en Figure 22. Dans ce cas nous avons aussi une couche réseau dans l'épitaxie mais le réseau est gravé avant collage, une étape de récroissance permet ensuite de déposer les puits quantiques et la couche de InP-n. Apres collage le guide d'onde est défini avec une seule étape de gravure qui définit un ruban droit. Cette structure a l'avantage de

se rapprocher le plus à la technologie qui est majoritairement utilisée dans le matériaux III-V pour des raison de fiabilité et robustesse. Cependant les couts de fabrication de cette solution sont plus élevés. Un alignement précis, donc onéreux, est nécessaire lors du collage pour assurer que le réseau soit bien superposé et parallèle au guide silicium, en plus l'étape d'écriture du réseau dans le wafer III-V suivi par une récroissance épitaxiale rajoute un coût non négligeable. Cette structure a fait l'objet d'un brevet pendant cette thèse.

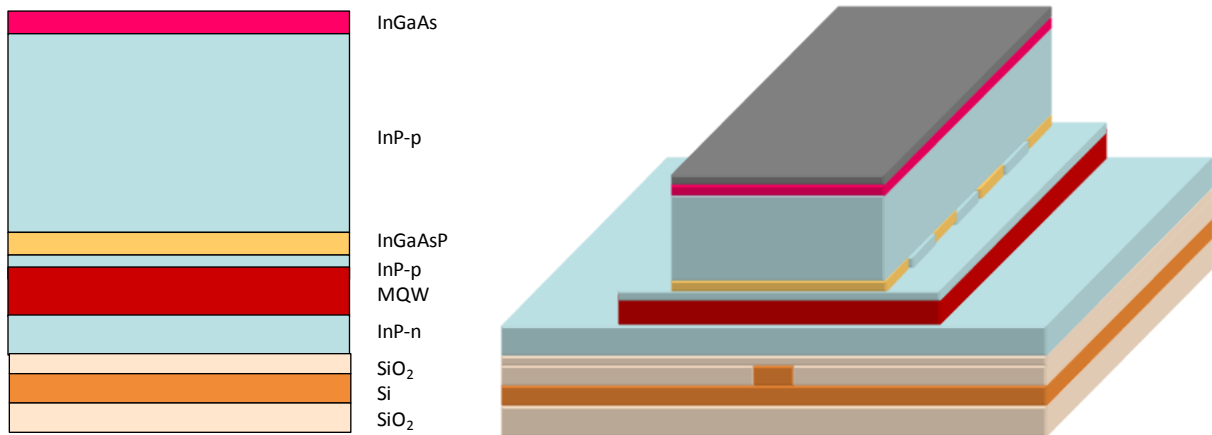


Figure 22: vue schématique d'un laser DFB avec réseau fabriqué avant collage

7.4.3.4 Laser DFB avec couche dans le guide silicium

Le réseau est cette fois localisé dans le silicium et non dans la partie III-V. Il s'agit d'une configuration qui a déjà été démontrée en littérature pour des lasers en configuration « évanescante ». Cette approche conduit à des valeurs du coefficient de couplage très élevé et donc à une faible rendement des lasers. Dans ce manuscrit on se concentre sur la configuration à transfert total de mode, donc au cas où la lumière est intégralement guidée par la partie III-V dans la section DFB du composant. Ce sera le silicium qui verra seulement une partie évanescente du mode optique, en permettant d'obtenir plus facilement de faibles valeurs du coefficient de couplage.

Une vue schématique de la structure proposée est présentée en Figure 23. Dans le silicium on trouve au centre le réseau de Bragg, obtenu en gravant un guide en arête de 1 µm de largeur, 400 nm d'hauteur et une gravure de 180 nm. Aux bords du réseau deux coupleurs adiabatiques permettent de transférer le mode du guide III-V au guide silicium.

Les simulations ont pour objectif d'évaluer l'impact de la variation d'épaisseur de la couche de collage sur les performances du composant, en particulier en termes de longueur d'onde émise et de coefficient de couplage. Les résultats sont montrés en Figure 3.28. Si on considère une valeur optimum d'épaisseur de 60 nm, une tolérance de fabrication de ± 10 nm enduit une incertitude de 0.72 nm sur la longueur d'onde émise et permet à la valeur de k de varier entre 45 et 70. Un contrôle fin de l'épaisseur de la couche de collage est donc indispensable pour obtenir un comportement reproductible des composants fabriqués.



Figure 23: vue schématique du dessus et coupe latérale d'un DFB hybride avec réseau dans le silicium

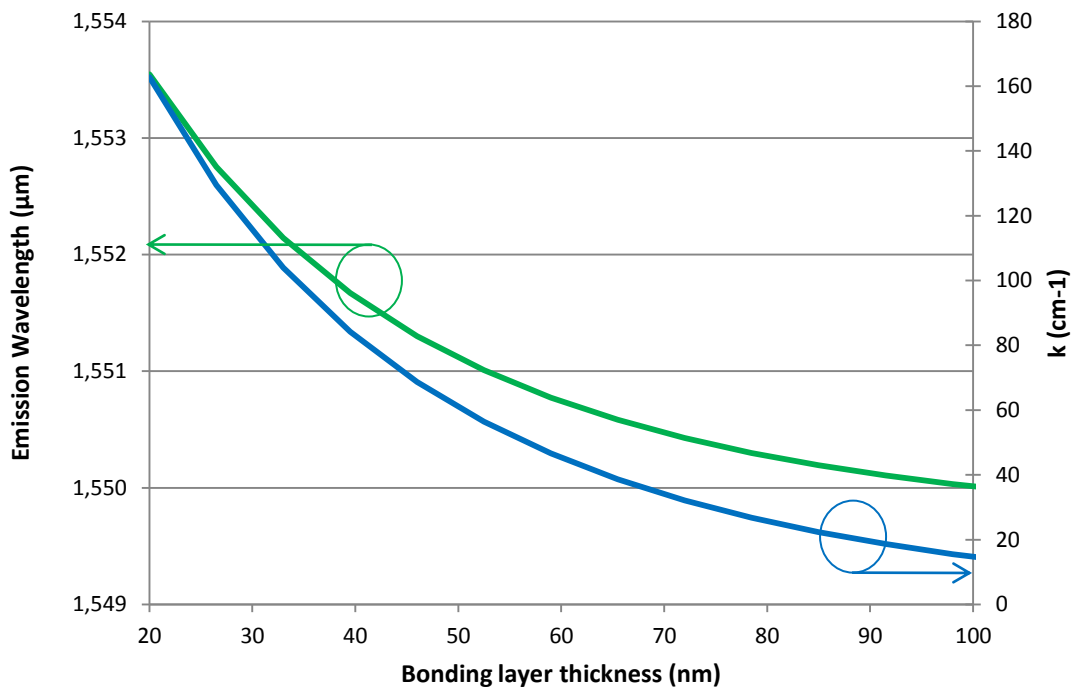


Figure 24 : longueur d'onde émise et coefficient de couplage simulés en fonction de l'épaisseur de la couche de collage

7.4.3.5 DFB laser à réseau d'échange

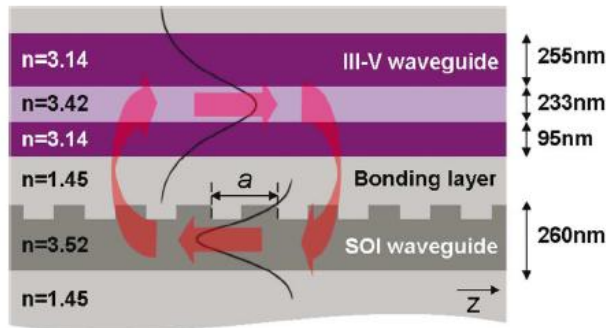


Figure 25: structure du laser DFB à réseau d'échange

Un nouveau type de laser DFB a été proposé récemment par T. Dupont et al. (21), l'idée est de profiter du couplage contra-directionnel entre le mode confiné dans le guide III-V et le mode confiné dans le silicium (Figure 3.29). Ce type de couplage permet d'obtenir un miroir distribué de type DFB et en même temps de partager la puissance optique entre les deux guides d'ondes. Ce type de design est compatible avec des épaisseurs de collage de l'ordre de 200 nm et relâche donc un certain nombre des contraintes d'intégration. Cependant aucune analyse théorique n'a été effectuée sur ce type de laser jusqu'à présent. Dans cette section du manuscrit nous analysons quantitativement ce type de DFB avec un modèle à modes couplés. Nous avons évalué en particulier le spectre d'émission et l'efficience externe de ces composants en configuration réseau uniforme et réseau à saut de phase.

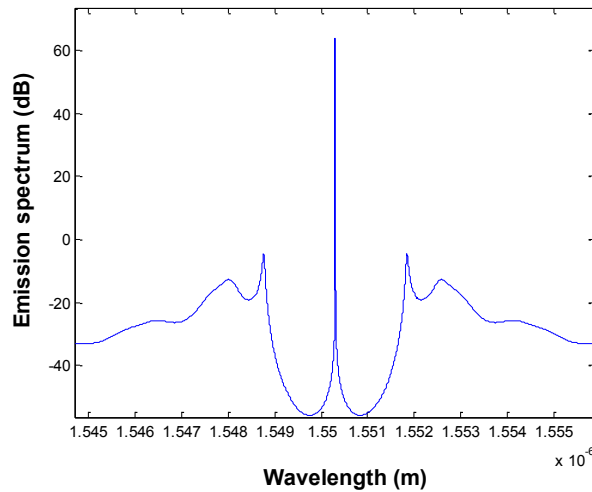


Figure 26: spectre d'émission pour un laser DFB à réseau d'échange avec saut de phase

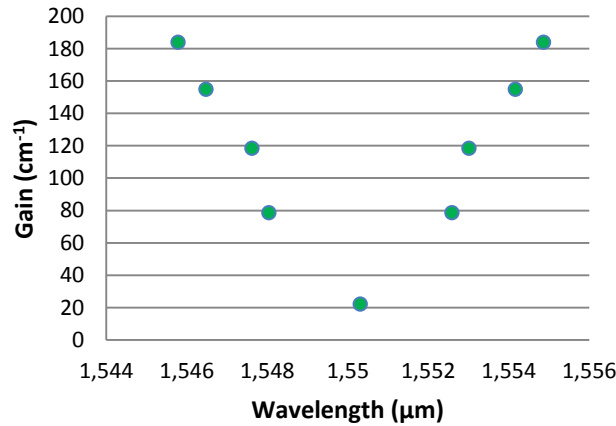


Figure 27: gain au seuil pour différents modes dans un laser DFB à réseau d'échange avec saut de phase

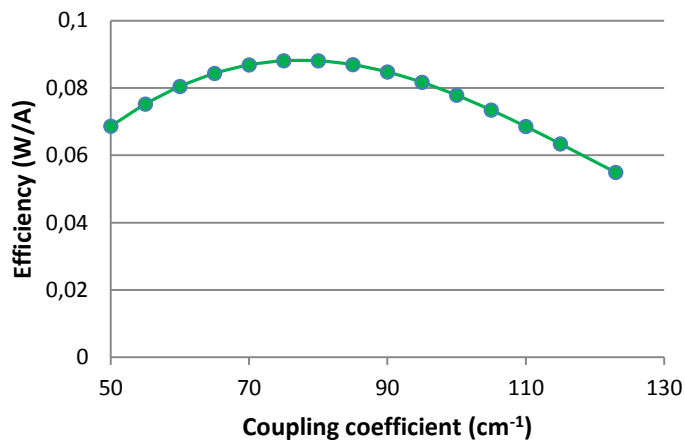


Figure 28: efficience externe du laser DFB à réseau d'échange avec saut de phase en fonction du coefficient de couplage

Les résultats des simulations sont présentés en Figure 3.33, Figure 3.34, Figure 3.35. Les simulations montrent que le laser DFB à réseau d'échange a des caractéristiques semblables à celles de DFB classiques. Surtout nos simulations montrent que ce type de laser a une efficience plutôt faible, limité d'une coté par le fort gain au seuil et de l'autre côté par le fort confinement des photons à l'intérieur de la cavité. Nous avons déterminé aussi la valeur optimale du coefficient de couplage qui permet d'obtenir l'efficience externe plus élevée.

7.4.3.6 Laser AWG

Les lasers AWG ont été introduits par M. Zirngibl et al. en 1994 (22). Ce type de composant permet la réalisation des sources laser multi longueur d'onde intégrées et de lasers à longueur d'onde sélectionnable. Dans le cas des lasers hybride cette géométrie est particulièrement intéressante vu que la taille des AWG est particulièrement réduite en technologie SOI par rapport aux technologies III-V.

En Figure 3.36 nous montrons les diagrammes de principe des deux configurations possibles. Toutes les parties en bleu dans la figure sont réalisées en silicium passif, lorsque les parties en rouge sont

réalisés en III-V, les guides d'onde silicium et les guides d'ondes III-V sont toujours reliés par des coupleurs adiabatiques. La première configuration, à gauche dans la figure, permet de réaliser un laser multi longueurs d'onde. Une série de sections d'amplification III-V sont placées sur les canaux du côté demultiplexé d'un AWG. Un miroir de Bragg large bande à haute réflexion (100%) est placé à la gauche de chaque amplificateur et un Bragg large bande avec une réflexivité de 30% est placé du côté multiplexé de l'AWG. Dans une géométrie de ce type chaque section d'amplifications est placée au milieu d'une cavité Fabry-Perot formée par le miroir de Bragg à sa gauche et le miroir à la droite de l'AWG. L'AWG se comporte comme un filtre spectral, qui sélectionne un mode particulier de la cavité Fabry-Perot. Vue que l'AWG sélectionnera une longueur d'onde différente pour chaque canal on obtiendra un laser multi longueur d'onde à la sortie multiplexeur du AWG.

La deuxième configuration, à droite dans la figure, permet de réaliser un laser à longueur d'onde sélectionnable. La structure est similaire à la précédente, à la différence que une section amplificatrice et un autre miroir de Bragg large bande et de réflectivité 30% s'ajoutent à la droite du AWG. Dans ce cas la cavité Fabry-Perot se forme à la droite du AWG, les canaux à la gauche se comportent comme des RSOA. En injectant du courant dans une des sections amplificatrices à gauche on va réinjecter dans la cavité Fabry-Perot de la puissance optique sur la bande de longueur d'onde filtré par le AWG. De cette façon on peut verrouiller l'émission du laser à la longueur d'onde du canal de l'AWG que l'on allume.

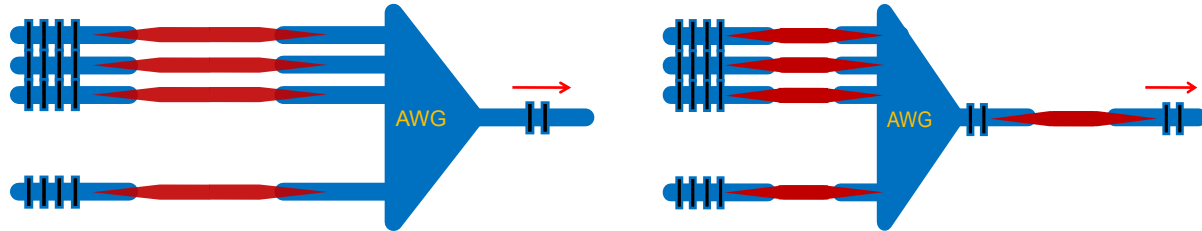


Figure 29: diagramme schématique d'un laser AWG hybride à gauche et d'un laser AWG hybride en configuration IFF à droite

7.5 Fabrication

La fabrication de nos composants peut être divisée en trois macro-parties : la fabrication du SOI, le collage, la fabrication du III-V.

La fabrication de la partie SOI de nos composants a été effectuée au CEA-LETI. Les substrats SOI (plaques 200 mm produites par SOITEC) utilisés dans ce travail sont composés d'une couche monocristalline de silicium au-dessus d'une couche épaisse (2 µm) d'oxyde de silicium sur un substrat silicium. Trois étapes successives de lithographie et de gravure ont été utilisées pour réaliser les structures passives dans la couche silicium. Pour chaque séquence, après une déposition d'un masque dure de silice, les structures ont été définies par une lithographie UV 193 nm suivie d'une gravure du masque dur. Les motifs sont transférés dans la couche silicium en utilisant un procès de gravure sèche à base de HBr.

Les plaques InP/InGaAsP ont été épitaxie au III-V lab par épitaxie à jet moléculaire.

Le collage moléculaire et le collage DVS-BCB ont été utilisés. Le premier a été réalisé au CEA-LETI, le second au IMEC-Gent.

La fabrication après collage a été effectuée au III-V lab. Ce travail se concentre principalement sur cette partie de la fabrication que j'ai intégralement mise au point pendant cette thèse. Ci-dessous je décris les résultats de mes expériences et je compare entre elles les différentes solutions envisagées.

Plusieurs étapes technologiques sont nécessaires pour réaliser les composants lasers. Une ou plusieurs étapes de gravure sèche et/ou humide permettent de définir le guide actif. Les lithographies UV 248 nm, 405 nm et également la lithographie électronique peuvent être utilisées. Des dépôts métalliques assurent les contacts n et p de la diode laser, des dépôts de silice ou de BCB permet d'obtenir l'isolation électrique entre différentes sections du composant.

Conceptuellement similaire par rapport aux procès de fabrications employés pour les composants III-V, la fabrication des composants hybrides est rendue complexe par la morphologie particulière des échantillons et par le manque de retour d'expérience sur ces structures.

7.5.1 Collage

La qualité du collage est d'extrême importance pour la qualité des lasers hybrides intégrés. Comme nous avons vu dans les sections précédentes, l'épaisseur de la couche de collage joue un rôle important pour les performances du laser. Le rendement du collage est aussi un paramètre important, spécialement en vue d'une réelle commercialisation de ces composants, mais il n'est pas encore au rendez-vous.

Dans ce travail nous avons utilisé deux techniques de collage et nous avons pu réaliser des composants performants soit avec le collage moléculaire soit avec le collage DVS-BCB. Cependant ces deux solutions présentent des caractéristiques différentes et aucune des deux ne s'est encore imposée comme le standard à employer.

Le collage moléculaire s'est démontré, pendant nos expériences, plus sensible aux défauts épitaxiales et aux contaminations des surfaces. La présence de défauts ou de particules peut amener à la formation de cloques comme on voit en Figure 4.4. Ces boules peuvent s'arracher pendant le procès, spécialement dans le cas de recuits rapides des échantillons.

Le collage DVS-BCB s'est démontré plus résistant de ce point de vue mais présente d'autres problèmes. La compatibilité avec le procès CMOS est à démontrer, la température maximale de recuit ne peut pas dépasser le 360-380°C, l'épaisseur de collage est difficile à maîtriser et le procès reste encore peu automatisé.

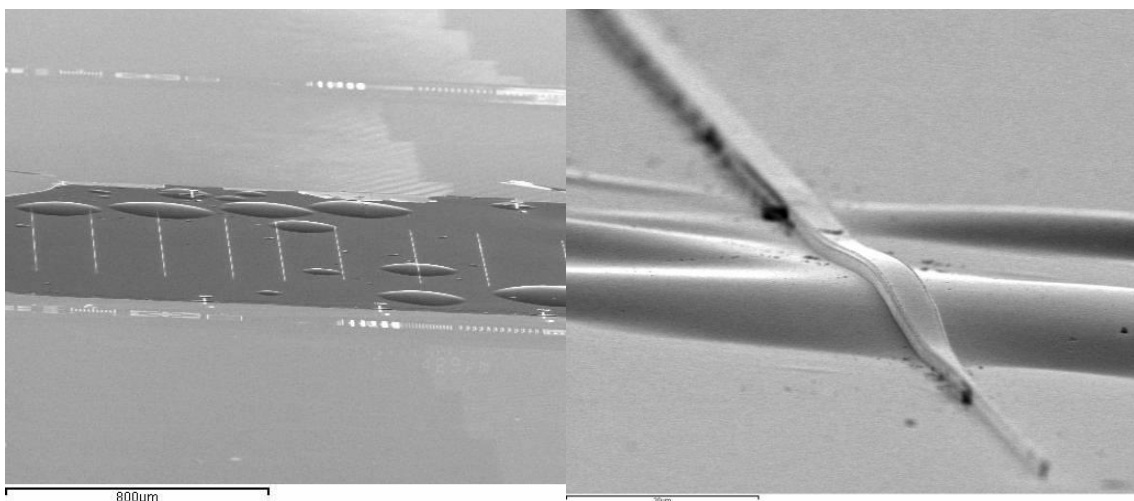


Figure 30 (a) photo MEB d'une vignette III-V collée sur une plaque SOI avec plusieurs défauts de collage
(b) photo MEB d'un ruban laser gravé sur un défaut

7.5.2 Lithographie

La lithographie de contact est sans doute la plus utilisée dans la technologie III-V à cause du faible coût qu'elle engendre. Cette technique est cependant complexe sur des échantillons hybrides pour deux raisons. La résolution de cette lithographie est fortement influencée par la qualité du vide qui s'installe entre le masque de lithographie et l'échantillon. Or la topologie et la forme irrégulières des échantillons hybrides ne permettent pas une bonne qualité de ce vide et donc de la lithographie. Topologie et forme imparfaites des échantillons sont dues aux défauts de collage et aux découpes de la plaque 200 mm. La découpe de la plaque qui vise à la rendre compatible avec les équipements utilisés pour la technologie III-V, conçus pour des tailles de plaque entre deux et quatre pouces.

En Figure 4.11 nous montrons une pointe de coupleur transférée dans le semiconducteur par lithographie de contact 405 nm. La pointe dans le masque chrome avait une largeur de 400 nm, mais, comme nous voyons dans l'image du microscope électronique à balayage, elle a une largeur de 1 μm une fois transférée dans l'échantillon.

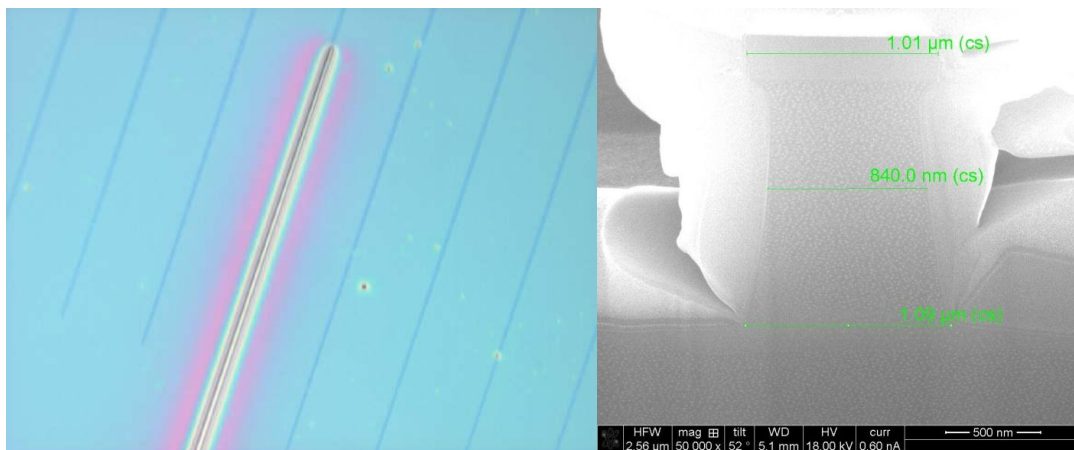


Figure 31: pointe de coupler définie par lithographie de contacte UV 405 nm, la largeur de départ sur le masque photo-lithographique était de 400 nm

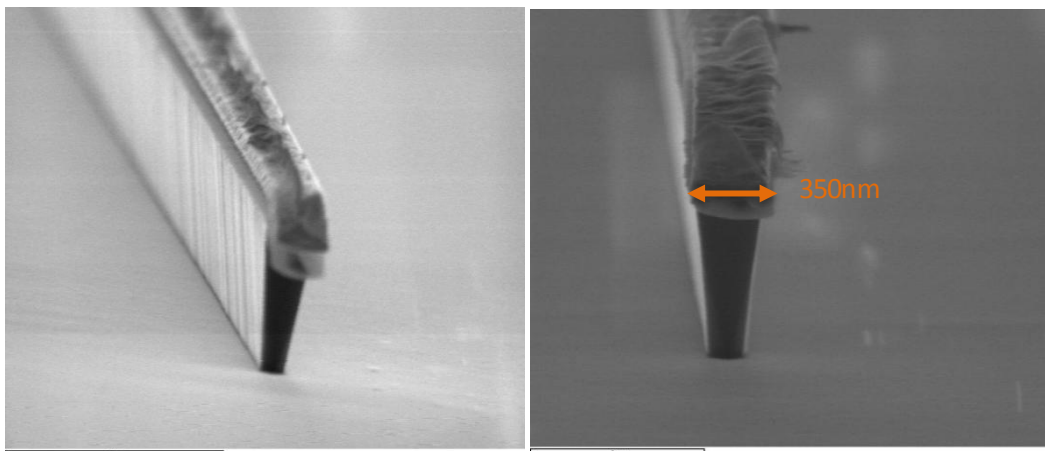


Figure 32: pointe de coupler définie par lithographie de contacte UV 248 nm, la largeur de départ sur le masque photo-lithographique était de 400 nm

Des meilleurs résultats ont été obtenus en passant d'une lithographie 405 nm à une lithographie 248 nm. En Figure 4.12 nous montrons des images MEB de la pointe de coupleur obtenue avec cette longueur d'onde UV. Au sommet de la gravure la largeur est d'environ 0.4 μm. Il faut souligner que ces résultats ne dépendent pas seulement du type de longueur d'onde UV utilisée. Selon la morphologie des échantillons les résultats connaissent une dispersion au niveau de la résolution, cependant la lithographie 248 nm s'est toujours révélée plus performante.

La lithographie électronique permet de résoudre les problèmes listés ci-dessus car elle n'est pas basée sur un contact physique entre le masque et l'échantillon. Des difficultés liées à la topologie et à la forme persiste en partie ; l'obtention d'un film homogène de résine étant difficile sur des substrats irréguliers. En Figure 4.14 et en Figure 4.15 nous présentons les résultats obtenus par lithographie électronique pour la définition de pointes à 200 nm et la gravure de réseau DFB le long du ruban.

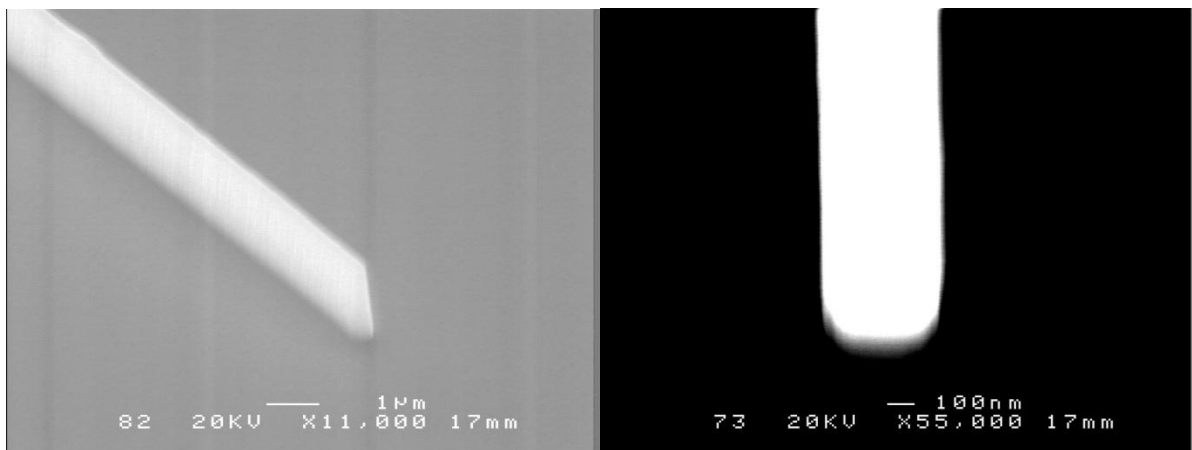


Figure 33: photos MEB d'une pointe transférée sur un échantillon hybride par lithographie e-beam et gravée par RIE

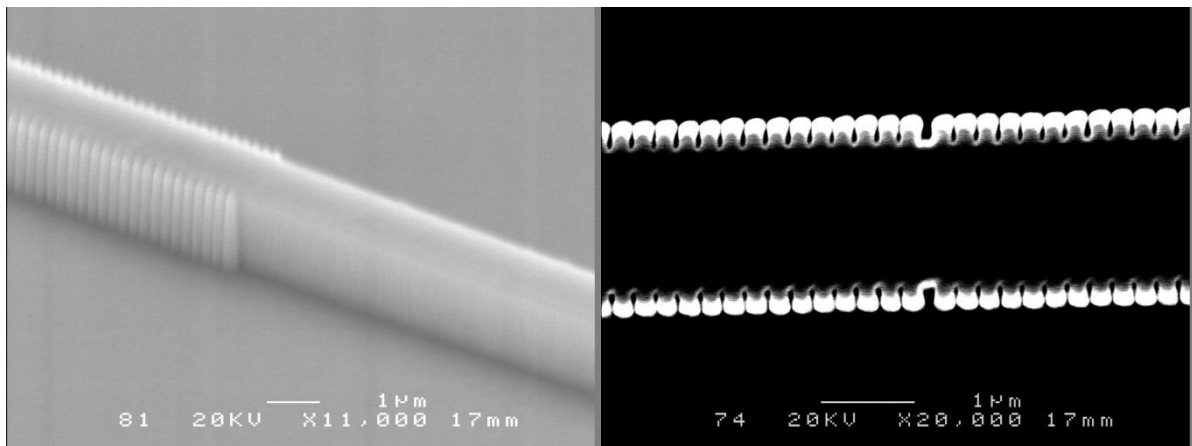


Figure 34: photos MEB d'un réseau de Bragg défini par e-beam et gravé le long le front du ruban par RIE, à droite un saut de phase dans le réseau

7.5.3 Gravure du III-V en configuration hybride

Nous avons étudié les différentes techniques de gravure sèche et humide en configuration hybrides. Les propriétés des gravures humides sur des échantillons hybrides se différencient peu de celles sur plaque III-V. Cependant, il faut tenir compte du changement d'orientation cristalline qui suit le collage, quand on utilise des bains de gravure anisotropes. Vu que l'épitaxie III-V est collée à l'envers sur la plaque SOI, avec la surface épitaxiée vers le bas et le substrat vers le haut, les plans cristallographiques sont inversés. En conséquence les solutions de gravure anisotropes, qui ont la caractéristique de révéler des plans cristallins, se comportent de façon très différent sur un substrat hybride par rapport à une plaque III-V.

Le comportement des gravures sèches est par contre nettement influencé par la structure hybride. Le substrat SOI se comporte comme un substrat isolant et modifie le comportement des plasmas de façon importante. La gravure RIE à base de méthane et hydrogène est la plus perturbée, la gravure

devient très inhomogène et lente, la formation de polymère sur la tête du masque de gravure est abondante, et la qualité des flancs de gravure très limitée.

La gravure IBE a introduit pendant nos essais des contaminations, probablement dues au redépôt du platine utilisé comme métal de contact et gravé au même temps que le semi-conducteur. Ces contaminations rendent le fond de gravure très rougeau et nous ont fait abandonné cette technique.

Finalement la gravure qui s'est comportée mieux a été la gravure ICP chlorée. Les fonds de gravure sont propres, les flans droits et peu rougeaux, l'uniformité excellente. Seul bémol de cette technique, elle grave aussi bien les semi-conducteurs III-V que le silicium ou la silice, dont la nécessité de protéger les zones qui ne sont pas couvertes par le III-V.

7.5.4 Enchainment techno

De cette série d'expériences nous avons pu définir un procédé de fabrication optimisé. Nous déposons sur toute la plaque une couche de titane et nous effectuons un recuit rapide à 400°C, nous déposons sur le titane un masque dur de silice par POCVD. Avec une lithographie de contact UV 248 nm nous définissant la forme du guide actif. Avec une gravure ICP chlorée nous gravons le titane, la couche ternaire de contact et nous démarrons la gravure de l'InP dopé p. La gravure de l'InP-p est terminée par gravure chimique sélective à base de HCl et H₃PO₄, cette solution arrête la gravure sur la couche SCH.

Un masque dur de silice est déposé, avec une lithographie contact UV 400 nm nous définissant la forme de la gravure de la couche puits quantiques. La gravure des puits est effectuée par RIE méthane-hydrogéné, nous arrêtons la gravure en tête de la couche de InP-n en utilisant un suivi interférométrique. Nous déposons un contact n du type titane/platine/or. Nous déposons par spin-coating une couche épaisse de BCB. Après recuit nous planarissons le BCB par plasma RIE en s'arrêtions sur la tête des rubans. Nous rechargeons les contacts p avec un alliage de type titane/platine/or, et nous ouvrons des voies dans le BCB pour pouvoir déposer la métallisation pour les contacts n.

7.6 Caractérisation

Dans cette section nous présentons les résultats de mesures obtenues sur les lasers fabriqués. Pendant les mesures les lasers sont placés sur un contrôleur de température. La puissance de sortie du laser est mesurée à l'aide d'un photodétecteur placé en face de la facette de sortie. Pour les mesures de spectre le faisceau laser a été couplé avec une fibre lentillée reliée à un analyseur de spectre. Les premiers résultats que nous avons obtenus sont montrés en Figure 5.3. Il s'agit de la caractéristique puissance-courant et du spectre d'émission d'un laser Fabry-Pérot du type décrit dans la section 7.3.2 basée sur un collage de type DVS-BCB. La mesure a été effectuée en régime d'injection impulsif. Dans ce cas le faisceau a été également couplé avec une fibre lentillée pour la mesure de puissance, nous estimons des pertes de couplage entre 6 et 8 dB.

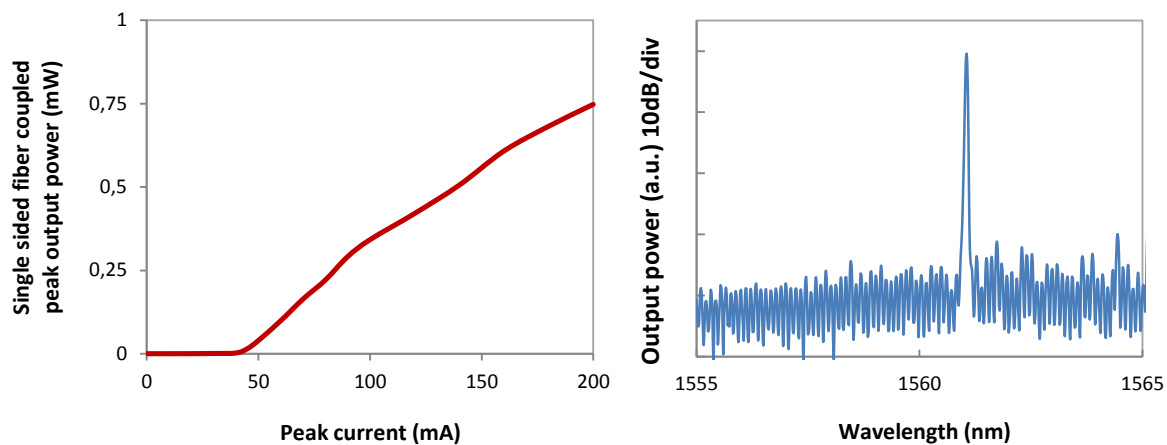


Figure 35: (a) caractéristiques puissance-courant en régime impulsif à 20°C (b) spectre optique du laser à 20°C pour un courant d'injection de 55 mA

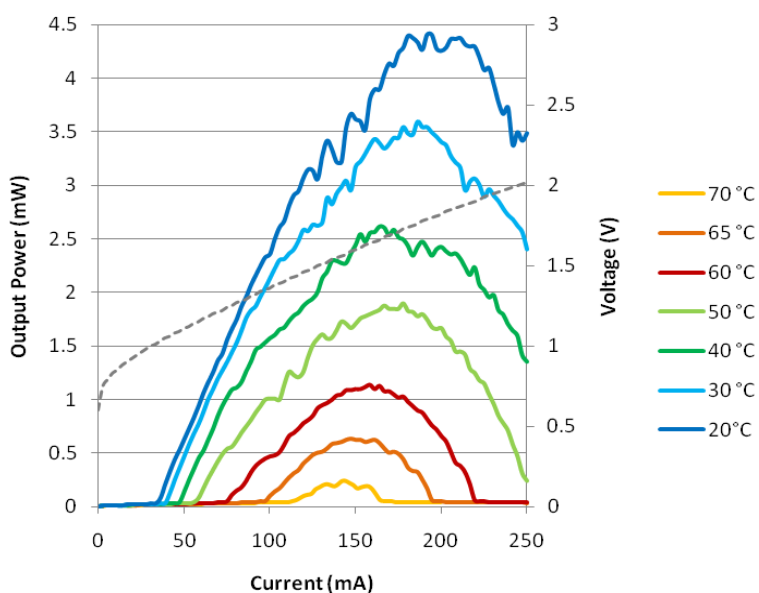


Figure 36: Puissance et tension (ligne pointillée) en fonction du courant injecté en régime continu pour différentes températures de fonctionnement, laser sans gravure de la couche active et avec collage DVS-BCB

En Figure 5.6 nous présentons les caractéristiques puissance-courant et tension-courant pour un laser Fabry-Pérot du type décrit dans la section 7.3.3 avec collage DVS-BCB. Les caractéristiques sont obtenues en régime continu pour différentes températures. Le spectre optique à 20°C est présenté en Figure 5.7.

Comme nous nous y attendions, cette structure présente des performances bien supérieures à celles du laser avec gravure de la couche active. Ces lasers présentent des seuils extrêmement faibles qui peuvent arriver à 28 mA à 20°C. Ce résultat représente l'état de l'art des lasers silicium Fabry-Pérot. La puissance maximale émise arrive à 4.5 mW et le laser émet encore plus que 1mW à 60°C. La résistance série est de 5 Ohms, le rendement externe est de 0,043 W/A.

Les deux designs présentent des spectres fortement perturbés, parfois monomode ; l'émission sur une seule longueur d'onde n'est cependant ni stable ni contrôlable. La perturbation du spectre Fabry-Pérot est due à la mauvaise qualité de la lithographie, l'impossibilité de définir des pointes fines pour le coupleur adiabatique réduit l'efficience de couplage. La puissance qui n'est pas couplée dans le guide silicium est réfléchie engendrant un système de cavités multiples. C'est l'accord de phase entre ces cavités, qui varie avec la température et l'injection, à déterminer les propriétés du spectre.

Nous n'avons pas pu effectuer des mesures de temps de vie statistiquement significatives, mais les propriétés supérieures en termes de robustesse de ces lasers par rapport à ceux fabriqués selon le précédent design ont été manifestes.

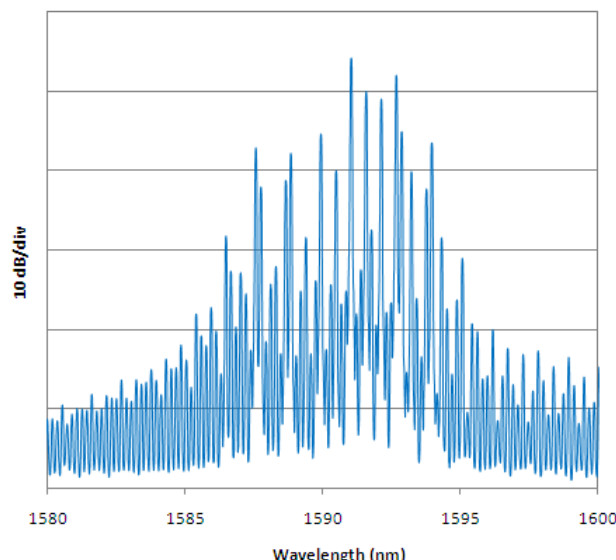


Figure 37: spectre optique du laser hybride Fabry-Pérot sans gravure de la couche active et avec collage DVS-BCB en régime continu

Des lasers qui reprennent la structure de la section 7.3.3 mais avec collage moléculaire ont été également fabriqués et caractérisés. Dans la Figure 5.11 nous présentons la caractéristique puissance courant et tension courant d'un de ces composants, en Figure 5.12 le spectre optique à 20°C. Les performances sont également positives mais légèrement inférieures. Il n'est pas possible d'attribuer cette différence au différent type de collage utilisé, la différence de performances est si faible qu'elle pourrait très bien être expliquée par une différence dans le procès de fabrication (différente

précision d'alignement, différente qualité du contact métal-semi-conducteur, ou encore épaisseur de la couche de collage différent).

Vu l'importance des effets thermiques sur le fonctionnement de ce genre de laser, les propriétés thermiques de ce dernier composant ont été également étudiées. Nous mesurons une température caractéristique T_0 de l'ordre de 48K et une température T_1 de 57K. Il s'agit de valeurs faibles même si elles sont comparables avec les valeurs obtenues pour des lasers III-V en InP/InGaAsP.

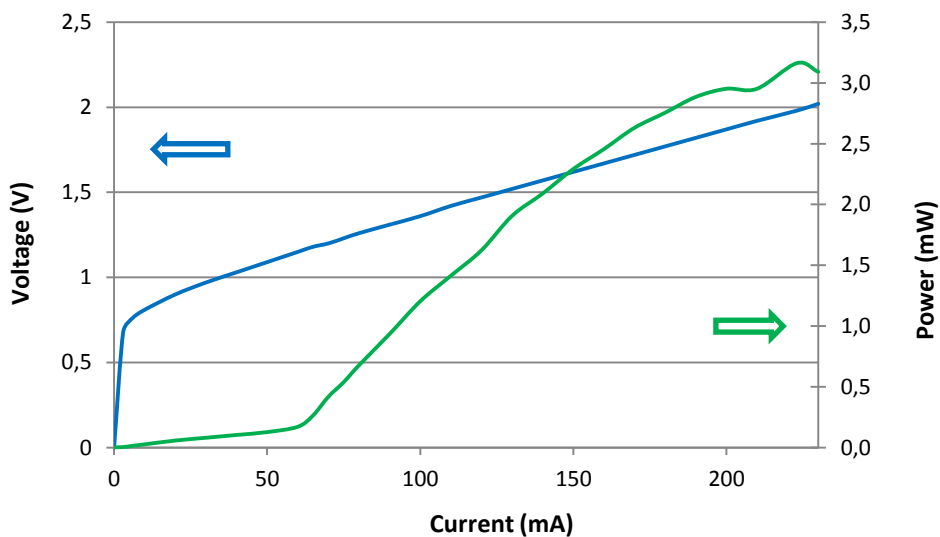


Figure 38: Caractéristiques $P(I)$ et $V(I)$ du laser hybride Fabry-Pérot basé sur un collage moléculaire

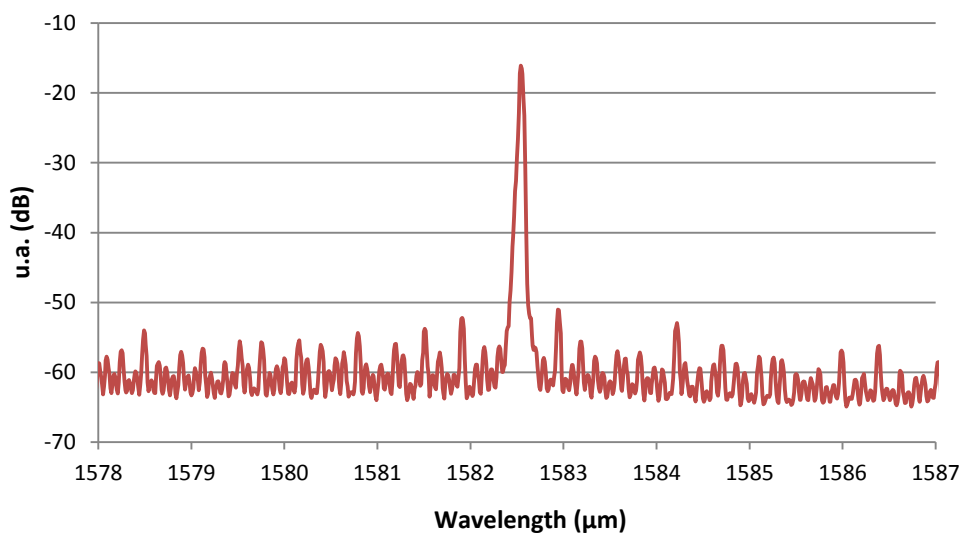


Figure 39: spectre optique du laser hybride Fabry-Pérot sans gravure de la couche active et avec collage moléculaire en régime continu à 20°C

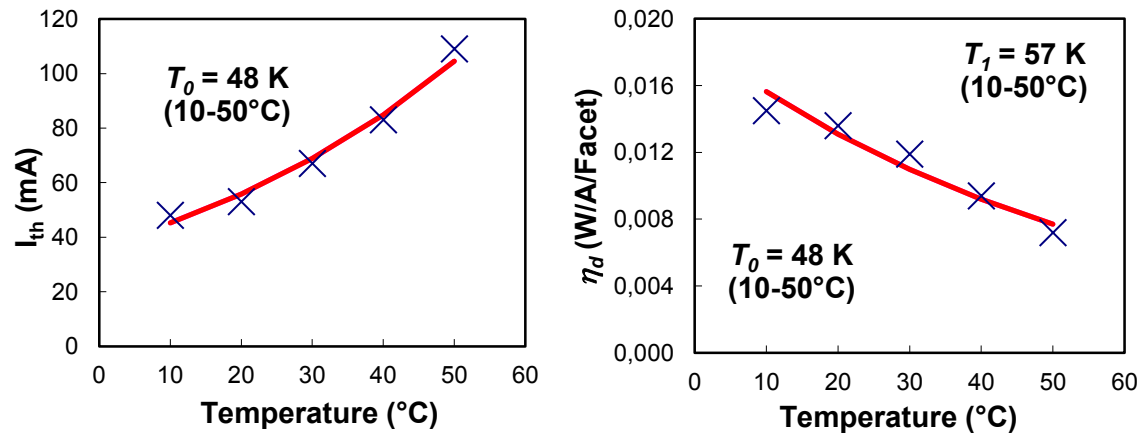


Figure 40: seuil et efficience externe du laser en fonction de la température

7.7 Conclusion

Les travaux présentés dans ce manuscrit portent sur la conception, la fabrication ainsi que la caractérisation des lasers hybrides III-V sur SOI pour des applications en télécommunications. L'hybridation III-V sur silicium repose sur un collage entre une plaque III-V entière ou découpée en vignettes et une plaque SOI. Des guides d'onde passifs en silicium sont structurés dans le SOI avant le collage, et des guides d'onde actifs sont structurés dans l'épitaxie III-V après le collage. Les lasers exploitent un transfert total de mode entre le guide actif et le guide passif par l'intermédiaire d'un coupleur adiabatique. La cavité laser est formée par l'ensemble du guide III-V, les coupleurs adiabatiques et les guides silicium. Le guide d'onde actif fourni le gain optique alors que la contreréaction optique est créée par des résonateurs ou de facettes dans les guides silicium.

Une étude complète du coupleur adiabatique a été effectuée. Une conception innovante basée sur un double coupleur adiabatique a été optimisée. Une nouvelle structure de guide actif III-V de ruban superficiel a été proposée et mise au point. Cette idée a fait l'objet d'un dépôt de brevet. La mise au point technologique de ces lasers hybrides a nécessité de grands efforts. Des lasers ont été réalisés selon l'idée du brevet, avec des conceptions optimisées et les procès de fabrication développés. Les performances ont atteint l'état de l'art. Plus particulièrement le seuil de ces composants est le plus faible parmi les résultats publiés dans la littérature pour des lasers hybrides du type Fabry-Pérot. Une version améliorée de cette conception, plus tolérante par rapport aux défauts de fabrication, a été également proposée sur des lasers hybrides avec l'épaisseur de guide silicium de 500 nm. Les composants basés sur cette conception sont actuellement en phase de fabrication.

La conception de laser hybride III-V sur SOI avec émission mono longueur d'onde a également été menée. Plusieurs solutions ont été envisagées. Une conception exploitant des anneaux résonateurs dans le silicium a été mise au point. Des premiers lasers de ce type ont été fabriqués, démontrant effectivement un fonctionnement mono-longueur d'onde. Des imperfections pendant la fabrication ont néanmoins perturbé le fonctionnement normal de ce type de laser. Des conceptions visant la réalisation de lasers DFB ont également été proposées et sont actuellement en fabrication. Une de ces conceptions, utilisant un réseau gravé dans la partie III-V avant le collage, a fait l'objet d'un brevet.

Tous ces travaux ont conduit à des avancées significatives dans la réalisation de lasers hybrides III-V sur SOI. Ils constituent une étape importante vers la réalisation de circuit photonique intégré en silicium.

Bibliographie

1. *Silicon Photonics: A Low Cost Integration Platform for Datacom and Telecom Applications.* **Asghari, Mehdi.** National Fiber Optic Engineers Conference, San Diego, 2008.
2. **Gunn, C.** CMOS Photonics for High-Speed Interconnects. *IEEE Micro.* 2006, Vol. 26, 2.
3. **Wada, K., Park, Sungbong and Ishikawa, Y.** Si Photonics and Fiber to the Home. *Proceedings of the IEEE.* 2009.
4. **J. Liu, X. Sun, R. Camacho-Aguilera, L. Kimerling, and J. Michel.** Ge-on-Si laser operating at room temperature. *Optical Letters.* 2010, Vol. 35.
5. **Razeghi, M., Defour, M. and R. Blondeau, F. Omnes, P. Maurel, O. Acher, F. Brillouet, J.C. C-Fan, J. Salerno.** First cw operation of a Ga_{0.25}In_{0.75}As_{0.5}P_{0.5}-InP laser on a silicon substrate. *Applied Physics Letters.* 1988, Vol. 53, 24.
6. **G. Roelkens, Y. De Koninck, S. Keyvaninia, S. Stankovic, M.Tassaert, M. Lamponi, Gh. Duan, D. Van Thourhout, R. Baets.** Hybrid Silicon Lasers. *SPIE.* 2011.
7. **A.W. Fang, H. Park, O. Cohen, R. Jones, M.J. Paniccia, J.E. Bowers.** Electrically pumped hybrid AlGaNAs-silicon evanescent laser. *Optics Express.* 2006, Vol. 14, pp. 9203-9210.
8. **A. W. Fang, B. R. Koch, R. Jones, E. Lively, D. Liang, Y.-H. Kuo, J.E. Bowers.** A Distributed Bragg Reflector Silicon Evanescent Laser. *Photonics Technology Letters.* 2008, Vol. 20, pp. 1667-1669.
9. **A.W. Fang, E. Lively, Y.-H. Kuo, D. Liang, J.E. Bowers.** A distributed feedback silicon evanescent laser. *Optics Express.* 2008, Vol. 16, pp. 4413-4419.
10. **G. Roelkens, J. Van Campenhout, J. Brouckaert, D. Van Thourhout, R. Baets, P. Rojo-Romeo et al.** III-V/Si photonics by die-to-wafer bonding. *Materials Today.* 2007, Vol. 10, pp. 36-43.
11. **L. Di, M. Fiorentino, J.E. Bowers, R.G. Beausoleil.** III-V-on-silicon hybrid integration, materials, devices, and applications. *IEEE Winter Topicals (WTM).* 2011.
12. **Roelkens, G., Van Thourhout, D. and Baets, R.** Ultra-thin benzocyclobutene bonding of III-V dies onto SOI substrate. *Electronics Letters.* 2005, Vol. 41, 9.
13. **B. Ben Bakir, A. Descos, N. Olivier, D. Bordel, P. Grosse, E. Augendre, L. Fulbert, and J. M. Fedeli.** Electrically driven hybrid Si/III-V Fabry-Pérot lasers based on adiabatic mode transformers. *Optics Express.* 2011, Vol. 19.
14. **Saleh, B.E.A. and Teich, M.C.** *Fundamentals of photonics.* s.l. : Wiley, 1991.
15. **Cook, J.S.** Tapered velocity couplers. *Bell Syst. Tech. Journals.* 1955.
16. **Fox, A. G.** Wave coupling by warped normal modes. *Bell Syst. Tech. Journals.* 1955.
17. **Sun, X., Liu, H-C and Yariv, A.** Adiabaticity criterion and the shortest adiabatic mode transformer in a coupled-waveguide system. *Optics Letters.* 2009, Vol. 34, 3.

18. **V. Jayaraman, Z.-M. Chuang, L.A. Coldren.** Theory, design, and performance of extended tuning range semiconductor lasers with sampled gratings. *Journal of Quantum Electronics*. 1993 йил, Vol. 29, 6.
19. **B. Liu, A. Shakouri, and J. E. Bowers.** Passive microring-resonator-coupled lasers . *Applied Physics Letters*. 2001, Vol. 79.
20. **Kogelnik, H. and Shank, C. V.** Stimulated emission in a periodic structure. *Applied Physics Letters*. 1971, Vol. 18, 4.
21. **Dupont, T., et al.** A III-V on silicon distributed-feedback laser based on exchange-Bragg coupling. *Proc. Group IV Photonics*. 2010.
22. **M. Zirngibl, C. H. Joyner, L. W. Stulz, U. Koren, M.-D. Chien, M. G. Young, and B. I. Miller.** Digitally Tunable Laser Based on the Integration of a Waveguide Grating Multiplexer and an Optical Amplifier. *Photonics Technologie Letters*. 1994, Vol. 6, 4.

